



**HAL**  
open science

# Anticiper la propagation des fissures en détectant des précurseurs dynamiques optiquement

Jianzhu Ju

► **To cite this version:**

Jianzhu Ju. Anticiper la propagation des fissures en détectant des précurseurs dynamiques optiquement. Chimie théorique et/ou physique. Université Paris sciences et lettres, 2021. Français. NNT : 2021UPSL089 . tel-03917146

**HAL Id: tel-03917146**

**<https://pastel.hal.science/tel-03917146v1>**

Submitted on 1 Jan 2023

**HAL** is a multi-disciplinary open access archive for the deposit and dissemination of scientific research documents, whether they are published or not. The documents may come from teaching and research institutions in France or abroad, or from public or private research centers.

L'archive ouverte pluridisciplinaire **HAL**, est destinée au dépôt et à la diffusion de documents scientifiques de niveau recherche, publiés ou non, émanant des établissements d'enseignement et de recherche français ou étrangers, des laboratoires publics ou privés.



**THÈSE DE DOCTORAT**  
**DE L'UNIVERSITÉ PSL**

Préparée à l'Ecole Supérieure de Physique et de Chimie  
Industrielles de la ville de Paris (ESPCI Paris)

**Anticiper la propagation des fissures en détectant des  
précurseurs dynamiques optiquement**

Anticipating crack propagation by detecting dynamic  
precursors with light

Soutenue par

**Jianzhu Ju**

Le 08 Décembre 2021

Ecole doctorale n° ED37

**Physique et chimie des matériaux**

Spécialité

**Physico-chimie**

Composition du jury :

Annie, COLIN Professor ESPCI, CNRS, Université de Bordeaux	<i>Présidente</i>
Jérôme, CRASSOUS Professor Université Rennes 1	<i>Rapporteur</i>
Stéphane, ROUX Professor ENS Paris Saclay	<i>Rapporteur</i>
Jian Ping, GONG Professor Hokkaido University	<i>Examineur</i>
Hanne, VAN DER KOOIJ Staff scientist Wageningen University & Research	<i>Examineur</i>
Luca, CIPELLETTI Professor Université Montpellier 2	<i>Examineur</i>
Tetsuharu, NARITA Chargé de recherche ESPCI, CNRS	<i>Directeur de thèse</i>
Costantino, CRETON Directeur de recherche ESPCI, CNRS	<i>Directeur de thèse</i>

---

## **Acknowledge**

Through my thesis, I received lots of help and support from my family, colleagues and friends and I would like to express my gratitude here.

I would like to thank my great supervisors, Costantino Creton and Tetsuharu Narita, for their guidance and support, not just in my research projects, but also in life. I would like to thank Luca Cipelletti (Montpellier University) and Chung Yuen Hui (Cornell University) for their valuable direction on my project. I couldn't accomplish my project without you.

My thanks go to my friends in the SIMM lab, especially Yuanyuan Wei, Zuxiang Xu, Gabriel Sanoja, Giorgia Scetta, Mohammad Asif Ali, Jean Comtet. I would also like to express my gratitude to my friends in Dodynet. We have spent so many happy time studying and relaxing together in the wonderful Dodynet events.

Finally, I would like to thank MARIE SKŁODOWSKA-CURIE ACTIONS Dodynet project for funding my PhD thesis and the opportunity to spend these happy three years in Europe.



GENERAL INTRODUCTION.....	2
1 Introduction and brief state of the Art: Energy dissipation mechanisms during fracture of soft polymer networks.....	5
1.1 Introduction.....	5
1.2 Polymer network and deformation .....	6
1.2.1 Deformation and elasticity of a single polymer chain.....	6
1.2.2 Deformation of an elastomer: network-affine network model.....	8
1.2.3 Strain hardening .....	10
1.2.4 Special network design based on interpenetrating network polymers	11
1.3 Overview of the fracture process of soft polymer networks.....	14
1.3.1 Linear elastic fracture mechanics.....	14
1.3.2 Dissipation behavior in polymer network.....	16
.1.3.2.1 Fracture energy threshold- Lake and Thomas model .....	16
.1.3.2.2 Viscoelastic dissipation.....	18
.1.3.2.3 Elastic blunting and local strain distribution .....	19
1.4 Crack tip characterization methods.....	22
1.4.1 Digital image correlation (DIC) .....	22
1.4.2 Mechanochemical tools for fracture characterization.....	23
1.4.3 Dynamic light scattering.....	25
1.4.4 Full scale measurement of the fracture behavior.....	25
1.5 Motivations and objectives of this work .....	26
1.6 Reference .....	29
2 Multispeckle diffusing wave spectroscopy as a tool to study heterogeneous mechanical behavior in soft solids.....	33
Abstract.....	33
2.1 Introduction.....	33
2.2 Optical theory.....	36

2.2.1	Dynamics Light scattering.....	36
.2.2.1.1	Scattering of multiple particles.....	36
.2.2.1.2	Autocorrelation functions of scattered light.....	37
.2.2.1.3	Characterization of Brownian motion and particle size.....	39
2.2.2	Diffusing wave spectroscopy.....	40
2.2.3	Multispeckle diffusing wave spectroscopy.....	43
.2.2.3.1	Multiple speckle imaging.....	43
.2.2.3.2	MSDWS and time/space resolution.....	44
.2.2.3.3	Testing geometry and autocorrelation function.....	47
.2.2.3.4	Dynamical processes probed by MSDWS.....	49
2.3	Material and methods.....	58
2.3.1	Materials.....	58
2.3.2	Experimental set-up.....	59
2.4	Method validation: uniaxial extension of PDMS.....	62
2.5	Measurement of heterogeneous deformation during adhesive debonding	64
2.6	Conclusions.....	74
2.7	Reference.....	75
2.8	Supporting Information:.....	80
3	Fast detection of early-stage damage in soft elastomers.....	82
	Abstract.....	82
3.1	Introduction.....	84
3.2	Results and Discussion.....	86
3.2.1	Simultaneous mapping of strain rate and damage.....	86
3.2.2	The contribution of slow crack propagation simulated by FEM.....	90
3.2.3	Damage prediction by MSDWS.....	94
3.3	Conclusions.....	98

3.4	Materials and methods .....	100
3.4.1	Material preparation .....	100
3.4.2	Optical measurement .....	100
.3.4.2.1	Confocal microscopy .....	100
.3.4.2.2	Multiple speckle diffusing wave spectroscopy.....	101
3.5	References .....	102
3.6	Supporting Information .....	104
3.6.1	Quantification of fluorescence intensity by confocal microscopy .	104
3.6.2	Strain rate mapping .....	106
.3.6.2.1	MSDWS .....	106
.3.6.2.2	Digital image correlation.....	109
.3.6.2.3	Finite element method (FEM) .....	111
3.6.3	Additional testing on natural rubber and pasta .....	121
4	In-situ 3D damage visualization at the crack tip in multiple network elastomers	127
4.1	Abstract .....	127
4.2	Introduction.....	128
4.3	Results and Discussion .....	130
4.3.1	Fast fracture.....	130
4.3.2	Delayed fracture .....	136
4.4	Conclusion .....	141
4.5	Materials and methods .....	143
4.5.1	Synthesis of Poly (ethyl acrylate) multiple network elastomers ...	143
4.5.2	Confocal microscopy.....	144
4.5.3	Digital image correlation .....	144
4.6	Reference .....	144
4.7	Supporting Information .....	147
4.7.1	Material preparation and measurement methods.....	147

4.7.2	Difficulties in dynamics measurement.....	147
4.7.3	Dynamic behavior before delayed fracture .....	148
5	Heterogeneous creasing and swelling in constrained hydrogel film.....	154
	Abstract.....	154
5.1	Introduction.....	156
5.2	Material and methods .....	159
5.2.1	Gel preparation and swelling .....	159
5.2.2	Data collection and processing.....	160
.5.2.2.1	Image collection.....	160
.5.2.2.2	Fitting of the autocorrelation function.....	161
.5.2.2.3	Time-averaged correlation maps .....	163
5.3	Morphological observation .....	164
5.4	MSDWS unveils multi-scale dynamics.....	166
5.4.1	Fast dynamics beyond swelling kinetics.....	166
5.4.2	Spatially and temporally heterogeneous swelling kinetics .....	168
5.5	Conclusions .....	177
5.6	Reference .....	178
5.7	Supporting information.....	181
5.7.1	Processing of raw speckle images .....	181
5.7.2	2D Fourier Transform processing of the images .....	182
5.7.3	Rotation of spiral pattern in round container .....	183
5.7.4	Supporting videos (available upon request).....	183
6	Conclusion and perspective.....	185
6.1	General conclusion.....	185
6.1.1	Optical methods for fracture characterization.....	185
6.1.2	Deformation heterogeneity as a sign of microscopic damage before fracture .....	186
6.1.3	Enhancement mechanism of fracture toughness in multiple network	



elastomers .....	187
6.1.4 Application of MSDWS to heterogeneous systems .....	187
6.2 Perspective .....	188
6.2.1 Synchronized and responsive controlling.....	188
6.2.2 Better understanding and application of MSDWS .....	189
6.2.3 Improving failure prediction with machine learning .....	189
6.3 Reference .....	190
Appendix.....	191

## General Introduction

## GENERAL INTRODUCTION

Fracture property of elastomers plays an essential role in both production and processing and in its numerous applications. Elastomers have the unique properties that they can have a reasonably large and nearly reversible deformability and strength at the same time, thanks to the network structural nature. On the other hand, the fracture of elastomers is different from that of other “hard” materials (typically like metal or glassy polymer) that display localized energy dissipation, in the fact that energy dissipation upon fracture can happen at larger and multiple length scales.

The primary objective of fracture research is to avoid or delay the structural failure. However, existing models of fracture of elastomers are mostly built based on the localized crack during propagation, at which stage macroscopic fracture is normally unstoppable. Studies have shown that microscopic change nucleates relative long time before macroscopically detectable propagation, but the systematic investigation has not been carried out due to the lack of dynamic characterization methods with sufficient resolution. In this thesis, we will focus on the characterization of the microscopic change related to the propagation nucleation and explore the possibility to predict or even prevent the macroscopic fracture by in-situ measurements.

To achieve this goal, spatially resolved measurement of the crack tip and surrounding region is required with fast enough resolution to extract the transient behavior before catastrophic fracture. Preferably, different measurements need to be performed simultaneously to observable behaviors over different length/time scales. In the thesis, spatially resolved multiple speckle diffusing wave spectroscopy (MSDWS) is intensively used to map the deformation rate heterogeneity before fracture, and is related to the level of covalent bond scission around the crack, visualized by confocal microscopy, mapping the activation into a fluorescent fragment of a force sensitive molecule called mechanophore.

The manuscript is organized into six chapters.

The first chapter is dedicated to the physical background of fracture in elastomer and the methods for crack characterization. The purpose is to give a general introduction of previous work on fracture and distinguish the discoveries made in this work from existing studies.

Chapters 2 to 5 are organized in the form of scientific papers.

In the second chapter, the application of MSDWS to the measurement of a spatially resolved deformation rate is introduced. We discuss the mathematical approach rationalizing the quantification of the deformation rate and the selection of the most relevant parameters in practical experimental measurements. As an example, the deformation rate on the interface during shear debonding of adhesive tapes is characterized and mapped with MSDWS.

In the third chapter, MSDWS is applied to characterize the fracture precursor before crack propagation in commercial PDMS elastomers (Sylgard 184). A large-scale deformation rate heterogeneity ( $\sim 1 \text{ cm}^2$ ) is detected a long time ( $\sim 10 \text{ min}$ ) before fracture, and attributed to the slow creation of a very localized ( $\sim 0.01 \text{ mm}^2$ ) damage around the crack. The discovery is applied to predict and prevent macroscopic fracture in practical condition.

In the fourth chapter, we studied the fracture behavior in multiple network elastomers made from poly (ethyl acrylate). As multiple networks are well-known to be able to dissipate energy by breaking bonds in a sacrificial network, we visualized here the 3D structure of the damaged region ahead of an open crack and found that multiple network elastomer show a self-strengthening mechanism around the crack tip that delocalizes the singularity in deformation and prevents propagation.

The fifth chapter is devoted to the characterization by MSDWS of the dynamics of surface creasing induced by constrained swelling in PVA hydrogel. The dynamics of heterogeneous swelling and creasing behavior is visualized by MSDWS with a high temporal resolution and results in observations that are different from existing classical models on gel swelling.

Finally, we summarize the general conclusion and discussed about the perspective based on this work in chapter six.

---

Chapter 1 Introduction and brief state of the Art:  
Energy dissipation mechanisms during fracture of  
soft polymer networks

# 1 Introduction and brief state of the Art: Energy dissipation mechanisms during fracture of soft polymer networks

## 1.1 Introduction

The purpose of this thesis is to study the fracture behavior of elastomers at the early stages of the failure process, i.e. before catastrophic propagation occurs. There have been many studies describing and discussing different energy dissipation mechanisms that dominate at different time or length scales,<sup>1-3</sup> but the focus has been mostly on the propagation stage where the assumption is that the elastic energy flow toward the crack tip (represented by the energy release rate  $\mathcal{G}$ ) is dissipated locally into heat due to a combination of molecular friction and local damage (bond scission), which is qualitatively represented by  $\Gamma$ , the fracture energy.<sup>4</sup> Much less has been done on the early stages of fracture, i.e. the criteria for crack nucleation or the existence of precursors to crack growth. It has been discovered that in delayed fracture,<sup>5-6</sup> microscopic change can be detected before the onset of crack propagation.<sup>7-8</sup> This implies that before commonly regarded “fracture”, the existence of fracture precursor already indicates the occurrence of macroscopic behavior. In this thesis, we focus on the in-situ characterization and detection of fracture precursor to explore the possibility to predict the macroscopic fracture behavior by optical methods.

In this chapter, we firstly introduce the underlining physics in the deformation and fracture of soft polymer networks. Then we briefly describe some characterization methods for crack tip investigation, which is important for the detection of fracture precursor in dynamic condition. Finally, we introduce the motivations and objectives of this thesis.

## 1.2 Polymer network and deformation

Polymers are macromolecules having the structure of long chains made of a large amount of repeating monomers. In the case of the crosslinked polymer network, chains are connected by crosslinkers and form a network structure, which largely changes the property of the material. In this part, we will firstly review the entropy elasticity and deformation of a single chain. After that, the deformation in network will be introduced.

### 1.2.1 Deformation and elasticity of a single polymer chain

Consider an ideal polymer chain made of  $N$  segments with length  $a$  as seen in Fig. 1.1, so that the mean-square end-to-end distance can be expressed as<sup>9</sup>:

$$\langle R^2 \rangle = Na^2 \quad 1.1$$

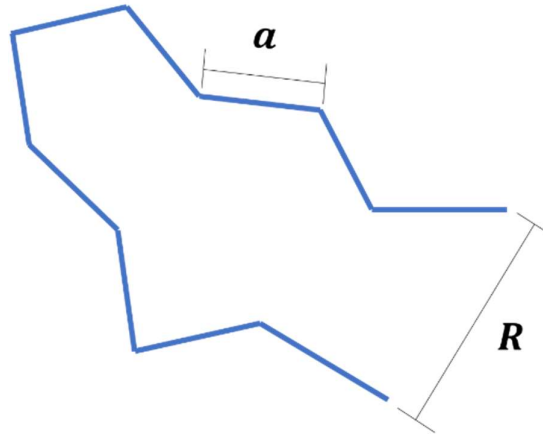


Fig. 1.1 An ideal molecular chain with  $N$  segment of length  $a$ .

Around the mean value, the end-to-end distance shows a Gaussian distribution. The probability that the distance locates between  $R$  and  $R+dR$  is:

$$P(N, R)dR = \left(\frac{3}{2\pi Na^2}\right)^{\frac{3}{2}} \left[ \exp\left(-\frac{3R^2}{2Na^2}\right) \right] dR \quad 1.2$$

The entropy of the polymer chain is the product of Boltzmann constant  $k$  by the logarithm of the number of states  $\Omega(N, R)$ :

$$S(N, R) = k \ln \Omega(N, R) \quad 1.3$$

$P(N, R)dR$  can also be given as the conformation concentration in the range of  $R$  to  $R+dR$ :

$$P(N, R)dR = \frac{\Omega(N, R)}{\int \Omega(N, R)} \quad 1.4$$

thus  $S(N, R)$  can be expressed by:

$$S(N, R) = k \ln P(N, R) + k \ln \int \Omega(N, R) dR \quad 1.5$$

and,

$$S(N, R) = k \left( -\frac{3R^2}{2Na^2} \right) + \frac{3}{2} k \ln \left( \frac{3}{2\pi Na^2} \right) + k \ln \int \Omega(N, R) dR . \quad 1.6$$

Note that the term  $\left[ \frac{3}{2} k \ln \left( \frac{3}{2\pi Na^2} \right) + k \ln \int \Omega(N, R) dR \right]$  is independent of  $R$ , thus normally expressed as  $S(N, 0)$ .

The Helmholtz free energy of the chain is:

$$F(N, R) = U(N, R) - TS(N, R) \quad 1.7$$

and the required force for the extension in the distance in the  $x$  direction  $R_x$  is:

$$f_x = \frac{\partial F(N, R)}{\partial R_x} \quad 1.8$$

In ideal chain without interchain energy change, the energy term  $U(N, R)$  is independent of  $R$ , so that:

$$f_x = T \frac{\partial S(N, R)}{\partial R_x} = \frac{3kT}{Na^2} R , \quad 1.9$$

where  $\frac{3kT}{Na^2}$  is called entropy elasticity constant.



## 1.2.2 Deformation of an elastomer: network-affine network model

Now we consider a polymer network made of  $n$  strands with  $N$  segments each. As seen in Fig. 1.2. one define the initial size of the sample as  $L_{x0}$ ,  $L_{y0}$  and  $L_{z0}$  and deformation in each direction as  $\lambda_x$ ,  $\lambda_y$  and  $\lambda_z$ , respectively. For each strand, in the initial size, mean square end-to-end distance is isotropic:

$$\langle R_{x0}^2 \rangle = \langle R_{y0}^2 \rangle = \langle R_{z0}^2 \rangle = \frac{Na^2}{3} \quad 1.10$$

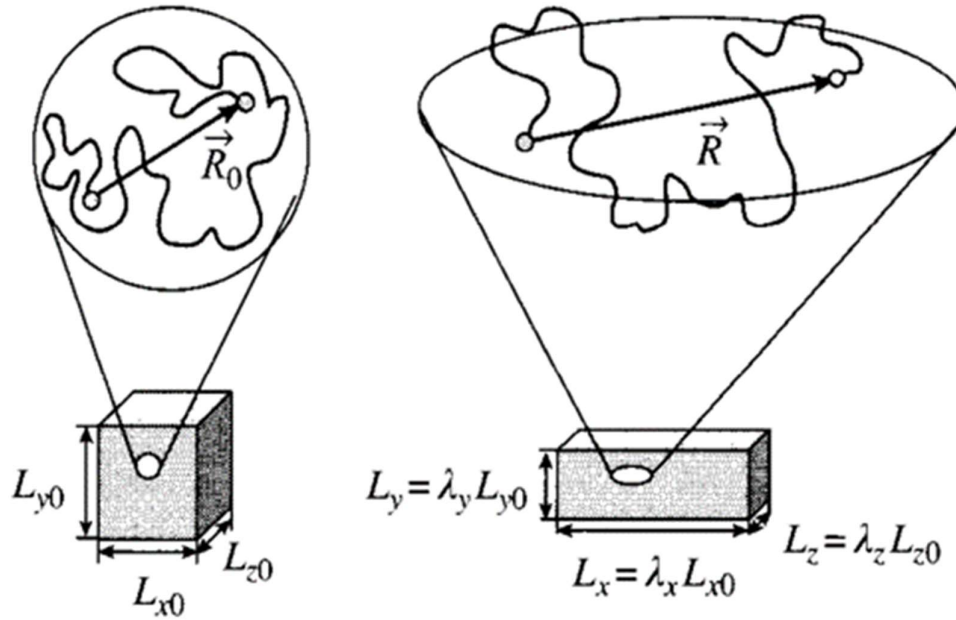


Fig 1.2 Affine network model where the deformation of every strand is same as the macroscopic deformation.

Eq. 1.6 is here expanded to 3D:

$$S(N, R) = -\frac{3k(R_x^2 + R_y^2 + R_z^2)}{2Na^2} + S(N, 0) \quad 1.11$$

The entropy change during deformation can be obtained:

$$S(N, R) - S(N, R_0) = -\frac{3k}{2Na^2} [R_{x0}^2(\lambda_x^2 - 1) + R_{y0}^2(\lambda_y^2 - 1) + R_{z0}^2(\lambda_z^2 - 1)] \quad 1.12$$

Using Eq. 1.10, the total entropy change can be rewritten as:

$$\Delta S = -\frac{nk}{2} [\lambda_x^2 + \lambda_y^2 + \lambda_z^2 - 3] \quad 1.13$$

which makes the free energy change:

$$\Delta F = \frac{nkT}{2} [\lambda_x^2 + \lambda_y^2 + \lambda_z^2 - 3]. \quad 1.14$$

If the network is incompressible, the volume is constant upon a uniaxial deformation  $\lambda_x$  in x direction, we have:

$$\lambda_x \lambda_y \lambda_z = 1 \quad 1.15$$

$$\lambda_y = \lambda_z = \frac{1}{\sqrt{\lambda_x}}. \quad 1.16$$

The free energy change becomes:

$$\Delta F = \frac{nkT}{2} \left( \lambda_x^2 + \frac{2}{\lambda_x} - 3 \right) \quad 1.17$$

and the force along deformation direction is:

$$f_x = \frac{\partial \Delta F}{\partial L_x} = \frac{\partial \Delta F}{\partial \lambda_x L_{x0}} = \frac{nkT}{L_{x0}} \left( \lambda_x - \frac{1}{\lambda_x^2} \right) \quad 1.18$$

The true stress and engineering stress are respectively:

$$\sigma_{true} = \frac{f_x}{L_y L_z} = \frac{nkT}{V} \left( \lambda_x^2 - \frac{1}{\lambda_x} \right) \quad 1.19$$

$$\sigma_{eng} = \frac{f_x}{L_{y0} L_{z0}} = \frac{nkT}{V} \left( \lambda_x - \frac{1}{\lambda_x^2} \right). \quad 1.20$$

This expression indicates that the stress is proportional to the strand density  $n/V$ , thus we find the modulus of the network as:

$$G = \frac{nkT}{V}, \quad 1.21$$

where the modulus for each strand is  $kT$ .

When the number-average molecular weight of each strand is  $M_n$  and the density is  $\rho$ ,  $n = 1$  would correspond to:

$$\nu = \frac{N_A \rho}{M_n} \quad 1.22$$

where  $N_A$  is Avogadro's number. Thus  $G$  can also be written as:

$$G = \frac{\rho N_A k T}{M_n} \quad 1.23$$

Classical models in fracture mechanics commonly focus on the linear elastic behavior which only considers small deformation. In reality, materials normally break at strain over 10% and with the existence of a crack, localized strain is even larger. In this region, non-linear behavior is dominating and rather complex.

### 1.2.3 Strain hardening

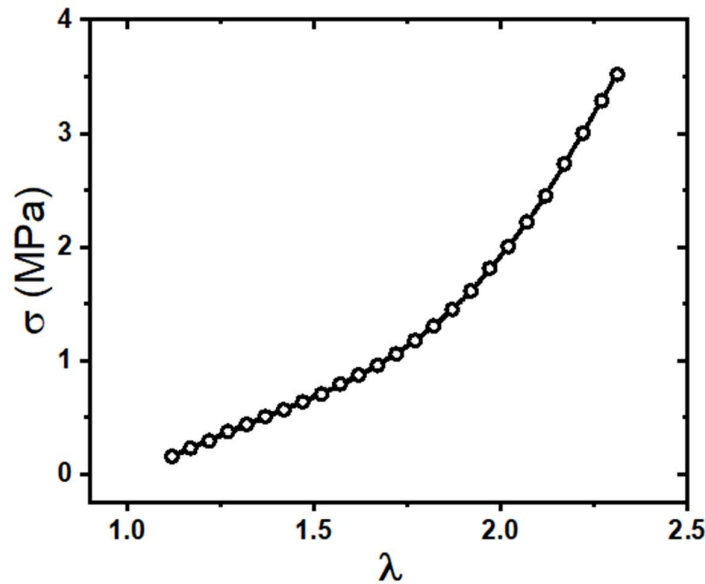


*Fig. 1.3 A stress stretch-curve during the uniaxial extension of an elastomer presenting strain hardening.*

Due to the finite extensibility of polymer chains, materials can exhibit strain hardening, i.e., an increase of the modulus at large strain. As seen in the example shown in Fig. 1.3,

when the elastomer is under uniaxial extension, the slope of stress-strain curve increases from around  $\lambda = 1.8$ . For some materials, it is hard to observe strain hardening since the presence of flaws leads to fracture before reaching large strains. However, due to the stress concentration around the crack tip (crack is also a flaw), large strain is commonly reached near the crack tip within the framework of the study of fracture.<sup>10</sup> Gent proposed a simple constitutive model of strain hardening that defines the maximal value  $J_m$  of the first strain invariant  $J$ .<sup>11</sup> In the model, the nominal stress in uniaxial extension  $\sigma_N$  is expressed by:<sup>12</sup>

$$\sigma_N = \frac{G(\lambda - \frac{1}{\lambda^2})}{(1 - \frac{J}{J_m})}, \quad 1.24$$

where

$$J(\lambda) = \lambda^2 + \frac{2}{\lambda} - 3. \quad 1.25$$

From Gent's model, it can be deduced from eq. 1.24 that, when  $\lambda$  approaches  $\lambda_m$ ,  $\frac{\partial \sigma_N}{\partial \lambda}$  dramatically increases, corresponding to strain hardening. Other than the finite extensibility of the polymer strands, structural changes such as strain induced crystallization,<sup>13</sup> or structure orientation<sup>14</sup> can also lead to strain hardening. Crystallization due to localized high strain in front of a mode I crack, also results in strain hardening, which further complicates the description of the fracture process.<sup>15-16</sup>

#### 1.2.4 Special network design based on interpenetrating network polymers

Conventional unfilled elastic soft materials typically are brittle and very sensitive to flaws – they can be broken more easily when there is stress localization. Many strategies have been developed to enhance the strength of polymer network materials without sacrificing elasticity and high modulus, such as making composites with fillers<sup>1</sup> and customizing the network structure to introduce viscoelasticity.<sup>17</sup> Among these strategies, double network (DN), a sub class of interpenetrated networks, is a popular approach to enhance the mechanical strength while retaining the extendibility and stiffness of polymer networks.<sup>18-19</sup> These interpenetrated networks of polymers commonly contain a brittle

network with limited extensibility and a network with longer chains maintaining material integrity, as seen in Fig. 1.4.<sup>18, 20-21</sup>

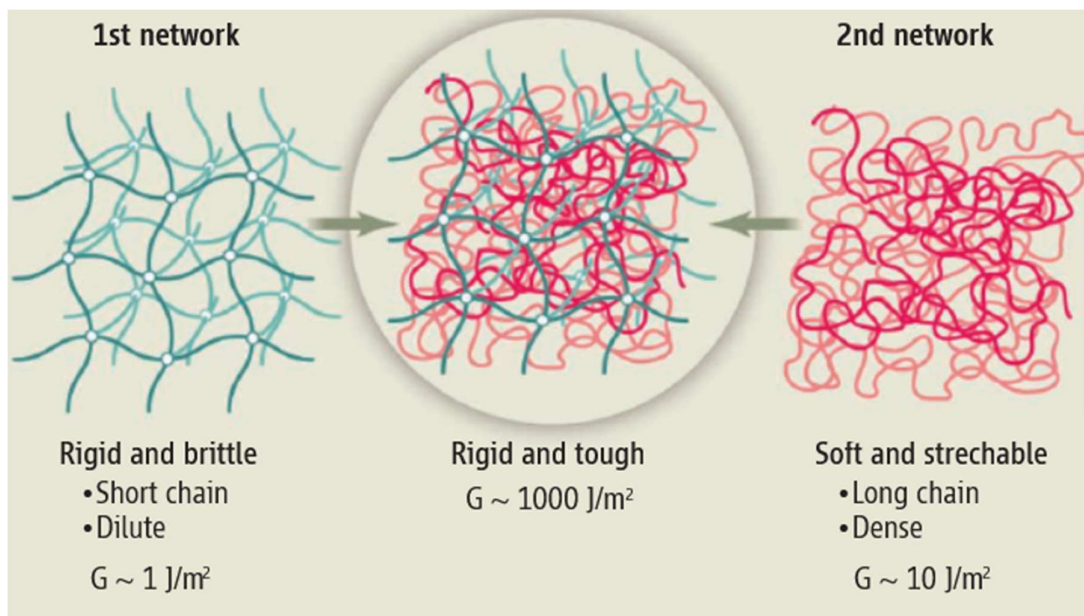
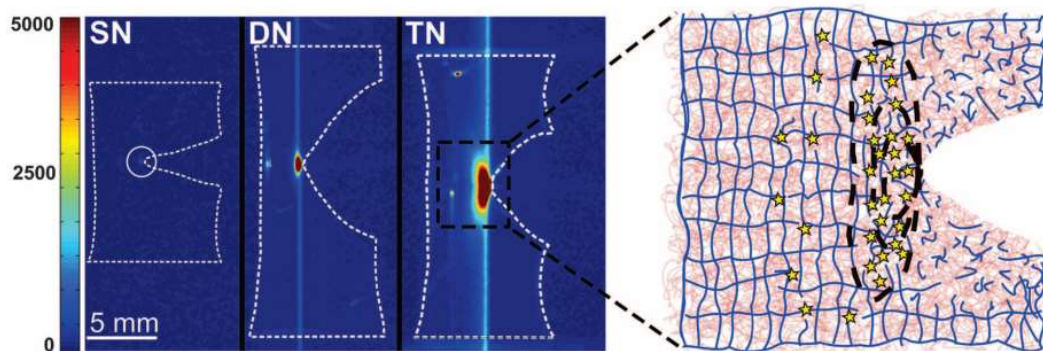


Fig. 1.4 Schematic drawing of the design of double network.<sup>18,20</sup>

Remarkably, the energy dissipation mechanism by scission of bonds in the brittle network (sacrificial network<sup>21-22</sup>) makes multiple network elastomers and hydrogels much more resistant to fracture. A fracture energy over  $1000 \text{ J/m}^2$  can be achieved, much larger than the single network from same monomer ( $1 \sim 10 \text{ J/m}^2$ ). It has been reported that in Multiple network elastomers (MNE) the strain concentration around the crack induces a localized damage, but at a larger length scale ( $\sim \text{mm}$ ).<sup>21</sup> Using mechanosensitive molecules emitting light when they break, Ducrot et al. observed the damage zone size during the propagation of a crack in SEN samples of SN (single network), DN (double network) and TN (triple network) of poly (ethyl acrylate) elastomers (Fig. 1.5). They found that the size of the damaged region increased dramatically with the introduction of matrix networks. The molecular fracture of the sacrificial network around the crack dissipates energy and delays the propagation of the crack.



*Fig. 1.5 Images of the fluorescence intensity recorded during the fracture and propagation of single-edge notched poly (ethyl acrylate) elastomers.*

Based on the design of the double network structure, more advanced strategies have been developed to further enhance the mechanical performance or achieve specific material properties. Instead of permanent damage by covalent bonds scission, physically crosslinked networks or networks with reversible covalent bonds can play the role as sacrificial network and can reform after being damaged.<sup>23-24</sup> The design of the hybrid physical- and chemical double networks can also provide self-healing properties within a certain time-scale.<sup>25-26</sup>

## 1.3 Overview of the fracture process of soft polymer networks

The fracture process of soft materials shows unique behaviors due to the complex hierarchical structure. In polymer networks, one has to include different dimensional scales (i.e. mesh size and crack/ flaw size, sample size) and time scales (considering viscoelasticity).<sup>27</sup> More practically, abundant structural heterogeneities may play important roles, such as strain induced crystallization, chain breakage and orientation. It is common to define the characteristic length scale over which mechanisms dominate, so that different mechanisms can be separated and used to analyze the fracture behavior.

One of the unique properties of soft polymer networks is the ability to significantly swell in a good solvent. A swollen polymer network is called a gel. Specifically, hydrogels are gel swollen in water, which can typically contain more than 90 % of water without breaking the network integrity. In Chapter 5, the swelling and creasing of hydrogel in a constrained geometry is studied to observe the heterogeneous behavior in the earlier stage of elastic instabilities. In the investigation of fracture behavior, which is the main topic of this thesis, we focus on elastomers, the polymer network material without solvent.

### 1.3.1 Linear elastic fracture mechanics

Linear elastic fracture mechanics (LEFM)<sup>28</sup> was established by assuming linear elasticity in the bulk of the material while the very small region around the crack is described by a singular stress field. The strain energy release rate  $\mathcal{G}$  describes the energy flow around the crack due to the far field loading and is given by:

$$\mathcal{G} = \frac{\partial U_w}{\partial A} - \frac{\partial U_{el}}{\partial A} \quad 1.26$$

where  $U_w$  and  $U_{el}$  are the external work and elastic stored energy, respectively.  $A$  is the crack surface area.  $U_w - U_{el}$  essentially describes how much elastic energy is available for crack propagation, i.e. for the creation of two crack surfaces. The exact expression of  $\mathcal{G}$  depends on the testing geometry. The energy cost (dissipation) per unit of creation of new surface  $\Gamma$ , is the fracture energy. The equilibrium/propagation condition is expressed by:

$$G \geq \Gamma \quad 1.27$$

In a simple geometry, where a crack in an infinite plate is defined as seen in Fig. 1.6, the stress field around the crack is expressed as the function of distance  $r$  from the crack tip:

$$\sigma(r) = \frac{K}{\sqrt{r}} \quad 1.28$$

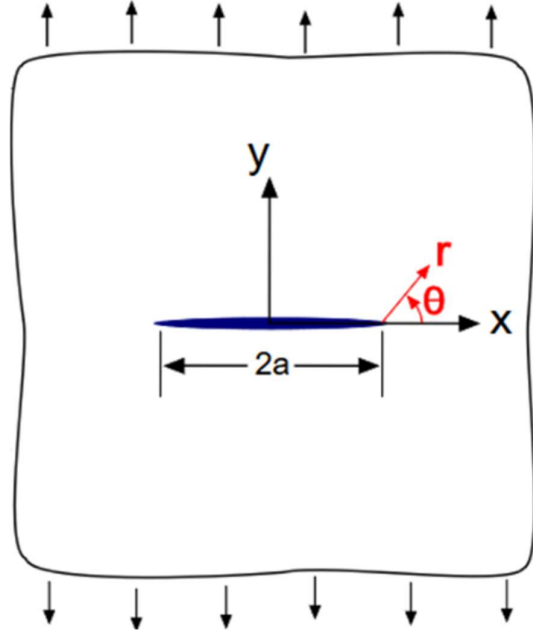


Fig. 1.6 A infinite plate with crack under uniaxial deformation.

where  $K$  is stress intensity factor<sup>29</sup>, which describes the stress distribution around the crack:

$$K = S\sigma_{\infty}\sqrt{\pi r} \quad 1.29$$

$\sigma_{\infty}$  is remote stress, which is the stress far away from the tip. Since the bulk region is linearly elastic, we have:

$$\varepsilon(r) = \frac{\sigma(r)}{E} = \frac{K}{E\sqrt{r}} \quad 1.30$$

The displacement field can be described:



$$u(r) = \int \varepsilon(r) dr = \frac{K}{E} \sqrt{r} \quad 1.31$$

The displacement field is a function of  $r$ , whose radius of curvature at the vertex is:

$$\rho_v = \frac{\partial^2 u}{\partial r^2} = \frac{K^2}{E^2} \quad 1.32$$

Irwin reported that  $\mathcal{G}$  is a function of  $K$  as<sup>30</sup>:

$$\mathcal{G} = \frac{K^2}{E} \quad 1.33$$

Using Eq. 1.27 and 1.32:

$$\rho_v = \frac{\mathcal{G}}{E} \geq \frac{\Gamma}{E} = \rho^* \quad 1.34$$

Eq 1.34 gives the critical radius  $\rho^*$  of crack curvature at propagation which defines an important physical length, so-called elasto-adhesive length which defines the region near the crack tip below which deformation is in the large strain regime. For most stiff materials (for example, metals),  $\rho^*$  has a scale below molecular dimension, so that LEFM can be well applied. However, for soft polymer material with moduli at MPa or less, typical values of  $\rho$  ranges from tens of microns to a few mm and calculations of  $\mathcal{G}$  with LEFM become approximate.

## 1.3.2 Dissipation behavior in polymer network

### 1.3.2.1 Fracture energy threshold- Lake and Thomas model

Essentially, fracture takes place by the breaking of covalent bonds in polymer chains. Thomas and Lake et al. proposed a model linking tear energy and bonds rupture in the polymer strands.<sup>3, 31</sup>

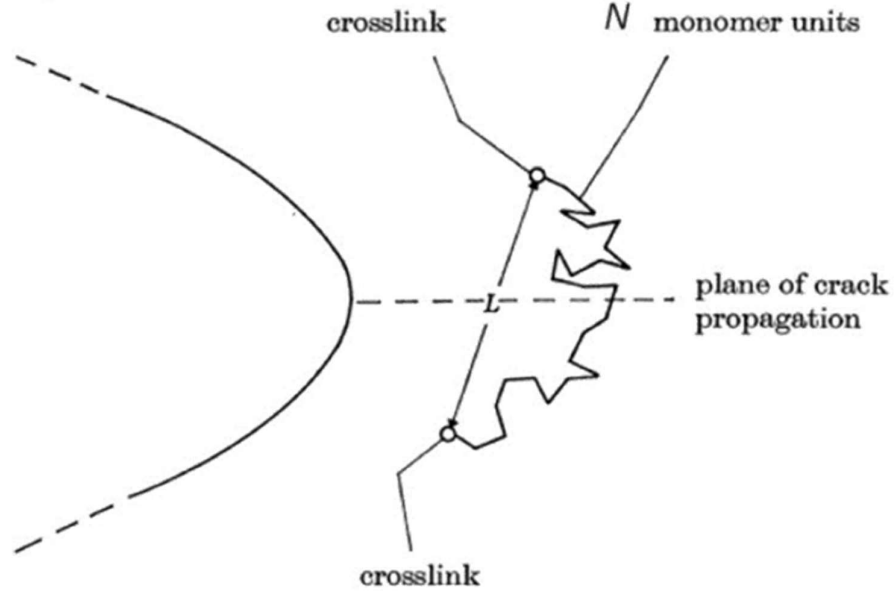


Fig. 1.7 Schematic diagram of the strand between two crosslinking points across the plane crack propagation.

To actually break a single bond, the required energy is proposed to be the same as that needed to break all the bonds in the strands.  $\Gamma$  can be obtained in this case by the bond energy  $U_b$  accumulated in the whole extended chain:

$$\Gamma = U_b N v L_c \quad 1.35$$

where  $N$  is the covalent bonds and  $L_c$  is the distance between two crosslinks, as seen in Fig. 1.7.

If we simply use an ideal chain model and assume that  $L$  has the value of square root of  $\langle R^2 \rangle$ :

$$L = N^{\frac{1}{2}} a \quad 1.36$$

$$\Gamma = U_b N^{\frac{3}{2}} v a \quad 1.37$$

Here the segment size  $a$  (as seen in Fig. 1.1) represents the monomer size.  $M_n$  in this case can be simply expressed as the total molecular weight of the strand where  $m$  is the monomer molar mass:

$$M_n = NmN_A \text{ and } N = \frac{M_n}{mN_A} \quad 1.38$$

Recall that modulus  $G$  is related to molecule weight of the strand (Eq. 1.23). Using Eq. 1.22, 1.23 and 1.29, we have:

$$\Gamma = \frac{U_b a \rho N_A}{M_n} \left( \frac{M_n}{m N_A} \right)^{\frac{3}{2}} = \frac{U_b a \rho}{(m)^{\frac{3}{2}}} \left( \frac{M_n}{N_A} \right)^{\frac{1}{2}} = U_b a \left( \frac{\rho}{m} \right)^{\frac{3}{2}} \left( \frac{kT}{G} \right)^{\frac{1}{2}} \quad 1.39$$

Simply,

$$\Gamma \propto G^{-\frac{1}{2}} \quad 1.40$$

If only energy dissipation by bond scission over one mesh size in the fracture plane is considered, the fracture can be described as a threshold fracture. It is commonly to consider bond dissociation energy  $U_{BDE}$  as  $U_b$  to estimate the scale of threshold of  $\Gamma$ , in the order of 10~100 J/m<sup>2</sup>. Recent work has argued that  $U_b$  may not be directly related to  $U_{BDE}$ , but depends on the force-extension relationship of the polymer chain.<sup>32</sup>

In practice, energy dissipation can take place at different length scales and be much more complex.

### .1.3.2.2 Viscoelastic dissipation

In the Lake and Thomas model, energy dissipation is limited to the length scale of the network mesh. However, when the crack propagation is not slow enough, the energy can be dissipated over a larger region in particular for viscoelastic materials. It has been known and reported for a long time that the fracture energy significantly increases with crack propagation velocity. Given that the probability of bond breaking for covalent bonds at room temperature is independent of rate, the viscoelastic nature of the polymer chain is coupled to the energy dissipation by bond scission. In principle, when the temperature approaches the glass transition temperature, the energy is increasingly dissipated into the bulk material over the time scale of the experiment. Note that the bond scission in the bulk close to glass transition temperature  $T_g$  has been reported for simple crosslinked networks<sup>33</sup> and for polymer melts close to  $T_g$ .<sup>34</sup>

Consider the crack propagation velocity  $V_c$  and a distance from the crack tip  $r$  (using the

geometry shown in Fig. 1.6). An estimate of the characteristic dissipation frequency can be obtained by:

$$\omega_d = \frac{V_c}{r} \quad 1.41$$

This characteristic frequency of the experiment should be compared to the chain relaxation time scales to assess the viscoelastic dissipation and such an approach has been used for the characterization of fracture in viscoelastic materials.<sup>35-38</sup> Conversely if the characteristic frequency at which the material is dissipative is known (from linear rheology), the value of the distance from the crack tip  $r$  where dissipation is maximal, can be obtained approximately. However, the characteristic length obtained from this procedure for elastic networks of low  $T_g$  is below the length scale of 0.01 nm, even smaller than the molecule size.<sup>2, 27</sup> This points out that a dissipation criterion depending only on frequency is not enough and other mechanisms close to the crack tip must be active.

#### .1.3.2.3 Elastic blunting and local strain distribution

From the Lake and Thomas model, a threshold value of applied  $G$  can be defined as the critical condition of crack propagation. In this case, an increase of nominal stress will always lead to crack propagation. However, this LEFM approach assumes that the crack remains sharp (large strain is not allowed). If one considers that the large strain deformation can occur around the crack, energy can be dissipated over a much larger region and the crack can open more. This subject was firstly investigated by Hui et al. where the concept of crack blunting was proposed.<sup>2</sup>

Instead of a sharp tip, the deformable crack is described as a long, thin ellipse, with half-length and half-height of  $A$  and  $B$ , respectively, as seen in Fig. 1.8.

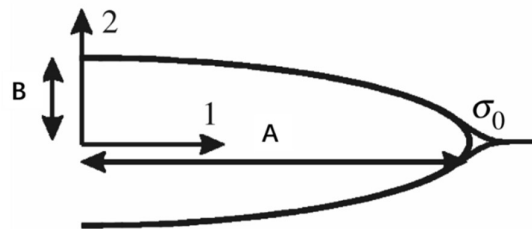


*Fig. 1.8 An elliptical crack with half-length and half-height of  $A$  and  $B$ , respectively.*

The radius of curvature is given by:

$$R_c = \frac{B^2}{A} \quad 1.42$$

In this geometry, the maximum stress close to the tip  $\sigma_{max}$  has been calculated:<sup>39</sup>

$$\sigma_{max} = \frac{2\sigma_{\infty}A}{B} = \frac{2\sigma_{\infty}\sqrt{A}}{R_c} \quad 1.43$$

Instead of propagating, the crack length,  $A$  remains constant and the deformation around the crack may lead to an increase of  $R_c$ . So that, for a given applied remote stress  $\sigma_{\infty}$ ,  $\sigma_{max}$  is smaller than the value considering a sharp tip. Phenomenologically, the crack is “opening” with increasing  $R_c$ , which is called elastic blunting. From simulation work or digital image correlation (DIC), the highly deformed region can be clearly visualized (Fig. 1.9).<sup>40</sup>

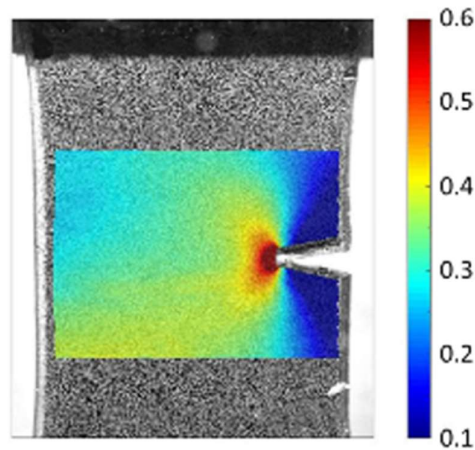


*Fig. 1.9 Strain distribution around the crack after deformation, visualized with finite element method (FEM).<sup>40</sup>*

Note that the above discussion only considers the deformation itself. Practically, polymer chains cannot be extended indefinitely without inducing structural changes in the material because of the presence of the chemical crosslinks. The complexity of the stress and strain field at the crack tip raises questions about the description of fracture, whose

characterization requires detection methods with suitable temporal and spatial resolutions, since the mechanical and structural change occur locally around the crack and are highly time-dependent before and during the propagation of the crack. In the next section, we will introduce several methods that are commonly applied for crack tip characterization.

## 1.4 Crack tip characterization methods

### 1.4.1 Digital image correlation (DIC)

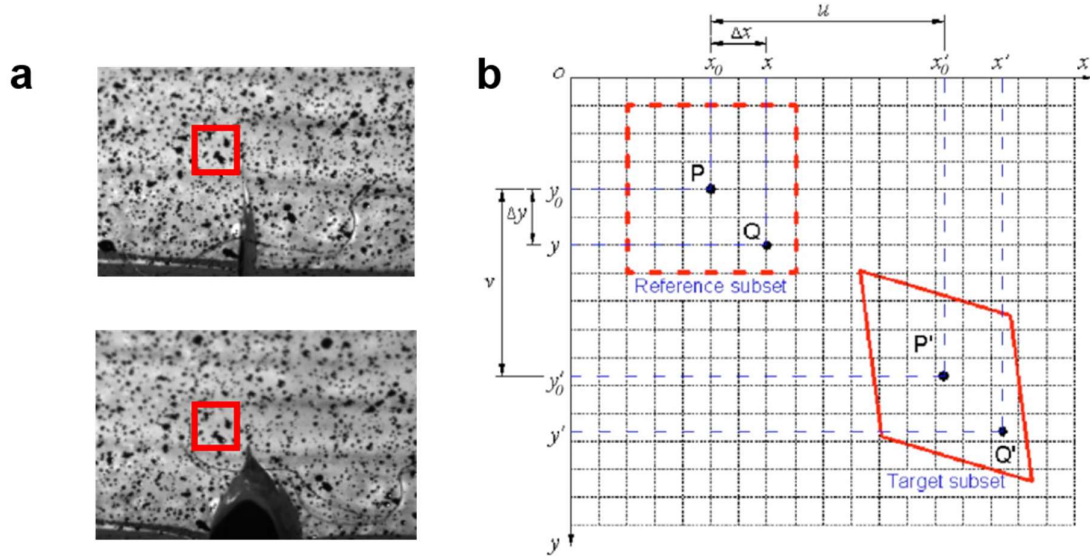


Fig. 1.10 (a) The images of a notched elastomer before (top) and after (bottom) stretching. (b) the reference subset and target subset for DIC.<sup>41</sup>

Digital image correlation (DIC) is a powerful and common method to measure the spatially resolved displacement/deformation in solid mechanics. The principle of DIC is to track the displacement of the subset (a region of interests (ROI) in the images) in a matrix extracted from greyscale images. As seen in Fig. 1.10(a), the surface of the notched elastomer is prepared by spray painting, which provides the speckles for recognizing the patterns. In the region around a deformed crack, the displacement of a subset can be detected, as seen Fig. 1.10(b). The displacement of the single subset,  $(u, v)$ , is obtained from DIC by solving normalized least-square correlation functions. With the spatially resolved displacement field  $u(x, y)$  and  $v(x, y)$ , the displacement gradient can be calculated by:<sup>41</sup>

$$u(x, y) = a_0 + a_1x + a_2y \quad 1.44a$$

$$v(x, y) = b_0 + b_1x + b_2y \quad 1.44b$$

where

$$a_1 = \varepsilon_{xx}, \quad b_2 = \varepsilon_{yy} \quad \text{and} \quad a_2 + b_1 = \varepsilon_{xy} + \varepsilon_{yx} \quad 1.45$$

The 2D displacement gradient tensor  $\mathbf{F}$  is denoted by:

$$\mathbf{F} = \begin{bmatrix} \varepsilon_{xx} & \varepsilon_{xy} \\ \varepsilon_{yx} & \varepsilon_{yy} \end{bmatrix} \quad 1.46$$

Note that the resolution of DIC merely depends on the image resolution and field size. Full-field deformation can be calculated from imaging of the whole sample,<sup>40</sup> while microscopic displacement can also be obtained from images by microscopy.<sup>42</sup>

More detailed information about DIC and how it was used in this thesis is also provided in Chapter 3.

### 1.4.2 Mechanochemical tools for fracture characterization

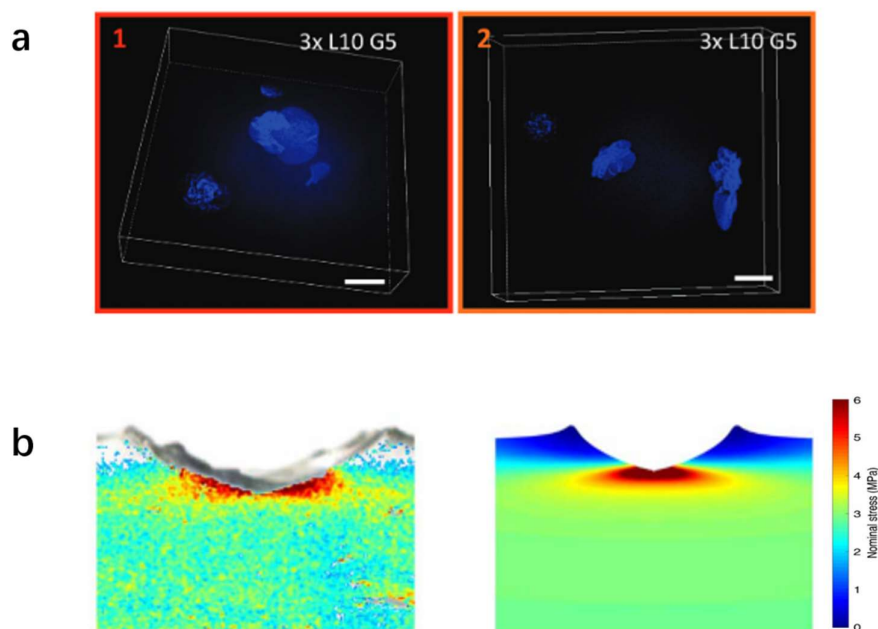


*Fig. 1.8 (a) Fluorescence intensity due to mechanophore activation from bonds breakage in poly (ethyl acrylates) networks labeled by mechanofluorescent polymer.<sup>43</sup> (b) Stress map calculated from the chromatic change in poly (ethyl acrylates) networks (with spiropyran force-activated mechanophore cross-linker.)<sup>44</sup>*

Mechanochemistry investigates molecules that undergo a chemical reaction under the



action of force.<sup>45</sup> In materials science, mechanophore molecules have been developed where the force activated chemical reaction has an optically detectable response. Either the molecule becomes fluorescent or it emits light upon scission (luminescent<sup>34</sup>) or under stress/extension.<sup>46</sup> With reasonable sensitivity to stress and damage during mechanical testing, mechanophore has been widely applied to quantitatively study mechanical response with optical observations, as seen in Fig. 1.8. As discussed in section 1.2.4,<sup>21</sup> during crack propagation of double networks, bond scission can be observed with activated mechanophores at a sub-macroscopic scale ( $\sim$ mm) around the crack tip, where energy is dissipated by massive breaking of sacrificial bonds in the localized region. Mechanophore mapping confirms that the breaking of molecular bonds takes place over a large length scale around the notch, providing important informations to understand the mechanism of toughening of double network materials.

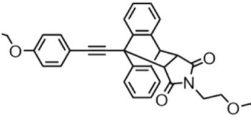
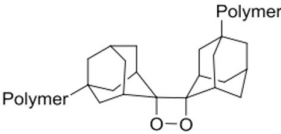
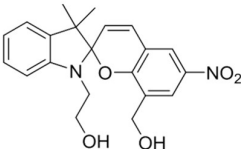
	Example	Emission spectrum
Mechanofluorescent polymer (Emission under excitation)		Dimer of anthracene: red fluorescence  $\pi$ -extended anthracene: blue fluorescence
Mechanoluminescent polymer (Emission without excitation)		1,2-Dioxetane: bright blue light
Mechanochromic polymer (Color in response of stress)		Spiropyran: colorless to purple  Rhodamine: dark red

Table 1.1 Examples of mechanophores.

Several different mechanophores are summarized in Table 1.1. Based on the activation mechanism, different strategies need to be applied during measurement. For example, with the bis(adamantyl)-1,2-dioxetane bisacrylate (BADOBA) crosslinker, transient luminescence is related to ongoing breaking of crosslinkers, which can be observed by a sensitive camera in a dark room.<sup>21, 47</sup> it is not suitable for long experiments with low level

emission since once the bond is broken the emission stops.

The Diels adder adduct of  $\pi$ -extended anthracene used as a diacrylate cross-linker on the other hand is fluorescent after breaking under UV illumination,<sup>33, 48</sup> so that accumulated damage can be quantified, where some bleaching under long time exposure also needs to be considered.<sup>49</sup>

In Chapter 3 and 4, we labeled Poly(dimethylsiloxane) and poly (ethyl acrylate) multiple network elastomers with  $\pi$ -extended anthracene diacrylate mechanophore as crosslinkers to visualize the damage behavior before and during crack propagation. With confocal microscopy, we then mapped and measured the fluorescence intensity to quantify the damage kinetics in the 3D configuration around the crack tip with micron scale resolution. More experimental details are shown in Chapters 3 and 4.

### 1.4.3 Dynamic light scattering

Visible light can be scattered by structures having different refraction indexes, such as heterogeneous concentration<sup>50</sup> and fillers<sup>51</sup>. For transparent (non-scattering) materials, one can add small amounts of probe particles with a significantly larger refraction index into the material, and light scattering will then measure the behavior of the probe motion to characterize the behavior of the material itself.

By the time auto-correlation function of the dynamically scattered light intensity, the motion/dynamics of the probe particles can be measured. The probe particle can interact with the material itself which depends on the inherent mechanical properties of the material, or it can be displaced affinely with the material as the result of the deformation field in mechanical testing.

In this thesis, we developed an advanced modification of dynamics light scattering (DLS), called multiple speckle diffusing wave spectroscopy (MSDWS), and intensively applied it to the characterization of fracture precursors. This advanced light scattering method is further discussed in detail in Chapter 2.

### 1.4.4 Full scale measurement of the fracture behavior

We summarize here the methods we showed in this section in Table 1.2. By the combination of different optical characterization methods during in-situ measurement,

different length/time scales can be covered, providing a full scale information of fracture behavior.

	Detection Length (of the motion/structure)	Field range	Time Resolution
DIC	Sub-pixel displacement (~1 $\mu\text{m}$ for full field mapping)	Full field (~5 cm)	Camera frequency (~100 fps)
Mechanophore by confocal microscopy	Molecular response (~nm)	1~5 mm	Scanning frequency (Up to 2 fps)
Dynamic Light scattering	Displacement of $1/k$ ( $k$ wave vector) (~50 nm)	Full field (~5 cm)	Camera frequency (~100 fps)

*Table 1.2 Different optical characterization methods and corresponding time/space resolution.*

## 1.5 Motivations and objectives of this work

We have introduced briefly different energy dissipation mechanisms during the fracture of elastomer materials. Due to the high level of deformation and rich structural heterogeneity of elastomers in service, energy dissipation mechanisms can occur over multiple time- and space- scales and are specific for each material. When the characteristic length of the different mechanisms overlaps with each other, existing models are not sufficient to describe and predict the fracture behavior. More importantly, most of the publications focus on the (steady) propagation stage where steady-state is already reached, but much less on how the propagation nucleates. A major challenge for the experimental investigation is that fracture is normally a catastrophic and dynamic process, where the macroscopic change (the propagation of a crack) occurs rapidly (~ 1

s). Fatigue testing of notched samples under a moderate but cyclic load is an alternative approach to study dynamic microscopic change by observing the accumulated change in structure over cyclic loading.<sup>52-53</sup> Post-mortem measurements on broken samples to observe the structure and morphology on the crack surface can provide some informations on the criteria needed for crack growth<sup>33, 54</sup> but the transient information may be lost after the release of the tension and deformation.

Essentially, the objective of the study of fracture is to detect clues to avoid the fracture from happening. However, when a steady propagation is reached, full rupture of the material is unstoppable in most cases. Remarkably, it has been recently reported that before the onset of macroscopic fracture by crack propagation at fixed deformation, some microscopic changes can be detected in advance.<sup>7-8</sup> The existence of these fracture precursors indicates the possibility to anticipate the macroscopic crack propagation by in-situ crack characterization. However, so far the study of fracture precursors has remained at the stage of post-processing the data, when fracture already took place. The main objective of this thesis is to apply advanced methods to directly characterize the precursors and onset of fracture in dynamic conditions in real time. We aim to predict the fracture before macroscopic changes occur and extend the warning time for fracture prevention.

Achieving this goal requires methods with sufficient time- and space- resolution and the test geometry should be suitable to be combined with fracture testing. Thanks to the development of optical technologies and digital image processing, a variety of in-situ measurement methods are able to provide the quantitative characterization of transient microscopic behaviors. As described in Section 1.5, different methods can be applied for in-situ crack characterization to investigate dynamic fracture precursors. For example, the combination of confocal microscopy and mechanochemistry can provide a time-resolved 3D mapping of molecular bond scission that can be taken as a damage variable. The fraction of broken crosslinker in the polymer network can be obtained after a careful calibration.<sup>33</sup> For the measurement of the spatially resolved deformation field, digital image correlation has been largely developed where displacement can be quantitatively measured with sub-pixel resolution in in the right conditions.<sup>40</sup> In this thesis, we intensively used multiple speckle diffusing wave spectroscopy (MSDWS) to measure the subtle changes in strain rate to visualize transient responses before and during fracture.

MSDWS is an advanced modification of conventional dynamic light scattering (DLS) where the decorrelation of multiply scattered light intensity can be used to quantify nanometric displacement of the probe in the material. The method has been reported previously to detect microscopic behavior before macroscopic transition<sup>7-8</sup> but here we further develop the applicability of this novel method to take the full use of its excellent resolution and apply it to more practical and complex conditions.

By the combined application of MSDWS, confocal microscopy DIC, and finite element simulation, we make a first attempt to complete the full picture of transient behaviors *before* and during dynamic fracture for two sets of model materials: a commercially available nano-filled polydimethylsiloxane (Sylgard 184) and a series of model multiple network poly (ethyl acrylate) elastomers developed in our laboratory that display significant toughening and very different crack propagation patterns. These transient behaviors can be applied to predict and prevent crack propagation in practical conditions. As an experiment-focused study, we hope that our observations will also trigger theoretical study of fracture mechanics and provide some insight for the design of material with better fracture resistance.

Finally, a remark to the reader. The manuscript has been organized as a set of papers and each chapter contains its own state of the art and bibliographic information. Furthermore, I participated in several scientific collaborations during my PhD and some of these collaborations led to publications where I am included as a coauthor. For the sake of coherence this work is not included in the main manuscript but can be found as published papers at the end.

## 1.6 Reference

1. Gent, A., Adhesion and strength of viscoelastic solids. Is there a relationship between adhesion and bulk properties? *Langmuir* **1996**, *12* (19), 4492-4496.
2. Hui, C.-Y.; Bennison, S.; Londono, J., Crack blunting and the strength of soft elastic solids. *Proceedings of the Royal Society of London. Series A: Mathematical, Physical and Engineering Sciences* **2003**, *459* (2034), 1489-1516.
3. Lake, G.; Thomas, A., The strength of highly elastic materials. *Proceedings of the Royal Society of London. Series A. Mathematical and Physical Sciences* **1967**, *300* (1460), 108-119.
4. Creton, C.; Ciccotti, M., Fracture and adhesion of soft materials: a review. *Rep Prog Phys* **2016**, *79* (4), 046601.
5. Wang, X.; Hong, W., Delayed fracture in gels. *Soft Matter* **2012**, *8* (31).
6. Bonn, D.; Kellay, H.; Prochnow, M.; Ben-Djemaa, K.; Meunier, J., Delayed fracture of an inhomogeneous soft solid. *Science* **1998**, *280* (5361), 265-267.
7. van der Kooij, H. M.; Dussi, S.; van de Kerkhof, G. T.; Frijns, R. A.; van der Gucht, J.; Sprakel, J., Laser Speckle Strain Imaging reveals the origin of delayed fracture in a soft solid. *Science advances* **2018**, *4* (5), eaar1926.
8. Aime, S.; Ramos, L.; Cipelletti, L., Microscopic dynamics and failure precursors of a gel under mechanical load. *Proc Natl Acad Sci U S A* **2018**, *115* (14), 3587-3592.
9. Rubinstein, M.; Colby, R. H., *Polymer physics*. Oxford university press New York: 2003.
10. Krishnan, V. R.; Hui, C. Y.; Long, R., Finite strain crack tip fields in soft incompressible elastic solids. *Langmuir* **2008**, *24* (24), 14245-14253.
11. Gent, A. N., A new constitutive relation for rubber. *Rubber chemistry and technology* **1996**, *69* (1), 59-61.
12. Horgan, C. O.; Saccomandi, G., Phenomenological hyperelastic strain-stiffening constitutive models for rubber. *Rubber chemistry and technology* **2006**, *79* (1), 152-169.
13. Cui, K.; Meng, L.; Tian, N.; Zhou, W.; Liu, Y.; Wang, Z.; He, J.; Li, L., Self-acceleration of nucleation and formation of shish in extension-induced crystallization with strain beyond fracture. *Macromolecules* **2012**, *45* (13), 5477-5486.
14. Sbrescia, S.; Ju, J.; Engels, T.; Van Ruymbeke, E.; Seitz, M., Morphological origins of temperature and rate dependent mechanical properties of model soft thermoplastic elastomers. *Journal of Polymer Science* **2021**, *59* (6), 477-493.
15. Rong, G.; Hamed, G.; Jiang, J., Comparison of the strength of normal and edge-cut tensile specimens of styrene-butadiene rubber and natural rubber with similar crosslink density. *Rubber Chemistry and Technology* **2016**, *89* (4), 631-639.
16. Kurelec, L.; Teeuwen, M.; Schoffeleers, H.; Deblicq, R., Strain hardening modulus as a measure of environmental stress crack resistance of high density polyethylene. *Polymer* **2005**, *46* (17), 6369-6379.
17. Persson, B.; Albohr, O.; Heinrich, G.; Ueba, H., Crack propagation in rubber-like materials. *Journal of Physics: Condensed Matter* **2005**, *17* (44), R1071.
18. Gong, J. P.; Katsuyama, Y.; Kurokawa, T.; Osada, Y., Double-Network Hydrogels with Extremely High Mechanical Strength. *Advanced Materials* **2003**, *15* (14), 1155-1158.
19. Millereau, P.; Ducrot, E.; Clough, J. M.; Wiseman, M. E.; Brown, H. R.; Sijbesma, R. P.; Creton, C., Mechanics of elastomeric molecular composites. *Proceedings of the National Academy of Sciences* **2018**, *115* (37), 9110-9115.
20. Gong, J. P., Materials both tough and soft. *Science* **2014**, *344* (6180), 161-162.

21. Ducrot, E.; Chen, Y. L.; Bulters, M.; Sijbesma, R. P.; Creton, C., Toughening Elastomers with Sacrificial Bonds and Watching Them Break. *Science* **2014**, *344* (6180), 186-189.
22. Fantner, G. E.; Hassenkam, T.; Kindt, J. H.; Weaver, J. C.; Birkedal, H.; Pechenik, L.; Cutroni, J. A.; Cidade, G. A.; Stucky, G. D.; Morse, D. E.; Hansma, P. K., Sacrificial bonds and hidden length dissipate energy as mineralized fibrils separate during bone fracture. *Nat Mater* **2005**, *4* (8), 612-6.
23. Sun, J.-Y.; Zhao, X.; Illeperuma, W. R.; Chaudhuri, O.; Oh, K. H.; Mooney, D. J.; Vlassak, J. J.; Suo, Z., Highly stretchable and tough hydrogels. *Nature* **2012**, *489* (7414), 133-136.
24. Schäfer, S.; Kickelbick, G., Double Reversible Networks: Improvement of Self-Healing in Hybrid Materials via Combination of Diels–Alder Cross-Linking and Hydrogen Bonds. *Macromolecules* **2018**, *51* (15), 6099-6110.
25. Long, R.; Mayumi, K.; Creton, C.; Narita, T.; Hui, C.-Y., Time dependent behavior of a dual cross-link self-healing gel: Theory and experiments. *Macromolecules* **2014**, *47* (20), 7243-7250.
26. Long, R.; Mayumi, K.; Creton, C.; Narita, T.; Hui, C.-Y., Rheology of a dual crosslink self-healing gel: Theory and measurement using parallel-plate torsional rheometry. *Journal of Rheology* **2015**, *59* (3), 643-665.
27. Creton, C.; Ciccotti, M., Fracture and adhesion of soft materials: a review. *Reports on Progress in Physics* **2016**, *79* (4), 046601.
28. Griffith, A. A., VI. The phenomena of rupture and flow in solids. *Philosophical transactions of the royal society of london. Series A, containing papers of a mathematical or physical character* **1921**, *221* (582-593), 163-198.
29. Irwin, G.; de Wit, R., A summary of fracture mechanics concepts. *Journal of Testing and Evaluation* **1983**, *11* (1), 56-65.
30. Irwin, G., Linear fracture mechanics, fracture transition, and fracture control. *Engineering fracture mechanics* **1968**, *1* (2), 241-257.
31. Akagi, Y.; Sakurai, H.; Gong, J. P.; Chung, U.-i.; Sakai, T., Fracture energy of polymer gels with controlled network structures. *The Journal of chemical physics* **2013**, *139* (14), 144905.
32. Wang, S.; Panyukov, S.; Rubinstein, M.; Craig, S. L., Quantitative Adjustment to the Molecular Energy Parameter in the Lake–Thomas Theory of Polymer Fracture Energy. *Macromolecules* **2019**, *52* (7), 2772-2777.
33. Sloopman, J.; Waltz, V.; Yeh, C. J.; Baumann, C.; Göstl, R.; Comtet, J.; Creton, C., Quantifying Rate- and Temperature-Dependent Molecular Damage in Elastomer Fracture. *Physical Review X* **2020**, *10* (4).
34. Chen, Y.; Spiering, A.; Karthikeyan, S.; Peters, G. W.; Meijer, E.; Sijbesma, R. P., Mechanically induced chemiluminescence from polymers incorporating a 1, 2-dioxetane unit in the main chain. *Nature chemistry* **2012**, *4* (7), 559-562.
35. Sun, T. L.; Luo, F.; Hong, W.; Cui, K.; Huang, Y.; Zhang, H. J.; King, D. R.; Kurokawa, T.; Nakajima, T.; Gong, J. P., Bulk energy dissipation mechanism for the fracture of tough and self-healing hydrogels. *Macromolecules* **2017**, *50* (7), 2923-2931.
36. Schapery, R. A., A theory of crack initiation and growth in viscoelastic media. *International Journal of fracture* **1975**, *11* (1), 141-159.
37. Gennes, P. d., Simple views on adhesion and fracture. *Canadian Journal of Physics* **1990**, *68* (9), 1049-1054.
38. Long, R.; Hui, C.-Y.; Gong, J. P.; Bouchbinder, E., The fracture of highly deformable soft materials: A tale of two length scales. *Annual Review of Condensed Matter Physics* **2021**, *12*, 71-94.
39. Timoshenko, S.; Goodier, J., Two-dimensional problems in polar coordinates. In

*Theory of Elasticity*, McGraw-Hill New York: 1970; pp 65-149.

40. Liu, M.; Guo, J.; Hui, C. Y.; Zehnder, A. T., Application of Digital Image Correlation (DIC) to the Measurement of Strain Concentration of a PVA Dual-Crosslink Hydrogel Under Large Deformation. *Experimental Mechanics* **2019**.
41. Pan, B.; Xie, H.; Guo, Z.; Hua, T., Full-field strain measurement using a two-dimensional Savitzky-Golay digital differentiator in digital image correlation. *Optical Engineering* **2007**, *46* (3), 033601.
42. Han, K.; Ciccotti, M.; Roux, S., Measuring nanoscale stress intensity factors with an atomic force microscope. *EPL (Europhysics Letters)* **2010**, *89* (6), 66003.
43. Morelle, X. P.; Sanoja, G. E.; Castagnet, S.; Creton, C., 3D fluorescent mapping of invisible molecular damage after cavitation in hydrogen exposed elastomers. *Soft Matter* **2021**, *17* (16), 4266-4274.
44. Chen, Y.; Yeh, C. J.; Qi, Y.; Long, R.; Creton, C., From force-responsive molecules to quantifying and mapping stresses in soft materials. *Science advances* **2020**, *6* (20), eaaz5093.
45. Chen, Y.; Mellot, G.; van Luijk, D.; Creton, C.; Sijbesma, R. P., Mechanochemical tools for polymer materials. *Chemical Society Reviews* **2021**, *50* (6), 4100-4140.
46. Davis, D. A.; Hamilton, A.; Yang, J.; Cremer, L. D.; Van Gough, D.; Potisek, S. L.; Ong, M. T.; Braun, P. V.; Martínez, T. J.; White, S. R., Force-induced activation of covalent bonds in mechanoresponsive polymeric materials. *Nature* **2009**, *459* (7243), 68-72.
47. Clough, J. M.; Creton, C.; Craig, S. L.; Sijbesma, R. P., Covalent Bond Scission in the Mullins Effect of a Filled Elastomer: Real-Time Visualization with Mechanoluminescence. *Advanced Functional Materials* **2016**, *26* (48), 9063-9074.
48. Gostl, R.; Sijbesma, R. P., pi-extended anthracenes as sensitive probes for mechanical stress. *Chem Sci* **2016**, *7* (1), 370-375.
49. Qian, H., The connection between molecular switches and mechanophores. *Chem* **2021**, *7* (4), 831-833.
50. Murase, H.; Ohta, Y.; Hashimoto, T., A new scenario of shish-kebab formation from homogeneous solutions of entangled polymers: Visualization of structure evolution along the fiber spinning line. *Macromolecules* **2011**, *44* (18), 7335-7350.
51. Eric, H.; Ruili, W.; Xx, Z., Silica fillers of varying size and their effect on mechanical and optical properties. *Frontiers in Bioengineering and Biotechnology* **2016**, *4*.
52. Scetta, G.; Euchler, E.; Ju, J.; Selles, N.; Heuillet, P.; Ciccotti, M.; Creton, C., Self-Organization at the Crack Tip of Fatigue-Resistant Thermoplastic Polyurethane Elastomers. *Macromolecules* **2021**.
53. Mzabi, S.; Berghezan, D.; Roux, S.; Hild, F.; Creton, C., A critical local energy release rate criterion for fatigue fracture of elastomers. *Journal of Polymer Science Part B: Polymer Physics* **2011**, *49* (21), 1518-1524.
54. Andersson, H.; Persson, C., In-situ SEM study of fatigue crack growth behaviour in IN718. *International Journal of Fatigue* **2004**, *26* (3), 211-219.



---

Chapter 2 Multispeckle diffusing wave  
spectroscopy as a tool to study heterogeneous  
mechanical behavior in soft solids

## 2 Multispeckle diffusing wave spectroscopy as a tool to study heterogeneous mechanical behavior in soft solids

Jianzhu Ju <sup>a</sup>, Luca Cipelletti <sup>b,c</sup>, Tetsuharu Narita <sup>\*, a,d</sup>, Costantino Creton <sup>\*, a,d</sup>

<sup>a</sup> Sciences et Ingénierie de la Matière Molle, CNRS UMR 7615, ESPCI Paris, PSL Université, Paris, France

<sup>b</sup> Laboratoire Charles Coulomb (L2C), University of Montpellier, CNRS, Montpellier, France

<sup>c</sup> Institut Universitaire de France

<sup>d</sup> Global Station for Soft Matter, Global Institution for Collaborative Research and Education, Hokkaido University, Sapporo, Japan

### Abstract

Multiple speckle diffusing wave spectroscopy (MSDWS) can be applied to measure spatially heterogeneous mechanical behavior in soft solids, with high sensitivity to deformation and both spatial and temporal resolution. In this paper, we discuss the mathematical approach behind the quantification of the deformation rate from MSDWS data and provide guidelines for optimizing the selection of experimental parameters in measurements. After validating the method in extensional tests on an elastomer, we provide an example of the potentiality of MSDWS by measuring the spatial distribution of the deformation rate during shear debonding of adhesive tapes. We quantitatively characterize the deformation rate heterogeneity related to shearing and peeling under loading and show that an increase in deformation localization is detected hundreds of seconds before full debonding. This behavior, previously predicted by theory and simulation, is here demonstrated experimentally for the first time.

### 2.1 Introduction

The mechanical response of soft materials under external loading provides valuable

---

\*correspondence authors: [tetsuharu.narita@espci.fr](mailto:tetsuharu.narita@espci.fr), [costantino.creton@espci.fr](mailto:costantino.creton@espci.fr)

information about the structural composition and the application properties under dynamic conditions, especially for soft materials with high deformability and viscoelasticity. In common tests on soft solids, such as shear rheology and uniaxial stretching, one assumes that the material properties are spatially homogeneous, so that the remote stress under deformation (or macroscopic strain under creep stress) completely defines the mechanical response.<sup>1-2</sup> However, it is commonly reported, especially at large deformations<sup>3-4</sup> or with the existence of flaws,<sup>5-7</sup> that the material properties and in particular their mechanical response can be spatially heterogeneous and deviate from that inferred from simple models assuming homogeneity.

Although measurement of macroscopic mechanical response can also unveil local failure<sup>8-10</sup> and structural transitions,<sup>11-12</sup> the most direct and reliable way to investigate such phenomena is the full-field measurement on the whole sample, with both temporal and spatial resolution. Several imaging methods such as digital image correlation (DIC),<sup>13</sup> birefringence imaging,<sup>14-15</sup> and mechanophore fluorescence mapping<sup>16-17</sup> can provide spatially-resolved information on the mechanical response. Among these methods, DIC measures the spatially-resolved deformation field and is commonly used for mechanical measurement in soft materials, since it can be easily combined with ordinary testing systems.<sup>18-19</sup> DIC quantifies the displacement of region of interests (ROIs) of the sample by comparing two images of the sample surface. To optimize the DIC algorithm, the surface should be spray-painted with a highly contrasted, speckled pattern. However, the observations of spray-painted samples bring several limitations: (1) DIC is essentially a surface measurement, where the bulk deformation cannot be detected. In fact, any contribution due to the bulk needs to be minimized, to avoid interfering with the surface imaging. Furthermore, (2) spray painting may be difficult or even impossible for some materials, such as hydrogels with a high water content.<sup>5</sup> Sprayed speckles can also lose their original shape at large strains and detach from the sample surface, making the correlation of images difficult.<sup>20</sup> Finally, (3) although DIC provides in general excellent spatial resolution and high sensitivity to displacement, both spatial resolution and sensitivity are limited by the characteristic size of the speckled pattern, which can be difficult to reduce, e.g. as needed when working with small sample surfaces.

Multiple speckle diffusing wave spectroscopy (MSDWS) uses a similar way to measure mesoscopic deformation. In contrast to usual DIC, however, no spray painting is needed:

speckles are generated from multiply scattered light upon illuminating a turbid sample with coherent laser light.<sup>20-22</sup> The intensity correlation of speckled patterns is extremely sensitive to the displacement of the scatterers, down to the scale of nanometers.<sup>20</sup> Accordingly, MSDWS has been applied to dynamics characterization in soft,<sup>23-24</sup> granular<sup>22</sup> and polymeric<sup>20-21</sup> <sup>25</sup> materials taking advantage of its excellent time resolution and displacement sensitivity. In this work, we apply MSDWS to quantitatively measure the spatially heterogeneous deformation of soft solids. The main purpose of this work is to explore under what conditions MSDWS may be applied and explain the requirements and limitations related to the method, making it more accessible to other users.

The rest of the paper is organized as follows. In section 2.2, we introduce the general background of the optics, including dynamic light scattering (DLS), diffusing wave spectroscopy (DWS), multiple speckle diffusing wave spectroscopy (MSDWS) and its application to the measurement of heterogeneous deformation. Focusing on the case of soft solids, we show how to simplify the mathematical processing to directly obtain mechanical parameters from in-situ imaging, addressing practical issues commonly associated to this kind of measurements. In section 2.3, we introduce the set-up and the preparation of the material. In section 2.4, we first describe uniaxial extension tests on an elastomer that demonstrate and validate the method. Then in section 2.5 we apply the method described in this work to obtain spatial maps of the deformation rate during debonding of an adhesive double-sided tape, a quantity that was experimentally not accessible in previous works on adhesion.

## 2.2 Optical theory

### 2.2.1 Dynamics Light scattering

When light propagates through heterogeneous media, the propagation will deviate from the original direction due to fluctuations of the refractive index. Microscopically, we consider a particle illuminated by the incident coherent light with wavelength  $\lambda$ . When the particle size is close to or smaller than  $\lambda$ , the energy transfer during the scattering is small compared to incident energy. When the scattering particles are moving around an equilibrium location (e.g. Brownian motion), the motion of the particles will be reflected in the fluctuation of the scattered light intensity. In this way, the motion and the particle information can be obtained from dynamic light scattering (DLS).

#### 2.2.1.1 Scattering of multiple particles

The technique of dynamic light scattering is based on the electromagnetic nature of light. In the case of a collimated coherent beam of the same wavelength (laser), the phase difference in different scattering events can be extracted from intensity correlation.

First, we consider two particles with coordinate vectors  $\vec{r}_1$  and  $\vec{r}_2$ , as seen in Fig. 2.1(a). When parallel incident laser light propagates into the system, two beams of light with light vector  $\vec{E}_0$  are scattered by the two particles respectively, and the light intensity:

$$I_0 = |\vec{E}_0|^2 \quad 2.1$$

Experimentally, we observe the light intensity from a direction with a scattering angle of  $\theta$  from incident direction and from a distance  $r$ . Note that  $r$  is much larger than  $(\vec{r}_1 - \vec{r}_2)$ , since  $(\vec{r}_1 - \vec{r}_2)$  typically has the length scale of the microscopic structure. The scattering vector  $\vec{q}$  can be defined, with direction of the difference between the vectors of the incident and scattered light (as seen in Fig. 2.1(b)<sup>26</sup>) and having a length of:

$$|\vec{q}| = \frac{4\pi}{\lambda} \sin \theta \quad 2.2$$

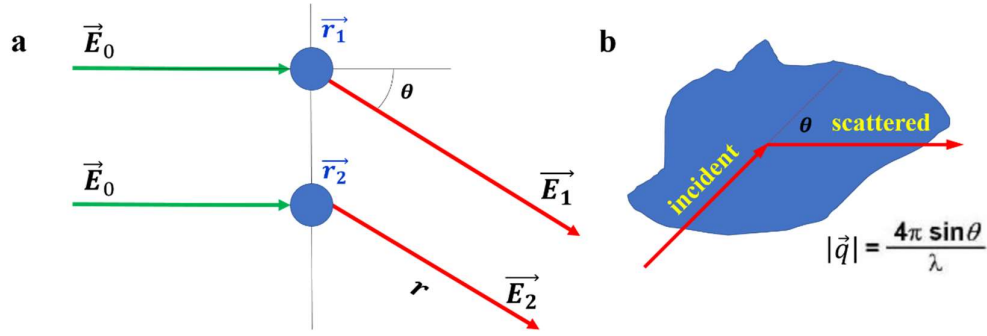


Fig. 2.1 (a) Scattering of light by two particles. (b) Schematic drawing of scattering vector  $\vec{q}$ .

The vectors of scattered lights are:

$$\vec{E}_1 \propto \frac{1}{r} \vec{E}_0 e^{i\vec{q}\vec{r}_1} \quad 2.3$$

$$\vec{E}_2 \propto \frac{1}{r} \vec{E}_0 e^{i\vec{q}\vec{r}_2} \quad 2.4$$

In this case, the total intensity of scattered light in the direction is:

$$I_{s,total} = |\vec{E}_1 + \vec{E}_2|^2 \propto \frac{2I_0}{r^2} (1 + e^{i\vec{q}(\vec{r}_1 - \vec{r}_2)}) \quad 2.5$$

As a result, when the relative location of the two particles changes, the intensity will also change correspondingly.

Now we consider that the laser beam is scattered by a system with multiple particles with coordinate  $\vec{r}_1, \vec{r}_2, \vec{r}_3 \dots$ . When the number of scattering particles,  $N$ , is sufficiently low, most of the light will go through the system without getting scattered, while we can consider that the number of scattering events is proportional to  $N$ . Similarly, we will have the total intensity along the same observation direction:

$$I_{s,total} = \left| \sum_i^N \vec{E}_i \right|^2 \propto \frac{I_0}{r^2} (N + \sum_{i \neq j}^N e^{i\vec{q}(\vec{r}_i - \vec{r}_j)}) \quad 2.6$$

The term  $\vec{r}_i - \vec{r}_j$  actually gives the phase difference after scattering by particles  $i$  and  $j$ .

### .2.2.1.2 Autocorrelation functions of scattered light

For a system in which particles are moving randomly (motion dynamics depending on the surrounding condition from the system), the measured scattered light intensity will

fluctuate over time. Scattered light intensity exhibiting fluctuations is schematically shown as a function of time in Fig. 2.2 (a).

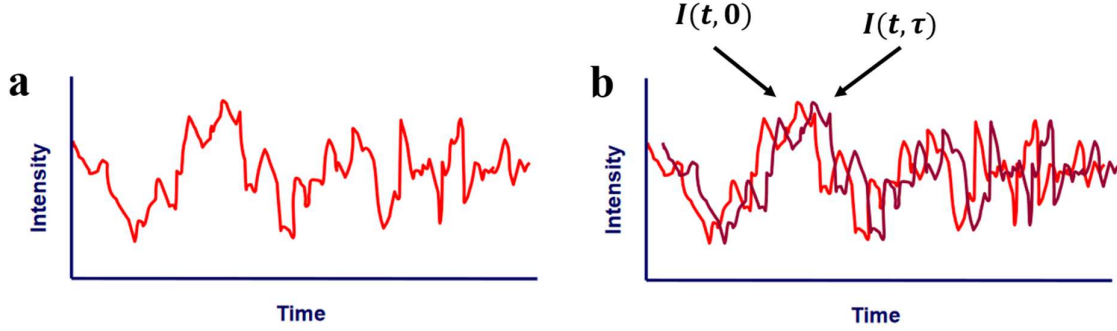


Fig. 2.2 (a) Scattered light intensity as a function of time. (b) Correlation between  $I(t)$  and  $I(t + \tau)$ .

The characteristic times of the fluctuations are directly related to those of the particle dynamics. In order to determine them, the time-averaged normalized intensity autocorrelation function  $g_2$  is calculated as a function of the correlation time  $\tau$ :

$$g_2(\tau) = \frac{\langle I(t) \cdot I(t+\tau) \rangle_t}{\langle I(t) \rangle_t^2} \quad 2.7$$

Here  $\langle \dots \rangle_t$  indicates time averaging. From Fig. 2.2(b), when  $\tau = 0$ , the correlation between the original curve and itself will give the maximum correlation of 1. While with increasing  $\tau$ , correlation will be progressively lost, thus  $g_2(\tau)$  is a decreasing function. To simplify modeling, the field autocorrelation function  $g_1$  is commonly applied, which indicates the correlation of electric field strength (sometimes  $g_E$ ):

$$g_1(\tau) = \frac{\langle E(t) \cdot E(t+\tau) \rangle_t}{\langle |E(t)| \rangle_t^2} \quad 2.8$$

$g_2(\tau)$  is converted into  $g_1(\tau)$  with the Siegert relation:

$$g_2(\tau) = 1 + g_1^2(\tau) \quad 2.9$$

The motion of the particles is normally described by the mean-square displacement (MSD):

$$\langle \Delta r^2(\tau) \rangle = \langle |\vec{r}(t) - \vec{r}(t + \tau)|^2 \rangle_t \quad 2.10$$

One has the relationship with  $g_1(\tau)$ :<sup>27</sup>

$$g_1(\tau) = g_1(0) \cdot \exp \left[ \frac{-q^2 \langle \Delta r^2(\tau) \rangle}{6} \right] \quad 2.11$$

### .2.2.1.3 Characterization of Brownian motion and particle size

Brownian motion was first discovered by Robert Brown in 1827 when he observed pollen immersed in water with microscope. The behavior was later discussed by Albert Einstein who concluded that the fluctuation of a big particle is due the collision between the molecules in the liquid, as seen in Fig. 2.3.

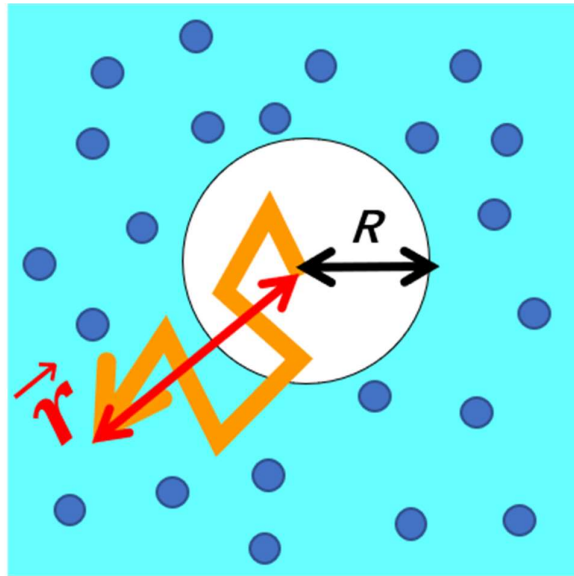


Fig. 2.3 Brownian motion of a particles in the liquid.

The Brownian motion can be described by the Einstein diffusion equation:

$$\frac{\partial \rho}{\partial t} = D \frac{\partial^2 \rho}{\partial x^2} \quad 2.12$$

Where  $\rho$  is the transition probability of the particle, and  $D$  is diffusion coefficient, given by:

$$D = \frac{kT}{6\pi\eta R_h} \quad 2.13$$

$\eta$  is the viscosity of the liquid and  $R_h$  is the hydrodynamic radius. The relationship



between MSD and diffusion coefficient is:

$$\langle \Delta r^2(\tau) \rangle = 6D\tau \quad 2.14$$

From Eq. 2.11,  $\langle \Delta r^2(\tau) \rangle$  can be obtained from the intensity autocorrelation function by DLS so that  $D$  can be calculated. From Eq. 2.13, if the temperature and the viscosity are known, the particle size can be determined, which is one of the most important standard applications of DLS.

### 2.2.2 Diffusing wave spectroscopy

For DLS, ideally the light only gets scattered once before being detected. The detectable  $\langle \Delta r^2(\tau) \rangle$  is of the order of  $q^{-2}$ , and the measured dynamics will strongly depend on the detection direction ( $\vec{q}$ ). The DLS analysis that we discussed in the previous section only considers single scattering.

Diffusing wave spectroscopy (DWS) is a modification of DLS, where multiply scattered light is collected for the calculation of the autocorrelation function (Fig. 2.4).<sup>28-29</sup> The autocorrelation function is obtained after time averaging, and the displacements of each particle are accumulated to the total displacement. In this case, the detectable  $\langle \Delta r^2(\tau) \rangle$  for DWS is much smaller than that of DLS, and the result is not  $q$  dependent. For DLS, there have been strategies to remove the multiply scattered part. In contrast, for DWS, normally the polarized part is removed from the scattered light since multiple scattering will erase all the polarization. Experimentally, a polarizer is placed before detection and adjusted to reach the minimal scattered light intensity.

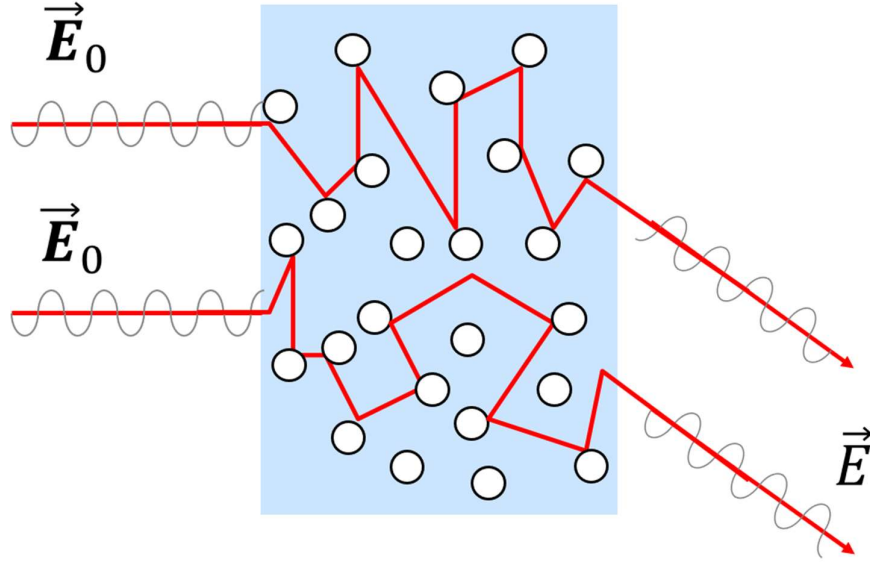


Fig. 2.4 Multiple scattering in DWS.

If Eq. 2.11 is to be extended to multiple scattering, the phase difference between scattered light will be accumulated in each individual scattering event. First, we introduce the mean free path  $l$ , which is the average distance between two scattering events. In dilute suspension,  $l$  can be expressed as:

$$l = \frac{1}{\rho_p \sigma} \quad 2.15$$

$\rho_p$  is the number density of the particles and  $\sigma$  is scattering cross-section.

The transport mean free path  $l^*$  is defined as the minimal path length required for light propagation to achieve a random direction:

$$l^* = \frac{l}{\langle 1 - \cos \theta \rangle} \quad 2.16$$

$\theta$  is the scattering angle of each scattering event. For small particles ( $R_h \ll \lambda$ ), scattering follows Rayleigh scattering, the light propagation after a single scattering event is already random, so we have  $l = l^*$ . For larger particles whose size is comparable to the wavelength,  $l^*$  can be experimentally measured.  $l^*$  gives actually the limit of the spatial resolution of DWS, typically of the order of 100  $\mu\text{m}$ . For the autocorrelation function of DWS, we define  $\varphi$  as the phase shift from the incident light, so that the scattered light vector can be expressed as:

$$\vec{E} \propto \frac{1}{r} |\vec{E}_0| e^{i\varphi(t)} \quad 2.17$$

where  $\vec{E}_0$  is the incident light vector. The phase shift  $\varphi$  in a path of multiple scattering (scattering events: 1, 2, ...,  $N$ ) can be expressed as:

$$\varphi(t) = \sum_{i=0}^N \vec{k}_i(t) [\vec{r}_{i+1}(t) - \vec{r}_i(t)] \quad 2.18$$

Similarly to Eq. 2.8, the time averaged  $g_1(\tau)$  in multiple scattering is given by:

$$g_1(\tau) = \frac{\langle E(t)^* E(t+\tau) \rangle_t}{\langle |E(t)| \rangle_t^2} = \sum_p \frac{\langle I_p \rangle_t}{\langle I_{total} \rangle_t} \langle e^{i(\varphi(t) - \varphi(t+\tau))} \rangle_t = \sum_p \frac{\langle I_p \rangle_t}{\langle I_{total} \rangle_t} \langle e^{-i\Delta\varphi(\tau)} \rangle_t \quad 2.19$$

For the path with a big scattering number,  $\Delta\varphi(t)$  should be a random Gaussian variable. Therefore, we have,

$$\langle e^{-i\Delta\varphi(\tau)} \rangle_t = e^{-\frac{\langle \Delta\varphi(\tau)^2 \rangle_t}{2}} \quad 2.20$$

Using Eq. 2.18:

$$\begin{aligned} \Delta\varphi(t) &= \varphi(t) - \varphi(t + \tau) \\ &= \sum_{i=0}^N \vec{k}_i(t) [\vec{r}_{i+1}(t) - \vec{r}_i(t)] - \sum_{i=0}^N \vec{k}_i(t + \tau) [\vec{r}_{i+1}(t + \tau) - \vec{r}_i(t + \tau)] \end{aligned} \quad 2.21$$

Recalling the scattering vector (Eq. 2.2), we define here:

$$\begin{aligned} \vec{q}_i(t) &= \vec{k}_i(t) - \vec{k}_{i-1}(t) \\ \Delta\vec{k}_i(\tau) &= \vec{k}_i(t + \tau) - \vec{k}_i(t) \\ \Delta\vec{r}_i(\tau) &= \vec{r}_i(t + \tau) - \vec{r}_i(t) \end{aligned} \quad 2.22$$

$\Delta\vec{r}_i(\tau)$  is displacement vector. Then  $\Delta\varphi(t)$  becomes:

$$\Delta\varphi(\tau) = \sum_{i=1}^N \vec{q}_i(t) \Delta\vec{r}_i(\tau) + \sum_{i=0}^N \Delta\vec{k}_i(\tau) [\vec{r}_{i+1}(t) - \vec{r}_i(t)] \quad 2.23$$

In this section, we consider that the change of position over time is random. The deviation of the particle is much smaller compared to the average distance between particles, so that  $\Delta\vec{k}_i(\tau)$  can be regarded as orthogonal to the position difference vector  $\vec{r}_{i+1}(t) - \vec{r}_i(t)$

so that the second term of Eq 2.23 can be neglected. Therefore:

$$\Delta\varphi(\tau) = \sum_{i=1}^N \vec{q}_i(t) \Delta\vec{r}_i(\tau) \quad 2.24$$

And,

$$\begin{aligned} \Delta\varphi(\tau)^2 &= \sum_{i=1}^N \langle [\vec{q}_i(t) \Delta\vec{r}_i(\tau)]^2 \rangle \\ &= N \langle \vec{q}_i(t)^2 \rangle \langle \Delta\vec{r}_i(\tau)^2 \rangle \langle \cos^2 \gamma \rangle \\ &= \frac{N}{3} \langle \vec{q}(t)^2 \rangle \langle \Delta\vec{r}(\tau)^2 \rangle \end{aligned} \quad 2.25$$

Where  $\gamma$  is the angle between  $\vec{q}_i(t)$  and  $\Delta\vec{r}_i(\tau)$ . Using Eq. 2.2 and 2.16, we have

$$\langle \vec{q}(t)^2 \rangle = \left\langle \frac{4\pi}{\lambda} \sin\left(\frac{\phi}{2}\right) \right\rangle = 2k^2 \langle 1 - \cos\theta \rangle = 2k^2 \frac{l}{l^*} \quad 2.26$$

So that the first-order autocorrelation function can be expressed as:

$$g_1(\tau) = \sum_p \frac{\langle I_p \rangle_t}{\langle I_{total} \rangle_t} \exp\left(\frac{2k^2}{3} \frac{Nl}{l^*} \langle \Delta\vec{r}(\tau)^2 \rangle\right) \quad 2.27$$

$Nl$  gives the total path length of the propagation, here we define  $s = Nl \cdot \frac{\langle I_p \rangle_t}{\langle I_{total} \rangle_t}$  can be regarded as the fractional intensity of each path, which is only dependent on  $s$ , so that it can be expressed by  $P(s)$ . Finally,  $g_1(\tau)$  is a function of  $s$  and  $\langle \Delta\vec{r}(\tau)^2 \rangle$ :

$$g_1(\tau) = \sum_s P(s) \exp\left(\frac{2k^2}{3} \frac{s}{l^*} \langle \Delta\vec{r}(\tau)^2 \rangle\right) \quad 2.28$$

The  $s$  dependence of  $g_1(\tau)$  differs with different experimental geometries and materials.

## 2.2.3 Multispeckle diffusing wave spectroscopy

### 2.2.3.1 Multiple speckle imaging

Speckle is generated when photons travel in random paths and the random dephasing produces a statistical distribution of light intensity.<sup>30</sup> In conventional DLS and DWS, the intensity is collected by a single point detector as a function of time, which is a single speckle spot. The autocorrelation function is calculated after time averaging over a reasonable duration for an ergodic system at equilibrium with short characteristic

decorrelation times. The collection period can be divided into segments, so that a time resolved measurement can be achieved within the resolution of each segment time.<sup>31</sup>

There are various situations where the time averaging does not provide accurate measurements. When the dynamics are very slow, the duration of a measurement becomes longer than the patience of the experimentalists. When the system is out of equilibrium, including under non-stationary mechanical/rheological solicitations, the dynamics continue to evolve during a measurement. It is still possible to perform time resolved measurements if the decorrelation times are sufficiently faster than their evolution. And more importantly, when the system is non-ergodic, dynamics depend on the position of the speckle, and the ensemble averaging is not equal to the time averaging. Gels are typical non-ergodic examples. Crosslinked polymer chains or probe particles embedded in the network do not explore all the possible configurations of the scattered light as their position is restricted.

The ensemble averaged autocorrelation function can be obtained by using images containing multiple speckles,<sup>31-32</sup> where a camera instead of a single point detector is used to measure the scattered intensity from different positions. By dividing 2D images into region of interests (ROI) and processing results in ROIs separately, spatially resolved autocorrelation functions can be calculated without time averaging. For relatively transparent media where single scattering dominates, multiple speckle dynamics light scattering is commonly called photon correlation imaging (PCI). For turbid media, the technique is called multispeckle diffusing wave spectroscopy (MSDWS), which is the main method of this thesis.

#### .2.2.3.2 MSDWS and time/space resolution

For DWS, since the results is  $q$  independent, it is convenient to apply the CCD camera instead to acquire intensity scattered from different locations in the system. The acquired data in one image can be enormous with the high resolution of the camera (typically in the scale of  $1000 \times 1000$  pixels). In this case, the limitation of the spatial resolution is actually the speckle size. Speckles are the results of interferences of many waves with the same wavelength, which can be observed when a rough surface is illuminated by a laser.<sup>21</sup> For DWS applications, the speckle size is typically  $10 \mu\text{m}$ , which is adjustable by optical parameters. With multi-speckle diffusing wave spectroscopy (MSDWS), it is possible to

achieve a high level of time and spatial resolution at the same time. Depending on the set-up geometry, MSDWS can be divided into backscattered MSDWS and transmitted MSDWS, as seen in Fig. 2.5.

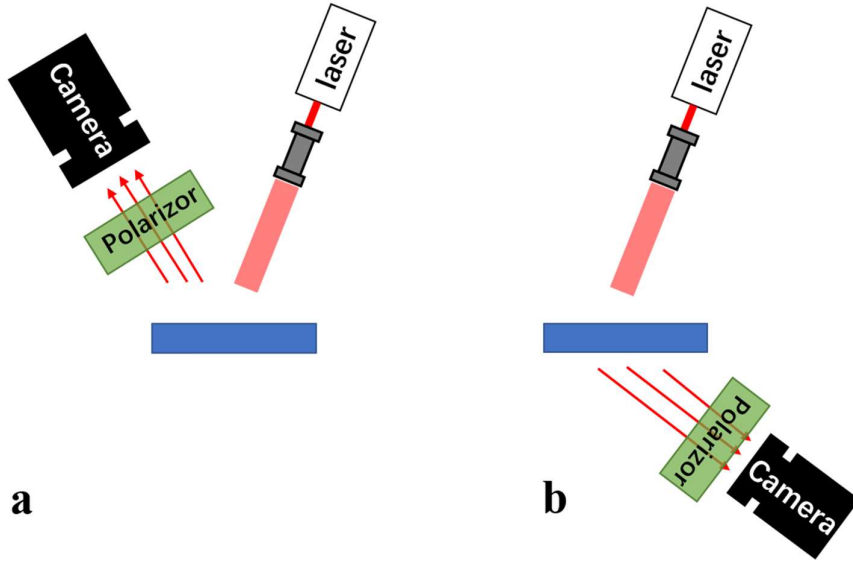


Fig. 2.5 MSDWS set-up configuration. (a) Backscattering. (b) Transmission.

In MSDWS, instead of a time average (widely applied for DLS measurement), an ensemble average in space is performed in a region of interest (ROI) containing multiple speckles (Fig. 2.6):<sup>21, 33</sup>

$$C(\vec{r}, t, \tau) = \frac{\langle I_p(t)I_p(t+\tau) \rangle_{\vec{r}}}{\langle I_p(t) \rangle_{\vec{r}} \langle I_p(t+\tau) \rangle_{\vec{r}}} - 1 \quad 2.29$$

In equation 2.29,  $t$  is the experimental time and  $\tau$  is the time interval for the correlation calculation. Images are divided into small regions of interest, so that spatially resolved dynamics can be obtained.  $I_p$  is the intensity of the  $p$ -th pixel, and  $\langle \dots \rangle_{\vec{r}}$  provides the ensemble average over a small region with center position  $\vec{r}$ .  $C(\vec{r}, t, \tau)$  at a fixed time  $t_0$  and position  $\vec{r}_0$  is the univariate function of  $\tau$ ,  $C(\tau)_{\vec{r}_0, t_0}$ , whose decorrelation kinetics as the function of  $\tau$  presents the  $t$  dependent local behavior.

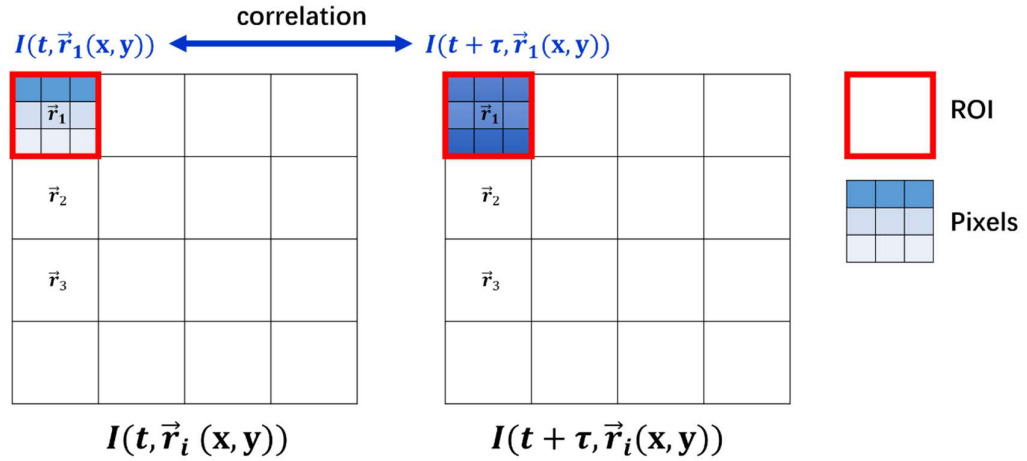


Fig. 2.6 Schematic diagram of spatial ensemble average in MSDWS to achieve time and space resolution simultaneously. Here ROIs are selected to be 9 pixels for simple demonstration. Actual pixels number required to have reliable space resolved results is much higher than that.

For pixels inside one same speckle, the intensity is almost identical. For the choice of the size of the ROI, the trade-off between spatial resolution and noise level needs to be considered. Autocorrelation functions in ROI with different sizes during a static measurement on a PDMS elastomer are shown in Fig. 2.7. It can be seen that with an ROI of 20 pixel×20 pixel, the data quality is less noisy. With speckle size around a few pixels, ROI size with 10 to 20 pixels is normally used.

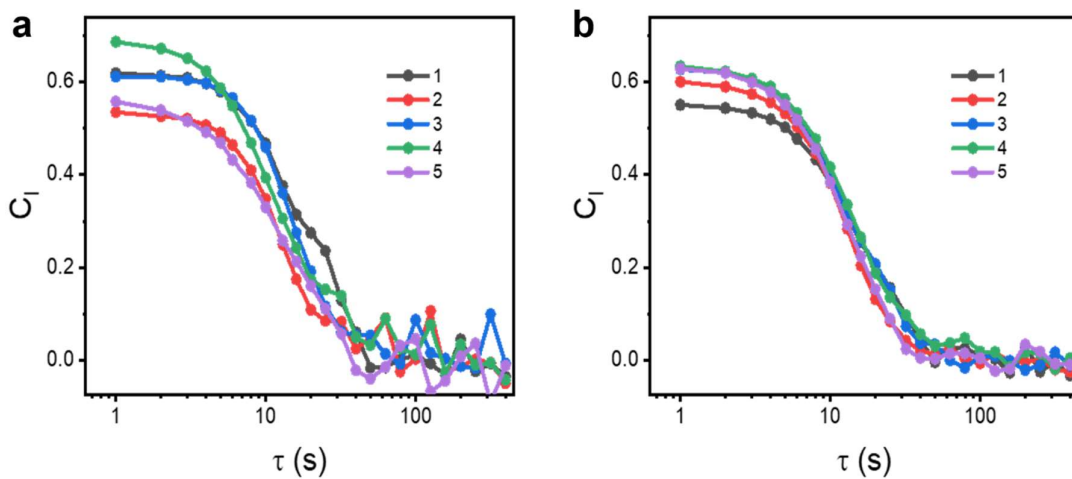


Fig. 2.7 Autocorrelation function  $C_1 (= g_2 - 1)$  by ROI with different size. (a) 15 pixel×15

*pixel (b) 20 pixel × 20 pixel.*

### .2.2.3.3 Testing geometry and autocorrelation function

In this work, we focus on MSDWS in the backscattering geometry.<sup>33</sup> The experimental set-up is schematically shown in Fig. 2.8(a). An expanded laser beam homogeneously illuminates the surface of a sample which contains a sufficient amount of scatterers. The backscattered light is collected by a high-speed camera, which makes an image of the sample surface. Due to the coherence of the laser light, the images have a speckled appearance (inset of Fig. 2.8(a)). The speckles result from the interference between photons that have penetrated in the sample and have been scattered due to local fluctuations of the material refractive index. These fluctuations may arise from concentration or composition fluctuations of the raw material, or may be due to the addition of probe particles with a refractive index different from that of the material. For the turbid samples that we shall consider here, the majority of the backscattered light is due to multiple scattering. Multiple scattering is characterized by the transport mean free path  $l^*$ , the length scale over which a photon is scattered a sufficiently number of times for its propagation direction to be randomized.<sup>33</sup>  $l^*$  typically ranges from a few  $\mu\text{m}$  up to hundreds of  $\mu\text{m}$ . Although the camera images the sample surface, the speckle pattern depend on the path of the photons in the bulk of the sample, such that the method is sensitive to deformations occurring in a sample layer of thickness up to about  $8l^*$ .<sup>34-35</sup> This makes the method suitable for mapping the in-plane deformation. For a deformation field with a gradient along the depth direction, the measurement and quantification require careful discussion and approximation, and will not be discussed here.



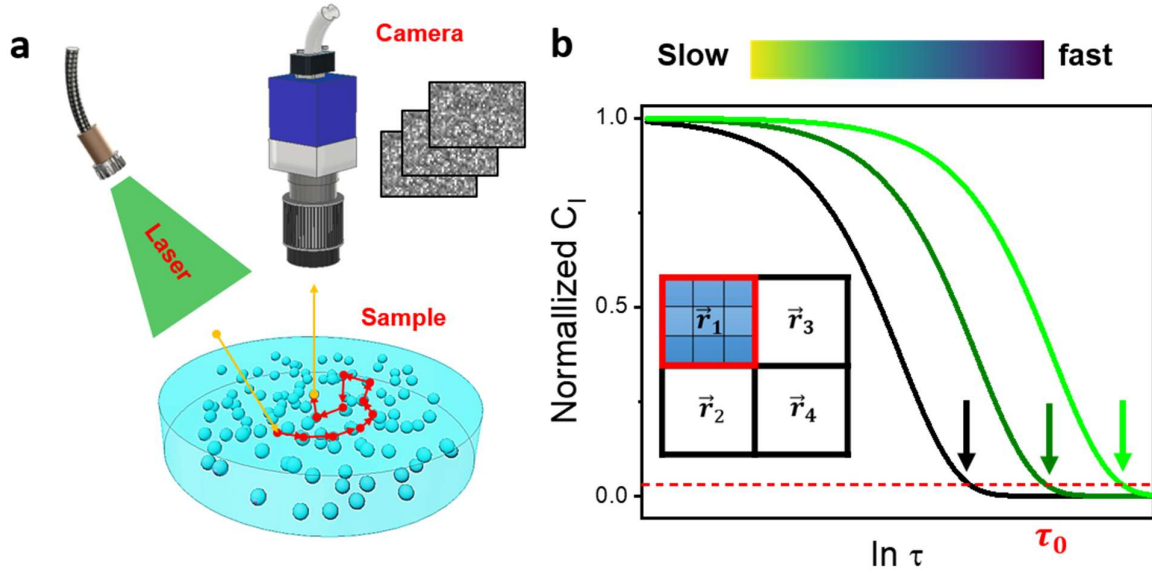


Fig. 2.8(a) Schematic of MSDWS measurement in backscattering geometry. (b) Autocorrelation functions for system with different dynamics.

When the scatterers are in motion due to thermal energy or owing to an external drive, the intensity of the scattered light fluctuates with time, at a rate related to the rate at which scatterers are displaced. At a fixed time  $t_0$  and position  $\vec{r}_0$ ,  $C(\vec{r}, t, \tau)$  is a function of the time delay  $\tau$  only,  $C(\tau)_{\vec{r}_0, t_0}$ , whose decay time quantifies the  $t$ -dependent local dynamics (denoted by  $C(\tau)$  in the following text for simplicity). A convenient functional form that describes well  $C(\tau)$  under many experimental conditions is:<sup>20, 36</sup>

$$C(\tau) = A \exp\left(-2\epsilon \sqrt{\left(\frac{\tau}{\tau_0}\right)^p + a}\right) + B \quad 2.30$$

$\epsilon$  depends on the polarization of the incident and detected light, a typical value being  $\epsilon = 1.8$  when no polarizer is used before detection.<sup>20</sup>  $a = 3l^*/l_a$  depends on the ratio of the transport mean free path  $l^*$  and the absorption length  $l_a$  (usually,  $a \ll 1$ ), which needs to be experimentally determined.  $\tau_0$  is the characteristic time of decorrelation, corresponding to the time scale over which  $C(\tau)$  decreases to around  $\exp(-2\epsilon)$  after normalization, and the scatterers are displaced over a distance of the order of  $1/k$  (typically, around 50 nm).  $k$  is the wave vector of the laser light ( $k = 2n\pi/\lambda$ , with  $n$  the refractive index and  $\lambda$  the in-vacuo laser wavelength).  $B$  is the baseline of the correlation function: ideally,  $B=0$ , but measurement noise and other artifacts often result in a non-

zero baseline<sup>37</sup>. In practice,  $B$  is determined from the long-time behavior of  $C(\tau)$  and subtracted off the experimental curve.  $A$  is a normalization factor set by imposing  $C(\tau) - B \rightarrow 1$  for  $\tau \rightarrow 0$ . Eq. 2.30 generalizes the usual form of the correlation function in the backscattering geometry<sup>26</sup>, with  $\left(\frac{\tau}{\tau_0}\right)^p = k^2 \langle \Delta r^2(\tau) \rangle$ , with  $\langle \Delta r^2(\tau) \rangle$  the mean square displacement of the scatterers. Note that by construction Eq. 2.30 cannot capture complex dynamics, e.g. stemming from the coexistence of two distinct dynamical processes occurring on different time scales. Nonetheless, Eq. 2.30 is sufficiently flexible to reproduce a variety of microscopic motions of interest, from Brownian motion (corresponding to  $p = 1$ ) to the ballistic motion resulting from an applied deformation at constant rate ( $p = 2$ ). Given the functional form of  $C(\tau)$ ,  $\tau_0$  is also the time scale where the autocorrelation function is most sensitive to a change in the probed dynamics. Accordingly,  $\tau_0$  is commonly used for quantifying and comparing different dynamical processes.<sup>4, 38-39</sup> Examples of autocorrelation functions are shown in Fig. 2.8(b), which illustrates that slower dynamics corresponds to a slower decay rate of  $C$  and hence a larger  $\tau_0$  value.

#### .2.2.3.4 Dynamical processes probed by MSDWS

Coexisting dynamic processes yielding multiple modes of decorrelation are commonly reported in DWS measurements<sup>40-42</sup>. Understanding these dynamics is the key challenge posed by the method. The measured dynamics is often attributed to a single relaxation mechanism, since it is very difficult to reproduce and analyze the form of the autocorrelation function in the general case. However, this requires a careful examination and choice of the system and experimental parameters. Here we briefly review the most common contributions to the dynamics of soft solids and discuss the coupling between them. In particular, we show that in a wide range of practical mechanical testing conditions, MSDWS results can be safely analyzed by considering only the contribution due to the affine deformation field, which greatly simplifies the processing.

One source of dynamics for scatterers in a soft solid is thermally activated motion. Let us first consider the case of a soft solid whose turbidity is high enough for MSDWS to be viable with no addition of probe particles. Thermal energy results in (overdamped) fluctuations of the structure around its equilibrium position (think, e.g., of the fluctuations of strands in a colloidal gel or of network vibrations in elastomers). The

amplitude of these fluctuations depends on the elastic modulus of the material, and is typically on the order of several nm for stiff materials up to tens of  $\mu\text{m}$  for very weak colloidal gels<sup>43-44</sup>. Since multiple scattering is sensitive to motion down to the nm scale<sup>26</sup>, these fluctuations are potentially captured by the correlation function. However, their typical time scale is quite fast, typically 0.001 s or less<sup>41, 44-45</sup>. On longer time scales, fluctuations are limited by the sample structure,<sup>46-47</sup> so that this fast decorrelation mode normally does not lead to a full decorrelation. Because MSDWS uses a relatively slow detector (typically, a CMOS camera run at a frame rate of about 1 kHz at most), thermal fluctuations do not have a measurable impact on  $C$ , because they occur out of the experimentally accessible time window. More specifically, they result in overall lower levels of the correlation function measured by MSDWS, independently of  $\tau$ , which is corrected for by the normalization factor  $A$  in Eq. 2.30. The situation is similar for samples to which particle probes have been added to enhance scattering, as long as the particles are large enough to be effectively trapped in the sample structure (e.g. if they are larger than the mesh size for gels and elastomers), as is the case for microrheology<sup>43</sup>.

An additional source of dynamics in soft solids is the slow evolution of the sample, also referred to as aging<sup>38, 48-49</sup>. Aging is due to the fact that many soft solids are out-of-equilibrium systems, slowly evolving towards (but often never reaching in accessible time scales) the most thermodynamically stable configuration. In the last two decades, ultraslow relaxations associated with aging have been uncovered in a wide range of systems, from gels to dense, repulsive systems.<sup>50-52</sup> These relaxation modes often lead to ballistic dynamics, which have been ascribed to the progressive release of internal stress stored when forming the sample<sup>53-54</sup>. Even when measured with techniques such as MDWS that are extremely sensitive to motion on small length scales, the decay time of these modes may be as large as hundreds or thousands of seconds<sup>4</sup> and it further increases with sample age. As we shall see, the decay time associated with an imposed mechanical deformation is typically smaller, on the order of a few seconds at most. Thus, aging dynamics usually do not interfere with the dynamics measured while mechanically driving a soft solid. However, one should always check this point, by running a preliminary measurement on the sample at rest. Should the spontaneous dynamics be fast enough to potentially interfere with those measured under a mechanical drive, it is preferable to let the sample age until the spontaneous dynamics become slow enough.

A third source of dynamics, specific to soft solids under mechanical loading, stems from the deformation field induced by loading. Indeed, light scattering is sensitive to the relative motion of the scatterers. Since the deformation field is not uniform, scatterers are displaced by a position-dependent amount, which results in the decorrelation of the scattered light. The scatterers displacement contains in general an affine contribution (i.e. the displacement field expected for an ideal, homogeneous elastic body under the same loading conditions) and, possibly, non-affine contributions.<sup>55</sup> We first discuss the affine contribution, assuming that non-affine dynamics may be neglected. Under these conditions, the autocorrelation function can be related to the strain field by:<sup>20, 36</sup>

$$C(\tau) = A \exp\left(-2\epsilon \sqrt{3k^2 l^{*2} f[\mathbf{U}(\tau)] + a}\right) + B \quad 2.31$$

$\mathbf{U}(\tau)$  is a rank-two tensor describing the strain field over the time interval  $\tau$ , and  $f[\mathbf{U}(\tau)] = [\text{Tr}(\mathbf{U})^2 + 2\text{Tr}(\mathbf{U}^2)]/15$ .<sup>20, 56-57</sup> Assuming that  $\tau$  is short enough for the deformation to occur at constant rate,  $\mathbf{U}(\tau)$  may be expressed as the product of the rate of deformation tensor  $\mathbf{d}$ <sup>58-59</sup> times the time interval:

$$U_{ij}(\tau, t) = d_{ij}(t)\tau \quad 2.32$$

By replacing Eq. 2.32 in Eq. 2.31 and comparing with the general form, Eq. 2.30, one finds that for a deformation at a constant rate

$$3k^2 l^{*2} \tau^2 f[\mathbf{d}] = \left(\frac{\tau}{\tau_0}\right)^p \quad 2.33$$

This implies  $p = 2$  (ballistic dynamics) and

$$\tau_0 = \frac{1}{kl^* \sqrt{3f[\mathbf{d}]}}. \quad 2.34$$

As an example of simple test geometries, we shall consider uniaxial extension and simple shear and discuss typical time scales for  $\tau_0$  due to affine deformation.

For uniaxial extension along the  $x$  axis in a incompressible solid with true strain rate  $\dot{\lambda}_T$  one has:<sup>20</sup>

$$\mathbf{d} = \begin{bmatrix} \dot{\lambda}_T & 0 & 0 \\ 0 & -\frac{\dot{\lambda}_T}{2} & 0 \\ 0 & 0 & -\frac{\dot{\lambda}_T}{2} \end{bmatrix} \quad 2.35$$

For simple shear along the  $x$  direction at shear rate  $\dot{\gamma}$ :<sup>60-62</sup>

$$\mathbf{d} = \begin{bmatrix} 0 & \frac{\dot{\gamma}}{2} & 0 \\ \frac{\dot{\gamma}}{2} & 0 & 0 \\ 0 & 0 & 0 \end{bmatrix} \quad 2.36$$

Eq. 2.36 results from decomposing the shear rate tensor in the sum of two terms, corresponding to pure shear  $\mathbf{d}$  and pure rotation  $\mathbf{w}$ , respectively.<sup>62</sup> Recalling that MSDWS is only sensitive to the relative motion of the scatterers, one recognizes that the only term that contributes to the decay of the correlation function is the pure shear term, which corresponds to Eq. 2.36. Then, for uniaxial extension:

$$\tau_{0,ue} = \sqrt{\frac{5}{3}} \frac{1}{kl^*\dot{\lambda}_T} \quad 2.37$$

And for simple shear:

$$\tau_{0,ss} = \sqrt{5} \frac{1}{kl^*\dot{\gamma}} \quad 2.38$$

Above discussion shows that the MSDWS relaxation time in the backscattering geometry for a sample undergoing a macroscopic deformation depends on  $l^*$ , unlike the case of the spontaneous dynamics of a system at rest<sup>63</sup>. Indeed, in multiple scattering experiments  $l^*$  sets the scale over which the deformation is measured.<sup>39</sup> Note that even though the sample is moving as the measurement, the averaging window (ROI) is much larger than the displacement in the time scale of the full decorrelation of the autocorrelation function. The dynamics from the displacement itself will be discussed later.

As mentioned above, the minimum time delay accessible to MSDWS is about 1 ms. This sets a limit on the highest measurable deformation rate, since the relaxation time of the correlation function must be at list a few times the smallest  $\tau$ . Using typical parameter values  $l^* = 100 \mu\text{m}$ ,  $n=1.5$ ,  $\lambda = 532 \text{ nm}$ ,  $\tau_{0,\min} = 5 \text{ ms}$ , one obtains the following estimates:

$$\dot{\lambda}_{T,max} \approx \frac{7.3 \times 10^{-4}}{\tau_{0,ue min}} \approx 0.14 \text{ s}^{-1} \quad 2.39a$$

$$\dot{\gamma}_{max} \approx \frac{1.26 \times 10^{-3}}{\tau_{0,ss min}} \approx 0.25 \text{ s}^{-1} \quad 2.39b$$

To access higher deformation rates, one may reduce  $l^*$  by adding or increasing the concentration of tracer particle, by choosing tracer particles with a higher refractive index contrast with the sample, or by optimizing the size of the tracer particles, since  $l^*$  has a non-monotonic behavior with particle size<sup>63</sup>. Note that using a faster camera to decrease the minimum measurable relaxation time  $\tau_{0,min}$  may not be a useful strategy, because the relaxation dynamics due to thermal fluctuations discussed above would likely contribute to the decay of the correlation function, making data analysis difficult. The lower limit on the measurable deformation rate is of the order of a few  $10^{-6} \text{ s}^{-1}$ , set by the longest relaxation time achievable by MSDWS, which is of the order of a few hundreds of seconds at least. Therefore, the accessible range of deformation rates covers most of the conventional measurement of mechanical behavior in soft solids. Within the accessible strain rate interval, spatially and temporally resolved local strain rates can be directly quantified by MSDWS, provided that  $l^*$  is known, e.g. from an independent transmission measurement<sup>63</sup>. Alternatively,  $l^*$  may be deduced from Eqs 2.37 or 2.38, by imposing a known deformation rate to the sample. Note that the components of the deformation tensor can be directly calculated by MSDWS for simple, ideal deformation geometries. In the more general case (e.g. near to a fracture tip or in more complex geometries)  $\tau_0$  only provides the time scale over which  $\sqrt{\text{Tr}(\mathbf{D}^2)}$  reaches  $1/kl^*$  (see Eq. (5)), with no information on the individual components.

A fourth source of dynamics for soft solids loaded beyond their linear regime stems from rearrangements associated with plastic events<sup>23</sup>, which applies MSDWS to the detection of plastic events in a granular system. In general, we expect a plastic event occurring at a position  $\vec{r}_0$  to have a two-fold impact on the dynamics measured by MSDWS. On the one hand, the local configuration of the sample around  $\vec{r}_0$  is modified, e.g. as in T1 or T2 events in foams,<sup>64</sup> or in shear transformation zones in dense suspensions,<sup>65</sup> or in a bond breaking event in network-forming systems.<sup>24</sup> The size of the region directly modified by the plastic event depends on the system, but it is typically smaller than or comparable to  $l^*$ . On the other hand, a local plastic event modifies the internal stress state, which in turn

sets a strain field across the sample, including far from  $\vec{r}_0$ . MSDWS is sensitive to displacements down to the nm scale, but the spatial mapping of the dynamics is coarse-grained on a length scale  $\sim l^*$  or larger (hundreds of  $\mu\text{m}$ ). Consequently, it is likely that plastic events are not detected *per se*, but rather thanks to the strain field they set throughout the sample.

A final issue to be considered in space-resolved MSDWS measurements coupled to mechanical tests is the rigid displacement of the sample, and hence of the speckle pattern. The rigid displacement causes a loss of the correlation in the autocorrelation function<sup>20, 22, 66</sup> As a limiting case, consider a sample undergoing a pure translation. Due to the imaging geometry, the (otherwise frozen) speckle pattern drifts with respect to the detector, such that the intensity of any given pixel fluctuates as bright and dark speckles scroll in front of it. For a sample undergoing tensile or shear strain, a similar effect occurs and the measured loss of correlation is in general due to both a drift of the speckle pattern and its evolution associated with the change of the relative position of the scatterers, stemming from the sample deformation. Schemes have been proposed to disentangle the two contributions<sup>39, 67</sup>. Since these methods are computational demanding, it is interesting to discuss under what conditions the drift contribution may be safely neglected.

The drift contribution is negligible when  $\tau_{speckle}$ , the time it takes a speckle to travel the pixel size due to drift, is much longer than  $\tau_{0,def}$ , the relaxation time due to the relative motion of scatterers associated to the macroscopic deformation, see e.g. Eqs 2.37 and 2.38 for the case of extensional and shear tests. For the former, one has

$$\tau_{speckle} = \frac{l_{speckle}}{v} = \text{FOV}/(Nv), \quad 2.40$$

where  $l_{speckle}$  is the speckle size, which can be measured by calculating the spatial autocorrelation function of the speckle image<sup>68</sup>, FOV is the size of the field of view and  $v$  is the speckle drift velocity. The last equality stems from the speckle size being a fraction  $1/N$  of the FOV. The cameras used in MSDWS produce images with a linear size of several hundreds to a few thousands of pixels, while the speckle size ranges from a fraction of a pixel to several pixels: thus,  $N$  ranges from a few hundreds to few thousands.

We first consider an extensional test with only one clamp moving, and the other one fixed (commonly to a force sensor). The popular geometry consists in imaging the whole

sample, which allows to obtain full information on the sample response and to check for slippage at both clamps. Under these conditions,  $FOV = L$ ,  $L$  being the sample length. The largest velocity occurs at the moving clamp:  $v = \dot{\lambda}_T L$ . Inserting this expression in Eq. 2.40 and using Eq. 2.37, we find the following lower bound

$$\frac{\tau_{speckle}}{\tau_{0,ue}} \geq \sqrt{\frac{3}{5}} \frac{kl^*}{N} \quad 2.41$$

Using the same parameters as above ( $l^* = 100 \mu\text{m}$ ,  $n = 1.5$ ,  $\lambda = 532 \text{ nm}$ ), one finds  $\tau_{speckle}/\tau_{0,ue} \approx 1370/N$ . Remarkably, the ratio of the two characteristic times does not depend on the strain rate and may be tuned to be either smaller or larger than unity by varying the speckle size, which in turn controls  $N$ . For example, we will show in section 2.4 that in the experiments on a stretched PDMS elastomer presented here the speckle size was such that  $kl^* = 6969$ ,  $N = 682$  and  $\tau_{speckle} = 7.9\tau_{0,ue}$ . Under these conditions, the speckle pattern fluctuates (due to the affine displacement field) much faster than it translates (due to the drift associated to elongation), such that no drift correction needs to be implemented. On the contrary in the paper of Nagazi et al.<sup>20</sup>, the speckle size was designed to be smaller than the pixel size, such that  $\tau_{speckle} < \tau_{0,ue}$  and the strain rate field was inferred from the displacement field, measured using a computationally demanding method<sup>66</sup>.

For a shear test, we consider a sample of thickness  $d$  undergoing simple shear. We recall that MSDWS in the backscattering geometry is not sensitive to displacements in the full depth of the sample, but rather in a layer of thickness  $\sim 10l^*$  on the side of the illumination and collection optics.<sup>69</sup> Assuming that the sample is sheared at a rate  $\dot{\gamma}$  while keeping fixed one of its surfaces, one has to distinguish the two cases where the sample is illuminated on the fixed side or on the mobile side. For a sample illuminated on the fixed side and assuming  $d > 10l^*$ , the drift velocity averaged over the thickness of the probed layer is  $v = 5l^*\dot{\gamma}$ . Inserting this expression in Eq. 2.40 and using Eq. 2.38, one finds the lower bound

$$\frac{\tau_{speckle}}{\tau_{0,ss}} \geq \frac{FOV}{10} \frac{k}{N}. \quad 2.42$$

Note that the right-hand side of Eq. 2.42 is particularly simple, since it does not depend on strain rate nor on  $l^*$ . With the typical values used above,  $k \sim 1.7 \times 10^7 \text{ m}^{-1}$ , such that for



usual geometries ( $FOV \geq 1$  cm and  $N \sim 1000$ )  $\tau_{speckle}/\tau_{0,ue} \geq 20$ . Thus, for simple shear while imaging on the fixed side of the sample the speckles fluctuate much faster than they drift and no drift correction is required. This will be the situation for the experiments on the adhesive debonding reported in section 2.5.

If a sample of thickness  $d$  undergoing shear is imaged from the moving side, the drift velocity averaged over the layer probed by MSDWS is  $v = \dot{\gamma}(d - 5l^*)$  (assuming again that  $d > 10l^*$ ) In this case, the lower bound for the ratio of the drift and fluctuation times becomes

$$\frac{\tau_{speckle}}{\tau_{0,ss}} \geq \frac{FOV kl^*}{\sqrt{5} (d-5l^*)N}, \quad 2.43$$

which does not depend on the strain rate, but does depend on  $l^*$ . Inserting in Eq. 2.43 typical values for the various parameters ( $FOV = 1$  cm,  $l^* = 100$   $\mu$ m,  $d = 1$  mm), one finds  $\tau_{speckle}/\tau_{0,ue} \geq 16$ , showing that the drift correction may be safely neglected.

To summarize this section, we have shown that in the typical range of time delays probed by MSDWS coupled to mechanical tests ( $1$  ms  $< \tau_0 < 100$  s), the relaxation time of the intensity correlation function is directly related to the (local) deformation rate. The latter may be extracted from the MSDWS data provided that  $l^*$  is known and that the deformation geometry may be approximated by a simple geometry such as extension or shear. While in principle correcting the speckle images for drift may be necessary, we find that for typical experimental parameters this correction is not necessary, apart for tensile tests when the speckle size is small enough for thousands of speckles to fit in the (linear) size of the image.

### C. Comparison of MSDWS and DIC

As MSDWS and DIC provides similar information on the deformation rate spatial distribution, it is worth to quantitatively compare the two methods. Considering correlation is sufficient informative when  $\tau \approx 0.02\tau_0$  and  $C(\tau) \approx 0.93$ , this gives a strain accuracy for MSDWS ( $\approx f[\mathbf{U}(0.02\tau_0)]$ ) of the order of  $10^{-6}$ . This is more accurate than the reported testing by DIC, where strain resolution is limited to the scale of  $10^{-3}$  in practical experimental conditions.<sup>70-71</sup> Another advantage of MSDWS is the fact that the method only requires the material to be turbid (which may also be achieved by adding a small amount of highly scattering particles), with no need of surface treatment. More

importantly, MSDWS directly provides the scale of deformation rate, which can be more useful for the examination of subtle dynamic changes, compared to conventional strain measurements.

## 2.3 Material and methods

### 2.3.1 Materials

For the tensile tests, a Sylgard 184 PDMS elastomer was prepared with ratio of PDMS base and curing agent of 10:1. TiO<sub>2</sub> nanoparticles (diameter 250 nm, wt%=0.25%) were added before curing, to enhance the sample turbidity. TiO<sub>2</sub> nanoparticles were first mixed with the PDMS base and manually stirred. The suspension was then sonicated for 10 min to thoroughly disperse the particles and put in vacuum to remove bubbles formed during stirring and sonication. The suspension and curing agent were mixed and poured into a mold, then cured at 90 °C for 12 h. A sheet of elastomer of 4 mm thickness was thus obtained. The transport mean free path  $l^*$  of the PDMS elastomer was measured in a suspension containing TiO<sub>2</sub> nanoparticles with the same volume concentration as in the elastomers. The autocorrelation function from the suspension can be calculated from the known viscosity of water and matched to the experimental one, using  $l^*$  as the only fitting parameter<sup>63</sup>. For a PDMS wt% = 0.25 %, we find  $l^* \approx 430 \mu\text{m}$ .

Commercially available Polyacrylate pressure sensitive adhesive tapes were used to investigate debonding. The tapes are made of a copolymer of 2-ethylhexyl acrylate (88 % by weight) and acrylic acid (12 % by weight), filled with hollow glass microspheres (12% by weight, Type: Q-Cel® 5020 from Potters, with mean size of 60  $\mu\text{m}$ ). The copolymer was synthesized by UV-polymerization using Irgacure 184 (0.4 % by weight) as photoinitiator and 1,6-Hexanediol diacrylate (0,15% by weight) as crosslinker. The thickness is 1 mm and the tapes are cut to different sizes for measurement. To determine the photon mean transport path  $l^*$ , we used the method discussed at the end of Sec. 2.4 (measurement of the decay time of  $C(\tau)$  while applying a tensile strain at a known deformation rate), finding  $kl^* = 3323.4$ , corresponding to  $l^* \approx 190 \mu\text{m}$  assuming  $n = 1.47$  (the refractive index of 2-ethylhexyl acrylate).

### 2.3.2 Experimental set-up

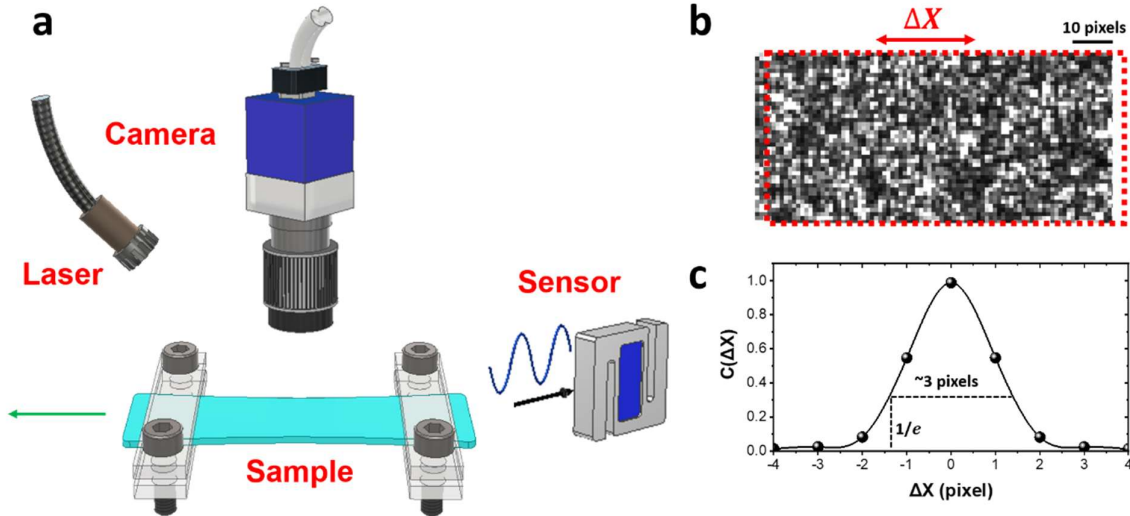


Fig. 2.9 (a) Experimental set-up for the uniaxial extension, combined with MSDWS measurement. (b) A typical speckle image and its displaced position. (c) Spatial autocorrelation function of image in (b), from which the size of the speckle is estimated at  $C = 1/e$ , around 3 pixels.

The uniaxial extension test of the elastomer was performed with a laboratory made set-up, see Fig. 2.9(a). The sample was fixed by two clamps connected to a Newport translational stage with step precision of 500 nm and a force sensor (KD40s, with full scale of  $\pm 50$  N and precision of 0.1%). The whole sample surface was illuminated by an expanded laser beam with wavelength of 532 nm, and images of the backscattered light were collected simultaneously to the mechanical response (force measured by the sensor and nominal displacement imposed by the motor), using a CMOS camera (BASLER acA2000-340km). Fig. 2.9(b) shows a typical speckle image where the presence of speckles can be detected. Spatial autocorrelation (using spatial displacement  $\Delta X$  instead of time interval  $\tau$  in Eq. 2.29 for the correlation, as seen in Fig. 2.9(b)) is calculated and shown in Fig. 2.9(c). The size of speckle is estimated by the full width at  $C = 1/e$ , around 3 pixels. Inserting image size  $N = 2048$  pixels in the horizontal direction (also the deformation direction),  $n = 1.43$  for PDMS<sup>72</sup> and  $l^* = 430$   $\mu\text{m}$  into Eq. 2.41, one has  $\tau_{\text{speckle}} = 7.9\tau_{0,ue}$ , so that there is no need for drift correction.

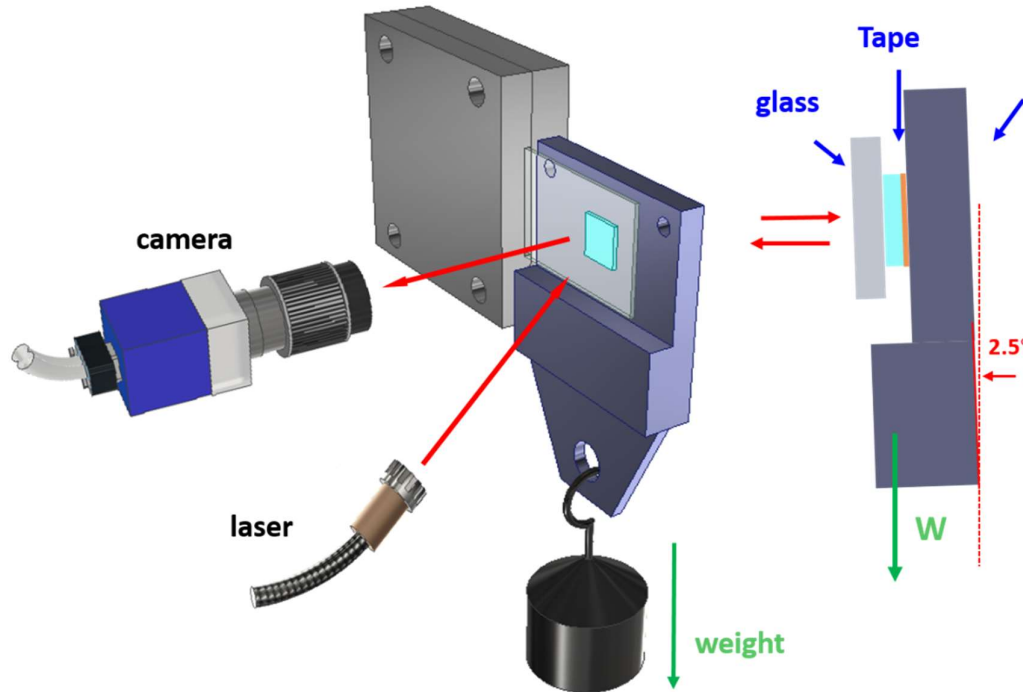


Fig. 2.10 Experimental set-up for the measurement of adhesive debonding under single-lap shear.

The debonding process of a pressure sensitive adhesive tape under single-lap shear<sup>73-74</sup> (tape fixed between two rigid substrates and exposed to translational shear stress) was measured with the set-up shown in Fig. 2.10. First, the tape was glued to an aluminum plate using instant glue (Loctite 406) to ensure adhesion stronger than at the debonding interface. Then, a glass microscope slide with a thickness of 3 mm was pressed to the other side of the tape, using a weight of 0.3 N for 10 min. A shear stress was imposed to the tape by holding the glass slide fixed in a vertical plane, while hanging a weight to the aluminum plate. Rectangular samples were used, with different sizes as shown in Table 2.1. The position of the loading axis was set to be around the midplane of the tape, to avoid torque on the tape, which may result in strong peel stresses and cleavage in the bulk region. A small angle around  $2.5^\circ$  is introduced between the aluminum plate and the vertical axis, so that a small component of the load provides compression on the tape, to avoid possible normal tension that strongly changes the debonding conditions. In this geometry, the tape is under simple shear conditions and adhesive debonding is studied under creep deformation. The weight  $W$  was adjustable from 1.5 N (the weight of the

aluminum plate alone) to 21.5 N. Macroscopic shear stress during creep,  $\tau_{macro} = W/A$ , where  $A$  is the area of the glass-tape interface. The laser illumination and the imaged surface is on the side of the glass-tape interface, which is static until debonding. To estimate whether any drift correction may be needed, we use a slightly modified version of Eq. 2.42, because here  $d/l^* \sim 5$  and MSDWS probes the dynamics across the full thickness of the sample. The average drift velocity of the measured layer is  $v = 2.5l^*\dot{\gamma}$  and  $\tau_{speckle}/\tau_{0,ue} = FOV k/5N = 107$ , where we have used  $k = 1.67 \times 10^7 \text{ m}^{-1}$ ,  $N = 250$ ,  $FOV \approx 0.8 \text{ cm}$  for the biggest sample ( $8.4 \text{ mm} \times 7.6 \text{ mm}$ , where  $N$  is maximal). Since  $\tau_{speckle} \gg \tau_{0,ss}$ , no drift correction was necessary for shearing, either.

$\tau_{macro}$ (MPa)	Tape size (length $\times$ width, mm)	W (N)
0.26	$8.4 \times 7.6$	16.5
0.49	$5.2 \times 5.5$	13.5
0.62	$5.2 \times 5.1$	16.5
0.72	$4.5 \times 3.5$	11.5
0.88	$5.1 \times 3.6$	16.5

*Table 2.1 Parameters for debonding tests under shearing.*

The samples were illuminated by a diode green laser with  $\lambda = 532 \text{ nm}$ . Speckle images in the backscattering geometry were collected using a CMOS camera (BASLER acA2000-340km). To optimize the time resolution and speckle quality, the exposure time was set to 0.03 s. The strong spatial fluctuations of intensity due to the speckled appearance of the images makes it difficult to obtain morphological information on the surface, such as evidence of cavitation<sup>75</sup> and fibrillation<sup>76</sup> that typically occur during debonding. The morphological information can be extracted by averaging several speckle images acquired over a time interval longer than  $\tau_0$ , such that intensity fluctuations average out. The displacement  $L$  of the aluminum plate can be measured as a function of time by tracking the reference point on the aluminum substrate and the macroscopic shear strain can be defined as  $\gamma_{macro} = L/d$ , where  $d$  is the sample thickness, 1 mm for all measurements.

## 2.4 Method validation: uniaxial extension of PDMS

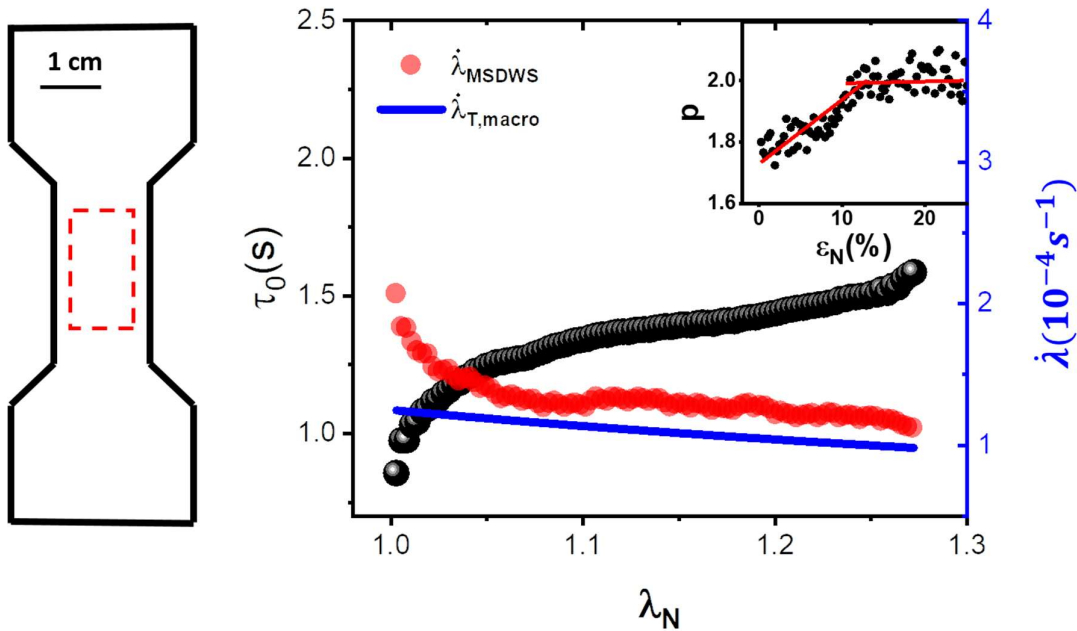


Fig. 2.11 Measurement of the deformation rate in the central region of a dog-bone PDMS sample, schematically shown on the left. Relaxation time  $\tau_0$  measured by MSDWS (black circles) and corresponding experimental (red) and nominal (blue) strain rate  $\dot{\epsilon}$  are shown as a function of  $\epsilon_N$ . Inset:  $p$  as the function of  $\epsilon_N$ .

We first validate MSDWS applied to mechanical tests in uniaxial extension of a dog-bone PDMS sample to which a nominal strain rate  $\dot{\lambda}_N = 1.25 \times 10^{-4} \text{ s}^{-1}$  is applied. The autocorrelation function is calculated for a ROI located in the center of the sample (with size of  $1 \text{ cm} \times 2 \text{ cm}$ , indicated by the dashed rectangle in Fig. 2.11). The autocorrelation function is fitted to Eq. 2.30, using  $a$ ,  $p$  and  $\tau_0$  as fitting parameters. We find that  $a$  is around 0.015 from fittings at different  $\lambda_N$ , so that the absorption is very low. Note that  $a$  should be essentially constant throughout the experiment but its fitted value strongly depends on data quality. In the following fittings, we used a constant value  $a = 0.015$ . The relaxation time  $\tau_0$  is plotted as a function of the nominal strain  $\lambda_N$  in Fig. 2.11. We find that  $\tau_0$  is slightly smaller than 1 s at the beginning of the test and increases up to about 1.5 s with growing strain. Assuming that the observed dynamics are only due to the imposed strain, the strain rate  $\dot{\lambda}_{MSDWS}$  is calculated from  $\tau_0$  using Eq. 2.37 with  $l^* = 430 \text{ }\mu\text{m}$ . A sharp decrease is detected in the initial stage of the test ( $\lambda_N < 1.1\%$ ), after which

$\dot{\lambda}_{T,MSDWS}$  keeps decreasing, but more slowly. Due to the shrinkage of the cross-sectional area upon stretching, the true strain rate may be calculated from the macroscopic nominal strain and macroscopic nominal strain rate:

$$\dot{\lambda}_{T,macro} = \frac{\dot{\lambda}_N}{\lambda_N} \quad 2.44$$

We found that the macroscopic values obtained from Eq. 2.44 match well with  $\dot{\lambda}_{MSDWS}$  for  $\lambda_N > 1.1$ , with around 15 % of deviation. Concomitantly, the exponent  $p$  (inset of Fig. 2.11) increases from 1.8 and plateaus to  $p = 2$  for  $\lambda_N > 1.1$ . This suggests that there is an initial regime where other relaxation mechanisms, in addition to affine displacements, contribute to the decorrelation of the autocorrelation function. We speculate that these additional relaxation mechanisms may be due to heterogeneity of the local environment of the probe particles and from residual stresses generated when clamping the sample. Indeed, in preliminary tests on the same material with no extension, we observed enhanced dynamics upon clamping, which slowly relaxed over several hours<sup>77</sup>. The contribution of these additional mechanisms becomes negligible beyond  $\lambda_N = 1.1$ , where the evolution of  $\dot{\lambda}_T$  as measured macroscopically and by MSDWS match very well.

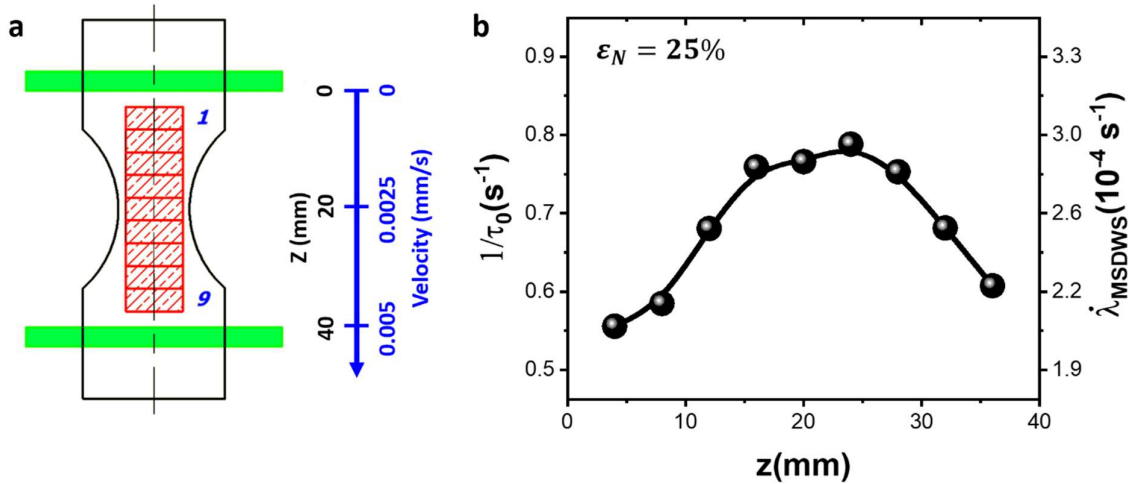


Fig. 2.12 (a) PDMS dog bone sample with varying width along the stretching direction. The green rectangles indicate the clamp positions. A tensile strain is imposed by moving the bottom clamp at a velocity of 0.005 mm/s. (b)  $v_0$  and the corresponding local strain rate measured by MSDWS at different position.

We argued in Sec. 2.3B that no correction for the sample drift was required in the



experiments on PDMS reported here. To validate experimentally this result, the contribution of the rigid displacement is investigated using a customized dog bone sample, whose width along the extension direction varies, as shown in Fig. 2.12(a). A tensile strain is imposed by moving one clamp at a velocity of 0.005 mm/s, such that the displacement velocity is proportional to the distance  $z$  from the fixed clamp. The sample length is 40 mm and the nominal strain rate is  $\dot{\lambda}_N = 1.25 \times 10^{-4} \text{ s}^{-1}$ . Leveraging on the space resolution afforded by MSDWS, we measure  $\tau_0$  for several ROIs, at different positions as shown in Fig. 2.12(a). The corresponding  $\dot{\lambda}_{MSDWS}$  values are calculated using Eq.2.37 and are shown in Fig. 2.12(b). Overall,  $\dot{\lambda}_{MSDWS}$  is of the same order of magnitude but somehow higher than its macroscopic counterpart,  $\dot{\lambda}_N$ , reflecting enhanced deformation rates as expected due to strain concentration where the sample width is smaller. The same argument explains why  $\dot{\lambda}_{MSDWS}$  peaks around  $z = 22$  mm, close to the middle part of the sample, where the width is smallest. Crucially,  $\dot{\lambda}_N(z)$  is nearly symmetric around the middle of the sample, reflecting the symmetry of the sample shape. If sample drift would contribute significantly to the decay of  $C(\tau)$ , this symmetry would be broken and the decay would be faster at larger  $z$ , where the drift velocity is higher. Thus, the test on the dog bone sample with variable width confirms that here the dynamics is dominated by the relative motion of the particles, so that only the strain rate is measured, regardless of the drift velocity.

The experiments on PDMS under uniaxial extension confirm that the spatially-revolved strain rate can be effectively measured by MSDWS. Furthermore, the combination of MSDWS and uniaxial extension provides a simple way to estimate  $l^*$  for a (solid) sample with unknown scattering properties, by tuning  $l^*$  in order to match the MSDWS strain rate to the macroscopic one. This provides a simple alternative to optical methods to measure  $l^*$ , which are often quite delicate to implement, especially for solid samples<sup>20, 22</sup>. We shall use this method to determine  $l^*$  for the adhesive tapes discussed in the next section.

## 2.5 Measurement of heterogeneous deformation during adhesive debonding

MSDWS is applied here to measure the spatially resolved shear deformation rate at the interface between a soft adhesive film under fixed shear stress  $\tau_{macro}$  and a glass

substrate during adhesive debonding, with the set-up shown in Fig. 2.10. First, for different  $\tau_{macro}$ , the nominal (macroscopic) shear strain  $\gamma_{macro}(t)$  is measured from the macroscopic displacement in the vertical direction of the aluminum substrate and shown in Fig. 2.13(a).  $\gamma_{macro}(t)$  as a function of time exhibits a typical creep behavior for all  $\tau_{macro}$ . A rapid increase in  $\gamma_{macro}$  right after loading is observed, followed by a steady growth of  $\gamma_{macro}$  exhibiting a power law behavior with an exponent around 0.25. Finally, a sudden increase of  $\gamma_{macro}(t)$  is detected at a critical value of  $t$ , corresponding to the full debonding. The shear strain where debonding occurs  $\gamma_b \sim 3$  is practically independent of the value of  $\tau_{macro}$ , consistent with a strong strain hardening typical of crosslinked adhesives.<sup>78</sup> The values of time when  $\gamma_{macro}$  reaches 1,  $t_{\gamma=1}$ , are plotted as a function of  $\tau_{macro}$  in Fig. 2.13(b) to compare the debonding kinetics. The debonding time itself is not used to compare debonding kinetics as it can depend strongly on the edge effects at the interface. We found that  $t_{\gamma=1}$  decreases exponentially with  $\tau_{macro}$ , indicating the strong dependence on applied load of the creep failure kinetics. This type of experiment is classically carried out in industry and the only time measured is the failure time. Yet the debonding mechanisms are difficult to investigate and so are the heterogeneities in stress. A recent study on a similar shear failure geometry combining a fracture mechanics approach of shear failure and a finite strain modeling, showed clearly the heterogeneity of the load along the bonded surface.<sup>79-80</sup> We now focus on the mapping of the deformation rates on the interfaces with the glass.

Images of the interface at different times after loading are displayed in Fig. 2.13(c) for  $\tau_{macro} = 0.26$  MPa. These images are averaged over 25 images with interval larger than  $\tau_0$  (interval is adjusted at different periods over experiments to optimize time resolution and image quality), in order to smooth the spatial fluctuations of intensity due to the speckles and make various morphologies visible. As seen from the enlarged images inserted in Fig. 2.13(c) taken for the test at  $\tau_{macro} = 0.26$  MPa, signs of fibrillation are visible on the top edge of the sample, while they are not visible from the images on the bottom edge in a different optical condition. With increasing  $\gamma_{macro}$ , fibrils develop further and can partially detach from the substrate. After 25 h of loading, 2 h before full debonding and with enhanced contrast, most of the top edge is still attached to the glass substrate with no substantial debonding. At the center of the sample, no particular morphological change is observed from these images.

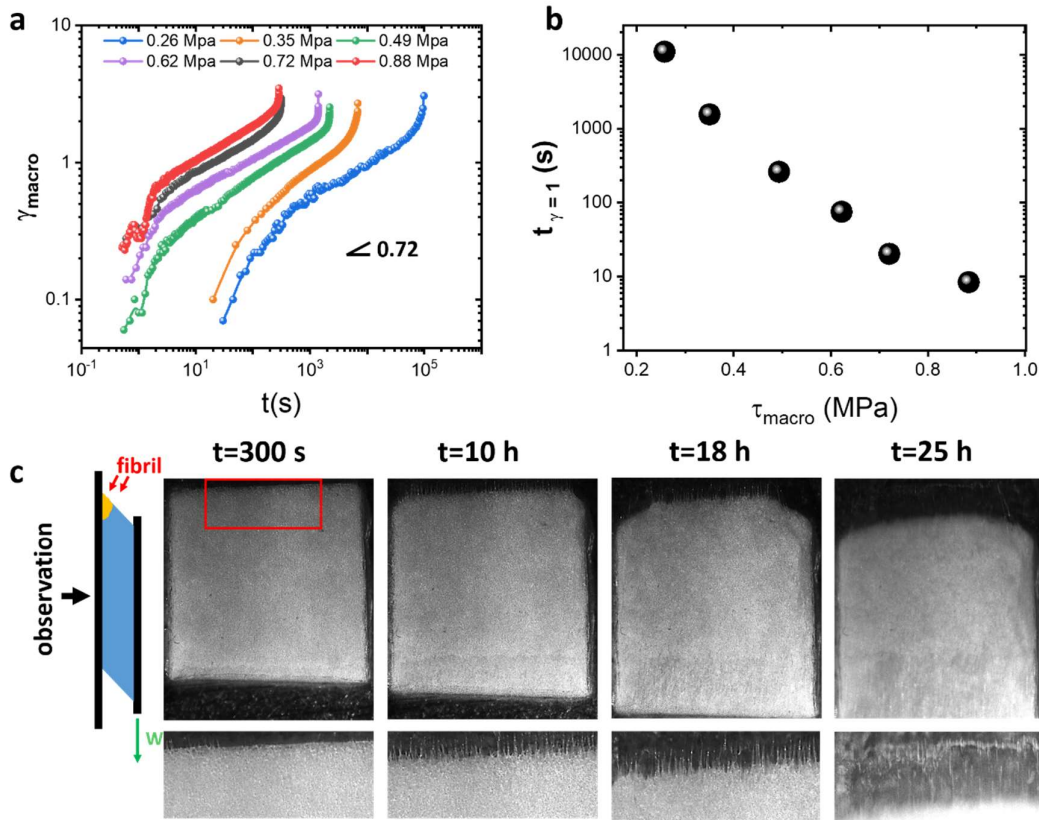


Fig. 2.13 (a)  $\gamma(t)$  as a function of time under different  $\tau_r$ . (b) The time where  $\gamma_{\text{macro}}$  reaches  $1$   $t_{\gamma=1}$ , as a function of  $\tau_{\text{macro}}$ . (c) Interface images at different times for  $\tau_r=0.26$  MPa. Inset: enlarged images from the region indicated by the red rectangle.

In the previous study on deformation during adhesive debonding in peel or probe tack tests, it was not possible to measure the in-plane deformation distribution of the debonding interface since the interface is static and bulk deformation is hard to visualize.<sup>81-83</sup> In experiments, debonding was studied by inspecting the sample from the side<sup>84-85</sup>, which does not allow for the full characterization of the large-shear edge region. In the bulk region, DIC can also be applied in this case to measure if there is a slippage at the interface between the substrate and the tape, but the measurement of the deformation field requires speckles that are normally prepared by spray painting, which will largely change the adhesive strength on the interface. By contrast, MSDWS allows for measuring the deformation rate over a layer of thickness several  $l^*$  without changing its mechanical properties.<sup>69</sup> For our sample, for which  $d \approx 5l^*$ , this corresponds to the full thickness of the tape, for which we can thus visualize and quantify any heterogeneity in

the mechanical behavior. In the central region of the tape, where shear localization and peeling are not dominating, we expect the deformation measured by MSDWS to match the macroscopic strain inferred from the aluminum plate displacement, provided that the deformation is homogeneous through the thickness. We compare the MSDWS strain rate and the macroscopic one for a sample with  $\tau_r=0.62$  MPa, from the beginning of loading up to  $t = 1404$  s, when debonding occurs. The MSDWS shear strain rate  $\dot{\gamma}_{MSDWS}$  is calculated from the fitted relaxation time  $\tau_{0,ss}$  of  $C(\tau)$  using Eq. 2.38, with  $kl^* = 3323.4$  independently measured in an uniaxial extension test on the bare tape (see Fig. 2.S1 in the supporting information). The MSDWS data are obtained by averaging  $C(\tau)$  in a square region of size  $1.5 \text{ mm} \times 1.5 \text{ mm}^2$  located in the center of the sample as, indicated in Fig. 2.14. The macroscopic strain rate is obtained by numerically differentiating  $\gamma_{macro}$  after smoothing the data with a sliding window of 60 s, to reduce noise. Fig. 2.14 shows that that  $\dot{\gamma}_{MSDWS}$  matches well the overall trend of  $\dot{\gamma}_{macro}$ , although the MSDWS strain rate is systematically larger than the macroscopic one by around 20 %. Such a discrepancy may be due to uncertainties in the sample thickness  $d$  used to calculate the macroscopic strain rate or in the value of  $kl^*$  obtained from the uniaxial extension test. Furthermore, we analyze the MSDWS data for both the uniaxial extension test and under shear with the formalism of Sec. 2.2B, which applies to semi-infinite samples, while for our tape samples the condition  $d \gg l^*$  is not met. Given that the ratio between the microscopic and macroscopic strain rates is close to unity and constant throughout the test, this difference has no impact on the discussion that will follow. We emphasize that the strain rate inferred from MSDWS has a much lower noise than the macroscopic data, because of the superior sensitivity to motion of MSDWS, as well as due the fact that macroscopic strain data need to be differentiated, which is a notorious source of experimental noise.

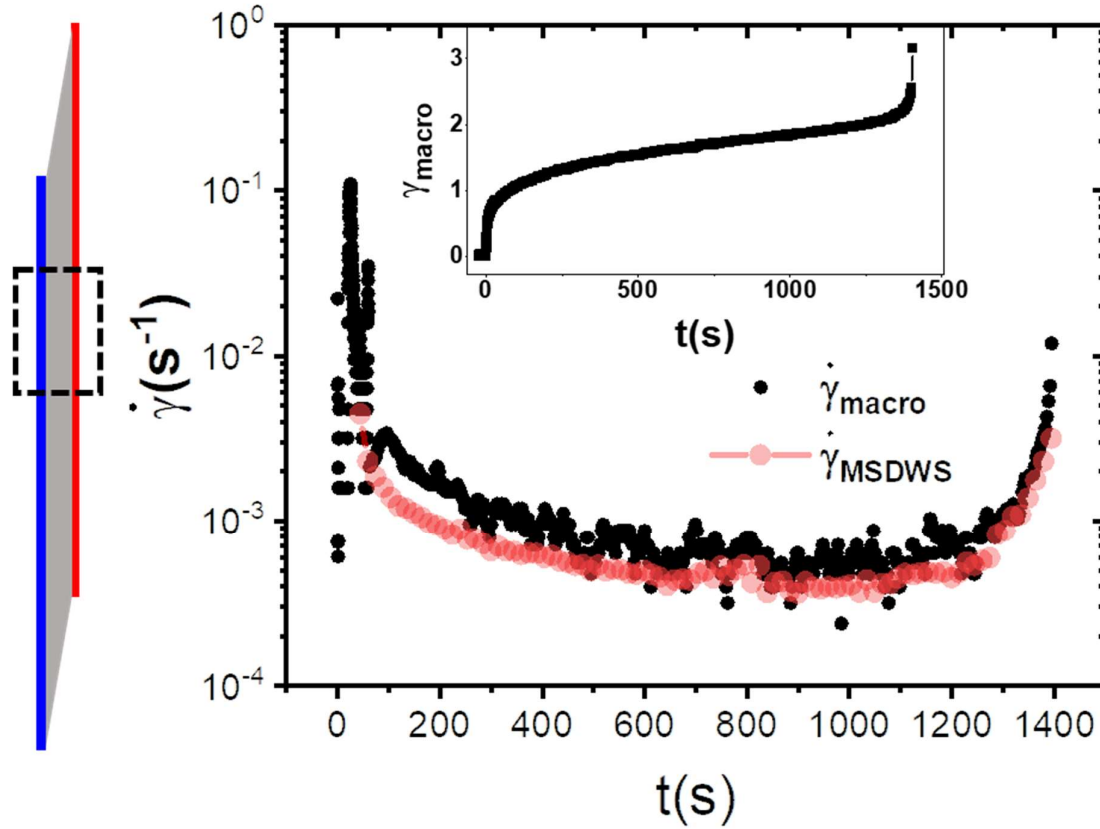


Fig. 2.14 Sketch on the left: side view of the sheared adhesive tape, the dashed rectangle indicates the location of the ROI for which the MSDWS data shown on the right are collected. Right:  $\dot{\gamma}_{MSDWS}$  and  $\dot{\gamma}_{macro}$  as a function of time for  $\tau_{macro} = 0.62$  MPa. Inset:  $\gamma_{macro}$  for  $\tau_{macro} = 0.62$  MPa.

To further characterize the spatial distribution of the strain rate,  $\dot{\gamma}_{MSDWS}$  maps of the whole interface at different times are shown in Fig. 2.15 (a), for the case of  $\tau_{macro} = 0.62$  MPa. The maps are obtained from spatially resolved autocorrelation functions by dividing the imaged interface in ROIs with size  $0.3 \times 0.3$  mm<sup>2</sup>. The area of the tape that initially adheres to the glass slide is indicated by the red rectangle. Higher  $\dot{\gamma}_{MSDWS}$  values are detected at the edges, around a central area that bears most of the applied stress. These areas with a higher deformation rate propagate towards the inner region as creep proceeds and debonding sets in. It has been reported that during shear of a single-lap joint, strain and stress at the interface are relatively uniform along the tape, but both shear and peel stress peak at the edge.<sup>86</sup> Previously, this behavior could only be predicted

theoretically or investigated numerically. By contrast, MSDWS reveals the spatial distribution of the deformation rate distribution in the adhesion plane. Furthermore, the boundaries of the central area that bears most of the stress can be assessed more reliably than by looking at the emergence of morphological features, as in Fig. 2.13(c). Note that high values of  $\dot{\gamma}$  originate here from both localized shear and peel at the edge, which cannot be distinguished from each other. From about 150 s before global debonding, the local strain rate at the top and bottom edges are significantly enhanced, up to about twice the macroscopic strain rate.

We now turn to a more detailed analysis and quantify the observations in Fig. 2.15(a), we calculate the profile of the local strain as a function of the distance  $y$  from the top edge, by averaging  $\dot{\gamma}_{MSDWS}$  over the width of the hatched region, shown in Fig. 2.15(a). We show in Fig. 2.15(b) profiles of the local shear rate, normalized by the macroscopic one, for various  $t$  after loading the sample. When approaching the debonding time, regions exhibiting high deformation rates further penetrate towards the central region of the sample and  $\dot{\gamma}_{MSDWS}/\dot{\gamma}_{macro}$  can locally reach values as high as 2. Crucially, this marked growth of the local strain rate occurs at a time when  $\dot{\gamma}_{macro}$  has not shown obvious increase and the sample is far from full debonding ( $\gamma_{macro}$  around 1.7 while  $\gamma_b \approx 3$ ), which occurs at  $t = 1404$  s. These results demonstrate the superior sensitivity and richness of information of spatially-resolved MSDWS, which allow one to detect subtle changes in the deformation rate, hundreds of seconds before the emergence of any macroscopic precursor of debonding.

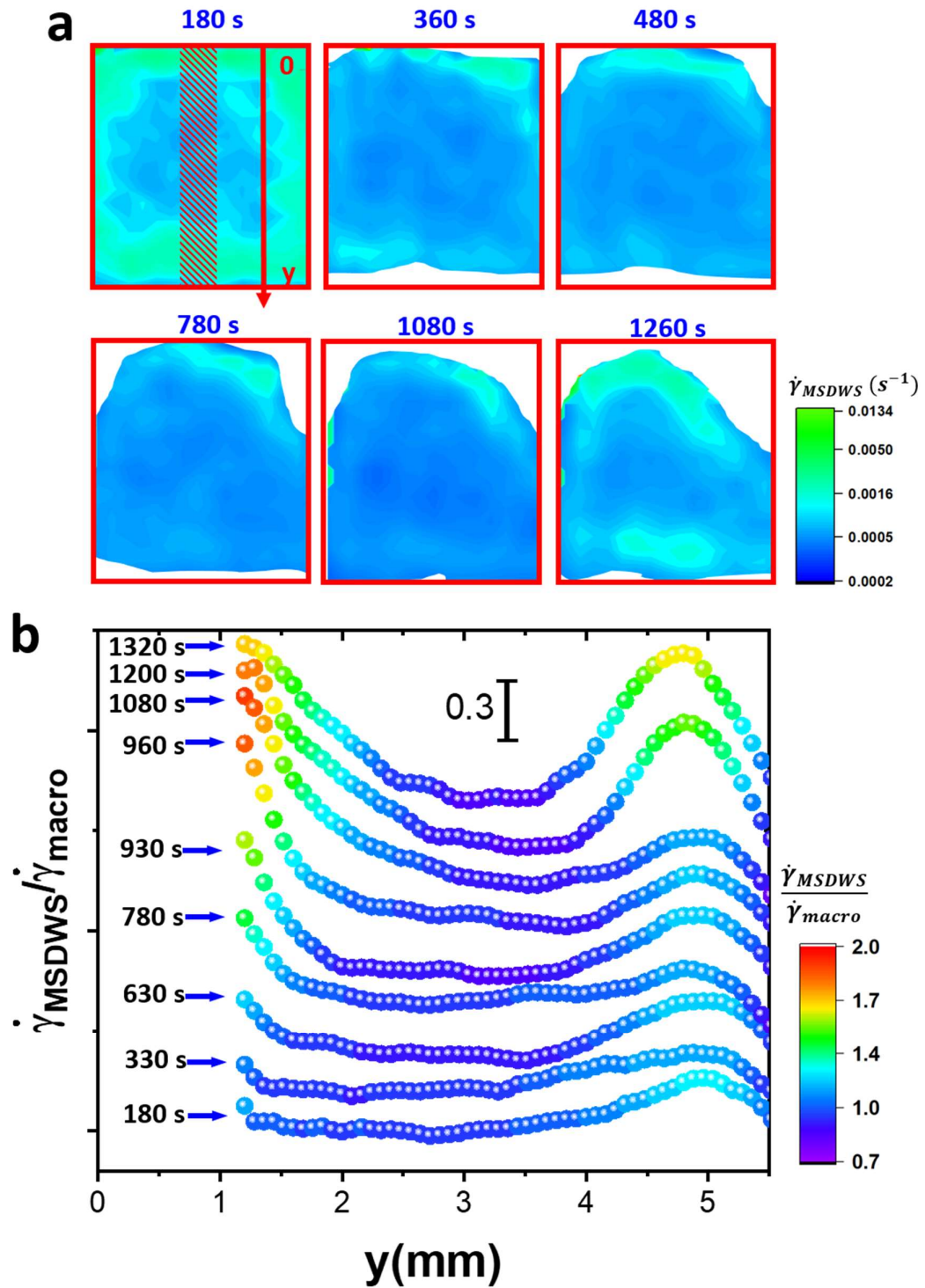


Fig. 2.15 (a)  $\dot{\gamma}_{MSDWS}$  maps at different times  $t$  after loading and adhesive tape under shear with  $\tau_{macro} = 0.62$  MPa (same test as in Fig. 2.14). The region that is initially bonded is indicated by the red rectangle. (b) Normalized shear rate  $\dot{\gamma}_{MSDWS}/\dot{\gamma}_{macro}$  calculated for the shaded region in (a), as a function of the distance  $y$  from the top edge. Curves are offset

vertically for clarity, where a vertical distance is indicated, corresponding to a change of 0.3 in  $\dot{\gamma}_{MSDWS}/\dot{\gamma}_{macro}$ . Data are color-coded according to the color bar shown on the right.

The results shown in Fig. 2.15 were obtained by calculating the local shear rate from the characteristic time  $\tau_0$  determined by a fit of the full autocorrelation function. This procedure leads to excellent results, but is somehow time consuming. Indeed, for each  $t$  and each position  $\vec{r}$  of interest one needs to first calculate  $C(t, \tau, \vec{r})$  for a sufficiently large sets of time delays, and then perform a non-linear fit on each  $C(\tau)$  function. To speed up the processing, for each  $t$  one may simply calculate a dynamic activity map (DAM), i.e. a spatial map of the degree of correlation at a fixed time delay  $\tau$ .<sup>87</sup> Assuming that the decay of the autocorrelation function may be attributed only to the affine deformation and taking for simplicity  $a = 0$ , from Eqs. 2.31, 2.32 and 2.38 one has

$$\left( -\frac{\ln \frac{C(\tau) - C(\infty)}{C(0) - C(\infty)}}{2\epsilon} \right)^2 = 3k^2 l^{*2} f[\mathbf{d}(\tau)] = \frac{\tau^2 \dot{\gamma}_{MSDWS}^2 k^2 l^{*2}}{10}$$

$$C(\infty) = B, C(0) - C(\infty) = A, \quad 2.45$$

such that

$$\dot{\gamma}_{MSDWS} = \frac{\sqrt{10} \ln \frac{C(0) - C(\infty)}{C(\tau) - C(\infty)}}{2\epsilon k l^* \tau}. \quad 2.46$$

In Eq. 2.46,  $C(0)$  and  $C(\infty)$  are the correlation value at zero delay and infinite delay, respectively, which can be approximately calculated as the correlation of one image with itself and with images at a large time delay  $\tau$ . In writing Eq. 2.46, we have used the expression of  $\mathbf{d}$  for simple shear; but of course, one can write similar equations of different deformation geometries, e.g. for uniaxial extension using Eq. 2.37. Using Eq. 2.46, the DAMs can thus be directly converted to maps of the local strain rate<sup>88-89</sup>. This procedure is much faster than the fitting scheme described above, essentially because the correlation coefficients  $C$  need to be calculated only for one lag value.

Fig 2.16(a) shows DAMs calculated at  $t = 1080$  s for  $\tau = 0.18$  s and 0.6 s, also at  $\tau_{macro} = 0.62$  MPa. The two maps show qualitatively similar dynamics distributions: at the top-right corner where the debonding starts, the value of  $C(\tau)$  is lower, implying that the dynamics is faster. Note that, by choosing different values of  $\tau$ , one can tune the sensitivity



of the DAM to deformations occurring on different time scales, striking the desired balance between measuring the “instantaneous” deformation (by keeping  $\tau$  as small as possible) and assessing the cumulated deformation (by increasing  $\tau$ ). Fig 2.16(b), compares the maps of the local strain obtained either from the DAM shown on the in Fig 2.16(a), or by fitting the full autocorrelation function. The spatial distributions obtained from the two methods are very similar, demonstrating the soundness of the approach based on the DAMs. For these data, the gain in time when using the DAMs is quite substantial, since the full fitting procedure was about 100 times slower than the DAM one. A few remarks on the limits of the DAM approach are of interest. First, we note that retrieving the deformation rate from a DAM is only valid when the autocorrelation functions have the same shape over the whole image. Furthermore, when the magnitude of the deformation rate varies too much over the imaged sample or with time, the DAM approach significantly loses accuracy, due to the exponential shape of the autocorrelation function, which makes the DAMs poorly sensitive to deformation for time delays too small or too large compared to the relaxation time of  $C$ . Finally, the amplitude of the autocorrelation function,  $A$  in Eq. 2.31, depends on the coherence of the scattered light, which may vary over the imaging field. In practice, the most reliable and efficient approach would mix both fitting and using DAMs: (1) correlation functions calculated in real time on a subset of the acquired images should be monitored, in order to determine the optimal  $\tau$  for DAMs. (2) Renormalization of the correlation value by spatially resolved  $A$  in the subset images.

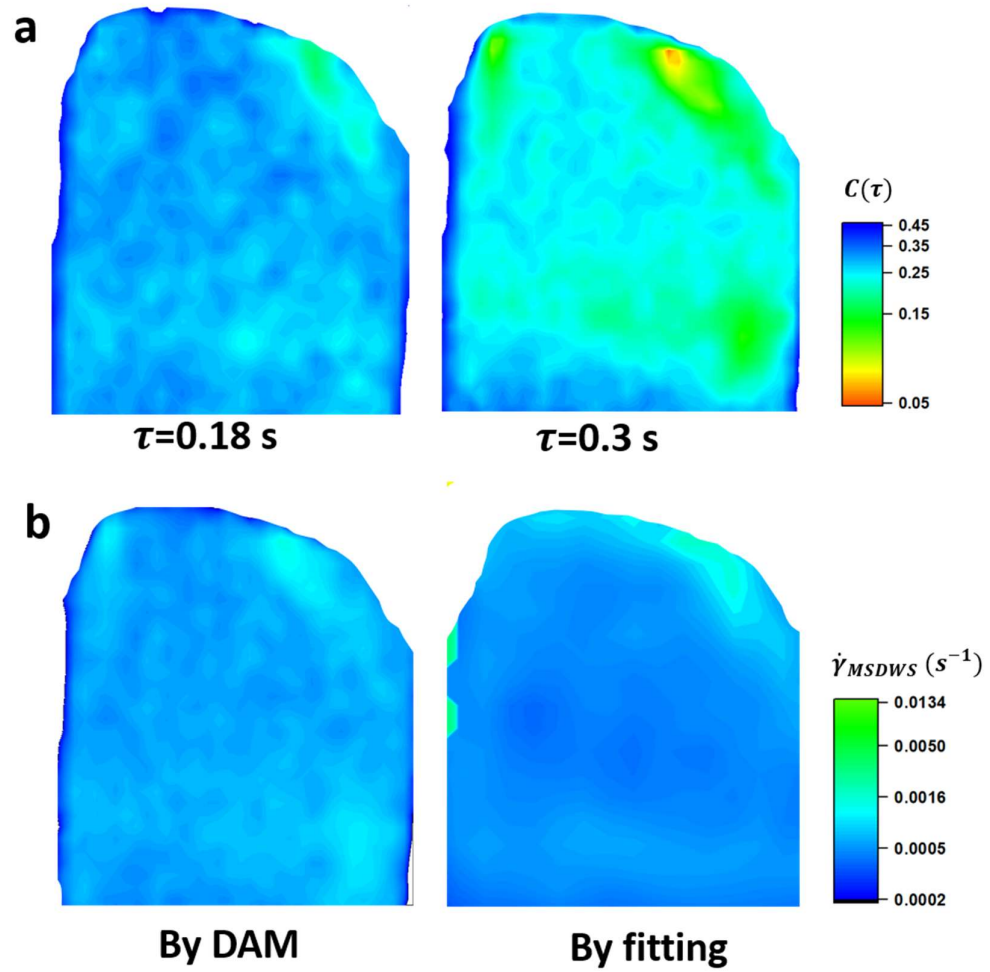


Fig. 2.16 (a) DAMs for  $\tau = 0.18 \text{ s}$  (left) and  $0.3 \text{ s}$  (right). (b)  $\dot{\gamma}_{MSDWS}$  map calculated from DAM (left) and fitting of autocorrelation function.

## 2.6 Conclusions

We have shown that MSDWS is a powerful tool for the measurement of spatially- and temporally-varying mechanical responses. Even though a complete modelling of the intensity autocorrelation function remains challenging, we have demonstrated that in a wide range of common testing situations it is possible to directly quantify the deformation rate distribution from the decay of space- and time-resolved correlation functions. MSDWS is relatively simple, requiring only illumination of the sample with coherent laser light and detection with a 2D sensor, typically a standard CMOS camera. Because MSDWS is not too sensitive to the exact illumination and detection parameters (angles of the incident and collected light with respect to the sample, acceptance angular range of the detector etc.), the requirements on optical alignment and the experimental environment are less strict than that in other optical methods. The tests on PDMS under elongation strain have allowed us to validate the theoretical analysis presented in Sec. 2.2. The method was then applied to the investigation of adhesive debonding, unveiling a heterogeneous deformation rate distribution and the emergence of microscopic precursors of failure hundreds of seconds before macroscopic debonding.

This paper provides theoretical and practical guidelines for using MSDWS as a powerful tool for measuring the local mechanical response of a loaded soft solid. A successful and efficient implementation requires a suitable combination of sample opacity ( $l^*$ ), range of deformation rate, testing geometry and data processing strategy. We hope that our work will further spur interest in this powerful method.

## 2.7 Reference

1. Wang, S.-Q.; Ravindranath, S.; Boukany, P., Homogeneous shear, wall slip, and shear banding of entangled polymeric liquids in simple-shear rheometry: A roadmap of nonlinear rheology. *Macromolecules* **2011**, *44* (2), 183-190.
2. Shi, H.; Roy, S.; Weinhart, T.; Magnanimo, V.; Luding, S., Steady state rheology of homogeneous and inhomogeneous cohesive granular materials. *Granular matter* **2020**, *22* (1), 1-20.
3. Coussot, P.; Ovarlez, G., Physical origin of shear-banding in jammed systems. *The European Physical Journal E* **2010**, *33* (3), 183-188.
4. Ballesta, P.; Duri, A.; Cipelletti, L., Unexpected drop of dynamical heterogeneities in colloidal suspensions approaching the jamming transition. *Nature Physics* **2008**, *4* (7), 550-554.
5. Liu, M.; Guo, J.; Hui, C. Y.; Zehnder, A. T., Application of Digital Image Correlation (DIC) to the Measurement of Strain Concentration of a PVA Dual-Crosslink Hydrogel Under Large Deformation. *Experimental Mechanics* **2019**.
6. Chen, W.; Lu, F.; Frew, D.; Forrestal, M., Dynamic compression testing of soft materials. *J. Appl. Mech.* **2002**, *69* (3), 214-223.
7. Lopez-Pamies, O.; Idiart, M. I.; Nakamura, T., Cavitation in elastomeric solids: I—a defect-growth theory. *Journal of the Mechanics and Physics of Solids* **2011**, *59* (8), 1464-1487.
8. Salmon, J.-B.; Colin, A.; Manneville, S.; Molino, F., Velocity profiles in shear-banding wormlike micelles. *Physical review letters* **2003**, *90* (22), 228303.
9. Fakhouri, S.; Hutchens, S. B.; Crosby, A. J., Puncture mechanics of soft solids. *Soft Matter* **2015**, *11* (23), 4723-4730.
10. Wang, Y.; Boukany, P.; Wang, S.-Q.; Wang, X., Elastic breakup in uniaxial extension of entangled polymer melts. *Physical review letters* **2007**, *99* (23), 237801.
11. Clough, J. M.; Creton, C.; Craig, S. L.; Sijbesma, R. P., Covalent Bond Scission in the Mullins Effect of a Filled Elastomer: Real-Time Visualization with Mechanoluminescence. *Advanced Functional Materials* **2016**, *26* (48), 9063-9074.
12. Ju, J.; Su, F.; Wang, Z.; Yang, H.; Tang, X.; Chen, X.; Lv, Y.; Lu, J.; Tian, N.; Li, L., Extension decelerated crystallization in  $\gamma$ -irradiated isotactic polypropylene: The role of asymmetric chain relaxation. *Polymer* **2017**, *131*, 68-72.
13. Mai, T.-T.; Okuno, K.; Tsunoda, K.; Urayama, K., Crack-Tip Strain Field in Supershear Crack of Elastomers. *ACS Macro Letters* **2020**, *9* (5), 762-768.
14. Sun, T. L.; Luo, F.; Hong, W.; Cui, K.; Huang, Y.; Zhang, H. J.; King, D. R.; Kurokawa, T.; Nakajima, T.; Gong, J. P., Bulk energy dissipation mechanism for the fracture of tough and self-healing hydrogels. *Macromolecules* **2017**, *50* (7), 2923-2931.
15. Cui, K.; Ye, Y. N.; Yu, C.; Li, X.; Kurokawa, T.; Gong, J. P., Stress relaxation and underlying structure evolution in tough and self-healing hydrogels. *ACS Macro Letters* **2020**, *9* (11), 1582-1589.
16. Chen, Y.; Yeh, C. J.; Qi, Y.; Long, R.; Creton, C., From force-responsive molecules to quantifying and mapping stresses in soft materials. *Science advances* **2020**, *6* (20), eaaz5093.
17. Millereau, P.; Ducrot, E.; Clough, J. M.; Wiseman, M. E.; Brown, H. R.; Sijbesma, R. P.; Creton, C., Mechanics of elastomeric molecular composites. *Proceedings of the National Academy of Sciences* **2018**, *115* (37), 9110-9115.
18. Pan, B.; Li, K., A fast digital image correlation method for deformation

- measurement. *Optics and Lasers in Engineering* **2011**, *49* (7), 841-847.
19. Pan, B., Digital image correlation for surface deformation measurement: historical developments, recent advances and future goals. *Measurement Science and Technology* **2018**, *29* (8), 082001.
  20. Nagazi, M.-Y.; Brambilla, G.; Meunier, G.; Marguerès, P.; Périé, J.-N.; Cipelletti, L., Space-resolved diffusing wave spectroscopy measurements of the macroscopic deformation and the microscopic dynamics in tensile strain tests. *Optics and Lasers in Engineering* **2017**, *88*, 5-12.
  21. Pine, D. J.; Weitz, D. A.; Zhu, J. X.; Herbolzheimer, E., Diffusing-wave spectroscopy: dynamic light scattering in the multiple scattering limit. *Journal de Physique* **1990**, *51* (18), 2101-2127.
  22. Erpelding, M.; Amon, A.; Crassous, J., Diffusive wave spectroscopy applied to the spatially resolved deformation of a solid. *Phys Rev E Stat Nonlin Soft Matter Phys* **2008**, *78* (4 Pt 2), 046104.
  23. Amon, A.; Nguyen, V. B.; Bruand, A.; Crassous, J.; Clement, E., Hot spots in an athermal system. *Phys Rev Lett* **2012**, *108* (13), 135502.
  24. van der Kooij, H. M.; Dussi, S.; van de Kerkhof, G. T.; Frijns, R. A.; van der Gucht, J.; Sprakel, J., Laser Speckle Strain Imaging reveals the origin of delayed fracture in a soft solid. *Science advances* **2018**, *4* (5), eaar1926.
  25. Erpelding, M.; Dollet, B.; Faisant, A.; Crassous, J.; Amon, A., Diffusing-Wave Spectroscopy Contribution to Strain Analysis. *Strain* **2013**, *49* (2), 167-174.
  26. McKelvy, M. J.; Diefenbacher, J.; Chizmeshya, A. V.; Wolf, G.; Marzke, R.; Béarat, H. In *Enhancing the Observation of Above and Below Ground Carbon Sequestration Processes under In Situ Pressure and Temperature Conditions*, Proceedings of the 30th International Technical Conference on Coal Utilization & Fuel Systems, 2005.
  27. Koniakhin, S.; Eliseev, I.; Terterov, I.; Shvidchenko, A.; Eidelman, E.; Dubina, M., Molecular dynamics-based refinement of nanodiamond size measurements obtained with dynamic light scattering. *Microfluidics and Nanofluidics* **2015**, *18* (5-6), 1189-1194.
  28. Furst, E. M.; Squires, T. M., *Microrheology*. Oxford University Press: 2017.
  29. Brown, W., *Dynamic light scattering: the method and some applications*. Clarendon Press Oxford: 1993; Vol. 313.
  30. Piederrière, Y.; Cariou, J.; Guern, Y.; Le Jeune, B.; Le Brun, G.; Lotrian, J., Scattering through fluids: speckle size measurement and Monte Carlo simulations close to and into the multiple scattering. *Optics Express* **2004**, *12* (1), 176-188.
  31. Norisuye, T.; Morinaga, T.; Tran-Cong-Miyata, Q.; Goto, A.; Fukuda, T.; Shibayama, M., Comparison of the gelation dynamics for polystyrenes prepared by conventional and living radical polymerizations: a time-resolved dynamic light scattering study. *Polymer* **2005**, *46* (6), 1982-1994.
  32. Zakharov, P.; Bhat, S.; Schurtenberger, P.; Scheffold, F., Multiple-scattering suppression in dynamic light scattering based on a digital camera detection scheme. *Applied optics* **2006**, *45* (8), 1756-1764.
  33. Pine, D. J.; Weitz, D. A.; Chaikin, P. M.; Herbolzheimer, E., Diffusing wave spectroscopy. *Phys Rev Lett* **1988**, *60* (12), 1134-1137.
  34. Zakharov, P.; Völker, A.; Buck, A.; Weber, B.; Scheffold, F., Quantitative modeling of laser speckle imaging. *Optics letters* **2006**, *31* (23), 3465-3467.
  35. Sessoms, D. A.; Bissig, H.; Duri, A.; Cipelletti, L.; Trappe, V., Unexpected spatial distribution of bubble rearrangements in coarsening foams. *Soft Matter* **2010**, *6* (13), 3030-3037.
  36. Cardinaux, F.; Cipelletti, L.; Scheffold, F.; Schurtenberger, P., Microrheology of giant-

- micelle solutions. *EPL (Europhysics Letters)* **2002**, *57* (5), 738.
37. Duri, A.; Ballesta, P.; Cipelletti, L.; Bissig, H.; Trappe, V., Fluctuations and noise in time-resolved light scattering experiments: measuring temporally heterogeneous dynamics. *Fluctuation and noise Letters* **2005**, *5* (01), L1-L15.
38. Viasnoff, V.; Lequeux, F.; Pine, D., Multispeckle diffusing-wave spectroscopy: A tool to study slow relaxation and time-dependent dynamics. *Review of scientific instruments* **2002**, *73* (6), 2336-2344.
39. Wu, X.; Pine, D.; Chaikin, P.; Huang, J.; Weitz, D., Diffusing-wave spectroscopy in a shear flow. *JOSA B* **1990**, *7* (1), 15-20.
40. Narita, T.; Beauvais, C.; Hébraud, P.; Lequeux, F., Dynamics of concentrated colloidal suspensions during drying-aging, rejuvenation and overaging. *The European Physical Journal E* **2004**, *14* (3), 287-292.
41. Narita, T.; Mayumi, K.; Ducouret, G.; Hébraud, P., Viscoelastic Properties of Poly(vinyl alcohol) Hydrogels Having Permanent and Transient Cross-Links Studied by Microrheology, Classical Rheometry, and Dynamic Light Scattering. *Macromolecules* **2013**, *46* (10), 4174-4183.
42. Aime, S.; Ramos, L.; Cipelletti, L., Microscopic dynamics and failure precursors of a gel under mechanical load. *Proc Natl Acad Sci U S A* **2018**, *115* (14), 3587-3592.
43. Waigh, T. A., Microrheology of complex fluids. *Reports on progress in physics* **2005**, *68* (3), 685.
44. Krall, A.; Weitz, D., Internal dynamics and elasticity of fractal colloidal gels. *Physical review letters* **1998**, *80* (4), 778.
45. Krajina, B. A.; Tropini, C.; Zhu, A.; DiGiacomo, P.; Sonnenburg, J. L.; Heilshorn, S. C.; Spakowitz, A. J., Dynamic light scattering microrheology reveals multiscale viscoelasticity of polymer gels and precious biological materials. *ACS central science* **2017**, *3* (12), 1294-1303.
46. Xu, J.; Viasnoff, V.; Wirtz, D., Compliance of actin filament networks measured by particle-tracking microrheology and diffusing wave spectroscopy. *Rheologica Acta* **1998**, *37* (4), 387-398.
47. Mason, T. G.; Gang, H.; Weitz, D. A., Diffusing-wave-spectroscopy measurements of viscoelasticity of complex fluids. *JOSA A* **1997**, *14* (1), 139-149.
48. Li, Q.; Peng, X.; McKenna, G. B., Long-term aging behaviors in a model soft colloidal system. *Soft Matter* **2017**, *13* (7), 1396-1404.
49. Lee, J. Y.; Hwang, J. W.; Jung, H. W.; Kim, S. H.; Lee, S. J.; Yoon, K.; Weitz, D. A., Fast dynamics and relaxation of colloidal drops during the drying process using multispeckle diffusing wave spectroscopy. *Langmuir* **2013**, *29* (3), 861-866.
50. Sreekumari, A.; Ilg, P., Slow relaxation in structure-forming ferrofluids. *Physical Review E* **2013**, *88* (4), 042315.
51. Li, J.; Ngai, T.; Wu, C., The slow relaxation mode: from solutions to gel networks. *Polymer journal* **2010**, *42* (8), 609-625.
52. Sasaki, S.; Koga, S., Slow relaxation of the elastic n-isopropylacrylamide gel. *Macromolecules* **2002**, *35* (3), 857-860.
53. Cipelletti, L.; Ramos, L.; Manley, S.; Pitard, E.; Weitz, D. A.; Pashkovski, E. E.; Johansson, M., Universal non-diffusive slow dynamics in aging soft matter. *Faraday discussions* **2003**, *123*, 237-251.
54. Bouchaud, J.-P., Anomalous relaxation in complex systems: from stretched to compressed exponentials. *Anomalous Transport* **2008**, 327-345.
55. Basu, A.; Wen, Q.; Mao, X.; Lubensky, T.; Janmey, P. A.; Yodh, A., Nonaffine displacements in flexible polymer networks. *Macromolecules* **2011**, *44* (6), 1671-1679.

56. Amon, A.; Mikhailovskaya, A.; Crassous, J., Spatially resolved measurements of micro-deformations in granular materials using diffusing wave spectroscopy. *Rev Sci Instrum* **2017**, *88* (5), 051804.
57. Bicout, D.; Maynard, R., Diffusing wave spectroscopy in inhomogeneous flows. *Physica A: Statistical Mechanics and its Applications* **1993**, *199* (3-4), 387-411.
58. Johnson, G. C.; Bammann, D. J., A discussion of stress rates in finite deformation problems. *International Journal of Solids and Structures* **1984**, *20* (8), 725-737.
59. Hughes, T. J.; Marsden, J., *Mathematical foundations of elasticity*. Citeseer: 1983.
60. Rickhey, F.; Kim, M.; Lee, H.; Kim, N., Evaluation of combined hardening coefficients of zircaloy-4 sheets by simple shear test. *Materials & Design (1980-2015)* **2015**, *65*, 995-1000.
61. Thiel, C.; Voss, J.; Martin, R. J.; Neff, P., Shear, pure and simple. *International Journal of Non-Linear Mechanics* **2019**, *112*, 57-72.
62. Lurie, A.; Belyaev, A., Stress tensor. In *Theory of Elasticity*, Springer: 2005; pp 29-76.
63. Weitz, D.; Pine, D., Diffusing-wave spectroscopy. In *Dynamic light scattering: The method and some applications*, Oxford University Press: 1993; pp 652-720.
64. Durand, M.; Stone, H. A., Relaxation time of the topological T 1 process in a two-dimensional foam. *Physical review letters* **2006**, *97* (22), 226101.
65. Schall, P.; Weitz, D. A.; Spaepen, F., Structural rearrangements that govern flow in colloidal glasses. *Science* **2007**, *318* (5858), 1895-1899.
66. Cipelletti, L.; Brambilla, G.; Maccarrone, S.; Caroff, S., Simultaneous measurement of the microscopic dynamics and the mesoscopic displacement field in soft systems by speckle imaging. *Opt Express* **2013**, *21* (19), 22353-66.
67. Houdoux, D.; Amon, A.; Marsan, D.; Weiss, J.; Crassous, J., Micro-slips in an experimental granular shear band replicate the spatiotemporal characteristics of natural earthquakes. *Communications Earth & Environment* **2021**, *2* (1), 1-11.
68. Goodman, J. W., *Speckle phenomena in optics: theory and applications*. Roberts and Company Publishers: 2007.
69. Durian, D. J., Accuracy of diffusing-wave spectroscopy theories. *Physical Review E* **1995**, *51* (4), 3350.
70. Lee, C.; Take, W. A.; Hoult, N. A., Optimum accuracy of two-dimensional strain measurements using digital image correlation. *Journal of Computing in Civil Engineering* **2012**, *26* (6), 795-803.
71. Acciaioli, A.; Lionello, G.; Baleani, M., Experimentally achievable accuracy using a digital image correlation technique in measuring small-magnitude (< 0.1%) homogeneous strain fields. *Materials* **2018**, *11* (5), 751.
72. Raman, K.; Murthy, T. S.; Hegde, G., Fabrication of refractive index tunable polydimethylsiloxane photonic crystal for biosensor application. *Physics Procedia* **2011**, *19*, 146-151.
73. Tong, L., Strength of adhesively bonded single-lap and lap-shear joints. *International Journal of Solids and Structures* **1998**, *35* (20), 2601-2616.
74. Kafkalidis, M.; Thouless, M., The effects of geometry and material properties on the fracture of single lap-shear joints. *International Journal of Solids and Structures* **2002**, *39* (17), 4367-4383.
75. Lakrout, H.; Sergot, P.; Creton, C., Direct observation of cavitation and fibrillation in a probe tack experiment on model acrylic pressure-sensitive-adhesives. *The Journal of Adhesion* **1999**, *69* (3-4), 307-359.
76. Pandey, V.; Fleury, A.; Villey, R.; Creton, C.; Ciccotti, M., Linking peel and tack

- performances of pressure sensitive adhesives. *Soft Matter* **2020**, *16* (13), 3267-3275.
77. Nagazi, M. Y. Cartographie de la dynamique microscopique dans la matière molle sous sollicitation. Montpellier, 2017.
78. Deplace, F.; Rabjohns, M. A.; Yamaguchi, T.; Foster, A. B.; Carelli, C.; Lei, C.-H.; Ouzineb, K.; Keddie, J. L.; Lovell, P. A.; Creton, C., Deformation and adhesion of a periodic soft-soft nanocomposite designed with structured polymer colloid particles. *Soft Matter* **2009**, *5* (7), 1440-1447.
79. Hui, C.-Y.; Liu, Z.; Minsky, H.; Creton, C.; Ciccotti, M., Mechanics of an adhesive tape in a zero degree peel test: effect of large deformation and material nonlinearity. *Soft matter* **2018**, *14* (47), 9681-9692.
80. Liu, Z.; Minsky, H.; Creton, C.; Ciccotti, M.; Hui, C.-Y., Mechanics of zero degree peel test on a tape—effects of large deformation, material nonlinearity, and finite bond length. *Extreme Mechanics Letters* **2019**, *32*, 100518.
81. Sugizaki, Y.; Suzuki, A., Unsteady peeling accompanied by oscillations of adhesive tape from a soft adherend. *Soft matter* **2019**, *15* (35), 7080-7088.
82. Ponce, S.; Bico, J.; Roman, B., Effect of friction on the peeling test at zero-degrees. *Soft matter* **2015**, *11* (48), 9281-9290.
83. Takahashi, K.; Oda, R.; Inaba, K.; Kishimoto, K., Scaling effect on the detachment of pressure-sensitive adhesives through fibrillation characterized by a probe-tack test. *Soft Matter* **2020**, *16* (28), 6493-6500.
84. McKinley, P.; Sinha, A.; Kamke, F. A., Understanding the effect of weathering on adhesive bonds for wood composites using digital image correlation (DIC). *Holzforschung* **2019**, *73* (2), 155-164.
85. Shi, H.; Fernandez Villegas, I.; Bersee, H. In *An investigation on the strain distribution of resistance welded thermoplastic composite joints*, 53rd AIAA/ASME/ASCE/AHS/ASC Structures, Structural Dynamics and Materials Conference 20th AIAA/ASME/AHS Adaptive Structures Conference 14th AIAA, 2012; p 1448.
86. Aydın, M. D., 3-D nonlinear stress analysis on adhesively bonded single lap composite joints with different ply stacking sequences. *The Journal of Adhesion* **2008**, *84* (1), 15-36.
87. Duri, A.; Sessoms, D. A.; Trappe, V.; Cipelletti, L., Resolving long-range spatial correlations in jammed colloidal systems using photon correlation imaging. *Physical review letters* **2009**, *102* (8), 085702.
88. Verho, T.; Karppinen, P.; Groschel, A. H.; Ikkala, O., Imaging Inelastic Fracture Processes in Biomimetic Nanocomposites and Nacre by Laser Speckle for Better Toughness. *Adv Sci (Weinh)* **2018**, *5* (1), 1700635.
89. van der Kooij, H. M.; Susa, A.; Garcia, S. J.; van der Zwaag, S.; Sprakel, J., Imaging the Molecular Motions of Autonomous Repair in a Self-Healing Polymer. *Adv Mater* **2017**, *29* (26).



## 2.8 Supporting Information:

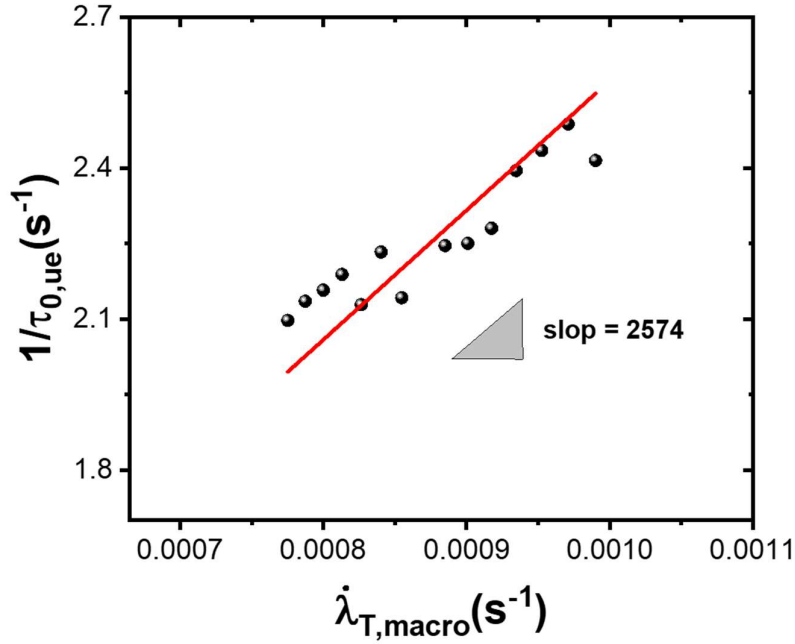
fitting of  $l^*$  in adhesive tapes

Fig. 2.S1  $1/\tau_{0,ue}$  as a function of  $\dot{\lambda}_{T,macro}$ , measured in tapes under uniaxial tension.

$\tau_{0,ue}$  of the adhesive tape is measured under uniaxial tension with set-up shown in Fig. 2.S1, with  $\dot{\lambda}_N = 0.001 s^{-1}$ . To obtain  $l^*$  from uniaxial tensile testing,  $1/\tau_{0,ue}$  is plotted as the function of  $\dot{\lambda}_{T,macro}$ , calculated using eq. 2.43, where  $1/\tau_{0,ue}$  should be proportional to  $\dot{\lambda}_{T,macro}$ , with slope scales with  $kl^*$  (see eq. 2.37). From 2.S1, a slop of 2574 is fitted from the scattered data points, corresponding to  $kl^* = 3323.4$

---

## Chapter 3. Fast detection of early-stage damage in soft elastomers

The finite element simulation in this chapter is performed by professor *Chung-Yuen Hui* and Zezhou Liu in Connell University, who will be coauthors of the paper being prepared based on this chapter.

### 3 Fast detection of early-stage damage in soft elastomers

Jianzhu Ju <sup>a</sup>, Gabriel Sanoja <sup>a</sup>, Luca Cipelletti <sup>b,c</sup>, Zezhou Liu <sup>d</sup>, Chung Yuen Hui <sup>d,e</sup>, Matteo Ciccotti <sup>a</sup>,  
Tetsuharu Narita <sup>\*,a,e</sup>, Costantino Creton <sup>\*,a,e</sup>

<sup>a</sup> Sciences et Ingénierie de la Matière Molle, CNRS UMR 7615, ESPCI Paris, PSL Université, Paris, France

<sup>b</sup> Laboratoire Charles Coulomb (L2C), University of Montpellier, CNRS, Montpellier, France

<sup>c</sup> Institut Universitaire de France

<sup>d</sup> Sibley School of Mechanical and Aerospace Engineering, Cornell University, Ithaca, NY 14853, USA

<sup>e</sup> Global Station for Soft Matter, Global Institution for Collaborative Research and Education, Hokkaido University, Sapporo, Japan

#### Abstract

Subcritical fracture of material takes place by slow accumulation of internal damages below the critical failure condition. While subcritical fracture accounts for most of the structural failures in use, it is challenging to understand its microscopic origin or prevent it in time, due to the lack of current non-destructive detection methods with suitable resolution. With simultaneous measurement of multiple speckle diffusing wave spectroscopy (MSDWS) and mechanophore mapping during the fracture of PDMS elastomers, we identify a fracture precursor in the form of large-scale strain rate acceleration ( $\sim \text{cm}^2$ ) at long times (up to thousands of seconds) before macroscopic fracture and attribute it to local molecular damage ( $\sim 0.01 \text{ mm}^2$  in plane). While the change in local damage is so far only detectable by the tool of mechanochemistry, its sign of accelerated deformation rate is significantly more observable by MSDWS with ordinary

---

\*correspondence authors: [tetsuharu.narita@espci.fr](mailto:tetsuharu.narita@espci.fr)

\*correspondence authors: [costantino.creton@espci.fr](mailto:costantino.creton@espci.fr)

imaging and processing. As tested in different conditions and materials, our work shows that MSDWS is a powerful tool to characterize and prevent microscopic damage, well before it becomes critical.

### 3.1 Introduction

Resistance to fracture of soft materials is typically characterized by a tensile test carried out until fracture, where parameters such as stretch and stress at break are commonly used. More recently, Suo et al. have argued that strain energy at break in unnotched samples defined as  $W$  in  $\text{J}/\text{m}^3$  can be a material parameter (at least at fixed geometry).<sup>1</sup> Alternatively, the fracture mechanics community has long used pre-notched samples and defined the fracture energy  $\Gamma$  as a critical strain energy release rate  $G_c$ , where the crack begins to propagate from the notch.<sup>2</sup> However, careful examination of the data shows that for soft materials, where dissipation takes place over several length/time scales, this critical transition is actually not very well defined. Due to viscoelasticity of the polymer networks,  $G$  not only depends on external loading history or sample geometry, but also can evolve with time in particular in fixed load conditions.<sup>3</sup> As a result, even below a critical stress/strain at break measured in continuous loading conditions, catastrophic fracture can take place under constant load after a long time, a phenomenon known as delayed fracture.<sup>3-5</sup> Similarly to delayed fracture under fixed load, when a notched sample is stretched at a constant rate, it has been commonly observed that there exists a transition from almost undetectable propagation rate to a fast propagation mode,<sup>6,7</sup> at which point a critical value of the energy release rate  $G_c$  can be obtained. The two behaviors share the same implicit hypothesis that the almost unpredictable sudden macroscopic failure follows a constant/steady mechanical process of accumulated molecular damage.<sup>5</sup> While slow propagation (including deformation and damage) of the crack can be observed after a long waiting time or a large number of loading cycles at low stretch (fatigue testing), this does not necessarily mean that the material will fail immediately but the eventual lifetime of the material depends on the accumulation of

localized damage. Localized accumulated damage accounts for most of the catastrophic fracture events in real life, so that the interesting and important question is how this transition to rapid propagation takes place and whether it is predictable. Unfortunately, this transition from slow/no propagation to rapid propagation of the crack is apparently a subcritical transition,<sup>3,8</sup> which generally occurs suddenly. Prediction and early detection of signs of damage would be highly desirable and this is the focus of our study. We will explore a novel method of early detection of delayed failure with fast and sensitive resolution.

Multispeckle diffusing wave spectroscopy (MSDWS) can detect nanometer scale motions of microscopic probes with a millisecond time resolution and its ultrasensitivity to affine deformation field in the soft material can be used as a tool to map spatially revolved strain rate.<sup>9,10</sup> Therefore in principle such an excellent sensitivity to microscopic displacements, could detect changes in local microscopic dynamics before a macroscopic event occurs<sup>8,11-13</sup>, such as the propagation of a crack. However, reported studies of early detection of dynamic precursors before sudden failure have remained at the stage of post processing of the data, and the existence of a precursor was only qualitatively discussed after catastrophic fracture, where structural characterization is no longer possible.<sup>8,14</sup> The real potential of the method we propose is: 1. To prevent substantial damage to occur by real-time detection; 2. To detect and analyze microscopic structural changes related to the growth of a precursor at an early stage (even hours) before failure. In this work, in order to maximize the insight, we combined fluorescence detection of bond scission with highly sensitive MSDWS detection of local dynamics and changes in local strain rates, as seen in Fig. 3.1(a).<sup>15</sup>

## 3.2 Results and Discussion

### 3.2.1 Simultaneous mapping of strain rate and damage

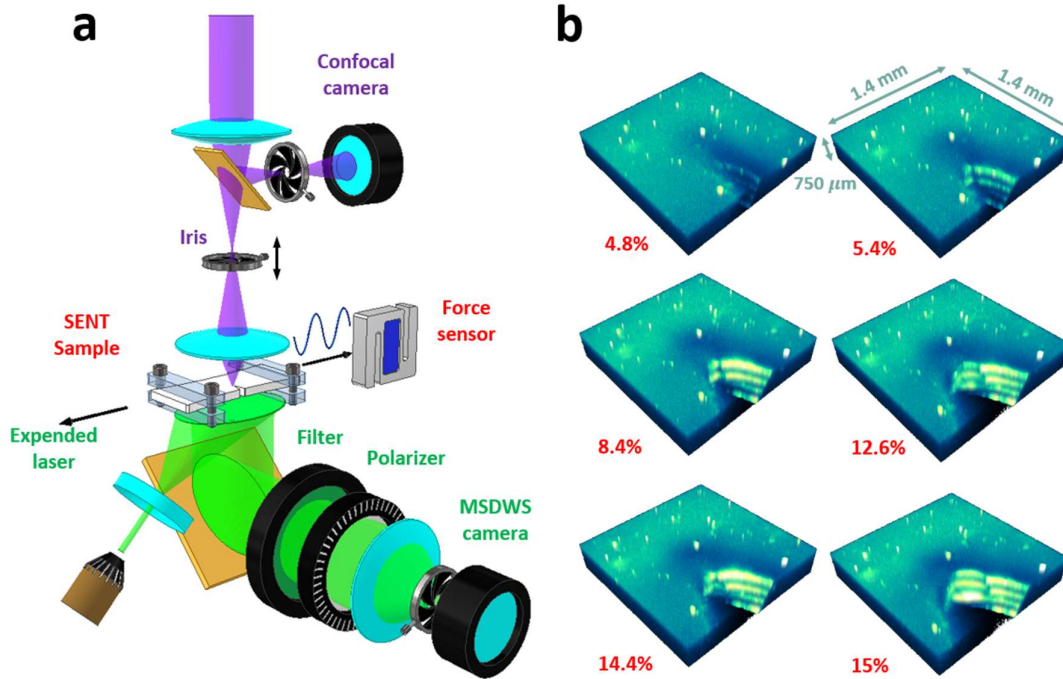


Fig. 3.1 (a) Simultaneous measurement set-up of MSDWS and confocal microscopy. (b) 3D image of bonds breaking around the crack tip during tensile testing of a notched sample.

Sylgard 184 polydimethylsiloxane (PDMS) is used as a model soft material (see materials and methods 3.5.1), with mechanophore diacrylate cross-linker<sup>16</sup> (0.1 wt%) and TiO<sub>2</sub> particles (diameter 250 nm, 0.25 wt%) embodied before curing. Single edge notch (SEN) samples (width × length: 9 mm × 15 mm, thickness 2 mm and notch length 1 mm, cut with a fresh razor blade) were tested in uniaxial tension at a constant stretch rate  $\dot{\lambda}_N = 5 \times 10^{-5} \text{ s}^{-1}$  in a specially designed tensile rig fitted with the observation set-up shown in Fig. 3.1(a). As confocal microscopy only detects a small field around the crack tip, the two crossheads moves oppositely (375 μm/s) so that the tip position is fixed in the stretch direction and slightly moved in the perpendicular direction. A spatially resolved

characterization of the dynamics over the whole sample surface was carried out by MSDWS in backscattering from the bottom of the sample while simultaneously fluorescence from the broken mechanophores was detected from the top, around the crack tip. Under continuous stretching, macroscopic fracture is detected at a nominal strain  $\varepsilon_f = 15.6\%$  (typically  $\varepsilon_f \sim 15\%$  for SEN samples), as detectable from bright field imaging.

Fig. 3.1(b) shows the 3D mapping by confocal microscopy of the fluorescence intensity due to mechanophore activation around the original open notch for different levels of crack opening. Briefly, as the sample is stretched, some of the crosslinker molecules break near the crack tip. When the mechanophore cross-linker is irreversibly broken, it becomes fluorescent under laser illumination, so that the accumulated bond scission can be measured by confocal microscopy.<sup>15,17</sup> To build each 3D image, 4 image slices (1.4 mm  $\times$  1.4 mm in plane with detection thickness 150  $\mu\text{m}$ ) scanning a depth of 750  $\mu\text{m}$  around the midplane of the sample are collected (see materials and methods 3.5.2.1 for detail). The dark strip patterns in 3D images correspond to the gaps between slices. While initial activation is due to the artificial cut of the notch, images show that the activation intensity due to bonds breaking increases already at strains much lower than  $\varepsilon_f$ . At the onset of propagation, massive damage is detected around the crack in the 3<sup>rd</sup> slice, with length around 450  $\mu\text{m}$  ( $\varepsilon_N=15\%$  in Fig. 3.1(b)). (also see Movie S1, available upon request).



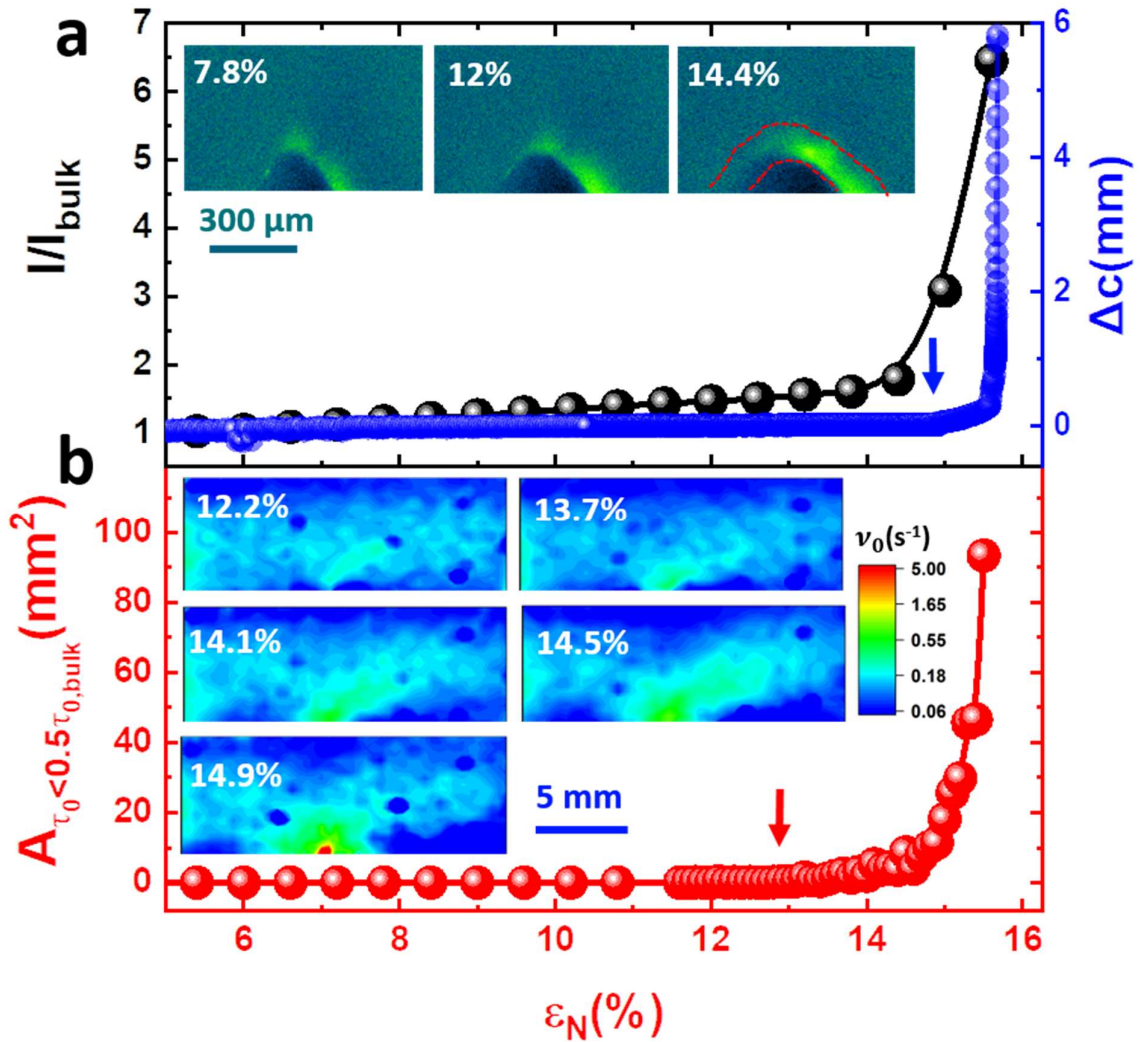


Fig. 3.2 (a) Averaged intensity (black) of mechanophore activation, renormalized by the bulk intensity and crack propagation length  $\Delta c$  (blue). Insert: 2D mechanophore maps at 400  $\mu m$  deep. (b) The area in  $v_0$  maps where  $v_0 > 2v_{0N}$ . Insert:  $v_0$  maps at different strains. The onset of precursor and propagation are indicated by arrows.

Area averaged fluorescence intensities  $I$  were calculated from the integration along the path of open crack edge with a width of 130  $\mu m$  (inserted in Fig. 3.2(a)), in the 3<sup>rd</sup> slice (see supporting information 3.6.1 for detail). The intensity is renormalized by bulk intensity ( $I_{bulk}$ ) to remove the influence of absorption and laser bleaching, and  $I/I_{bulk}$  is shown in Fig. 3.2(a). The rate of increase of  $I/I_{bulk}$  remains almost constant for  $\epsilon_N < 14\%$ .

At  $\varepsilon_N = 13.8\%$ , a larger increase in intensity occurs on the right side of the crack in 2D image, after which  $I/I_{bulk}$  increases faster. As also seen in Fig. 3.2(a), a slight change in crack length  $\Delta c$  is detectable starting at  $\varepsilon_N = 15\%$  ( $\Delta t = 100$  s before fracture), with first an ultraslow increase  $\sim 1.5\ \mu\text{m/s}$  and then 90% of the propagation occurring in the last 5 s. For  $13.8\% < \varepsilon_N < 15\%$ , there is only a rapid increase in fluorescence intensity without detectable crack propagation by bright field microscopy imaging with sub-micron resolution.

As described in detail in the methods section, MSDWS was used in parallel on the bottom face of the sample to map spatially the microscopic dynamics. Briefly, a characteristic rate  $v_0$  was fitted from the temporally and spatially resolved autocorrelation function. (see materials and methods 3.5.2.2 and supporting information 3.6.2.1). Then maps of  $v_0$  were built for different values of  $\varepsilon_N$  during the continuous stretching experiment and are shown in Fig. 3.2(b). For  $\varepsilon_N < 13.5\%$ , the  $v_0$  map remains almost identical with slightly higher values of  $v_0$  around the crack tip, where the faster dynamics region points to the right, consistent with the damaged region detected by fluorescence confocal microscopy in Fig. 3.2(a). The blue spots are the preexisting bubbles and defects in the material. For  $\varepsilon_N > 13.5\%$ , a significant heterogeneity in dynamics occurs in front of the crack and grows rapidly.

We can now relate the dynamic measurement obtained from the autocorrelation function to the strain rate. It can be shown (see Chapter 2 and supporting information 3.6.2) that  $v_0$  for these samples under strain is proportional to  $\sqrt{\text{Tr}(\mathbf{D}^2)}$ , where  $\mathbf{D}$  is the rate of deformation tensor in the deformed configuration. In uniformly deformed (unnotched) samples in uniaxial stretching,  $v_0$  scales with true strain rate along the stretch direction ( $\dot{\lambda}_T$ ). For example the nominal strain rate  $\dot{\lambda}_N = 5 \times 10^{-5}\ \text{s}^{-1}$  used in our experiments

corresponds to  $v_{0N} = 0.23 \text{ s}^{-1}$  and  $\dot{\lambda}_T$  corresponds to  $v_{0T} = v_{0N}/(1 + \varepsilon_N)$  (see Chapter 2, section 1.4). The region with  $v_0 > 2v_{0T}$  (roughly the green region in Fig. 3.2(b)) rapidly grows from a size around  $1 \text{ mm}^2$  ( $\varepsilon_N = 13.7 \%$ ) and reaches a size of  $10 \text{ mm}^2$  ( $\varepsilon_N = 14.75 \%$ ), much larger than the region of activation of the mechanophore.

Both mechanophore mapping of molecular damage and MSDWS dynamics mapping show that from around  $\varepsilon_N \sim 13.5 \%$  to just before rapid propagation, there exist detectable microscopic precursor events which grow in size as microscopic heterogeneities, while no macroscopic failure occurs. Remarkably, the time correspondence shows that the highly heterogeneous strain rate distribution over a large scale ( $1 \text{ cm}^2$  scale) is due to bonds breaking very close to the tip of the crack ( $0.01 \text{ mm}^2$  scale in plane). The size scale of the heterogeneous distribution of deformation rates is almost the same as the sample size, and observable around 7 min before macroscopic fracture, at our applied stretch rate.

### 3.2.2 The contribution of slow crack propagation simulated by FEM

Localized damage plays an important role in crack propagation while in existing models it is theoretically challenging to couple damage and deformation together.<sup>18</sup> An important question here is whether the increase in dynamics far from the crack tip is simply due to crack growth (below our resolution) or is related to the molecular damage detected by fluorescence. In order to check this hypothesis, a full-field finite element method (FEM) simulation considering only the contribution of deformation (but not allowing for changes in material properties due to damage) was carried out for the same materials. A neo-Hookean solid material model,<sup>19</sup> fitted to the uniaxial tension data is used to compute the simulation. We used FEM to calculate the full-field strain rate, with and without including slow propagation, respectively. Propagation is simulated here by simply

introducing an increasing crack length regardless of damage. Since MSDWS gives a scalar function ( $v_0$ ) of the rate of deformation tensor  $\mathbf{D}$ , digital image correlation (DIC)<sup>20</sup> is applied instead on a separate sample with a surface spray-painted with black ink to compare with a simulation. DIC measures spatially resolved deformations by comparing images containing speckles as references, which can directly provide components of the deformation rate tensor.  $\mathbf{D}$  and  $v_0$  are calculated with images collected from time  $t$  to  $t + T$  (see supporting information 3.6.2.2 for detail), where  $T$  is the time interval for correlation and averaging.

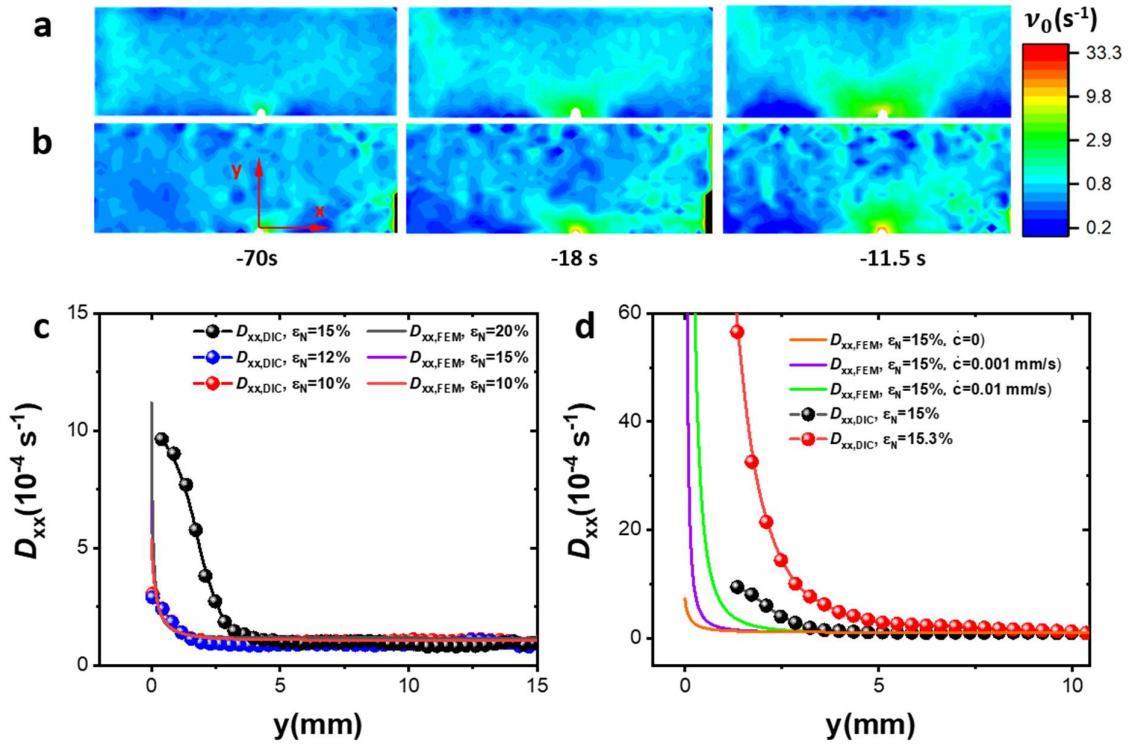


Fig. 3.3  $v_0$  maps calculated from MSDWS (a) and DIC (b) at different times before fracture. (c)  $D_{xx}$  as the function of distance  $y$  from crack tip with  $x = 0$  (as indicated in (b)) from DIC and FEM, regardless of propagation (d) Comparison between  $\dot{\epsilon}_{xx}$  from DIC and from FEM considering propagation.

MSDWS and DIC are performed separately on different samples in the same conditions (sample size 2 cm  $\times$  4 cm  $\times$  4 mm, initial crack length  $c = 2$  mm and  $\dot{\lambda}_N = 1.25 \times 10^{-4}$  s<sup>-1</sup>).

The sample tested with MSDWS failed at  $\varepsilon_f = 15.9\%$  while the sample tested by DIC failed at  $\varepsilon_f = 15.7\%$ . With DIC results,  $v_0$  can be calculated directly from  $\mathbf{D}$  (Fig. 3.3(a)) and compared with the direct result of MSDWS (Fig. 3.3(b)). The similarity is obvious, validating the use of MSDWS to map strain rate in these complex 2D conditions.

FEM and DIC results can now be compared in more detail by plotting strain rate along the stretching direction  $\mathbf{D}_{xx,FEM}$  and  $\mathbf{D}_{xx,DIC}$  as a function of  $y$  at  $x = 0$ , as seen in Fig. 3.3(c) (FEM without crack propagation) and (d) (with propagation). In the absence of propagation,  $\mathbf{D}_{xx,FEM}$  far from the tip ( $y > 0.1$  mm) remains almost constant with  $\varepsilon_N$  up to  $\sim 20\%$ . However, while at low strain,  $\mathbf{D}_{xx,DIC}$  matches well with  $\mathbf{D}_{xx,FEM}$ , starting from  $\varepsilon_N = 15\%$ ,  $\mathbf{D}_{xx,DIC}$  increases significantly more than  $\mathbf{D}_{xx,FEM}$  even millimeters from the tip, without detectable propagation of the crack by imaging, indicating the existence of fracture precursors. Even if  $\dot{c} = 0.01$  mm/s is assumed (minimal optically detectable crack speed  $\dot{c} \sim 1$   $\mu$  m/s),  $\mathbf{D}_{xx,DIC}$  is still well above  $\mathbf{D}_{xx,FEM}$  at  $\varepsilon_N = 15\%$  (Fig. 3.3(d)). Furthermore, at a slightly larger strain of  $\varepsilon_N = 15.3\%$  (24 s later), still without detectable propagation, a dramatic increase of  $\dot{\varepsilon}_{xx,DIC}$  is observed.

In conclusion, at small values of applied  $\varepsilon_N$ , the comparison between simulation (FEM) and experiments (MSDWS and DIC) shows a very good consistency. However for higher values of  $\varepsilon_N$  approaching macroscopic fracture, experimental values deviate largely from simulation values. If we now compare the MSDWS results and the mechanophore mapping, the acceleration of the local strain rate over a large volume actually corresponds to detectable chemical bond scission very close to the crack tip. Yet, the effect of bond scission is absent from our FEM model, as well as from similar theoretical<sup>3</sup> and experimental works<sup>4,8</sup> addressing subcritical fracture. Our insight points out the important information that existing models lack, to predict and describe the transient

behavior before fracture, where localized damage is not only negligible, but actually dominating. Localized damage can significantly affect the deformation at distances far from the crack tip, even in a model elastic solid like PDMS. Remarkably, while  $\varepsilon_N$  itself only substantially influences  $\dot{\varepsilon}_{xx}$  in a region very close to the crack tip (as seen in simulation results in the supporting information 3.6.2.3) and does not contribute to  $D_{xx}$  far from the tip, the rapid growth in strain heterogeneity before fracture shows strong instability in response of dynamic damage accumulation. As seen in fluorescence intensity in Fig. 3.2(a), even at very low  $\varepsilon_N$ , damage is accumulating around the crack. However, only after  $\varepsilon_N > 13.5\%$ , this accumulated damage leads to strain rate acceleration and fracture. This suggests a threshold level of damage above which propagation can be initiated. This threshold of damage level appears distinct from the *Lake-Thomas* model,<sup>21</sup> which considers bond scission only over one network mesh size (10 nm) ahead of crack as the threshold,<sup>22</sup> since the damage zone size is here around 100  $\mu\text{m}$  in our observation (Fig. 3.2(a)). This may be due to the well-known presence of silica nanoparticle in the Sylgard 184 that delocalize the damage.<sup>23</sup>

A similar behavior is also observed in a different experiment where the sample is stretched to different strains in a step-by-step fashion and held there for measurement, with a waiting period of 1 h after each step. In this experiment, strain is carefully increased by  $\Delta\varepsilon_N = 0.25\%$ , and when approaching  $\varepsilon_N = 15 \sim 16\%$ , smaller steps ( $\Delta\varepsilon_N = 0.0625\%$ ) are chosen to ensure that delayed fracture<sup>4,8</sup> takes place in the waiting period, instead of during the stretching step. In this static measurement, since the decorrelation modes can be due to diffusive motions other than the affine deformation field,<sup>24,25</sup> we implemented a modified processing of the raw data. Only correlation values at one fixed time interval  $T_{MSDWS}$  were calculated to build the dynamic activity map (DAM).<sup>8,10</sup> The reported correlation value decreases as decorrelation is faster, corresponding to a lower

intensity in the DAM. At  $\varepsilon_N = 15\%$ , an ultraslow propagation ( $\sim 20$  nm/s) and a slight increase of fluorescence intensity due to mechanophore activation is observed starting from a waiting time ( $t_w$ ) of 1700 s, as seen in Fig. 3.4(a). Using MSDWS with  $T_{MSDWS} = 40$  s, a fast dynamics region representing heterogeneity of deformation rate (Fig. 3.4(b)) can be clearly observed at  $t_w = 800$  s, 15 min before a slight propagation and damage is detected by confocal imaging (Fig 3.4(a) bottom) and 30 min before detectable by full-field imaging.

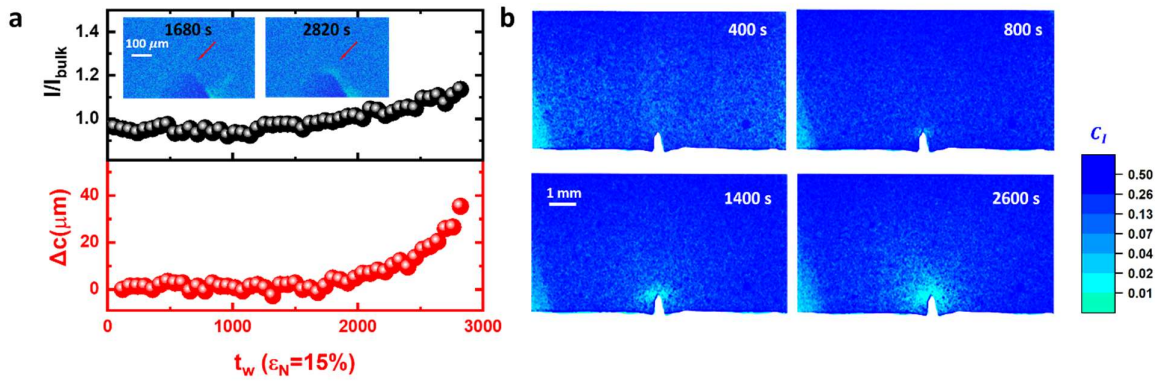


Fig. 3.4 (a) Renormalized Activation intensity (top) and propagation length (bottom) as the function of waiting time, detected by confocal microscopy. Inserted: 2D confocal images at 1680 and 2820 s, respectively. (b) DAMs from MSDWS at different waiting time, with time interval of 40 s.

### 3.2.3 Damage prediction by MSDWS

The large-scale strain rate acceleration response to a damage close to the crack tip (in both continuous and fixed loading) also suggests that a collection and analysis of ordinary full-field images can be used to predict and prevent damage at a very early stage, before it shows any perceptible impact. Instead of a commonly investigated strain map, our mapping of the dynamics essentially provides directly a differential diagnosis in response to the coupled effect of external load and local damage, so that the sensitivity of detection

of the subtle change in strain distribution can be maximized. Note that even though full-field DIC provides in principle similar informations in terms of strain rate distribution, the time resolution of DIC is limited by  $T_{min}$ , the required time interval to detect a heterogeneous strain rate distribution from the strain field. Longer  $T_{min}$  means slower response to an existing fracture precursor. For example in Fig. 3.3(b), for  $-70$  s,  $-18$  s and  $-11.5$  s before fracture,  $T_{min}$  are 20 s, 10 s and 4 s, respectively. In the case of delayed fracture, the delay in detection by DIC becomes critical, so that even during the entire  $t_w$  around 30 min before delayed propagation, no acceleration of deformation rate is detected by DIC ( $T_{min} > 1800$  s). On the other hand, the correlation time of MSDWS can be largely reduced by using DAM (typically required  $T_{MSDWS} \sim 0.05 \tau_0$ ), where a  $T_{MSDWS}$  of 40 s is enough to detect heterogeneity in delayed fracture.

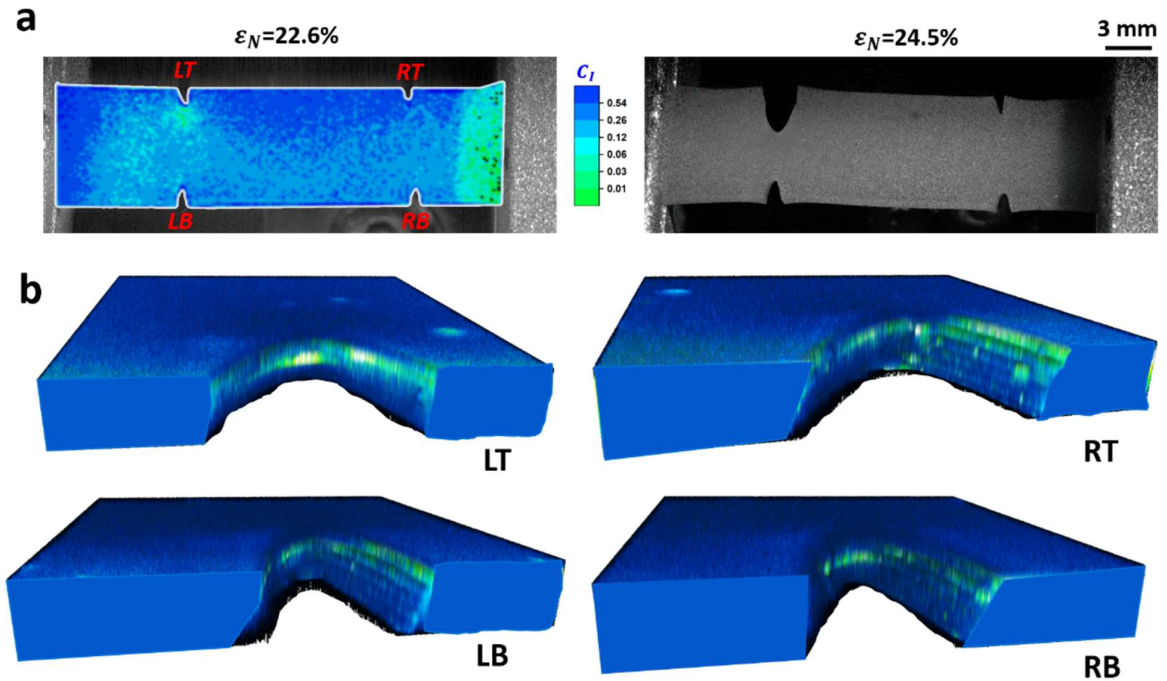


Fig. 3.5(a) Experimental procedure of the demonstration of fracture prediction/prevention. First loading (left): real-time dynamics activity map at  $\epsilon_N=22.6$  %. Second loading (right): propagation can be observed from  $\epsilon_N=24.5$  % (b) 3D image of the activation of mechanophore at each notch. Total size is  $1.4 \text{ mm} \times 1.4 \text{ mm}$ , with thickness of  $650 \text{ }\mu\text{m}$ .



Fig. 3.5 shows an example testing the predictive capability of MSDWS. 4 notches were placed on a PDMS sample previously labeled with mechanophores and the sample was stretched at  $\dot{\lambda}_N = 5 \times 10^{-5} \text{ s}^{-1}$ . By real-time processing of speckle images, a DAM can be obtained simultaneously during the measurement and used to predict the damage, with  $T_{MSDWS} = -0.75 \text{ s}$  (between the last collected image and the image 0.75 s before). Including the time for computing and image saving, an optimized time resolution of 1 s can be achieved. Similar to the results in Fig. 3.2(b), at  $\varepsilon_N = 22.6 \%$  ( $\varepsilon_f$  is found larger for multiple notched samples, around 20~25 %), significant differences between the 4 notches can be detected and only one of the notches is accompanied by a fast dynamic region, reaching a size  $\sim 0.5 \text{ cm}^2$  (Fig 3.5(a)). The sample is then removed from the tensile stage and the 4 notches are compared under confocal microscopy, as shown in Fig. 3.5(b). Obvious activation can only be detected in front of the crack “LT” which displays the fast dynamics region, confirming the results from real-time DAM. The unloaded sample is then reloaded and the final fracture occurs at the location where the crack region had a faster dynamics, at  $\varepsilon_N = 24.5 \%$ . Therefore, macroscopic failure has been successfully predicted, with a warning time of 300 s and warning macroscopic strain of 2 %, while there is only a very narrow region of molecular damage around the tip, within an area of  $0.01 \text{ mm}^2$  in plane. If a similar detection had been performed by DIC at that low level magnification, by calculating the transient deformation in a fixed period  $T$ , the trade-off between  $T_{min}$  and the displacement resolution of the image would have decreased the warning time to at most 10 seconds.

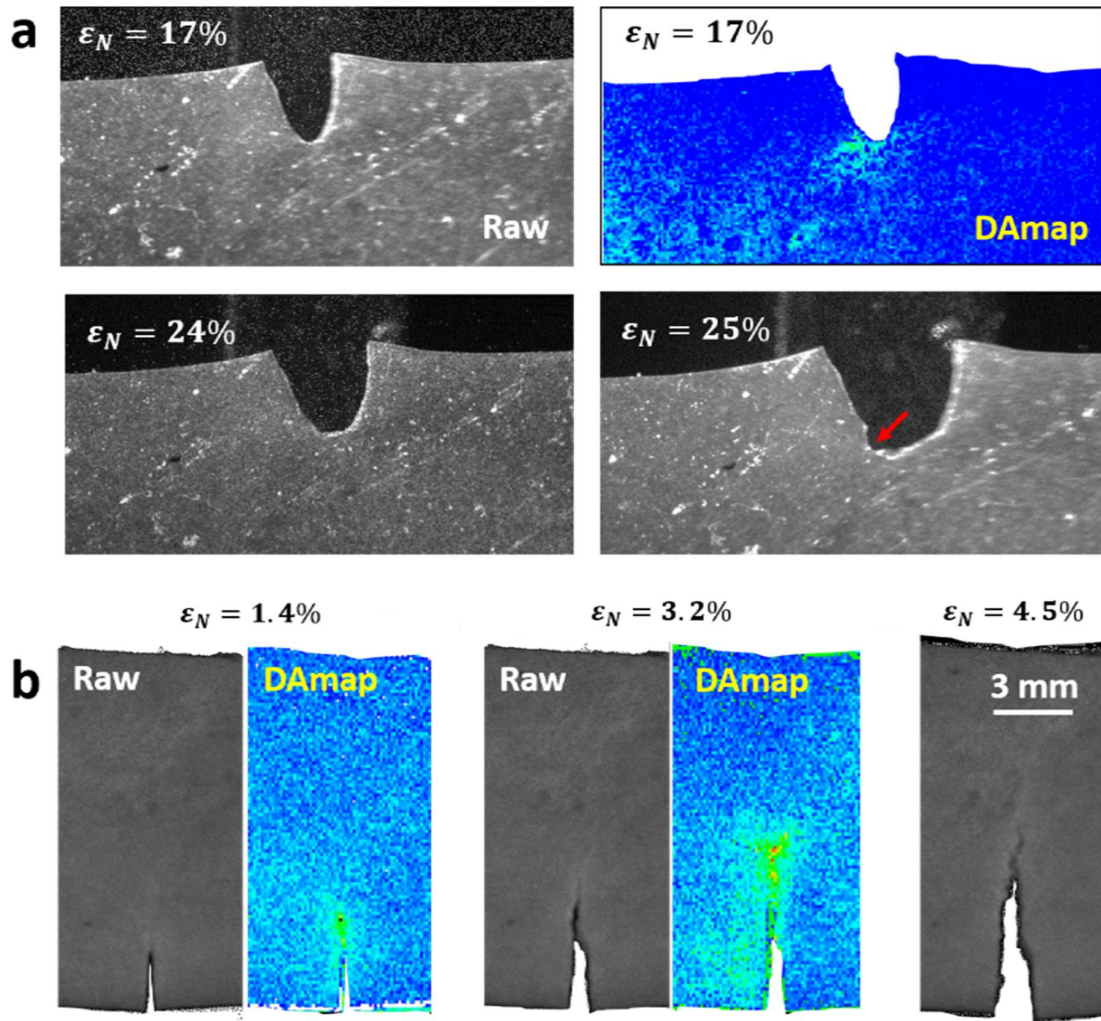


Fig. 3.6 (a) The prediction of “sideway” propagation in natural rubber. (b) Raw images and DAMs during the propagation of a piece of notched Tagliatelle pasta.

The detection of a large scale dynamic response is illustrated here with a PDMS elastomer, but commonly exists in different materials. MSDWS shows the advantages of ultrafast time resolution for microscopic damage, while the only requirements are the non-transparency, which is a common feature of many soft materials due to the presence of fillers, as well as absence of strong absorption of light (at the wavelength of the laser used). The methods can be used for semi-crystalline polymers,<sup>25</sup> filled soft materials<sup>26</sup> or any transparent material to which a small amount of high refractive index particles can be

mixed before shaping. We show two more examples of testing the onset of fracture on several additional materials, without further investigating specific fracture mechanisms. Uniaxial test ( $\dot{\lambda}_N = 2 \times 10^{-4} \text{ s}^{-1}$ ) was carried out on a SEN sample of natural rubber (Fig. 3.6(a)) where impurities provide multiple scattering. A sideways propagation<sup>27</sup> of the crack, classically observed in natural rubber due to strain-induced crystallization,<sup>28</sup> is observed at  $\varepsilon_N = 25 \%$ , apparent pointing to the left in front of the crack. In DAMs, a high dynamics region with a length around 2 mm can be already detected on the left side of the crack at  $\varepsilon_N = 17 \%$ , 400 s before any propagation can be detected by direct imaging. We also analyzed the crack propagation in a piece of notched dry tagliatelle pasta with  $\dot{\lambda}_N = 10^{-4} \text{ s}^{-1}$ , where ductile fracture starts from a very small strain, as shown in Fig. 3.6(b). Interestingly, the propagation path can be predicted well by DAM at much lower applied strain (details in the supporting information 3.6.3). Note that in these materials, localized dynamics are not necessarily due to changes in strain rate only, since MSDWS detects multiple contributions to the dynamics.<sup>25</sup>

### 3.3 Conclusions

In summary, during the fracture of PDMS elastomers, MSDWS reveals an increase in local strain rate acceleration a long time before macroscopic fracture, in both continuous and fixed loading conditions. Verified by FEM simulations and mechanophore mapping, the large-scale strain rate heterogeneity (over  $\sim 1 \text{ cm}^2$ ) is initiated by localized accumulated damage over a threshold ( $\sim 0.01 \text{ mm}^2$  around the crack tip), after which it dramatically grows and leads to macroscopic fracture. The large time/space scale of the dissipative behavior makes MSDWS a promising and convenient toolbox for early stage detection and prevention of microscopic damage in dynamic conditions even when observed with a standard camera over large scale samples. Additionally, the performance of the detection

of the heterogeneity by simple processing of ordinary low resolution imaging could be largely enhanced with machine learning methods,<sup>29</sup> so that with a defined threshold for acceptable warning time, macroscopic fracture can be prevented without knowing the detail of the material.

## 3.4 Materials and methods

### 3.4.1 Material preparation

PDMS elastomers are prepared from PDMS Sylgard 184 (Dow Corning) with a 10:1 ratio of PDMS base and curing agent. 4 g of PDMS base is first mixed with titanium dioxide (TiO<sub>2</sub>) nanoparticles (diameter 250 nm, 10 mg) and sonicated for 10 minutes to avoid aggregation of the nanoparticles. Curing agent (0.4 g) and Diels-Alder adduct mechanophore (5 mg, dissolved in 1 g toluene) are then added and the mixture is vacuumed for 10 minutes. Then the mixture is poured in the mold to prepare a film and cured in vacuum under 90 °C for 8 hours, so that toluene can be during evaporated during curing. The synthesis of mechanophore is described in detail in our previous work.<sup>15</sup>

### 3.4.2 Optical measurement

#### 3.4.2.1 Confocal microscopy

Confocal microscopy (Nikon AZ-100/C2+ confocal microscope) is applied here to map 3D fluorescence intensity due to damage. We used the objective AZ Plan Fluor 5×, with the focal length of 15 mm. The objective is zoomed by 3×, with the field of view 1.4 × 1.4 mm and image resolution of 0.68 μm/pixel (image size 2048 × 2048 pixel<sup>2</sup>) in the plane. Excitation and emission collection wavelength are 405 nm and 450 ~ 520 nm, respectively. In scanning confocal microscopy, a relatively long exposure time is required to acquire depth-resolved images with enough resolution and intensity, so that time resolution is poor. Furthermore, the fluorescence intensity of the activated mechanophore can be bleached after a long exposure under laser illumination. Considering the trade-off between image quality/time resolution and the need to avoid photobleaching, 4 slices (thickness 150 μm with exposure time 8 s) are scanned for each 3D image, with a depth resolution 200 μm and time resolution 2 min/scan, where images are collected at the beginning of each scan. The total scan thickness is 750 μm, around the midplane in thickness direction of the sample. Quantification of the data is shown in supporting information 3.6.1.

### .3.4.2.2 Multiple speckle diffusing wave spectroscopy

Time resolved Imaging of the whole sample was simultaneously performed with MSDWS, with a better time resolution (100 ms) but a worse spatial resolution (size of the region of interest (ROI): 0.3 mm × 0.3 mm and pixel size 0.01 mm/pixel) than confocal microscopy. The whole surface of the sample was illuminated homogeneously by an expanded green laser (wavelength 532 nm) and the speckles images were collected by a CMOS camera (BASLER acA2000-340km). The spatially resolved planar strain rate at the surface of the polymer network can be quantified from the autocorrelation function of the multiply scattered light intensity:

$$C_I(\vec{r}, t, \tau) = \frac{\langle I_p(t)I_p(t+\tau) \rangle_{\vec{r}}}{\langle I_p(t) \rangle_{\vec{r}} \langle I_p(t+\tau) \rangle_{\vec{r}}} - 1 \quad 3.1$$

$t$  and  $\tau$  are the experimental time and the time interval for correlation, respectively.  $I_p(t)$  is the intensity at the  $p$ -th pixel and  $\langle \dots \rangle_{\vec{r}}$  provides the average over the ROI with a center position at  $\vec{r}$ . The characteristic decorrelation time  $\tau_0$  of the autocorrelation function corresponds to the time over which the probe is displaced by  $1/k$  ( $k$  is the wave vector),  $\sim 50$  nm. At fixed  $t$  and  $\vec{r}$ ,  $\tau_0$  can be fitted by:<sup>30</sup>

$$C_I(\tau) = A \exp\left(-2\gamma \sqrt{\left(\frac{\tau}{\tau_0}\right)^p + a} + 2\gamma \sqrt{a}\right) + B \quad 3.2$$

and the characteristic decorrelation rate is defined as<sup>24,25</sup>:

$$\nu_0 = 1/\tau_0 \quad 3.3$$

This decorrelation rate can then be related to the

$$\nu_0 = \sqrt{3}kl^* \sqrt{f[\mathbf{D}]} \quad 3.4$$

is applied to visualize two-dimensional (2D) strain heterogeneity.  $\mathbf{D}$  is the symmetric part of velocity gradient tensor in the deformed state and  $f[\mathbf{D}] = 2Tr(\mathbf{D}^2)/15$ .<sup>8,25</sup>  $l^*$  is the transport mean free path<sup>31</sup>. More details are shown in supporting information 3.6.2.1.

### 3.5 References

- 1 Chen, C., Wang, Z. & Suo, Z. Flaw sensitivity of highly stretchable materials. *Extreme Mechanics Letters* **10**, 50-57 (2017).
- 2 Creton, C. & Ciccotti, M. Fracture and adhesion of soft materials: a review. *Rep Prog Phys* **79**, 046601, doi:10.1088/0034-4885/79/4/046601 (2016).
- 3 Wang, X. & Hong, W. Delayed fracture in gels. *Soft Matter* **8**, doi:10.1039/c2sm25553g (2012).
- 4 Bonn, D., Kellay, H., Prochnow, M., Ben-Djemaa, K. & Meunier, J. Delayed fracture of an inhomogeneous soft solid. *Science* **280**, 265-267 (1998).
- 5 Li, X. *et al.* Mesoscale bicontinuous networks in self-healing hydrogels delay fatigue fracture. *Proceedings of the National Academy of Sciences* **117**, 7606-7612 (2020).
- 6 Kolvin, I., Kolinski, J. M., Gong, J. P. & Fineberg, J. How supertough gels break. *Physical review letters* **121**, 135501 (2018).
- 7 Slooman, J. *et al.* Quantifying rate- and temperature-dependent molecular damage in elastomer fracture. *Physical Review X* **10**, 041045 (2020).
- 8 van der Kooij, H. M. *et al.* Laser Speckle Strain Imaging reveals the origin of delayed fracture in a soft solid. *Science advances* **4**, eaar1926 (2018).
- 9 Amon, A., Mikhailovskaya, A. & Crassous, J. Spatially resolved measurements of micro-deformations in granular materials using diffusing wave spectroscopy. *Rev Sci Instrum* **88**, 051804, doi:10.1063/1.4983048 (2017).
- 10 Le Bouil, A., Amon, A., McNamara, S. & Crassous, J. Emergence of cooperativity in plasticity of soft glassy materials. *Phys Rev Lett* **112**, 246001, doi:10.1103/PhysRevLett.112.246001 (2014).
- 11 Pommella, A., Cipelletti, L. & Ramos, L. Role of normal stress in the creep dynamics and failure of a biopolymer gel. *Physical Review Letters* **125**, 268006 (2020).
- 12 Cipelletti, L., Martens, K. & Ramos, L. Microscopic precursors of failure in soft matter. *Soft matter* **16**, 82-93 (2020).
- 13 Aime, S., Ramos, L. & Cipelletti, L. Microscopic dynamics and failure precursors of a gel under mechanical load. *Proc Natl Acad Sci U S A* **115**, 3587-3592, doi:10.1073/pnas.1717403115 (2018).
- 14 Slooman, J. *et al.* Quantifying Rate- and Temperature-Dependent Molecular Damage in Elastomer Fracture. *Physical Review X* **10**, doi:10.1103/PhysRevX.10.041045 (2020).
- 15 Lavoie, S. R., Long, R. & Tang, T. A rate-dependent damage model for elastomers at large strain. *Extreme Mechanics Letters* **8**, 114-124 (2016).
- 16 Long, R., Krishnan, V. R. & Hui, C.-Y. Finite strain analysis of crack tip fields in incompressible hyperelastic solids loaded in plane stress. *Journal of the Mechanics and Physics of Solids* **59**, 672-695 (2011).
- 17 Krishnan, V. R., Hui, C. Y. & Long, R. Finite strain crack tip fields in soft incompressible elastic solids. *Langmuir* **24**, 14245-14253 (2008).
- 18 Liu, M., Guo, J., Hui, C. Y. & Zehnder, A. T. Application of Digital Image Correlation (DIC) to the Measurement of Strain Concentration of a PVA Dual-Crosslink Hydrogel Under Large Deformation. *Experimental Mechanics*, doi:10.1007/s11340-019-00520-4 (2019).
- 19 Lake, G. & Thomas, A. The strength of highly elastic materials. *Proceedings of the Royal Society of London. Series A. Mathematical and Physical Sciences* **300**, 108-119 (1967).

- 20 Cipelletti, L., Brambilla, G., Maccarrone, S. & Caroff, S. Simultaneous measurement of the microscopic dynamics and the mesoscopic displacement field in soft systems by speckle imaging. *Opt Express* **21**, 22353-22366, doi:10.1364/OE.21.022353 (2013).
- 21 Nagazi, M.-Y. *et al.* Space-resolved diffusing wave spectroscopy measurements of the macroscopic deformation and the microscopic dynamics in tensile strain tests. *Optics and Lasers in Engineering* **88**, 5-12, doi:10.1016/j.optlaseng.2016.07.006 (2017).
- 22 Amon, A., Nguyen, V. B., Bruand, A., Crassous, J. & Clement, E. Hot spots in an athermal system. *Phys Rev Lett* **108**, 135502, doi:10.1103/PhysRevLett.108.135502 (2012).
- 23 Nagazi, M. Y., Dieudonné-George, P., Brambilla, G., Meunier, G. & Cipelletti, L. Phase transitions in polymorphic materials probed using space-resolved diffusing wave spectroscopy. *Soft matter* **14**, 6439-6448 (2018).
- 24 Lee, S. & Pharr, M. Sideways and stable crack propagation in a silicone elastomer. *Proc Natl Acad Sci U S A* **116**, 9251-9256, doi:10.1073/pnas.1820424116 (2019).
- 25 Marano, C., Boggio, M., Cazzoni, E. & Rink, M. Fracture phenomenology and toughness of filled natural rubber compounds via the pure shear test specimen. *Rubber Chemistry and Technology* **87**, 501-515 (2014).
- 26 Bapst, V. *et al.* Unveiling the predictive power of static structure in glassy systems. *Nature Physics* **16**, 448-454 (2020).
- 27 Clough, J. M., Creton, C., Craig, S. L. & Sijbesma, R. P. Covalent bond scission in the Mullins effect of a filled elastomer: real-time visualization with mechanoluminescence. *Advanced Functional Materials* **26**, 9063-9074 (2016).
- 28 Göstl, R. & Sijbesma, R.  $\pi$ -extended anthracenes as sensitive probes for mechanical stress. *Chemical science* **7**, 370-375 (2016).
- 29 Pine, D. J., Weitz, D. A., Chaikin, P. M. & Herbolzheimer, E. Diffusing wave spectroscopy. *Phys Rev Lett* **60**, 1134-1137, doi:10.1103/PhysRevLett.60.1134 (1988).



## 3.6 Supporting Information

### Fast detection of early-stage damage in soft elastomers

Jianzhu Ju <sup>a</sup>, Gabriel Sanoja <sup>a</sup>, Luca Cipelletti <sup>b,c</sup>, Zezhou Liu <sup>d</sup>, Chung Yuen Hui <sup>d,e</sup>, Matteo Ciccotti <sup>a</sup>,  
Tetsuharu Narita <sup>\*,a,e</sup>, Costantino Creton <sup>\*,a,e</sup>

<sup>a</sup> Sciences et Ingénierie de la Matière Molle, CNRS UMR 7615, ESPCI Paris, PSL Université, Paris, France

<sup>b</sup> Laboratoire Charles Coulomb (L2C), University of Montpellier, CNRS, Montpellier, France

<sup>c</sup> Institut Universitaire de France

<sup>d</sup> Sibley School of Mechanical and Aerospace Engineering, Cornell University, Ithaca, NY 14853, USA

<sup>e</sup> Global Station for Soft Matter, Global Institution for Collaborative Research and Education, Hokkaido University, Sapporo, Japan

#### 3.6.1 Quantification of fluorescence intensity by confocal microscopy

An example of images in one scan at  $\varepsilon_N=5\%$  and  $15\%$  are shown in Fig. 3.S1(a), respectively. The intensity decreases with depth, due to absorption in the bulk material. Slight activation around the crack is already observable at  $\varepsilon_N=5\%$ , due to the initial cutting of the crack by a razor blade. Intensity at all depths increases with  $\varepsilon_N$ , while just before propagation ( $\varepsilon_N=15\%$ ), a strongly activated region is detected only at the 3<sup>rd</sup> layer. This indicates that damage at propagation is not homogeneous along the thickness. A 3D image of the fluorescence intensity can be visualized with the volume view of the software “NIV-elements viewer” provided by Nikon, as seen in Fig. 3.S1(b). Maximum intensity projection is applied here to enhance the 3D structure visualization. The streaks in the 3D figure is from the separated steps in a single scan, but not structure along the depth direction.

---

\*correspondence authors: [tetsuharu.narita@espci.fr](mailto:tetsuharu.narita@espci.fr)

\*correspondence authors: [costantino.creton@espci.fr](mailto:costantino.creton@espci.fr)

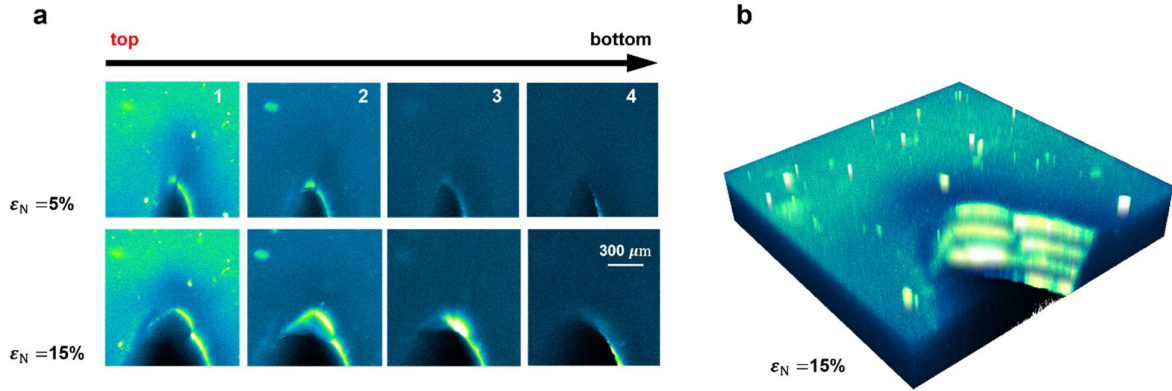


Fig. 3.S1 (a) Separate 2D images during scan at  $\epsilon_N = 5$  and  $15 \%$ , respectively. (b) 3D mapping of fluorescence intensity at  $\epsilon_N = 15 \%$ .

Fig. 3.S2(a) shows the images at the 3<sup>rd</sup> layer at different  $\epsilon_N$ . To quantify the activation due to damage and compare with strain rate mapping results, the averaged intensity  $I$  in the region along the deformed crack profile (with width of  $130 \mu\text{m}$ ) is calculated in the 3<sup>rd</sup> layer, as indicated in Fig. 3.S2(a). The intensity is renormalized by the averaged intensity in a region far away from the crack ( $I_{bulk}$ ), to remove the effect of bleaching during UV illumination and the absorption.  $I$  and  $I_{bulk}$  are calculated and shown in Fig. 3.S2(b), respectively. A small amount of decrease of  $I_{bulk}$  due to bleaching can be observed.

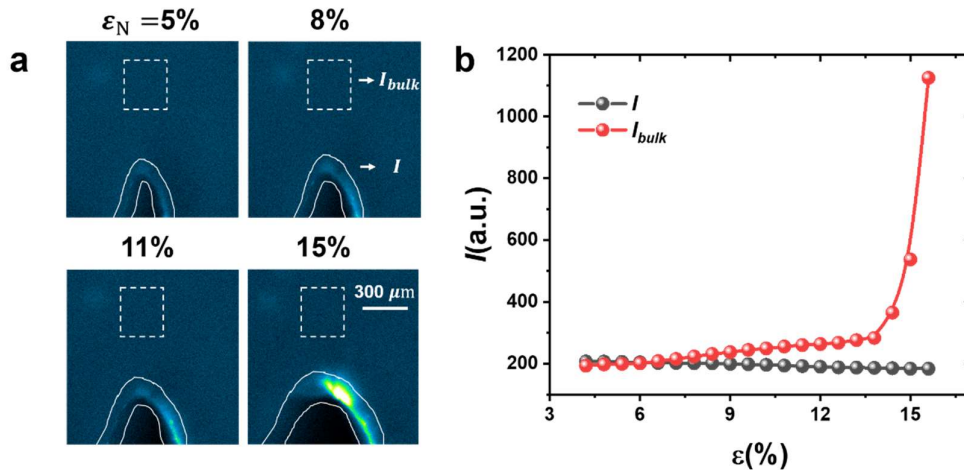


Fig. 3.S2 (a) Images of 3<sup>rd</sup> layer at different strain. Region for the calculation of  $I$  and  $I_{bulk}$  are indicated. (b)  $I$  and  $I_{bulk}$  of the 3<sup>rd</sup> layer, as functions of  $\epsilon_N$ .

### 3.6.2 Strain rate mapping

To understand the dynamic fracture mechanism, spatially resolved strain is determined by three different methods in this work: multiple speckle diffusing wave spectroscopy (MSDWS), digital image correlation (DIC) and finite element method (FEM). The three methods are introduced here, respectively. The undeformed sample parameters are the same for simulation and experiments: width  $w = 20$  mm, length  $l_0 = 40$  mm, and crack length  $c = 2$  mm, nominal stretch rate  $\dot{\lambda}_N = 1.25 \times 10^{-4} \text{ s}^{-1}$ , as indicated in Fig. 3.S3. Vertical and horizontal coordinates in the *deformed* configuration are indicated as  $y$  and  $x$ , respectively, with the crack tip (opened) as the origin of the coordinate for each  $\varepsilon_N$ . Correspondingly, the coordinates in the *undeformed* state is indicated by  $Y$  and  $X$ , respectively.

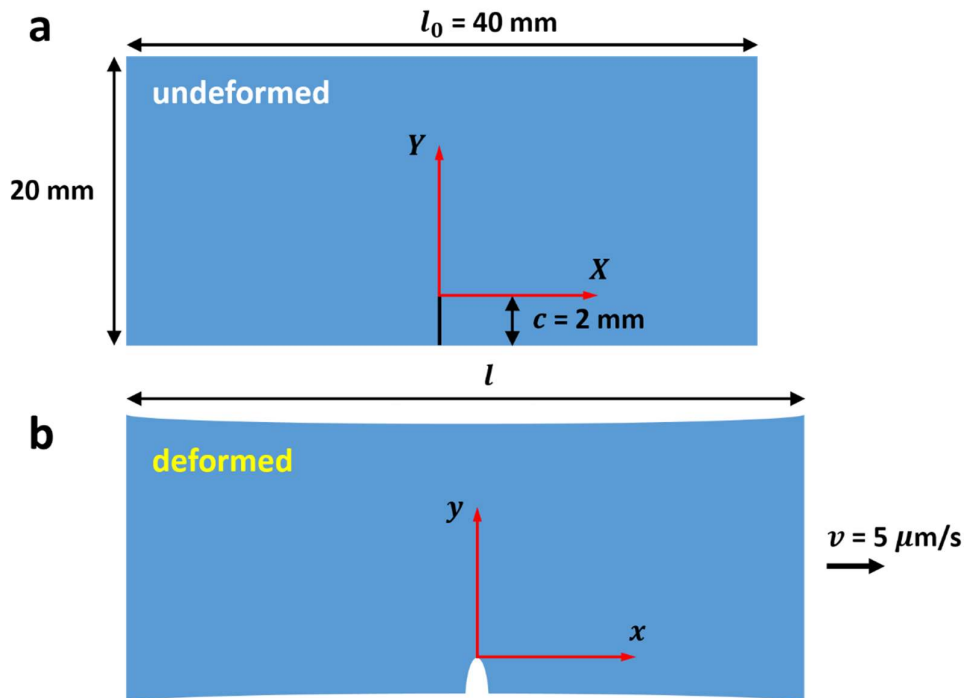


Fig. 3.S3 Sample parameter in the (a) undeformed and (b) deformed states.

#### 3.6.2.1 MSDWS

In a backscattering geometry, MSDWS extracts the quantified deformation rate from the intensity fluctuation rate of the back-scattered light. The spatially and temporally

resolved intensity autocorrelation function  $C_I(\vec{r}, t, \tau)$  is

$$C_I(\vec{r}, t, \tau) = \frac{\langle I_p(t)I_p(t+\tau) \rangle_{\vec{r}}}{\langle I_p(t) \rangle_{\vec{r}} \langle I_p(t+\tau) \rangle_{\vec{r}}} - 1 \quad (1)$$

where  $I_p$  is the intensity at p-th pixel, and  $\langle \dots \rangle_{\vec{r}}$  designates an average over a region of interest (ROI) with center around position  $\vec{r}$ .  $\tau$  is the time interval for correlation and  $t$  is the time after the onset of stretching. At fixed time  $t$  and position  $\vec{r}$ , the profile of  $C_I(\tau)$  can be related to velocity gradient tensor.<sup>9,25</sup> The autocorrelation function has the exponential form, as the function of  $\tau$ :<sup>30,32</sup>

$$C_I(\tau) = A \exp\left(-2\gamma \sqrt{\left(\frac{\tau}{\tau_0}\right)^p + a + 2\gamma\sqrt{a}}\right) + B \quad (2)$$

$\gamma$  is a coefficient decided by the polarization condition of the incident/detected light intensities. As a polarizer is applied in the set-up,  $\gamma = 2.7$  is used.<sup>25,33</sup>  $a$  depends on the ratio between the transport mean free path  $l^*$ <sup>34</sup> and sample thickness, which is experimentally determined in a unnotched sample under continuous stretching, around 0.02.<sup>30,32</sup>

$\tau_0(t)$  corresponds to the time scale where probe particles moves in the order of 50 nm ( $1/k$ , where  $k$  is wave vector), which can be applied to measure spatial resolved velocity gradient tensor in the deformed configuration.<sup>30</sup> We recall here the correspondence between  $\tau_0$  and velocity gradient tensor.<sup>9,35</sup> At a material point  $X$ ,  $\mathbf{F}^{0 \rightarrow t+\tau}$  denotes the deformation gradient at time  $t + \tau$ , where  $\tau$  is a very small time. We can always write:

$$\mathbf{F}^{0 \rightarrow t+\tau} = \mathbf{F}^{t \rightarrow t+\tau} \mathbf{F}^{0 \rightarrow t} \Rightarrow \mathbf{F}^{t \rightarrow t+\tau} = \mathbf{F}^{0 \rightarrow t+\tau} (\mathbf{F}^{0 \rightarrow t})^{-1} \quad (3)$$

$\mathbf{F}^{t \rightarrow t+\tau}$  is the deformation gradient using the configuration at time  $t$  (deformed coordinates) as the reference configuration. For small  $\tau$ ,

$$\mathbf{F}^{0 \rightarrow t+\tau} = \mathbf{F}(X, t + \tau) \approx \mathbf{F}(X, t) + \dot{\mathbf{F}}(X, t)\tau \quad (4)$$

$\dot{\mathbf{F}}(X, t)$  is the material velocity gradient. Substituting eq. 4 into eq. 3, we have

$$\mathbf{F}^{t \rightarrow t+\tau} = (\mathbf{F}^{0 \rightarrow t} + \dot{\mathbf{F}}(X, t)\tau)(\mathbf{F}^{0 \rightarrow t})^{-1} = \mathbf{I} + \dot{\mathbf{F}}(X, t)[\mathbf{F}(X, t)]^{-1} \quad (5)$$

It is well known that

$$\dot{\mathbf{F}}(X, t)[\mathbf{F}(X, t)]^{-1} = \mathbf{L}(x(X, t), t) \quad (6)$$

Which is the spatial velocity gradient tensor expressed in current coordinates  $x$ .

Therefore, eq. 5 implies that

$$\mathbf{F}^{t \rightarrow t+\tau} = \mathbf{I} + \mathbf{L}(x, t)\tau \quad (7)$$

Since

$$\mathbf{L} = \mathbf{D} + \mathbf{W} \quad (8)$$

where  $\mathbf{D} \Leftrightarrow D_{ij} = \frac{1}{2} \left( \frac{\partial v_i}{\partial x_j} + \frac{\partial v_j}{\partial x_i} \right)$  is the rate of deformation tensor and  $\mathbf{W}$  is the spin tensor,

which has no effect on deformation. Tensor  $\mathbf{U}$  is defined by

$$U_{ij} = D_{ij}(x, t)\tau \quad (9)$$

For a purely affine deformation with no additional dynamics, the autocorrelation function can be related to  $\mathbf{U}$  by<sup>30,32</sup>

$$C_I(\tau) = A \exp \left( -2\gamma \sqrt{3k^2 l^{*2} f[\mathbf{U}(\tau)] + a + 2\gamma \sqrt{a}} \right) + B \quad (10)$$

where  $f[\mathbf{U}(\tau)]$  is a function of  $U: f[\mathbf{U}] = [Tr^2(\mathbf{U}) + 2Tr(\mathbf{U}^2)]/15$ . For incompressible solid (such as elastomer),  $Tr(U) = 0$  so that  $f[\mathbf{U}] = 2Tr(\mathbf{U}^2)/15$ . Wave vector  $k = 2\pi n/\lambda$ ,  $\lambda = 532$  nm,  $n = 1.4$  is the index of refraction for PDMS<sup>36,37</sup> This also implies that  $p$  in eq. 2 should be 2, which provides a criterion to characterize the contributions to decorrelation mode of autocorrelation function. Inserting  $\tau = \tau_0$ , the simple expression can be found:

$$\sqrt{f[\mathbf{D}(t)]\tau_0^2} = \frac{1}{\sqrt{3kl^*}} \quad (11)$$

And characteristic rate  $\nu_0$  ( $\nu_0 = 1/\tau_0$ ) is defined by

$$\nu_0 = \sqrt{3kl^*} \sqrt{f[\mathbf{D}(t)]} \quad (12)$$

$\nu_0$  can be simply obtained from the fitting of autocorrelation function by eq. 2 and

increases with strain rate, so that it is applied here to map the strain rate distribution.

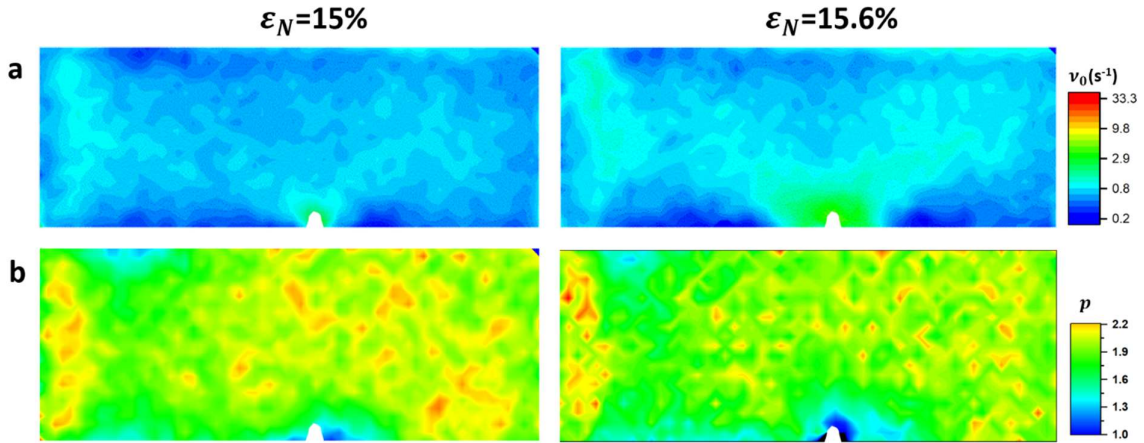


Fig. 3.S4 (a)  $v_0$  and (b)  $p$  map at  $\epsilon_N=15\%$  and  $15.6\%$ .

Fig. 3.S4 shows  $v_0$  (a) and  $p$  (b) distribution at  $\epsilon_N=15$  and  $15.6\%$ . High heterogeneity can be observed in  $v_0$  map, while in  $p$  map,  $p$  is around 2 everywhere over the sample. This indicates that the dynamics we observed here is dominated by affine deformation field during stretch. At  $\epsilon_N = 15.6\%$ , sharp transition to small  $p$  around 1 can be detected at close to the tip (around 1 mm), but it should not be due to different contribution to the autocorrelation function. At close to the crack tip, where dynamics decorrelation is very fast before fracture, fitting of exponent  $p$  is not very precise with limited data points at small  $\tau$ .

### .3.6.2.2 Digital image correlation

The quantitatively measurement of strain rate by MSDWS is an advanced but relatively new method. The application in the complex 2D condition can be validated by the comparison with digital image correlation (DIC).<sup>20,38</sup> On the other hand, FEM simulation results can be easily compared with DIC results, which measures velocity gradient tensor, instead of  $v_0$  in MSDWS.

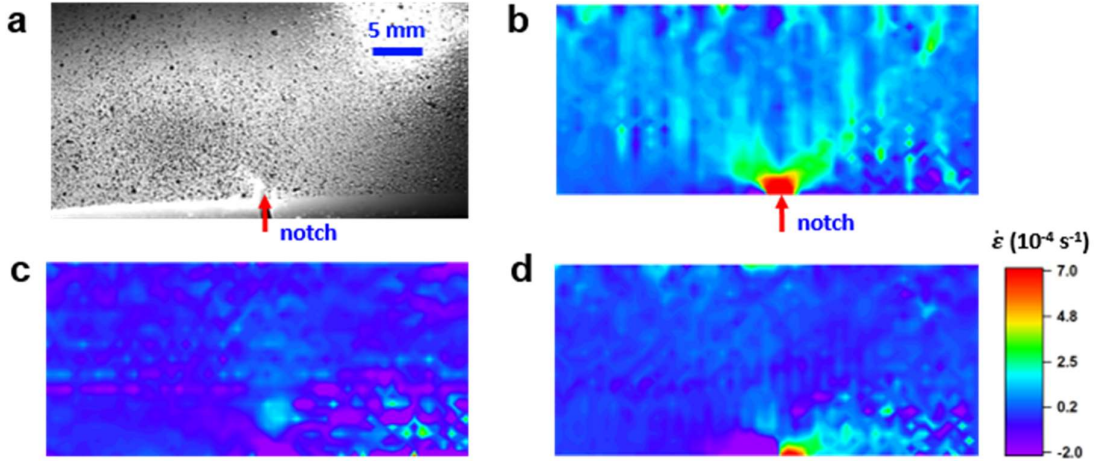


Fig. 3.S5 (a) PDMS sample prepared by spray painting for the measurement by DIC, at 25 s before fracture ( $\varepsilon_N=15.4\%$ ). DIC results are shown as (b)  $U_{xx}$ , (c)  $U_{yy}$  and (d)  $U_{xy}$ .

Strain rate is measured by DIC on a single-edge notched (SEN) sample with a surface spray-painted with black ink, as seen in Fig. 3.S5(a). Each spot has diameter around 0.1 mm, providing enough resolution for full-field mapping. The processing is done with the open resource program pyDIC, developed by Damien André. Corresponds to results by MSDWS,  $\mathbf{U}$  is first measured by DIC, where displacement is calculated with successive images and accumulated from  $t$  to  $t + T$ . Ideally, the averaging interval  $T$  should be small enough so that the change in strain rate can be negligible. An example is shown in Fig. 3.S5: (b)  $U_{xx}$ , (c)  $U_{yy}$  and (d)  $U_{xy}$  at 25 s before fracture ( $\varepsilon_N=15.4\%$ ), with  $T = 4$  s.

DIC can only measure deformation in the surface plane. As the thickness is small compared to the surface size of the sample, the shearing in the thickness direction is considered negligible ( $U_{xz} = U_{yz} = U_{zx} = U_{zy} = 0$ ) and we consider  $U_{xy} = U_{yx}$  for small  $T$ .

At each  $t$ ,  $\mathbf{U}$  is

$$\mathbf{U}(\vec{r}, t, T) = \begin{bmatrix} U_{xx}(\vec{r}, t, T) & U_{xy}(\vec{r}, t, T) & 0 \\ U_{xy}(\vec{r}, t, T) & U_{yy}(\vec{r}, t, T) & 0 \\ 0 & 0 & -U_{xx}(\vec{r}, t, T) - U_{yy}(\vec{r}, t, T) \end{bmatrix}, \quad (13)$$

and we have

$$\mathbf{D}(\vec{r}, t) = \mathbf{U}(\vec{r}, t, T)/T \quad (14)$$

In this way, equivalent values of  $\nu_0$  can be calculated from DIC to compare with MSDWS

and  $\mathbf{D}(\vec{r}, t)$  with FEM. Note that to grab the deformation rate of the whole surface, the displacement resolution of DIC is highly limited by the image resolution. Here the required minimal  $T$  to detect the heterogeneity in  $\mathbf{D}(\vec{r}, t)$  is denoted by  $T_{min}$ . For a dynamic measurement,  $T_{min}$  eventually limits the time response to a rapid change. On the other hand for MSDWS, fast detection can be largely accelerated by DAM, where time interval  $T_{MSDWS}$  typically needs to be over  $0.05\tau_0$  to visualize enough heterogeneity. The relative time resolution of MSDWS and DIC can be compared by comparing  $T_{min}$  with  $0.05\tau_0$  in MSDWS. Of course a higher magnification could be used in DIC to focus on the crack tip region but this requires in practice to know where the crack tip is, while the wide field image of MSDWS can detect heterogeneities over the whole sample.

### .3.6.2.3 Finite element method (FEM)

To compare with experimental results measuring Eulerian strain rate distribution, we are interested in the velocity gradient tensor and its symmetric part, which is the rate of deformation tensor. The finite element model is identical to the one we used in an earlier work<sup>19,39</sup> and is implemented in the commercial FEM software, Abaqus. Due to symmetry, only a half sample is modeled. On the bottom edge and directly ahead of the crack tip,  $X_1 > c$ , the vertical displacement and the shear stress are zero. On the top edge, a uniform vertical displacement  $\Delta$  is imposed while the horizontal displacement is constrained to be zero. Plane stress elements CPS4 are used. The smallest element size near the crack tip is  $5 \times 10^{-5} w$ . More details of finite element implementation can be found in our previous work.<sup>39</sup>

#### Calculation of spatial velocity gradient tensor

We assume plane stress deformation. In the simulation, the position of a material point  $\mathbf{X}$  in the reference undeformed configuration (at time  $t = 0$ ) is given  $\mathbf{X} = X_\alpha \mathbf{E}_\alpha$  with the origin ( $\mathbf{X} = \mathbf{0}$ ) at the undeformed crack tip. Here bold letters denote vector or tensor quantities and summation convention where sum over repeated index is used unless otherwise specified. The  $\mathbf{E}_\alpha$  are unit orthonormal basis vectors in the reference configuration. Since plane stress deformation is 2D,  $\alpha = 1, 2$ . The undeformed crack occupies  $X_1 \in (-c, 0)$ . Let  $\mathbf{y}(\mathbf{X})$  denote the position of the deformed material point  $\mathbf{X}$ .



**Note that the notation in this section differs from the notation in the manuscript.** Specifically, in this section, the crack lies along the 1 direction instead of the 2 direction. Thus,  $y_1 = x$  and  $y_2 = y$ .

The spatial velocity gradient tensor  $\mathbf{L}$  is the gradient of the velocity field  $\mathbf{v}$  in the current or deformed configuration, i.e.,

$$\mathbf{L} = \nabla_y \mathbf{v} \quad (15)$$

It is well known that the spatial velocity gradient tensor  $\mathbf{L}$  is related to the deformation gradient tensor  $\mathbf{F}$  by

$$\mathbf{L} = \dot{\mathbf{F}} \mathbf{F}^{-1} \quad (16)$$

, where  $\dot{\mathbf{F}}$  is the material velocity gradient (see Nonlinear solid mechanics, page 96, by G. A. Holzapfel, Wiley).

To compute  $\mathbf{L}$  near the crack tip, we use eq. 16. The matrix representing the deformation gradient tensor  $\mathbf{F}$  is

$$\mathbf{F} = \begin{bmatrix} y_{1,1} & y_{1,2} & 0 \\ y_{2,1} & y_{2,2} & 0 \\ 0 & 0 & \lambda_3 \end{bmatrix} \Rightarrow \dot{\mathbf{F}} = \begin{bmatrix} \dot{y}_{1,1} & \dot{y}_{1,2} & 0 \\ \dot{y}_{2,1} & \dot{y}_{2,2} & 0 \\ 0 & 0 & \dot{\lambda}_3 \end{bmatrix}$$

$$y_{\alpha,\beta} = \frac{\partial y_\alpha}{\partial X_\beta}, \dot{y}_{\alpha,\beta} = \frac{\partial}{\partial t} \left( \frac{\partial y_\alpha}{\partial X_\beta} \right) \quad (17)$$

, where  $\lambda_3$  is the stretch ratio in the out of plane direction. Incompressibility implies that

$$D = y_{1,1} y_{2,2} - y_{1,2} y_{2,1} = 1/\lambda_3 \quad (18)$$

Simple calculation shows that

$$\mathbf{F}^{-1} = \begin{bmatrix} \frac{y_{2,2}}{D} & -\frac{y_{1,2}}{D} & 0 \\ -\frac{y_{2,1}}{D} & \frac{y_{1,1}}{D} & 0 \\ 0 & 0 & 1/\lambda_3 \end{bmatrix} \quad (19)$$

Eq. 16, 18 and 19 imply that the matrix representing the spatial velocity gradient tensor  $\mathbf{L}$  is

$$\mathbf{L} = \dot{\mathbf{F}}\mathbf{F}^{-1} = \begin{bmatrix} L_{11} & L_{12} & 0 \\ L_{21} & L_{22} & 0 \\ 0 & 0 & \dot{\lambda}_3/\lambda_3 \end{bmatrix}, \quad (20)$$

where

$$\begin{aligned} L_{11} &= \frac{\dot{y}_{1,1}y_{2,2} - \dot{y}_{1,2}y_{2,1}}{D} \\ L_{12} &= \frac{-\dot{y}_{1,1}y_{1,2} + \dot{y}_{1,2}y_{1,1}}{D} \\ L_{21} &= \frac{\dot{y}_{2,1}y_{2,2} - \dot{y}_{2,2}y_{2,1}}{D} \\ L_{22} &= (-\dot{y}_{2,1}y_{1,2} + \dot{y}_{2,2}y_{1,1})/D \\ L_{33} &= \dot{\lambda}_3/\lambda_3 \end{aligned} \quad (21)$$

Note that since the trace of  $\mathbf{L}$  is zero, due to incompressibility, we have:

$$L_{11} + L_{22} + L_{33} = 0 \quad (22)$$

The nominal stress tensor or 1<sup>st</sup> Piola stress tensor  $\mathbf{S}$  is (the out of plane stresses are all zero),  $\alpha, \beta = 1, 2$

$$S_{\alpha\beta} = \mu(F_{\alpha\beta} - \lambda_3^2 F_{\beta\alpha}^{-1}) \quad (23)$$

The true stress tensor  $\boldsymbol{\tau}$  is

$$\tau_{\alpha\eta} = S_{\alpha\beta}F_{\eta\beta} = \mu(F_{\alpha\beta}F_{\eta\beta} - \lambda_3^2\delta_{\alpha\eta}) \quad (24)$$

Directly ahead of the crack tip, the shear stresses are zero, so that

$$\tau_{12} = 0 \Rightarrow (F_{11}F_{21} + F_{12}F_{22}) = 0 \quad (25)$$

However, directly in front of the crack tip:

$$u_2 = 0 \Rightarrow F_{21} = y_{2,1} = 0, F_{22} \neq 0 \quad (26)$$

Combining eq. 25 with eq. 26, we have

$$F_{12} = y_{1,2} = 0 \quad (27)$$

From eq. 21 and eq. 26-27, the deformation gradient tensor and the velocity gradient tensor are diagonal directly ahead of the crack tip. A result in mechanics tells us that the material time derivative of the left Cauchy-Green tensor  $\mathbf{b} = \mathbf{F}\mathbf{F}^T$  is (see Nonlinear solid mechanics, page 102, G. A. Holzapfel, John Wiley and Sons LTD) :

$$\dot{\mathbf{b}} = \mathbf{L}\mathbf{b}^T + \mathbf{b}\mathbf{L}^T \quad (28)$$

where a dot denotes material derivative. Since both  $\mathbf{b}$  and  $\mathbf{L}$  are diagonal directly ahead of crack, we must have

$$\mathbf{L}\mathbf{b}^T = \mathbf{b}\mathbf{L}^T = \mathbf{L}\mathbf{b} \Rightarrow \dot{\mathbf{b}} = 2\mathbf{L}\mathbf{b} \quad (29)$$

Since  $\mathbf{L}\mathbf{b}$  is also diagonal, so

$$\mathbf{L}\mathbf{b} = \begin{bmatrix} L_{11}b_{11} & & \\ & L_{22}b_{22} & \\ & & \otimes \end{bmatrix} \Rightarrow \dot{b}_{11} = 2L_{11}b_{11}, \dot{b}_{22} = 2L_{22}b_{22} \quad (30)$$

Thus, directly ahead of the crack tip, the spatial velocity gradient tensor is also the rate of deformation tensor or strain rate tensor since it is diagonal) is given by the logarithmic derivative of the components of the left Cauchy-Green tensor:

$$L_{11} = \frac{1}{2} \frac{\dot{b}_{11}}{b_{11}} = \frac{1}{2} (\ln b_{11}) \cdot$$

$$L_{22} = \frac{1}{2} \frac{\dot{b}_{22}}{b_{22}} = \frac{1}{2} (\ln b_{22}) \cdot \quad (31)$$

Eq. 31 is used to extract the velocity gradient component  $L_{22}$  from FEM simulations.

### Asymptotic analysis of spatial velocity gradient near the crack tip

Far away from the crack tip, the rate of deformation should be approximately given by the logarithmic strain rate  $\dot{l}(t)/l(t) = \frac{\dot{\lambda}_N}{(1+\varepsilon_N)l_0}$ . On the other hand, very close to the crack tip ( $R \rightarrow 0$ ), the upper bound of  $\mathbf{L}$  can be decided by the asymptotic solution of a plane stress crack in an incompressible neo-Hookean solid. For a Mode I crack, the in-plane near tip deformed coordinates  $y_\alpha$  are given by:<sup>39,40</sup>

$$y_1 = CR\cos\varphi$$

$$y_2 = a\sqrt{R}\sin(\varphi/2) \quad (32)$$

where  $(R, \varphi)$  are material polar coordinates in the reference configuration. Note that  $R = 0$  is the position of the undeformed crack tip. According to eq. 32, the asymptotic behavior of the in-plane deformation gradient are:

$$F_{11} = C, F_{12} = 0$$

$$F_{21} = \frac{\partial y_2}{\partial X_1} = \cos\theta \frac{\partial y_2}{\partial R} - \frac{\sin\varphi}{R} \frac{\partial y_2}{\partial \varphi} = a \left[ \cos\varphi \sin(\varphi/2) \frac{1}{2\sqrt{R}} - \frac{\sin\varphi}{2\sqrt{R}} \cos(\varphi/2) \right]$$

$$= \frac{a}{2\sqrt{R}} [\cos\varphi \sin(\varphi/2) - \sin\varphi \cos(\varphi/2)] = -\frac{a}{2\sqrt{R}} \sin(\varphi/2)$$

$$F_{22} = \frac{\partial y_2}{\partial X_2} = \sin\varphi \frac{\partial y_2}{\partial R} + \frac{\cos\varphi}{R} \frac{\partial y_2}{\partial \varphi} = a \left[ \sin\varphi \sin(\varphi/2) \frac{1}{2\sqrt{R}} + \frac{\cos\varphi}{2\sqrt{R}} \cos(\varphi/2) \right]$$

$$= \frac{a}{2\sqrt{R}} [\sin\varphi \sin(\varphi/2) + \cos\varphi \cos(\varphi/2)] = \frac{a}{2\sqrt{R}} \cos(\varphi/2) \quad (33)$$

Hence,

$$\mathbf{F} \underset{R \rightarrow 0}{\simeq} \begin{bmatrix} C & 0 & 0 \\ -\frac{a\sin(\varphi/2)}{2\sqrt{R}} & \frac{a\cos(\varphi/2)}{2\sqrt{R}} & 0 \\ 0 & 0 & \lambda_3 \end{bmatrix} \quad (34)$$

Next, we compute the near tip spatial velocity gradient tensor  $\mathbf{L}$ .

$$\dot{\mathbf{F}} \approx \begin{bmatrix} \dot{C} & 0 & 0 \\ -\frac{\dot{a}\sin(\varphi/2)}{2\sqrt{R}} & \frac{\dot{a}\cos(\varphi/2)}{2\sqrt{R}} & 0 \\ 0 & 0 & \dot{\lambda}_3 \end{bmatrix} \quad (35)$$

$$\mathbf{F} \approx \begin{bmatrix} C & 0 & 0 \\ -\frac{a\sin(\varphi/2)}{2\sqrt{R}} & \frac{a\cos(\varphi/2)}{2\sqrt{R}} & 0 \\ 0 & 0 & \lambda_3 \end{bmatrix} \Leftrightarrow \mathbf{F}^{-1} \approx \begin{bmatrix} \frac{a\cos(\varphi/2)}{2D\sqrt{R}} & 0 & 0 \\ \frac{a\sin(\varphi/2)}{2D\sqrt{R}} & \frac{C}{D} & 0 \\ 0 & 0 & 1/\lambda_3 \end{bmatrix} \quad (36)$$

where

$$D = \frac{C \cos(\varphi/2)}{2\sqrt{R}} \quad (37)$$

Combining eq. 36 and 37 gives the result,

$$\mathbf{F}^{-1} \approx \begin{bmatrix} 1/C & 0 & 0 \\ \frac{\tan(\varphi/2)}{c} & \frac{2\sqrt{R}}{a \cos(\varphi/2)} & 0 \\ 0 & 0 & 1/\lambda_3 \end{bmatrix} \quad (38)$$

Using eq. 16, 37 and 38:

$$\mathbf{L} \approx \begin{bmatrix} \dot{C}/C & 0 & 0 \\ 0 & \frac{\dot{a}}{a} & 0 \\ 0 & 0 & \dot{\lambda}_3/\lambda_3 \end{bmatrix} \quad (39)$$

Eq. 39 states that the in-plane components of the spatial velocity gradient tensor are bounded and independent of spatial coordinates or  $y$  (as long as  $y$  is small compared with crack length). This is an interesting result, since the stress and deformation gradient tensor are singular at the crack tip. Note that  $\mathbf{L}$  is symmetric near the crack tip, so it is also the rate of deformation tensor  $\mathbf{D}$  (or strain rate tensor) near the crack tip. It should be noted that the velocity gradient tensor given by Eq. 39 is only valid at distances very close to the crack tip, around 1/100 of crack length, which is 0.02 mm. However, the deformation field in this region cannot be accurately probed by our experimental techniques.

### Determination of crack tip parameters in SEN sample

The crack tip parameters  $a$  and  $C$  can be obtained from FEM. For our case we have a single-edge crack specimen loaded by applied displacement  $\Delta(t)$  at the grips. From eq. 97b in ref 9,<sup>39</sup> the energy release rate or  $J$  integral is related to the crack tip parameter  $a$  by

$$J = \frac{\mu\pi}{4} a^2 \quad (40)$$

Dimensional analysis implies that

$$J = \mu \left(\frac{\Delta}{l_0}\right)^2 c \bar{J} \left(\frac{\Delta}{l_0}, \frac{c}{w_0}, \frac{w_0}{l_0}\right) \quad (41)$$

where  $\bar{J}$  is a dimensionless function,  $c$  is the crack length and  $w_0$  is the initial width of the sample. Note  $\frac{\Delta}{l_0} = \varepsilon_N$  is the nominal strain in the sample. From (34) and (35), we have

$$a = \frac{2\sqrt{J}}{\sqrt{\mu\pi}} = \frac{2}{\sqrt{\pi}} \frac{\Delta}{l_0} \sqrt{c} \sqrt{\bar{J}\left(\frac{\Delta}{l_0}, \frac{c}{w_0}, \frac{w_0}{l_0}\right)} \quad (42)$$

A reasonable approximation for short cracks is

$$a = \frac{2\sqrt{J}}{\sqrt{\mu\pi}} \approx \frac{2}{\sqrt{\pi}} \frac{\Delta}{l_0} \sqrt{c} \sqrt{\bar{J}\left(\frac{\Delta}{l_0}, \frac{w_0}{l_0}\right)} \quad (43)$$

If both the nominal strain  $\varepsilon_N = \Delta/l_0$  and the crack length  $c$  increases with time, the change in the crack tip parameter  $a$  with time is

$$\dot{a} \approx \frac{2\sqrt{c}}{\sqrt{\pi}} \sqrt{\bar{J}\left(\frac{\Delta}{l_0}, \frac{w_0}{l_0}\right)} \left[ \left(\frac{\dot{\Delta}}{l_0}\right) + \frac{1}{2} \left(\frac{\Delta}{l_0}\right) \frac{\dot{c}}{c} \right] \quad (44)$$

Note that the 2<sup>nd</sup> term due to crack motion may not be small, since typically

$$\left(\frac{\dot{\Delta}}{l_0}\right) = \dot{\lambda}_N \ll \frac{1}{2} \frac{\dot{\Delta}}{l_0} = \frac{\dot{\varepsilon}_N}{2} \quad (45)$$

The other crack tip parameter  $C$  is related to the deformed crack profile, which can be evaluated using (27) and taking  $\varphi = \pm\pi$ , i.e.,

$$\begin{aligned} y_1 &= -CR \\ y_2 &= \pm a\sqrt{R} \Rightarrow y_2 = \pm a\sqrt{-y_1/C} \end{aligned} \quad (46)$$

The crack opening is parabolic and once  $a$  is determined by the J integral,  $C$  can be determined by fitting the crack opening profile. Dimensional analysis implies that

$$C = g\left(\frac{\Delta}{l_0}, \frac{c}{w}, \frac{w}{l_0}\right) \quad (47)$$

The method is applied to obtain the crack parameter  $C$ . Fig. 3.S6 (a) (black line shows the initial undeformed configuration and the deformed shape of the specimen after straining to 0 and 0.15 (nominal strain,  $\varepsilon_N$ ). The deformed shape of the crack is shown in Fig. 3.S6 (b). In these figures ( $x \equiv y_1, y \equiv y_2$ ) are the deformed coordinates.

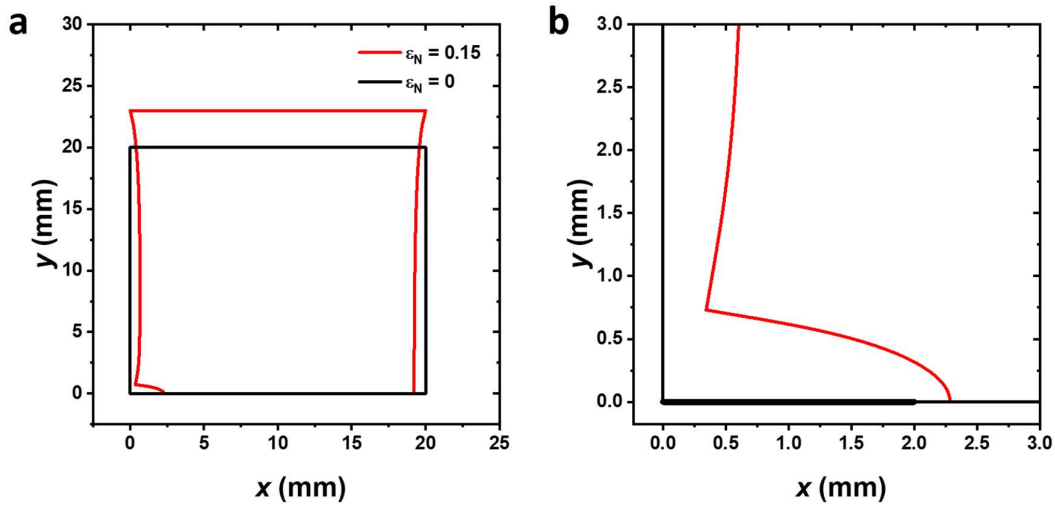


Fig. 3.S6 (a) Undeformed shape of specimen before loading (black line). Deformed shape of specimen after straining to 0 and 0.15 (nominal strain). (b) close up view of deformed crack shape. ( $x \equiv y_1, y \equiv y_2$ ) are the deformed coordinates.

Fig. 3.S7 shows the FEM energy release rate  $J$  versus the nominal strain and compare with our previous results,<sup>41</sup> which is given by

$$J = \mu \left( \lambda^2 + \frac{2}{\lambda} - 3 \right) c \frac{1.476\lambda + .2111}{\lambda - 0.5804}, \quad c/w \ll 1 \quad (48)$$

In Fig. 3.S7(a),  $J$  is normalized by  $\mu$  (the small strain shear modulus) and  $H = l_0/2$  is half of the sample height before deformation.

Recall that  $a$  is the crack tip parameter (see eq. 32). It is related to the energy release rate  $J$  by eq. 40. It also determines the strength of the dominant component of the true stress field  $\sigma_{yy}$ . This parameter is plotted against the nominal strain in Fig. 3.S7(b). We evaluate  $\dot{a}/a$  directly ahead of the crack numerically and this is shown in Figure 3.S7(c). Recall  $\dot{a}/a = L_{22}$  of the asymptotic velocity gradient tensor (see eq. 39).

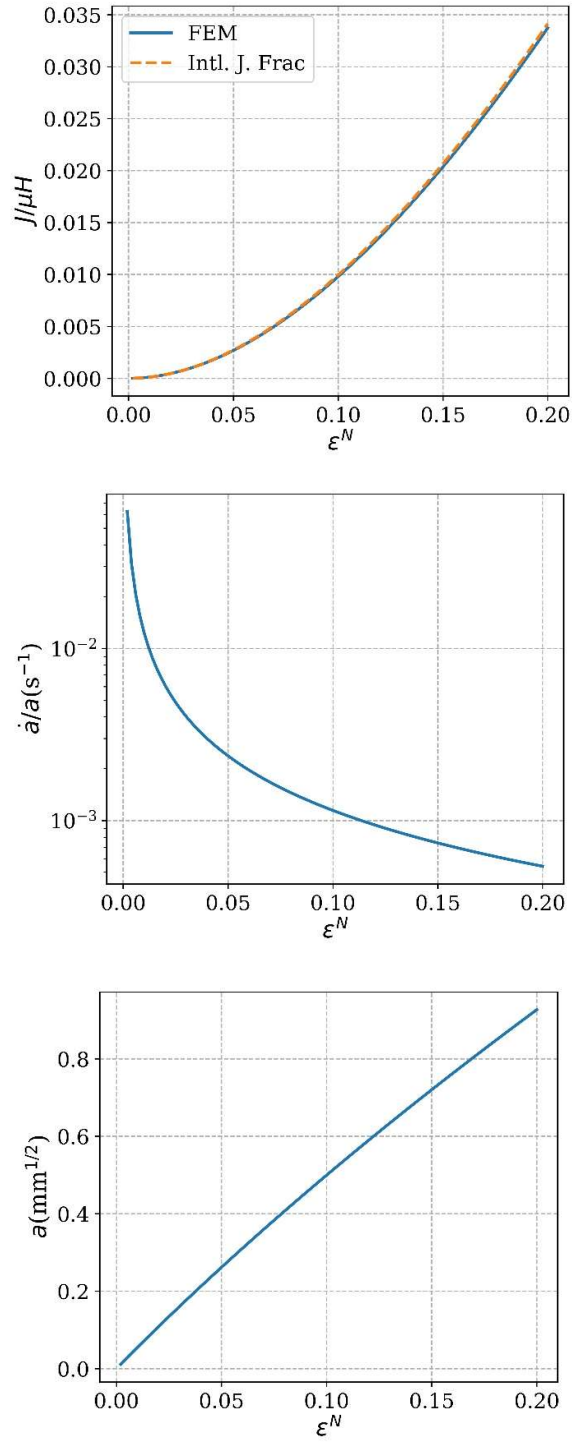


Fig. 3.S7 (a) Normalized energy release rate versus nominal strain (b) crack tip parameter  $a$  versus nominal strain, (c) asymptotic value of  $L_{22}$  (see eq.42) versus nominal strain.

### Calculation of velocity gradient tensor with small amount of crack growth



To distinguish the contribution of molecular damage from undetectable slow crack propagation, we introduce a small change in crack length in our simulation. Since material is rate independent, we carry out a simulation with a slightly longer crack  $\Delta c$ . The contribution of crack motion to the total  $\mathbf{L}$  is  $\frac{\delta L}{\delta c} \dot{c}$ , where  $\dot{c}$  is an experimentally determined quantity.

Dimensional analysis tells us that

$$\begin{aligned} F &= F(\bar{X}, \varepsilon_N(t), \bar{c}(t), \frac{w_0}{l_0}) \\ \bar{X} &= X/w_0 \\ \bar{c}(t) &= \frac{c(t)}{w_0} \end{aligned} \quad (49)$$

Therefore,

$$\dot{\mathbf{F}} = \frac{\partial \mathbf{F}}{\partial \varepsilon_N} \dot{\lambda}_N(t) + \frac{\partial \mathbf{F}}{\partial \bar{c}} \dot{\bar{c}}(t) (\bar{X}, \varepsilon_N(t), \bar{c}(t), \frac{w_0}{l_0}) \quad (50)$$

Hence

$$\mathbf{L} = \dot{\mathbf{F}} \mathbf{F}^{-1} = \left[ \frac{\partial \mathbf{F}}{\partial \varepsilon_N} \dot{\lambda}_N(t) + \frac{\partial \mathbf{F}}{\partial \bar{c}} \dot{\bar{c}}(t) \right] \mathbf{F}^{-1} (\bar{X}, \varepsilon_N(t), \bar{c}(t), \frac{w_0}{l_0}) = \mathbf{L}_{ncg} + \mathbf{L}_c \quad (51)$$

Thus, the spatial velocity gradient tensor due to crack growth and increase in nominal strain can be decomposed into two contributions, the first is due to the change in nominal strain, i.e.,

$$\mathbf{L}_{ncg} = \left[ \frac{\partial \mathbf{F}}{\partial \varepsilon_N} \dot{\lambda}_N(t) \right] \mathbf{F}^{-1} (\bar{X}, \varepsilon_N(t), \bar{c}(t), \frac{w_0}{l_0}) \quad (52)$$

without crack growth (ncg = no crack growth). The second contribution is due to crack growth, i.e.,

$$\mathbf{L}_c = \left[ \frac{\partial \mathbf{F}}{\partial \bar{c}} \dot{\bar{c}}(t) \right] \mathbf{F}^{-1} (\bar{X}, \varepsilon_N(t), \bar{c}(t), \frac{w_0}{l_0}) \quad (53)$$

## Summary

Finite element method is performed:

- (a) We use FEM to compute  $a$  and  $C$  in the specimen, and estimate an upper bound for

the rate of deformation

- (b) The velocity gradient tensor near the crack tip is bounded and is independent of spatial position. It is also the rate of deformation tensor  $\mathbf{D}$  since  $L_{12} = L_{21} \sim 0$ .
- (c) The change in velocity gradient tensor due to small change of crack tip position is computed using FEM.

### 3.6.3 Additional testing on natural rubber and pasta

Vulcanized natural rubber films with a thickness of 0.38 mm was cut into width of 15 mm and initial length of 25 mm with notch length of 1.5 mm. Tensile test on SEN sample was performed with  $\dot{\lambda}_N = 2 \times 10^{-4} \text{ s}^{-1}$ , and stress-strain curve is shown in Fig. 3.S8(a). As seen in Fig. 3.S8(b), slight propagation can be detected from  $\varepsilon_N = 25 \%$ , pointing to the left. The side-way propagation continues until around 30% and further stretching leads to massive propagation perpendicular to stretching direction (see  $\varepsilon_N = 31 \%$ ).

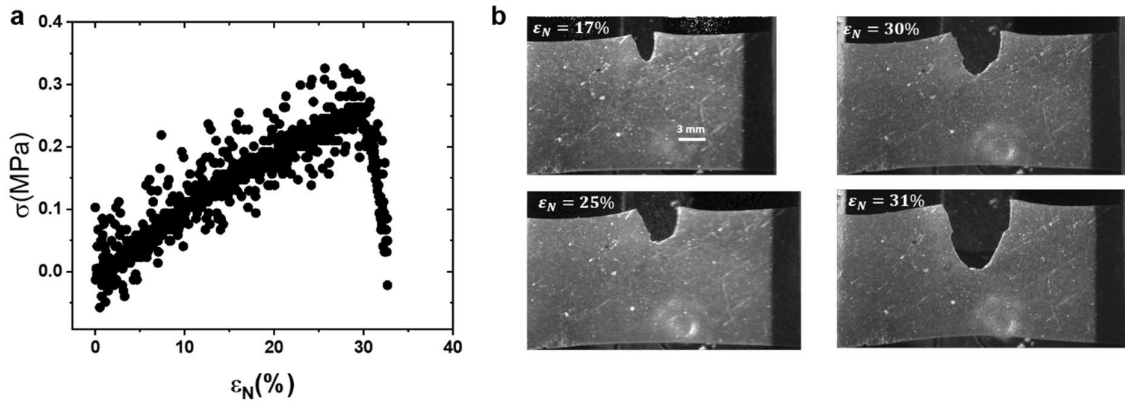


Fig. 3.S8 (a) Stress-strain curve for SEN natural rubber. (b) Propagation of the crack at different  $\varepsilon_N$ .

Dry pasta purchased from supermarket has thickness around 0.9 mm and width of 11 mm, which was cut into initial length of 30 mm with notch of 1.5 mm for experiments (stretching rate  $\dot{\lambda}_N = 10^{-4} \text{ s}^{-1}$ ). Stress-strain curve is shown in Fig. 3.S9(a). With the propagation of the crack, cross-section of the sample decreases and drop of stress can be observed from  $\varepsilon_N = 1.9 \%$ . Crack tip remains sharp over increasing  $\varepsilon_N$  and the propagation follows a zig-zag path, as seen in Fig. 3.S9(b).

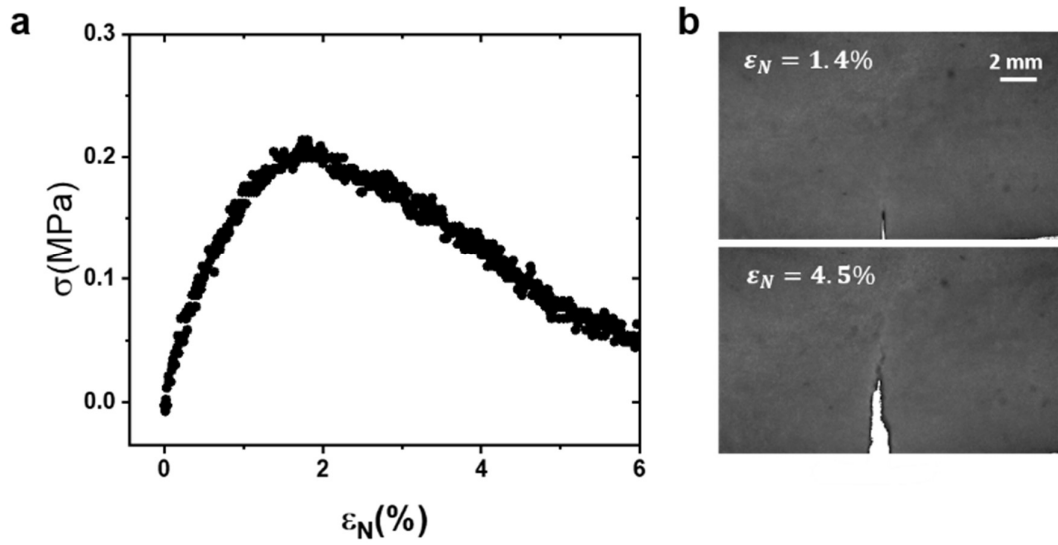


Fig. 3.9(a) Stress-strain curve for SEN pasta. (b) Images showing the propagation of the crack at  $\varepsilon_N = 1.4$  and 4.5 %, respectively.

## Reference

- 1 Chen, C., Wang, Z. & Suo, Z. Flaw sensitivity of highly stretchable materials. *Extreme Mechanics Letters* **10**, 50-57 (2017).
- 2 Creton, C. & Ciccotti, M. Fracture and adhesion of soft materials: a review. *Rep Prog Phys* **79**, 046601, doi:10.1088/0034-4885/79/4/046601 (2016).
- 3 Wang, X. & Hong, W. Delayed fracture in gels. *Soft Matter* **8**, doi:10.1039/c2sm25553g (2012).
- 4 Bonn, D., Kellay, H., Prochnow, M., Ben-Djemaa, K. & Meunier, J. Delayed fracture of an inhomogeneous soft solid. *Science* **280**, 265-267 (1998).
- 5 Li, X. *et al.* Mesoscale bicontinuous networks in self-healing hydrogels delay fatigue fracture. *Proceedings of the National Academy of Sciences* **117**, 7606-7612 (2020).
- 6 Kolvin, I., Kolinski, J. M., Gong, J. P. & Fineberg, J. How supertough gels break. *Physical review letters* **121**, 135501 (2018).
- 7 Slooman, J. *et al.* Quantifying rate-and temperature-dependent molecular damage in elastomer fracture. *Physical Review X* **10**, 041045 (2020).
- 8 van der Kooij, H. M. *et al.* Laser Speckle Strain Imaging reveals the origin of delayed fracture in a soft solid. *Science advances* **4**, eaar1926 (2018).
- 9 Amon, A., Mikhailovskaya, A. & Crassous, J. Spatially resolved measurements of micro-deformations in granular materials using diffusing wave spectroscopy. *Rev Sci Instrum* **88**, 051804, doi:10.1063/1.4983048 (2017).
- 10 Amon, A., Nguyen, V. B., Bruand, A., Crassous, J. & Clement, E. Hot spots in an athermal system. *Phys Rev Lett* **108**, 135502, doi:10.1103/PhysRevLett.108.135502 (2012).
- 11 Le Bouil, A., Amon, A., McNamara, S. & Crassous, J. Emergence of cooperativity in plasticity of soft glassy materials. *Phys Rev Lett* **112**, 246001, doi:10.1103/PhysRevLett.112.246001 (2014).
- 12 Pommella, A., Cipelletti, L. & Ramos, L. Role of normal stress in the creep dynamics and failure of a biopolymer gel. *Physical Review Letters* **125**, 268006 (2020).
- 13 Cipelletti, L., Martens, K. & Ramos, L. Microscopic precursors of failure in soft matter. *Soft matter* **16**, 82-93 (2020).
- 14 Aime, S., Ramos, L. & Cipelletti, L. Microscopic dynamics and failure precursors of a gel under mechanical load. *Proc Natl Acad Sci U S A* **115**, 3587-3592, doi:10.1073/pnas.1717403115 (2018).
- 15 Slooman, J. *et al.* Quantifying Rate- and Temperature-Dependent Molecular Damage in Elastomer Fracture. *Physical Review X* **10**, doi:10.1103/PhysRevX.10.041045 (2020).
- 16 Clough, J. M., Creton, C., Craig, S. L. & Sijbesma, R. P. Covalent bond scission in the Mullins effect of a filled elastomer: real-time visualization with mechanoluminescence. *Advanced Functional Materials* **26**, 9063-9074 (2016).
- 17 Göstl, R. & Sijbesma, R.  $\pi$ -extended anthracenes as sensitive probes for mechanical stress. *Chemical science* **7**, 370-375 (2016).
- 18 Lavoie, S. R., Long, R. & Tang, T. A rate-dependent damage model for elastomers at large strain. *Extreme Mechanics Letters* **8**, 114-124 (2016).
- 19 Long, R., Krishnan, V. R. & Hui, C.-Y. Finite strain analysis of crack tip fields in incompressible hyperelastic solids loaded in plane stress. *Journal of the Mechanics and Physics of Solids* **59**, 672-695 (2011).
- 20 Liu, M., Guo, J., Hui, C. Y. & Zehnder, A. T. Application of Digital Image Correlation (DIC) to the Measurement of Strain Concentration of a PVA Dual-Crosslink

- Hydrogel Under Large Deformation. *Experimental Mechanics*, doi:10.1007/s11340-019-00520-4 (2019).
- 21 Lake, G. & Thomas, A. The strength of highly elastic materials. *Proceedings of the Royal Society of London. Series A. Mathematical and Physical Sciences* **300**, 108-119 (1967).
- 22 Valentin, J. D. *et al.* Substrate viscosity plays an important role in bacterial adhesion under fluid flow. *Journal of colloid and interface science* **552**, 247-257 (2019).
- 23 Clough, J. M., Creton, C., Craig, S. L. & Sijbesma, R. P. Covalent Bond Scission in the Mullins Effect of a Filled Elastomer: Real-Time Visualization with Mechanoluminescence. *Advanced Functional Materials* **26**, 9063-9074, doi:10.1002/adfm.201602490 (2016).
- 24 Cipelletti, L., Brambilla, G., Maccarrone, S. & Caroff, S. Simultaneous measurement of the microscopic dynamics and the mesoscopic displacement field in soft systems by speckle imaging. *Opt Express* **21**, 22353-22366, doi:10.1364/OE.21.022353 (2013).
- 25 Nagazi, M.-Y. *et al.* Space-resolved diffusing wave spectroscopy measurements of the macroscopic deformation and the microscopic dynamics in tensile strain tests. *Optics and Lasers in Engineering* **88**, 5-12, doi:10.1016/j.optlaseng.2016.07.006 (2017).
- 26 Nagazi, M. Y., Dieudonné-George, P., Brambilla, G., Meunier, G. & Cipelletti, L. Phase transitions in polymorphic materials probed using space-resolved diffusing wave spectroscopy. *Soft matter* **14**, 6439-6448 (2018).
- 27 Lee, S. & Pharr, M. Sideways and stable crack propagation in a silicone elastomer. *Proc Natl Acad Sci U S A* **116**, 9251-9256, doi:10.1073/pnas.1820424116 (2019).
- 28 Marano, C., Boggio, M., Cazzoni, E. & Rink, M. Fracture phenomenology and toughness of filled natural rubber compounds via the pure shear test specimen. *Rubber Chemistry and Technology* **87**, 501-515 (2014).
- 29 Bapst, V. *et al.* Unveiling the predictive power of static structure in glassy systems. *Nature Physics* **16**, 448-454 (2020).
- 30 Cardinaux, F., Cipelletti, L., Scheffold, F. & Schurtenberger, P. Microrheology of giant-micelle solutions. *EPL (Europhysics Letters)* **57**, 738 (2002).
- 31 Pine, D. J., Weitz, D. A., Chaikin, P. M. & Herbolzheimer, E. Diffusing wave spectroscopy. *Phys Rev Lett* **60**, 1134-1137, doi:10.1103/PhysRevLett.60.1134 (1988).
- 32 Weitz, D. & Pine, D. in *Dynamic light scattering: The method and some applications* 652-720 (Oxford University Press, 1993).
- 33 MacKintosh, F. C., Zhu, J.-X., Pine, D. & Weitz, D. Polarization memory of multiply scattered light. *Physical Review B* **40**, 9342 (1989).
- 34 Pine, D. J., Weitz, D. A., Zhu, J. X. & Herbolzheimer, E. Diffusing-wave spectroscopy: dynamic light scattering in the multiple scattering limit. *Journal de Physique* **51**, 2101-2127, doi:10.1051/jphys:0199000510180210100 (1990).
- 35 Bicout, D. & Maynard, R. Diffusing wave spectroscopy in inhomogeneous flows. *Physica A: Statistical Mechanics and its Applications* **199**, 387-411 (1993).
- 36 Cai, Z., Qiu, W., Shao, G. & Wang, W. A new fabrication method for all-PDMS waveguides. *Sensors and Actuators A: Physical* **204**, 44-47 (2013).
- 37 Brindise, M. C., Busse, M. M. & Vlachos, P. P. Density-and viscosity-matched Newtonian and non-Newtonian blood-analog solutions with PDMS refractive index. *Experiments in fluids* **59**, 1-8 (2018).
- 38 Mai, T.-T., Okuno, K., Tsunoda, K. & Urayama, K. Crack-Tip Strain Field in Supershear

- Crack of Elastomers. *ACS Macro Letters* **9**, 762-768, doi:10.1021/acsmacrolett.0c00213 (2020).
- 39 Krishnan, V. R., Hui, C. Y. & Long, R. Finite strain crack tip fields in soft incompressible elastic solids. *Langmuir* **24**, 14245-14253 (2008).
- 40 Long, R. & Hui, C.-Y. Crack tip fields in soft elastic solids subjected to large quasi-static deformation—a review. *Extreme Mechanics Letters* **4**, 131-155 (2015).
- 41 Liu, Z., Zakoworotny, M., Guo, J., Zehnder, A. T. & Hui, C.-Y. Energy release rate of a single edge cracked specimen subjected to large deformation. *International Journal of Fracture* **226**, 71-79 (2020).

---

Chapter 4. In-situ 3D damage visualization at the  
crack tip in multiple network elastomers

## 4 In-situ 3D damage visualization at the crack tip in multiple network elastomers

Jianzhu Ju <sup>a</sup>, Gabriel Sanoja <sup>a</sup>, Luca Cipelletti <sup>b,c</sup>, Tetsuharu Narita <sup>\*, a,d</sup>, Costantino Creton <sup>\*, a,d</sup>

<sup>a</sup> Sciences et Ingénierie de la Matière Molle, CNRS UMR 7615, ESPCI Paris, PSL Université, Paris, France

<sup>b</sup> Laboratoire Charles Coulomb (L2C), University of Montpellier, CNRS, Montpellier, France

<sup>c</sup> Institut Universitaire de France

<sup>d</sup> Global Station for Soft Matter, Global Institution for Collaborative Research and Education, Hokkaido University, Sapporo, Japan

### 4.1 Abstract

*Multiple network elastomers (MNEs) are a class of soft elastic materials with both high stiffness and high toughness. While the enhancement in fracture toughness of MNEs has been widely reported, understanding the origin of the toughening mechanism is challenging, due to the complex structure and lack of characterization methods. Here we map the 3D damage distribution during the opening of a crack by fluorescence measurement of mechanophore-labeled MNE. Together with deformation mapping by digital image correlation (DIC), we discover that the strain hardening of MNE provides a self-strengthening mechanism that limits strain localization and delays crack propagation, contributing to enhanced resistance to both fast and delayed fracture. The unprecedented visualization of 3D damage in MNE with micron resolution shows material response at the molecular scale, and the understanding on the toughening mechanism will push the development of advanced MNE materials.*

---

\*correspondence authors: [tetsuharu.narita@espci.fr](mailto:tetsuharu.narita@espci.fr), [costantino.creton@espci.fr](mailto:costantino.creton@espci.fr)



## 4.2 Introduction

Multiple network elastomers (MNE) are a class of recently developed soft materials with a novel combination of high stiffness, good reversible extensibility and high toughness.<sup>1-3</sup> Their excellent mechanical performance stems from the presence of energy dissipation mechanisms by the bond scission in an embedded sacrificial network, so that the material can be highly deformed after being damaged but while avoiding crack propagation.<sup>1,4</sup> When describing mechanical properties, the fracture resistance differs from the extensibility of the material, due to the sensitivity to flaws, which commonly exist in practical materials. When the flaw size exceeds a critical length (flaw sensitivity length),<sup>5,6</sup> the fracture stress becomes very sensitive to the flaw size. It has been reported that an ultrahigh fracture energy (over  $10^3 \text{ J/m}^2$ ) can be obtained by the design of multiple network polymer, so that flaw tolerance is also improved.<sup>2,7</sup> Although engineering of tough hydrogels by network design is becoming a new hot topic of polymer science,<sup>3,8,9</sup> applications of elastomers are more common while understanding better the molecular origin of the enhancement of the fracture toughness in MNE may be as essential.

As MNE potentially expand the space of applications of unfilled elastomers, the multiple interpenetrated network structure complexifies the possible energy dissipation mechanisms during fracture. Classically, the energy dissipation by bond scission can be described by the *Lake-Thomas* model,<sup>10</sup> which assumes that the minimum energy necessary to break a simple elastomer network is the simple product of the areal density of strands crossing the fracture plane by the average number of bonds per strand and by the energy per chemical bond. Such a dissipative mechanism would be restricted to the dimensions of a network mesh size ( $\sim 10 \text{ nm}$ ). However for MNE, molecular bonds break over a large scale that can extend easily over  $1 \text{ mm}$ ,<sup>1,11</sup> without necessarily leading to crack propagation. It is also well-known that at large deformations, strain localization may blunt the crack tip and reduce the stress concentration, delaying the growth of the crack. The size scale of the strain concentration, typically  $100 \text{ }\mu\text{m}$  around the crack tip,<sup>12,13</sup> implies that in MNE, the damaged region is also non-negligibly deformed. For the study of MNEs, the spontaneous structural heterogeneity at the macroscopic scale is the key feature of their fracture behavior, but has been so far only phenomenologically discussed.<sup>1,14</sup> Furthermore, how the damage is coupled into changes in localized

strain/stress governs the onset of catastrophic (fast) crack propagation. The investigation on the dynamic behavior of fracture in MNE requires in-situ characterization on both molecular and mechanical behavior, and advanced measurement methods need to be developed.

Mechanophore-based visualization techniques<sup>11,15,16</sup> provide a powerful tool to optically and quantitatively investigate the scission of molecular bonds, which is especially valuable for the study of MNE where bond scission takes place at a sub-macroscopic scale (> 0.1 mm). Mechanophore crosslinkers are activated upon breaking, and the fluorescence intensity can be detected by confocal microscopy to achieve a depth-resolved mapping.<sup>11,17,18</sup> In this work, we propose the simultaneous observation, using in-situ confocal microscopy, of 3D molecular damage during the fracture of MNE, and combine it with the full-field measurement of the deformation heterogeneity by digital image correlation (DIC). With the method, we aim to bridge the molecular mechanism of damage with the changes in mechanical properties to better understand and design MNEs.

### 4.3 Results and Discussion

Following our previous work on poly (ethyl acrylate) (EA) multiple networks<sup>1,19</sup>, double networks (DN) and triple networks (TN) were prepared by UV-polymerization of the swollen single network (SN), as previously described<sup>19</sup> and as seen in **Materials and methods**. SN is synthesized first and 5 mol% of the crosslinker is labeled with the mechanophore (non-fluorescent in the intact state). Then swelling in an EA monomer solution provides an isotropic pre-stretching of the first network (also called filler network), so that the difference in extensibility between filler network and second/third network (matrix network) results in the breaking of pre-stretched filler network as a sacrificial network.<sup>19</sup> From the isotropic swelling ratio measured by weight ratio  $\alpha$  ( $\alpha = m/m_0$ ), the pre-stretch  $\lambda_0$  of the first network is defined as  $\lambda_0 = \sqrt[3]{\alpha}$ ,<sup>19</sup> and given in Table 4.1 for the different materials. The initial thickness of SN is 0.8 mm and the thickness of DN and TN increase due to swelling, as seen in Table 4.1. Single edge notched (SEN) samples of SN, DN and TN are cut into samples of the same size: 15 mm (between clamps)  $\times$  6 mm for fracture testing. To avoid different initial damage along the thickness, the notch is prepared by pushing the razor blade into the lateral face of the sample, with an initial length around 1.5 mm (**Materials and methods**).

#### 4.3.1 Fast fracture

	SN	DN	TN
Pre-stretch $\lambda_0$	1	1.59	2.34
Thickness	0.8 mm	1.27 mm	1.83 mm
Young modulus $E$	0.47 MPa	0.96 MPa	1.36 MPa
Stretch ratio at break $\lambda_b$	1.19	1.5	2.31
Crack velocity	0.013 mm/s	0.05 mm/s*	200 mm/s

*Table 4.1 Sample specifications and mechanical properties of SN, DN and TN. \* The reproducibility of propagation in DN is poor, I found it is very sensitive to the initial cut.*

Fast fracture,<sup>20</sup> where a notched sample is continuously stretched until fracture, is studied

by uniaxial stretching of SEN samples at a stretch rate  $\dot{\lambda} = 10^{-4} \text{ s}^{-1}$ . Mechanical and optical tests are carried out in the set-up schematically described in Fig. 4.1(a), with simultaneous data acquisition by confocal microscopy (for damage visualization around the crack) and a CMOS camera (for full-field strain mapping by DIC). Details are provided in **Materials and methods**. Stress-strain curves until fracture are shown in Fig. 4.1(b) for SN, DN and TN, respectively. As previously reported,<sup>1,19,21</sup> a significant increase in modulus and strain at break is observed in multiple networks (see also Table 4.1).

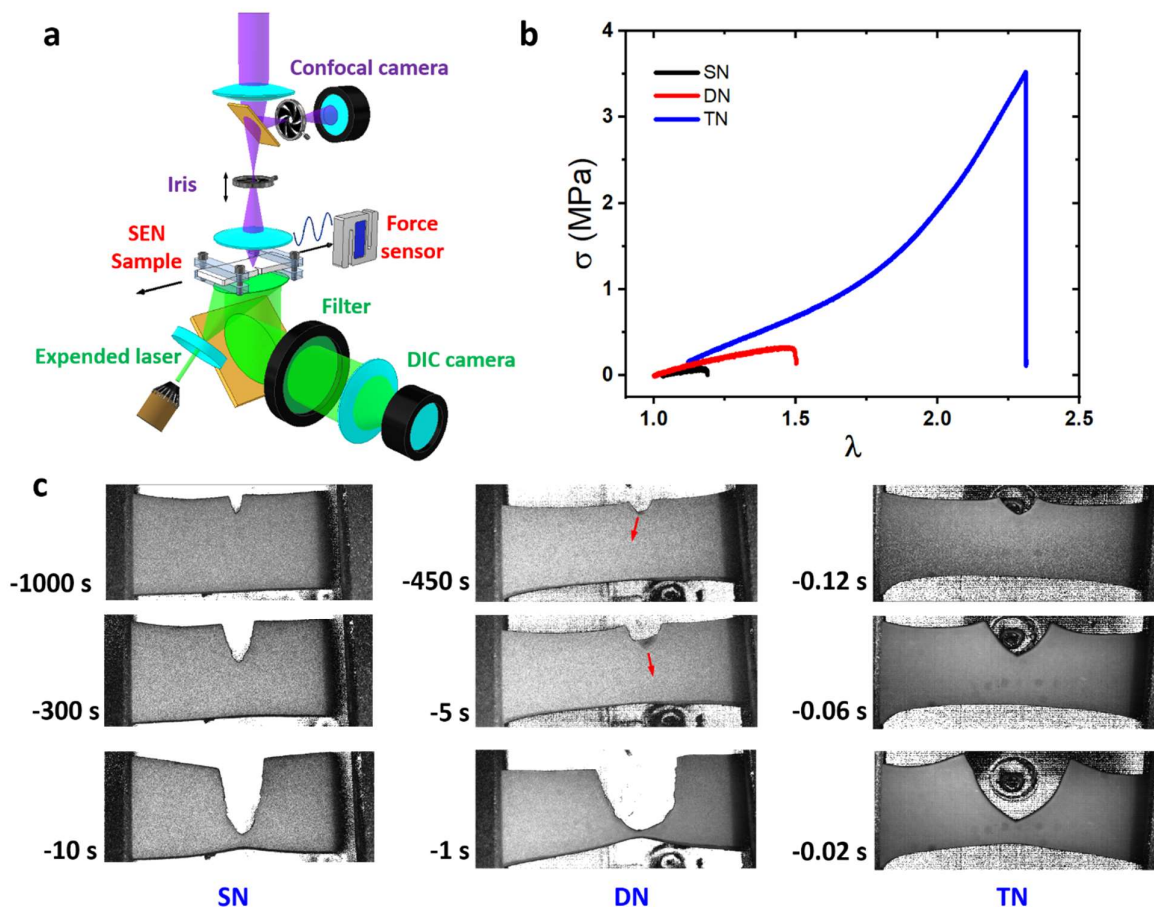


Fig. 4.1 (a) Simultaneous measurement set-up of DIC and mechanophore mapping. (b) Stress-strain curve during uniaxial extension of notched SN, DN and TN respectively, with stretch rate  $\dot{\lambda} = 10^{-4} \text{ s}^{-1}$  (c) Images during propagation with complete fracture as reference time.

Three materials made from the same monomer (EA) but with different network architectures, have distinct propagation modes. Fracture of the SN occurs by slow propagation of the crack that gradually takes place with increasing far-field strain over a long time ( $\sim 1000 \text{ s}$ ,  $\lambda \sim 0.1$ ). In the example of DN the crack does not propagate straight

and major propagation (moving through  $\sim 80\%$  of propagation length) lasts  $\sim 5$  s. Finally, propagation of the crack in TN is much faster and occurs over  $\sim 0.1$  s with a sharp crack tip. The propagation kinetics can also be detected by the drop in stress in Fig. 4.1(b), and the averaged propagation speed (from the time when crack reaches the midpoint of the sample along the propagation direction, to full fracture) is shown in Table 4.1.

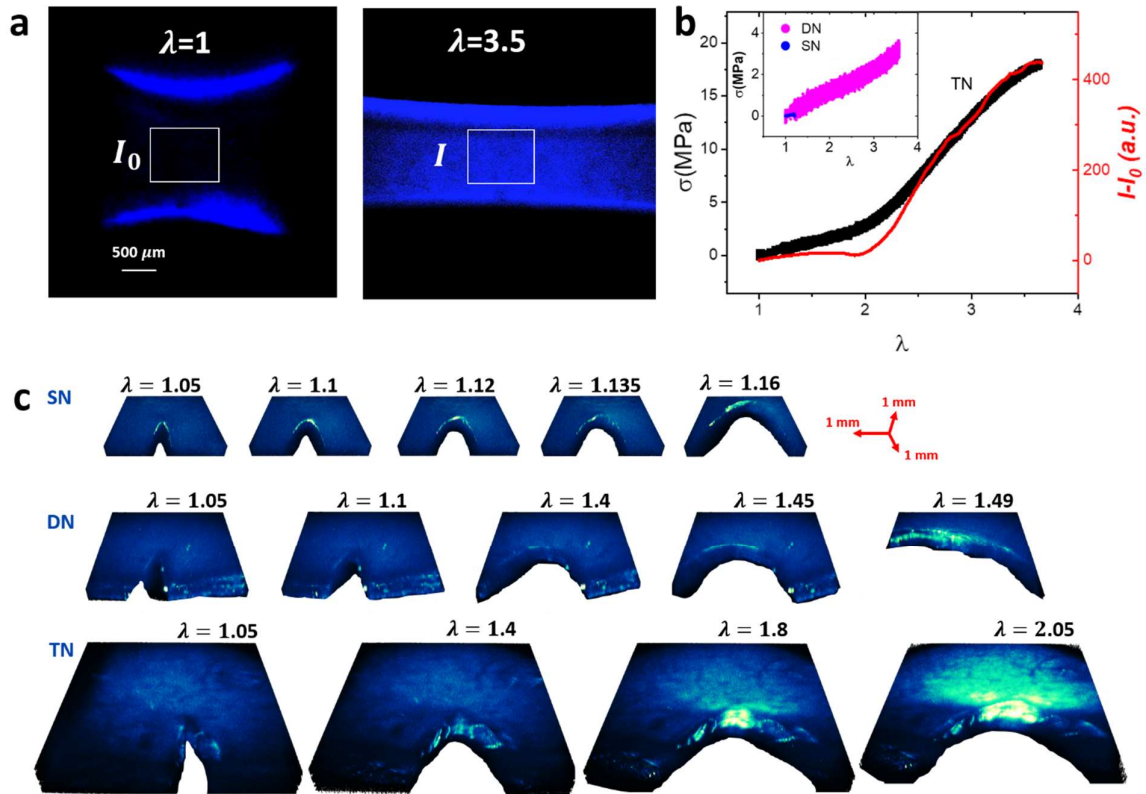


Fig. 4.2 (a) Fluorescence images of the dogbone TN sample (without a notch) undergoing uniaxial extension, at  $\lambda = 1$  and  $\lambda = 3.5$ . White square defined the region for the calculation of the average intensity. (b) Stress and change of fluorescence intensity ( $I - I_0$ ) as the functions of  $\lambda$ . Inserted: stress-stretch curve of DN and SN. (c) 3D damage map of fluorescence intensity by confocal microscopy, in SN, DN and TN at different  $\epsilon_N$ .

Beyond the macroscopic mechanical measurement and observation of the macroscopic propagation of the crack, we can gain some more local insight. Near the crack tip, the molecular scale bond scission (actually the scission of crosslinkers in the filler network) can be detected by confocal microscopy and the strain field of the material can be measured by DIC, respectively. Fig. 4.2(a) shows the response of bonds scission to uniaxial elongation, with a dogbone TN sample (without a notch, initial length between

crossheads: 5.5 mm) stretched at  $\dot{\lambda} = 10^{-4} \text{ s}^{-1}$ , observed under confocal microscopy. To characterize the accumulated damage during the elongation, the averaged fluorescence intensity (subtracted of the initial value  $I_0$  in the same region) is plotted as a function of  $\lambda$  in Fig. 4.2(b). To avoid the influence of the high intensity at the sample edge (due to the cutting from the punch for a dogbone shaped sample), a region of interest to define the averaged intensity is placed at the center of the sample as indicated in Fig. 4.2(a). As seen in the figure, the value of the normalized intensity is about 0 at low stretch, while it sharply increases from around  $\lambda = 1.8$ , following the trend of the curve of the stress in the same figure, exhibiting a strain hardening. This result indicates that the random scission of molecular bonds,<sup>19,21</sup> can be detected roughly at the onset of strain hardening emphasizing the much greater sensitivity of the fluorescent probe relative to the mechanoluminescent probe previously used.<sup>1</sup> Note that a slight strain hardening is also observed in the DN at  $\lambda \sim 2.4$ , without detectable fluorescence intensity change (inserted in Fig. 4.2(b)), more consistent with results obtained with luminescence on similar materials.<sup>1</sup> For SN, before reaching strain hardening, samples were already broken at the clamp at  $\lambda = 1.2$ .

Fig. 4.2 (c) shows the fluorescent images of the 3D damage mapping around the open crack. As damage occurs at different scales for different materials, resolutions and field sizes are chosen accordingly in Fig. 4.2 (c) but the center of the image is around the initial crack tip (see **Materials and methods 1.5.2**). In this acquisition method, 3D damage maps can be acquired with a time resolution of 1 min. The crack is gradually opened by increasing  $\lambda$ , which also results in changes in fluorescence intensity due to the activation of mechanophores upon molecular scission. Before propagation, SN and DN did not show any obvious activation due to damage apart from the initially present activation due to the cutting of the notch with the razor blade. However, during propagation (see Fig. 4.2 (c), at  $\lambda = 1.49$  for DN and  $\lambda = 1.16$  for SN) a stronger intensity can be observed at the tip of the crack in DN than in SN, qualitatively consistent with the observations previously made with mechanoluminescent molecules in a time resolved way during propagation.<sup>1</sup> For the experiment done on the TN, even though crack propagation occurs at  $\lambda = 2.3$ , massive damage far from the crack tip ( $\sim 1 \text{ mm}$ ) can already be observed at  $\lambda = 1.7$ . The spatial distribution of damage at large strain ( $\lambda = 1.8$  and  $\lambda = 2.05$  in Fig. 4.2(b)) in TN shows a similar pattern as the region of high strain around the crack, previously observed

on similar soft elastic materials by DIC and in simulations.<sup>22,23</sup> Compared to the SN, the damage in the filler network occurs over a much larger scale ( $\sim 0.05 \text{ mm}^2$  in DN and  $1 \text{ mm}^2$  in TN, at  $\lambda = 2.05$ ). While similar indirect evidence of damage at the crack tip has been reported with other methods<sup>1,11</sup>, this is the first high resolution ( $2 \text{ }\mu\text{m}/\text{pixel}$  in plane with depth resolution  $154 \text{ }\mu\text{m}/\text{slice}$  in depth for TN) 3D damage mapping of the extent of sacrificial network bond scission in an open crack before propagation.

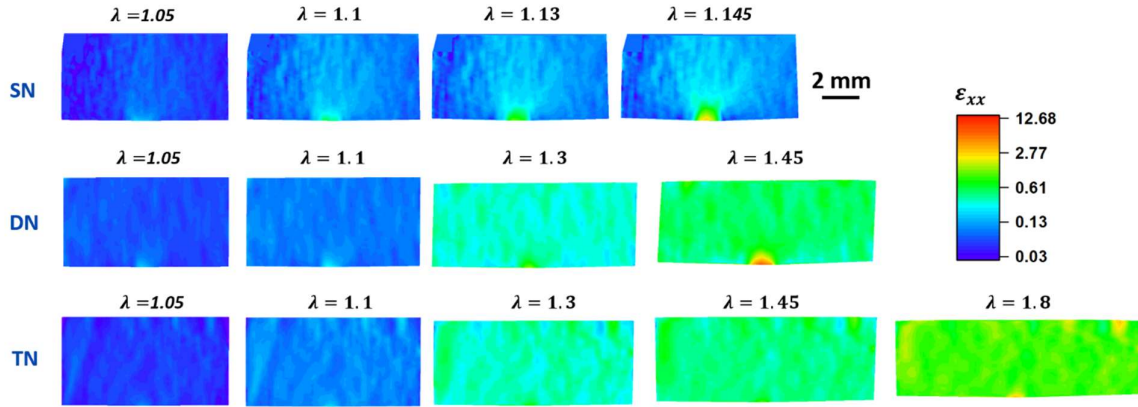


Fig. 4.3  $\varepsilon_{xx}$  map for SN, DN and TN at different  $\lambda$ .

We can now turn to DIC to characterize the strain field. Fig. 4.3 shows the spatial distribution of strain in the stretching direction  $\varepsilon_{xx}$  in the deformed configuration. Comparing the three materials, we find that the MNEs appear to be much less sensitive to the presence of a flaw (crack), so that for the same  $\lambda$ , the strain distribution is more homogeneous for DN and TN than for SN. Fig. 4.4 (a) shows  $\varepsilon_{xx}(y)$  as a function of distance from the crack tip ( $y$ ) along the symmetric line ( $x = 0$ ) for  $\lambda = 1.1$  and  $\lambda = 1.4$ . The value of renormalized  $\varepsilon_{xx}/\lambda$  at  $y = 0.3 \text{ mm}$  is extracted from the data to compare strain localization in different materials and is shown in Fig. 4.4(b) as a function of  $\lambda$ . For  $\lambda < 1.05$ ,  $\varepsilon_{xx}/\lambda$  ( $y = 0.3 \text{ mm}$ ) overlaps for all three materials, while an obvious deviation is detected at  $\lambda = 1.05$  for SN and at  $\lambda = 1.15$  for DN. Part of the results are measured at large  $\lambda$  where a slight propagation is already observed during stretching, but the extent of crack propagation (in results shown here) is less than the grid size (15 pixels) used in DIC. Before crack propagation occurs for each of the different materials,  $\varepsilon_{xx}$  ( $y = 0.3 \text{ mm}$ ) grows faster with  $\varepsilon_N$ , showing a fracture precursor, a similar behavior as what was reported in PDMS elastomers in Chapter 3.

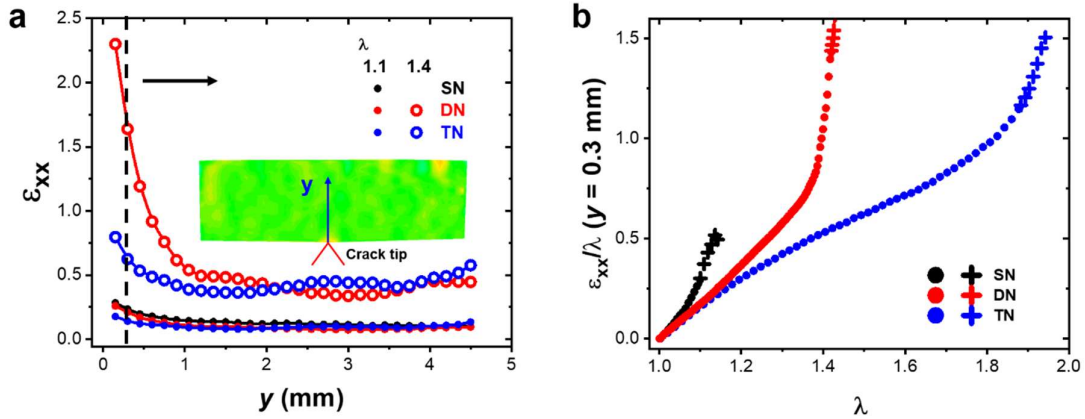


Fig. 4.4 (a)  $\epsilon_{xx}$  as the function of  $y$  at  $\epsilon_N = 0.1$  and  $0.4$ , respectively. (b)  $\epsilon_{xx}$  at  $y = 0.3$  mm from the crack tip as function of  $\epsilon_N$ . Results before propagation are indicated by “•”, and those after are indicated by “+”.

Simultaneous damage mapping and deformation mapping, together with the clear enhancement of the fracture resistance, show that for the DN and TN the deformation is *delocalized* around the crack. Since the filler network is prestretched in the MNE during preparation, the value of  $\lambda$  at which the strands of the filler network reach their maximum extensibility and where the MNE shows a strain hardening is much lower than what is expected in the SN made from the same monomer.<sup>19,21</sup> As seen in Fig. 4.2(a), in uniaxial tension the TN exhibits a strong strain hardening at a relative small  $\lambda_{sh,TN} \sim 1.8$ , much smaller than local deformation of TN around the crack tip (compared to  $\epsilon_{xx}+1$  measured from DIC). The material ahead of the crack is in its strain hardening region, so that the singularity results in a stiffer region around the crack tip which limits the strain localization in the surrounding region. Even at  $\lambda \ll \lambda_{sh,TN}$ , locally strain hardening is induced in MNE (as long as  $\epsilon_{xx}+1 > \lambda_{sh,TN}$ ), so that a smaller local  $\epsilon_{xx}$  is observed compared to SN. In other words, the stiffening accompanied by extensive damage of the MNE is due to a locally heterogeneous structure to obtain a deformation (but not stress) homogeneity. For SN, the crack may already propagate long before local strain hardening kicks in, so that the effect of delocalization is not observable. This behavior is similar to what was recently observed in thermoplastic polyurethanes under cyclic loading<sup>24</sup> and shows in more detail what flaw insensitivity may mean at the material scale, with the example of MNE. The key difference between MNE and materials such as glassy polymers<sup>25</sup> showing elastic-plastic behavior above a well-defined yield stress, is that the



damage is here progressive and its main role is a reduction of the local stress concentration, which certainly remains heterogeneous in the damage region. The question of the actual criterion for crack propagation in this damaged region remains however open and will be addressed next.

### 4.3.2 Delayed fracture

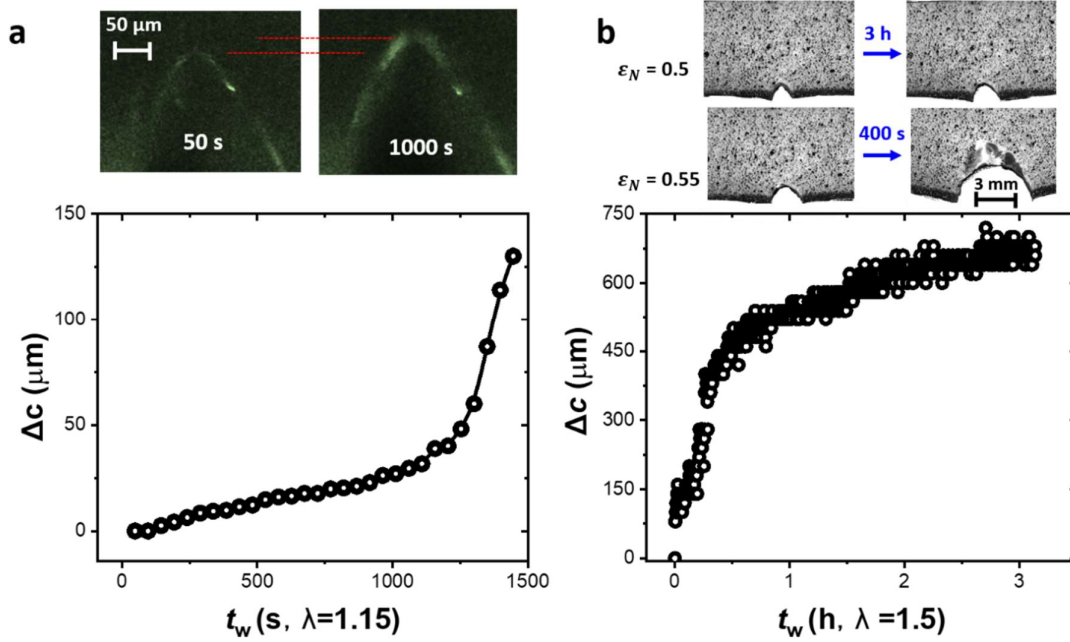


Fig. 4.5 Crack propagation length  $\Delta c$  at fixed displacement for (a) SN at  $\lambda = 1.15$  and (b) DN at  $\lambda = 1.5$ .

As multiple networks can survive significant internal molecular damage before breaking, the large scale structural and mechanical heterogeneity will probably also affect time-dependent response under deformation. The fracture propagation (or lack of) over a long time under fixed macroscopic strain (delayed fracture) can differ from that in fast fracture.<sup>20,26</sup> The occurrence of delayed fracture behavior was investigated in SN, DN, and TN at fixed strain, by increasing  $\lambda$  step-by-step with intervals of  $\Delta\lambda = 0.05$ . At the onset of propagation, the propagation length  $\Delta c$  can be even smaller than the variation in depth-dependent crack length due to the initial cutting, the value of  $\Delta c$  was measured by tracking the damaged region at a fixed depth from the surface by confocal microscopy, as shown in Fig. 4.5 (a) for SN. Propagation is first observed in SN at  $\lambda = 1.15$  where  $\Delta c$  is plotted as function of waiting time  $t_w$ , in Fig. 4.5(a). The crack initially grows at a speed  $\dot{c}$

around 40 nm/s, and gradually accelerates to  $\dot{c} \sim 300$  nm/s after  $t_w > 1300$  s, showing self-acceleration. Even though the crack propagation is still slow, this acceleration of the propagation at fixed  $\lambda$  will lead to final breaking of the material. For DN, the propagation first takes place at  $\lambda = 1.5$ , as shown in Fig. 4.5(b). Very differently from the case of the conventional network SN, the crack propagates first rather fast at  $\dot{c} \sim 400$  nm/s and then slows down to 30 nm/s after 1 h, showing self-stabilization. The crack barely advances after 3 hours at  $\lambda = 1.5$ , showing self-stabilization. At  $\lambda = 1.55$ , the nucleation of a new crack (at the crack tip) occurs and propagation leads to fracture after around 500 s, similar to fast fracture in Fig. 4.1(c).

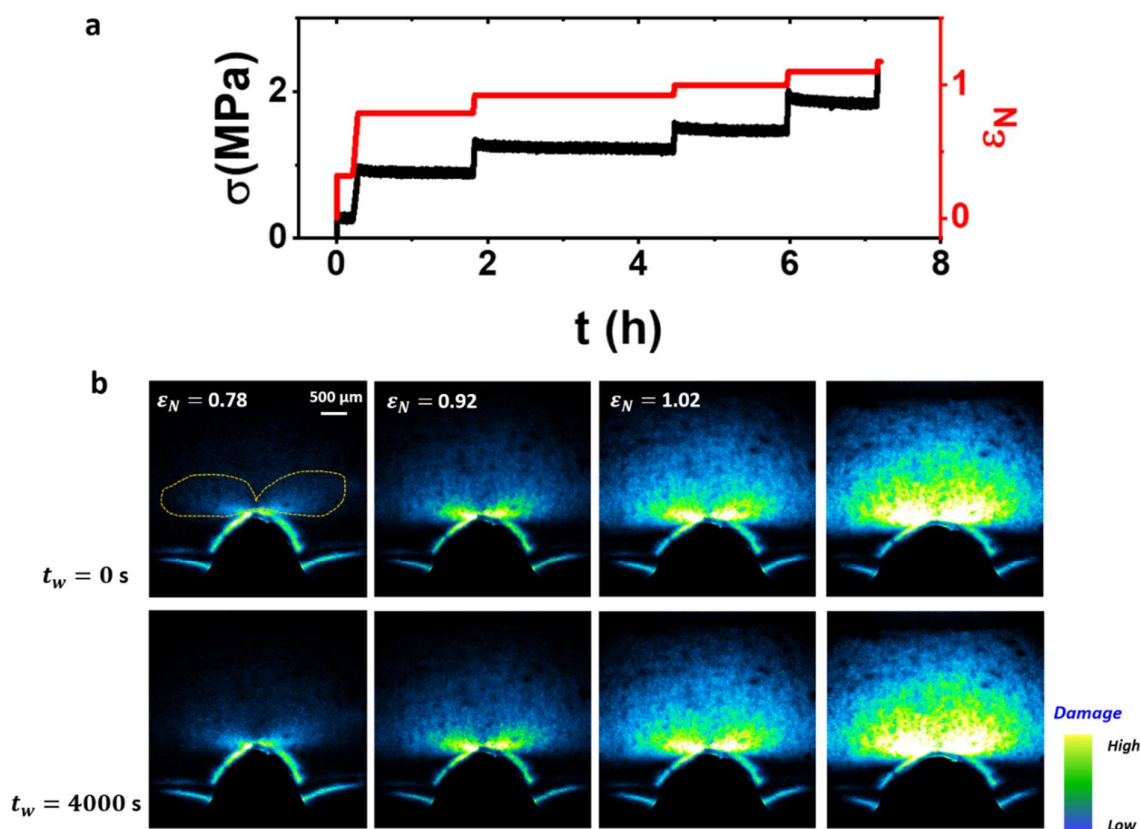


Fig. 4.6 (a) Stress-strain results as the function of time. (b) 2D damage map of TN at different  $\epsilon_N$ , right after stretching and after 4000 s of waiting.

It has been argued that delayed fracture occurs in elastomers via the progressive accumulation of undetectable damage.<sup>20,27</sup> As breakage of the sacrificial network takes place over a large scale in TN, the time dependent response of molecular damage can be quantified in our mechanophore labeled materials. A step-by-step stretching was

performed on a notched TN, by using a long waiting time (over an hour) after each stretching step to measure the response under fixed displacement. 4 steps of stretching to  $\lambda = 1.78, 1.92, 2.02$  and  $2.09$  were applied, as shown in Fig. 4.6(a). Crack growth only occurs at  $\lambda = 2.17$  during the last loading step from  $\lambda = 2.09$ . Fig. 4.6(b) shows the 2D damage map right after stretching ( $t_w = 0$  s) and at  $t_w = 4000$  s, for different value of applied stretch  $\lambda$ . The increase of the size and intensity of the damage region with  $\lambda$  can be clearly observed, similar to the case of continuous stretching in Fig. 4.2. At all  $\lambda$ , damage maps at  $t_w = 4000$  s are also slightly brighter than at  $t_w = 0$  s, showing the damage accumulation at fixed displacement. However, in hours of waiting at different  $\lambda$ , propagation is never observed. It is also confirmed by multiple experiments that in TN, even though a slight propagation can be observed during stretching at smaller  $\lambda$ , macroscopic propagation and fracture can only happen during continuous stretching (no delayed fracture at fixed stretch).

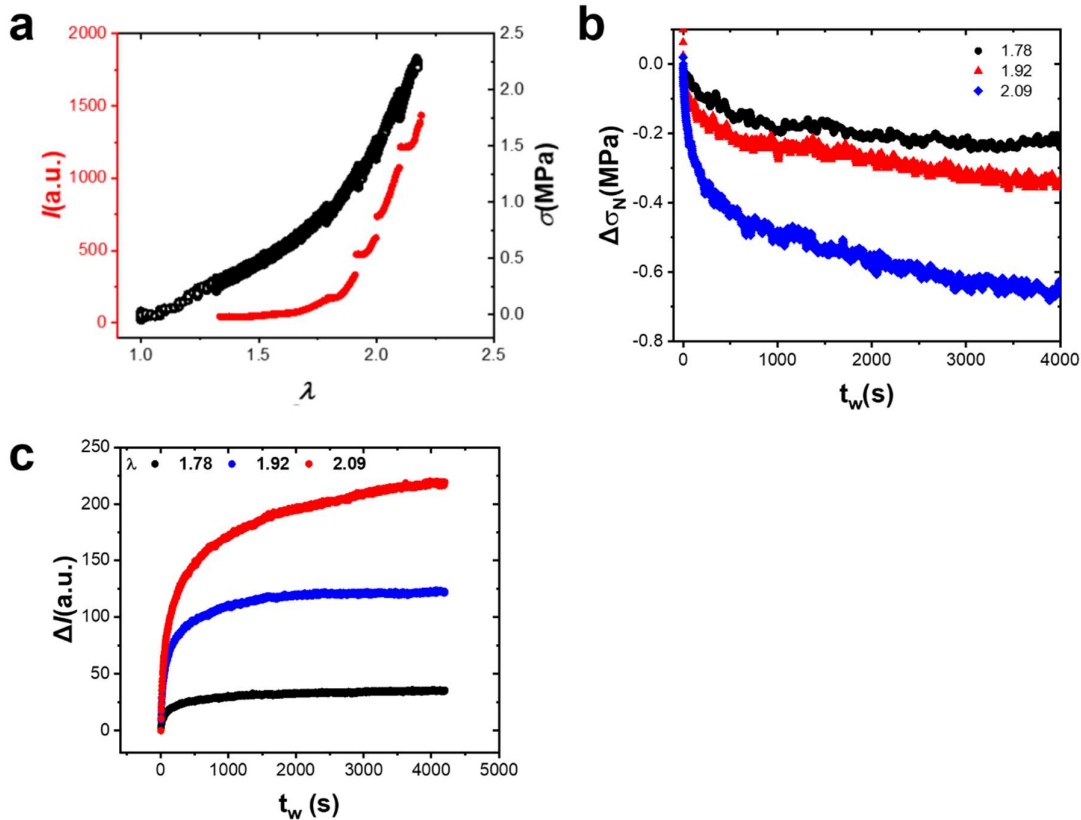


Fig. 4.7 (a) Stress and averaged fluorescence intensity calculated from the region indicated in Fig. 4.7(b), as the function of  $\lambda$  during stretching. (b) Stress reduction and (c) increase of fluorescence intensity ( $\Delta I$ ) as the function of waiting time ( $t_w$ ) after each stretching step.

The fluorescence intensity  $I$  averaged over an arbitrarily chosen region of interest around the crack (indicated in Fig. 4.6(b)) is characterized as a function of stretch and waiting time. Note that we use the same position of the ROI for different  $\lambda$ , as the position of the crack tip did not change much during deformation. Fig. 4.7(a) shows  $I$  during stretching (regardless of intensity change at fixed displacement) as a function of  $\lambda$ . Compared to bulk damage in unnotched samples (Fig. 4.2(a)), a detectable increase of fluorescence intensity around the crack starts at  $\lambda = 1.5$ , slightly earlier than the onset of strain hardening. At the beginning of each loading step to a higher value of  $\lambda$ , there is a plateau in fluorescence where crack is further opened without inducing more damage. This could be due to the relaxation occurring during the long waiting time, as seen with the slight decrease in stress of Fig. 4.7(b), where stress relaxation  $\Delta\sigma$  is the difference between measured  $\sigma$  and the stress right after loading at each step. In this way, the material has to be stretched a little more to further break bonds around the crack. The behavior is similar to what was observed in cyclic loading, where further breaking of molecular bonds can only be observed at a deformation higher than that of the previous cycle,<sup>1,28</sup> i.e. the so-called Mullins effect.<sup>29,30</sup> Between successive steps, there exists a gap of intensity, corresponding to the increase during the waiting time under fixed  $\lambda$ , as observed in Fig. 4.6(b). Damage accumulation kinetics during waiting time is indicated by an increase in intensity from initial value after stretching ( $\Delta I$ ) as a function of  $t_w$  at each  $\lambda$ , shown in Fig. 4.7(c). It is found that damage accumulates faster at larger  $\lambda$ , where at  $\lambda = 2.09$ , growth in 1000 s ( $\sim 200$  a.u.) is comparable to the absolute value ( $\sim 1000$  a.u.) in Fig. 4.7(a). For each step, damage rapidly increases in the first 500 s of wait and stabilizes later. After 1500 s. intensity remains almost constant.

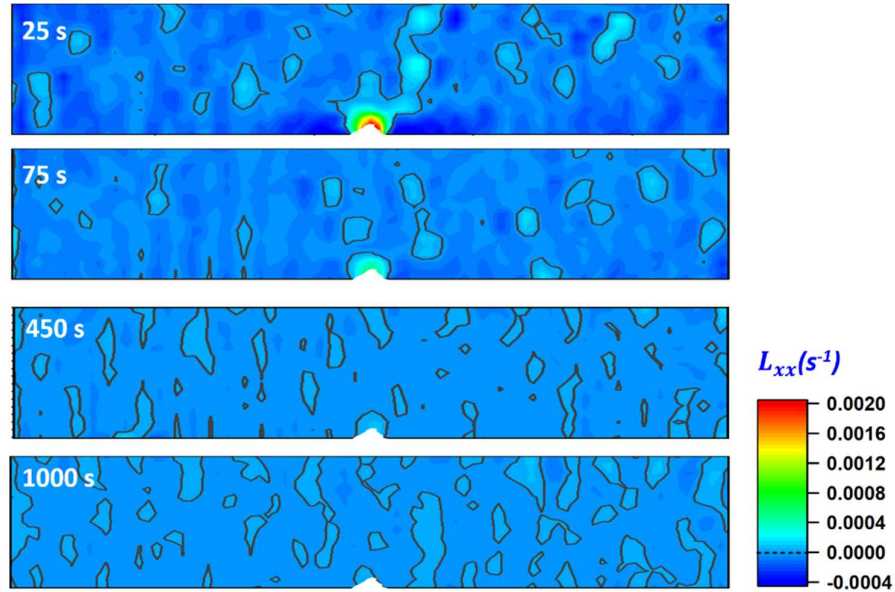


Fig. 4.8  $L_{xx}$  at different  $t_w$  for TN held at  $\lambda = 1.93$ . Black line indicates  $L_{xx} = 0$ .

The deformation map is also measured by DIC during  $t_w$  for TN (in a separate sample) at  $\lambda = 1.93$ . To highlight the subtle change, the velocity gradient tensor  $\mathbf{L}$  (see Chapter 3, supporting information) is calculated instead of  $\epsilon_{xx}$ , and  $L_{xx}$  (component along the stretching direction, see **Materials and methods**) is mapped in Fig. 4.8. At  $t_w = 25$  s, the region around the crack is further stretched ( $L_{xx} > 0$ ) without increasing  $\lambda$ , while far away from the crack, relaxation is dominating ( $L_{xx} < 0$ ) with only scattered stretched region, presumably due to the random molecular breakage in the bulk at large strain.<sup>19</sup> Similar to the damage kinetics from fluorescence intensity in Fig. 4.7 (c),  $L_{xx}$  is relatively fast at the beginning (reaching  $L_{xx} = 0.002$  s<sup>-1</sup> around the crack tip at  $t_w = 25$  s) and slows down with time. For  $t_w > 1000$  s, where damage barely increases, it is impossible to identify anymore the existence of a crack by monitoring the local values of  $L_{xx}$ . This indicates that the self-stabilization mechanism results in a homogeneous strain rate distribution in around 1000 s. Remarkably, the high level of  $L_{xx}$  concentration and slow down kinetics without crack propagation is only observable in TN, but not in SN and DN.

In addition to the DIC measurement provided in this section, MSDWS also provides a sensitive detection of microscopic motions (Chapter 3). We applied MSDWS to the delayed fracture of MNE, where motion below the time resolution of DIC and confocal microscopy can be detected, confirming our observation, as seen in the supporting

information.

Using damage/deformation maps at fixed displacement, we found from the combined damage accumulation kinetics (Fig. 4.7(c)) and strain rate evolution (Fig. 4.8) that the evolution of the existing damage at a fixed deformation has a self-stabilizing kinetics. Right after the cessation of the displacement step, the strain hardening of the materials as discussed in the fast fracture section (section 1.2), leads probably to a strong stress localization around the crack which naturally leads to a further stretching around the crack, with initially large values of  $L_{xx}$  in Fig. 4.8 and significant additional damage in Fig. 4.7. The interesting thing is that this additional damage (Figure 4.7c) and creep at the crack tip (Figure 4.8) is accompanied by an overall decrease of the stress (Figure 4.7b). On the other hand, it has been long known that the kinetics of creep increase with stress level.<sup>31-33</sup> Over long times, different creep kinetics homogenize the stress distribution and slow down both strain localization and damage accumulation, protecting TN from delayed fracture.

#### 4.4 Conclusion

Fracture resistance to both fast fracture and delayed fracture is tested in simple elastomers (SN) and MNE (DN and TN), respectively. With observation by confocal microscopy on mechanophore-labeled material, 3D damage maps before and during crack propagation are built in the open crack with micron resolution. Together with deformation mapping with DIC, we discovered that strain hardening in MNE provides a self-stabilizing mechanism and delocalizes the strain concentration over the surrounding region. As a result, the MNE shows an excellent resistance to crack growth, benefiting from a self-stabilization mechanism by stress rearrangement analogous to yielding.

In summary, the full scale observation of molecular damage and deformation distribution reveals the molecular level mechanism of fracture toughness enhancement in MNEs, where the contributions of molecular damage, strain concentration and stress concentration can be distinguished from each other. We push the understanding of flaw insensitivity beyond only a macroscopic mechanical description, showing that the inherent growth tendency of the flaw is mitigated by the strong non-linearity of the material. The discovery should be universal in different materials, but such a mechanism can only dominate in MNE, since the breakage of the sacrificial network in MNE reduces

the stress concentration at the crack tip and delays the propagation of the crack at large deformations. Yet the molecular criterion triggering propagation in the damaged zone remains elusive with the spatial and temporal resolution of our experiments.

## 4.5 Materials and methods

### 4.5.1 Synthesis of Poly (ethyl acrylate) multiple network elastomers

Single networks are synthesized by photo induced free radical polymerization. Ethyl acrylate monomer (purchased from TCI Chemicals, VWR or Sigma-Aldrich) is mixed with crosslinker 1,4-butanediol diacrylate (BDA, 0.5 mol%) and UV initiator 2-Hydroxy-2-methylpropiophenone (1.16 mol%). For sample labeled with mechanophores, the DielsAlder adduct mechanophore diacrylate cross-linker (DACL) synthesized in-house by a previously described method<sup>18</sup> is introduced (0.02 mol%). A customized mold is prepared with rectangular silicone frame (thickness 1 mm, length 8 cm and width 5 cm, with injection inlet), constrained between glass plates with PET films between silicone and glass. The mixture is injected into the mold and polymerized under UV (10  $\mu\text{m}/\text{cm}^2$ ) for 2 hours. After preparation, the elastomer is dried under vacuum and heated under 50  $^{\circ}\text{C}$  overnight. Initial thickness of SN is around 0.8 mm.

Double network is prepared by firstly swelling a single network in 40 g ethyl acrylate solvent, with crosslinker BDA (0.01 mol%), and initiator HMP (0.01 mol%), for 2 hours. Then the solvent in the swollen elastomer is polymerized under UV (10  $\mu\text{m}/\text{cm}^2$ ) for 2 hours. Triple network is made in a same way based on double network.

Elastomers are cut into rectangular samples with length (between the clamps) 15 mm and width 6 mm. Notches are made with razor blades with thickness of 0.1 mm. The ordinary manual cutting (pressing the blades on the surface of the sample) unavoidably creates initial massive activation of mechanophore and the crack profile is different along the thickness direction, as the elastomer is deformed upon cutting, especially for DN and TN. For an ordinary mechanical testing this effect can be ignored, while it interferes with the 3D damage visualization with micron resolution. To avoid the thickness dependent damage and crack profile, notches in DN and TN are made by approaching the sample perpendicularly onto a fixed razor with a speed of 0.05 mm/s and hold at cutting depth of 3 mm, to wait for the razor blade to break through the lateral surface. Even after breaking the surface, due to the friction and deformation, the notch length is not precisely controlled, but with an error within 0.5 mm. In this way, the notch length is around 1.5 mm, with less initial activation of mechanophore and relatively clear cut.



## 4.5.2 Confocal microscopy

A Nikon AZ-100/C2+ confocal microscope was used for the measurement, with the objective AZ Plan Fluor 5× (focal length of 15 mm). In confocal microscopy, depth-resolved images were collected with 14 slices (exposure time 4 s for each slice, depth-step: SN: 117 μm, DN: 130 μm and TN: 154 μm) for each scan, covering the total thickness of the material and one scan cycle is 60 s. The field size is 1.4 × 1.4 mm (objective: 3×) for SN, 2.8 × 2.8 mm (objective: 1.5×) for DN and 4.2 × 4.2 mm (objective: 1×) for TN, with total image size of 2048 × 2048 pixels. The wavelength of excitation and emission detection are 405 nm and 450 ~ 520 nm, respectively. With slices in one scan, 3D images can be generated and visualized here with maximum intensity projection to optimize the 3D feature in the image.<sup>34</sup>

## 4.5.3 Digital image correlation

Sample surface is prepared by spray painting. The surface is first brushed with white paint and sprayed with black ink. Images are collected by a CMOS camera (BASLER acA2000-340km). The bottom face of the sample is illuminated with an expanded green laser with wavelength of 532 nm. To avoid the interference of intensity fluctuation from excitation in confocal microscopy, a polarizer and a filter (only letting in green light) were applied before the camera to block the confocal laser. DIC is processed by the open resource program pyDIC, developed by Damien André.<sup>35</sup> Displacement and strain fields can be calculated from the analysis of successive images and added to obtain results in large strain. Results in this work are shown in the deformed configuration.

$\epsilon_{xx}$  can be directly calculated from DIC processing, with grid size 15 × 15 pixels (0.15 mm × 0.15 mm).  $L_{xx}$  at certain waiting time  $t_{w0}$  is calculated by  $\epsilon_{xx}$  from images  $t_{w0} - T$  to  $t_{w0} + T$  (using image at  $t_{w0} - T$  as reference state,  $T = 25$  s in Fig. 4.8):

$$L_{xx} = \frac{\epsilon_{xx}}{2T} \quad 4.1$$

## 4.6 Reference

- 1 Ducrot, E., Chen, Y. L., Bulters, M., Sijbesma, R. P. & Creton, C. Toughening Elastomers with Sacrificial Bonds and Watching Them Break. *Science* **344**, 186-

- 189, doi:10.1126/science.1248494 (2014).
- 2 Gong, J. P., Katsuyama, Y., Kurokawa, T. & Osada, Y. Double-network hydrogels with  
extremely high mechanical strength. *Advanced materials* **15**, 1155-1158 (2003).
- 3 Sun, J.-Y. *et al.* Highly stretchable and tough hydrogels. *Nature* **489**, 133-136 (2012).
- 4 Gong, J. P. Why are double network hydrogels so tough? *Soft Matter* **6**, 2583-2590  
(2010).
- 5 Chen, C., Wang, Z. & Suo, Z. Flaw sensitivity of highly stretchable materials. *Extreme  
Mechanics Letters* **10**, 50-57, doi:10.1016/j.eml.2016.10.002 (2017).
- 6 Gao, H., Ji, B., Jäger, I. L., Arzt, E. & Fratzl, P. Materials become insensitive to flaws at  
nanoscale: lessons from nature. *Proceedings of the national Academy of Sciences*  
**100**, 5597-5600 (2003).
- 7 Gong, J. P. Why are double network hydrogels so tough? *Soft Matter* **6**,  
doi:10.1039/b924290b (2010).
- 8 Zhao, X. Designing toughness and strength for soft materials. *Proc Natl Acad Sci U  
S A* **114**, 8138-8140, doi:10.1073/pnas.1710942114 (2017).
- 9 Matsuda, T., Kawakami, R., Namba, R., Nakajima, T. & Gong, J. P. Mechanoresponsive  
self-growing hydrogels inspired by muscle training. *Science* **363**, 504-508 (2019).
- 10 Lake, G. & Thomas, A. The strength of highly elastic materials. *Proceedings of the  
Royal Society of London. Series A. Mathematical and Physical Sciences* **300**, 108-119  
(1967).
- 11 Matsuda, T., Kawakami, R., Nakajima, T. & Gong, J. P. Crack tip field of a double-  
network gel: Visualization of covalent bond scission through mechanoradical  
polymerization. *Macromolecules* **53**, 8787-8795 (2020).
- 12 Hui, C.-Y., Bennison, S. & Londono, J. Crack blunting and the strength of soft elastic  
solids. *Proceedings of the Royal Society of London. Series A: Mathematical, Physical  
and Engineering Sciences* **459**, 1489-1516 (2003).
- 13 Creton, C. & Ciccotti, M. Fracture and adhesion of soft materials: a review. *Rep Prog  
Phys* **79**, 046601, doi:10.1088/0034-4885/79/4/046601 (2016).
- 14 Brown, H. R. A model of the fracture of double network gels. *Macromolecules* **40**,  
3815-3818 (2007).
- 15 Gostl, R. & Sijbesma, R. P. pi-extended anthracenes as sensitive probes for  
mechanical stress. *Chem Sci* **7**, 370-375, doi:10.1039/c5sc03297k (2016).
- 16 Chen, Y., Mellot, G., van Luijk, D., Creton, C. & Sijbesma, R. P. Mechanochemical tools  
for polymer materials. *Chemical Society Reviews* **50**, 4100-4140 (2021).
- 17 Stratigaki, M. *et al.* Fractography of poly (N-isopropylacrylamide) hydrogel  
networks crosslinked with mechanofluorophores using confocal laser scanning  
microscopy. *Polymer Chemistry* **11**, 358-366 (2020).
- 18 Slooman, J. *et al.* Quantifying Rate- and Temperature-Dependent Molecular  
Damage in Elastomer Fracture. *Physical Review X* **10**,  
doi:10.1103/PhysRevX.10.041045 (2020).
- 19 Millereau, P. *et al.* Mechanics of elastomeric molecular composites. *Proceedings of  
the National Academy of Sciences* **115**, 9110-9115 (2018).
- 20 Tang, J., Li, J., Vlassak, J. J. & Suo, Z. Fatigue fracture of hydrogels. *Extreme Mechanics  
Letters* **10**, 24-31, doi:10.1016/j.eml.2016.09.010 (2017).
- 21 Chen, Y., Yeh, C. J., Qi, Y., Long, R. & Creton, C. From force-responsive molecules to  
quantifying and mapping stresses in soft materials. *Science advances* **6**, eaaz5093  
(2020).
- 22 Mai, T.-T., Okuno, K., Tsunoda, K. & Urayama, K. Crack-Tip Strain Field in Supershear  
Crack of Elastomers. *ACS Macro Letters* **9**, 762-768,

- doi:10.1021/acsmacrolett.0c00213 (2020).
- 23 Liu, M., Guo, J., Hui, C. Y. & Zehnder, A. T. Application of Digital Image Correlation (DIC) to the Measurement of Strain Concentration of a PVA Dual-Crosslink Hydrogel Under Large Deformation. *Experimental Mechanics*, doi:10.1007/s11340-019-00520-4 (2019).
- 24 Scetta, G. *et al.* Self-Organization at the Crack Tip of Fatigue-Resistant Thermoplastic Polyurethane Elastomers. *Macromolecules* (2021).
- 25 Brown, H. A molecular interpretation of the toughness of glassy polymers. *Macromolecules* **24**, 2752-2756 (1991).
- 26 Wang, X. & Hong, W. Delayed fracture in gels. *Soft Matter* **8**, doi:10.1039/c2sm25553g (2012).
- 27 van der Kooij, H. M. *et al.* Laser Speckle Strain Imaging reveals the origin of delayed fracture in a soft solid. *Science advances* **4**, eaar1926 (2018).
- 28 Clough, J. M., Creton, C., Craig, S. L. & Sijbesma, R. P. Covalent Bond Scission in the Mullins Effect of a Filled Elastomer: Real-Time Visualization with Mechanoluminescence. *Advanced Functional Materials* **26**, 9063-9074, doi:10.1002/adfm.201602490 (2016).
- 29 Webber, R. E., Creton, C., Brown, H. R. & Gong, J. P. Large strain hysteresis and mullins effect of tough double-network hydrogels. *Macromolecules* **40**, 2919-2927 (2007).
- 30 Diani, J., Fayolle, B. & Gilormini, P. A review on the Mullins effect. *European Polymer Journal* **45**, 601-612 (2009).
- 31 Blum, W. & Eisenlohr, P. Dislocation mechanics of creep. *Materials Science and Engineering: A* **510**, 7-13 (2009).
- 32 Throdahl, M. Aging of Elastomers. Comparison of Creep with Some Conventional Aging Methods. *Rubber Chemistry and Technology* **22**, 699-711 (1949).
- 33 Aso, O., Eguiazabal, J. & Nazabal, J. The influence of surface modification on the structure and properties of a nanosilica filled thermoplastic elastomer. *Composites science and technology* **67**, 2854-2863 (2007).
- 34 Mroz, L., Hauser, H. & Gröller, E. in *Computer Graphics Forum*. 341-350 (Wiley Online Library).
- 35 André, D. <<https://gitlab.com/damien.andre/pydic>> {
- 36 Pine, D. J., Weitz, D. A., Zhu, J. X. & Herbolzheimer, E. Diffusing-wave spectroscopy: dynamic light scattering in the multiple scattering limit. *Journal de Physique* **51**, 2101-2127, doi:10.1051/jphys:0199000510180210100 (1990).
- 37 Pine, D. J., Weitz, D. A., Chaikin, P. M. & Herbolzheimer, E. Diffusing wave spectroscopy. *Phys Rev Lett* **60**, 1134-1137, doi:10.1103/PhysRevLett.60.1134 (1988).

## 4.7 Supporting Information

### **Dynamics measurement by multiple speckle diffusing wave spectroscopy (MSDWS)**

MSDWS is also applied to poly(ethyl acrylate) elastomers to study the temporally and spatially resolved dynamics, at fixed displacement, similar to section 4.3. We do not fully understand the results but provide the information for the future work.

#### 4.7.1 Material preparation and measurement methods

Before polymerization of SN, titanium dioxide (TiO<sub>2</sub>) nanoparticles (diameter 250 nm, 1 wt%) was mixed with ethyl acrylate monomer inside the glovebox under controlled atmosphere. The mixture was sealed and sonicated for 10 min to avoid aggregation. After mixing with nanoparticles, we performed the polymerization and swelling in the same method as described in the main text. The obtained SN containing nanoparticles were used to synthesize DN and TN, without further addition of nanoparticles.

MSDWS measurement is performed simultaneously with confocal testing, with the same protocol as section 3.3.1.

#### 4.7.2 Difficulties in dynamics measurement

Let us comment on experimental difficulties during sample preparation with the nanoparticles and measurements. During preparation and the early stage of UV polymerization, dramatic sedimentation of the inorganic nanoparticles is observed. This is due to the high density of TiO<sub>2</sub> nanoparticles and the low viscosity of the ethyl acrylate monomer. We had much less pronounced sedimentation for PDMS elastomer in Chapter 3, as the PDMS base is more viscous. Also, the change in the number density  $N$  of the particles in DN and TN elastomers is significant as the volume is increasing during swelling. The ratio of sample thickness  $L$  and  $l^*$  (transport mean free path)<sup>36</sup> is commonly applied to examine the scattering condition ( $L/l^* \gg 1$  for ideal multiple scattering). In single network,  $l^*_{SN}$  has the relationship with  $N$ , which only depends on the preparation of SN:<sup>37</sup>

$$l_{SN}^* = \frac{1}{N\sigma} \quad 1$$

where  $\sigma$  is the scatter cross-section, considered constant. As the elastomer goes through isotropic swelling with swelling ratio is  $\lambda_0^3$  (1D pre-stretch ratio  $\lambda_0$ ), we have:

$$\frac{L}{l^*} = \frac{N\sigma\lambda_0 L}{\lambda_0^3} = \frac{1}{\lambda_0^2} \frac{L}{l_{SN}^*} \quad 2$$

It can be found that in the multiple network, scattering is approaching to single scattering condition (smaller  $L/l^*$ ) as increasing  $\lambda_0$ . As a result, the samples of DN and TN exhibit less opacity visible in naked eyes. The combined effect of sedimentation and pre-stretch in MNE largely reduced the volume concentration of nanoparticle, so that the light scattering is not ideal multiple scattering. In a continuous stretching condition, measured dynamics is not only contributed by strain rate (see chapter 2).

The swollen network with embodied particles with fixed size may also generate external void around the particles, which may lead to additional dynamics measured from DWS. At fixed displacement, relaxation, propagation and the unknown interaction with the swollen may all be detectable by MSDWS during measurement.

### 4.7.3 Dynamic behavior before delayed fracture

In the simultaneous measurement of confocal microscopy and MSDWS, we mainly studied delayed fracture behavior, since it provides an ideal condition for damage visualization. Sample is loaded to different strains and held for a long time for observation.

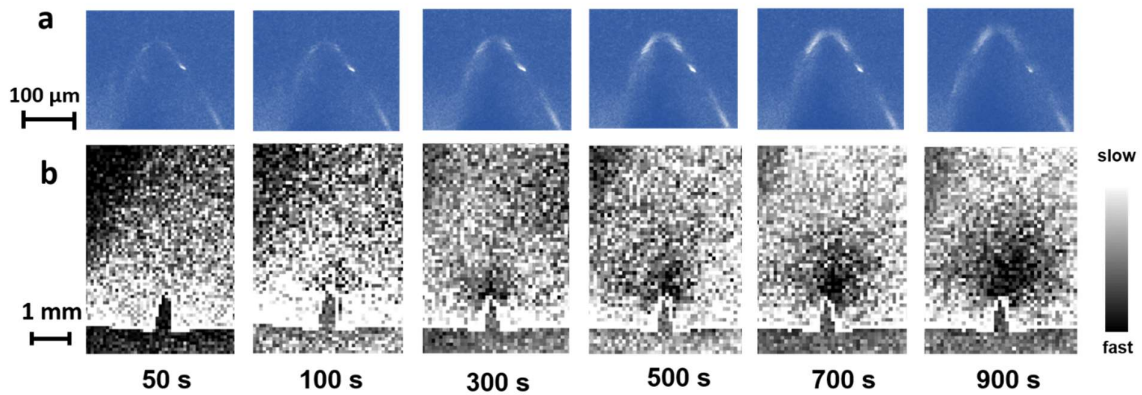


Fig. 4.S1 Imaging of a SEN SN sample under tension. (a) Crack propagation and damage around the tip, measured by confocal microscopy. (b) Dynamic activity map (DAM) during the crack propagation.

Fig. 4.S1 (a) shows the activation intensity measured by confocal microscopy, in SN held at  $\lambda = 1.15$ . Slow propagation is observed, with a slightly increasing intensity. For MSDWS, the spatially resolved dynamics can be quantified from the autocorrelation function of the multiply scattered light intensity (see details in section 3.3.2):

$$C_I(\vec{r}, t, \tau) = \frac{\langle I_p(t)I_p(t+\tau) \rangle_{\vec{r}}}{\langle I_p(t) \rangle_{\vec{r}} \langle I_p(t+\tau) \rangle_{\vec{r}}} - 1 \quad 3$$

where  $I_p$  is the intensity in the image at  $p$ -th pixel.  $t$  and  $\tau$  are experimental time and time interval for correlation, respectively.  $\langle \dots \rangle_{\vec{r}}$  indicates the ensemble average in the region with center position  $\vec{r}$ . Characteristic time  $\tau_0$  can be fitted from autocorrelation function at fixed time and position from:

$$C_I(\tau) = A \exp\left(-2\gamma \sqrt{\left(\frac{\tau}{\tau_0}\right)^p + a} + 2\gamma \sqrt{a}\right) + B \quad 4$$

A smaller  $\tau_0$  corresponds to faster decorrelation, so faster dynamics. Before discussing the dynamics around the crack, it is necessary to characterize the dynamics of the bulk of the material (far from the crack) which exhibit relaxation and influences the dynamics around the crack. In Fig.4.S2, the fitted characteristic time  $\tau_0$  in the bulk (the corresponding ROI is shown as the red rectangle) is plotted as a function of the waiting time  $t_w$ .  $\tau_0$  increases with  $t_w$  almost linearly, and no stabilization is observed at the studied  $t_w$ , corresponding to the continuous slowing down of the bulk dynamics.

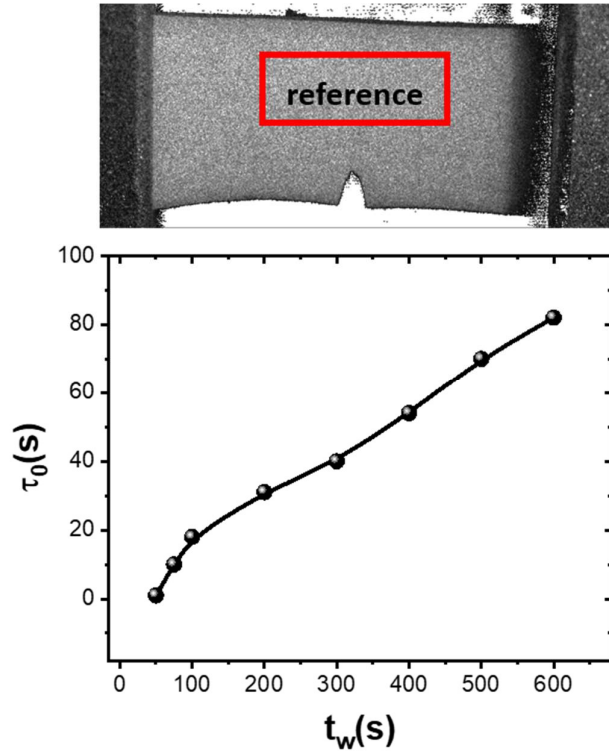


Fig. 4.S2  $\tau_0$  fitted from reference region in the bulk.

Dynamic activity maps (DAMs) are built by converting the correlation value at fixed  $\tau$  ( $T_{MSDWS}$ ) into greyscale and the lower intensity in DAM corresponds to faster dynamics. In the DAM of the SEN SN sample (Fig. 4.S1(b)), to separate the dynamics change due to the crack tip behavior from bulk dynamics, we used the fitted characteristic time  $\tau_0$  in the bulk (Fig. 4.S2) as  $T_{MSDWS}$  in Fig.4.S1(b). In this way, we used the bulk dynamics as a reference and estimated the area having faster dynamics than the bulk (thus activated by local damage). Note that the slowing down dynamics in Fig. 4.S2 is not due to the change of strain rate as discussed in Chapter 2, but unknown effect of relaxation. Fast dynamics (lower intensity) in DAMs can be detected with initial size around  $1 \text{ mm}^2$  ( $t = 300 \text{ s}$ ) and grows to around  $8 \text{ mm}^2$  at  $t = 900 \text{ s}$ . By comparing this result to those of the PDMS elastomer (Chapter 3), we conclude that the propagation and fracture in SN is similar to that in simple elastomers.

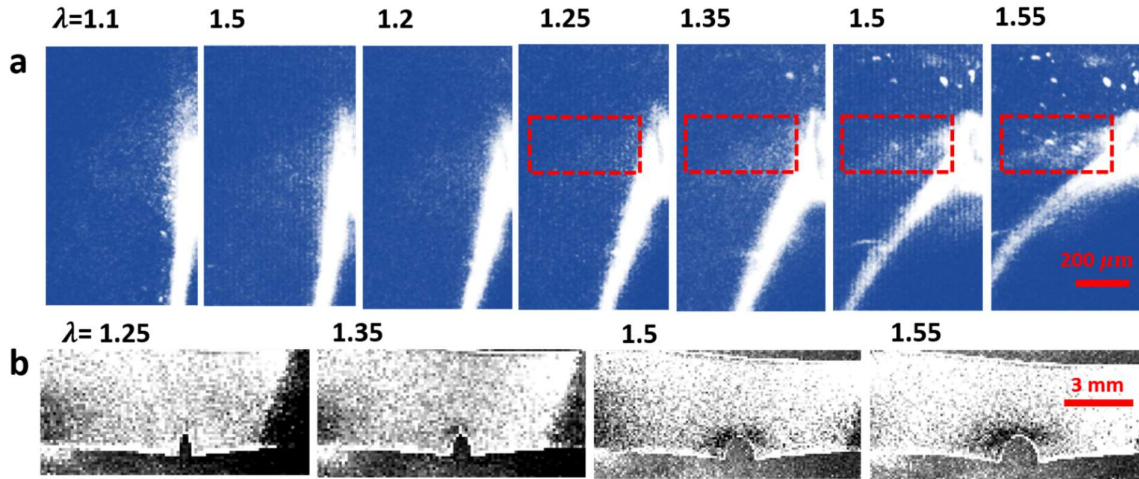


Fig. 4.S3 Imaging of a SEN DN sample under tension. (a) Fluorescence image around the crack tip at different stretch ratio, measured by confocal microscopy. (b) Dynamic activity map (DAP) at different stretch ratio, with  $T_{MSDWS} = 15$  s (see section 3.3.2).

Fig. 4.S3 (a) shows the activation intensity measured by confocal microscopy in the DN, right after stretching for different  $\lambda$  ( $t_w = 0$ ). A stronger activation can be detected with increasing  $\lambda$  and a slow propagation as in Fig. 4.5 is detected at  $\lambda = 1.55$ . More damage in the sacrificial network results in a permanent faster dynamics around the crack, as seen in DAMs right after stretching in Fig. 4.S3(b). The faster dynamics does not evolve with time but the size increases with applied strain, corresponding to the increasing activation due to damage in Fig. 4.S3(a). *Strangely, this effect is not observable in TN, where more damage is induced in the material.* As propagation at fixed displacement starts from a relative fast speed (Fig. 4.5), MSDWS does not provide important information on delayed fracture behavior.

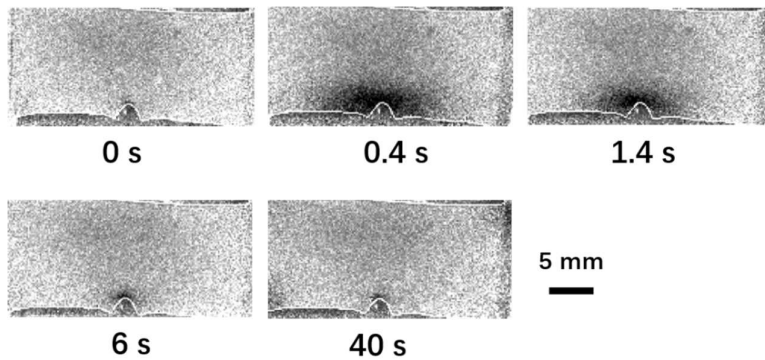


Fig. 4.S4 Transient dynamics in DN, takes place in 40 s, at  $\lambda = 1.4$ , with  $T_{MSDWS} = 0.4$  s.



As seen in Fig. 4.5, crack propagates step-by-step at  $\lambda = 1.55$  for DN. Interestingly, a similar behavior can be observed at much lower  $\lambda$ , but in terms of a change in transient dynamics instead of a detectable propagation. As seen in Fig. 4.S4, transient and fast dynamics are observed over a period around 40 s at  $\lambda = 1.4$  in DN. At 0.4 s (relative time), the high dynamics area peaks at around 30 mm<sup>2</sup> and slows down rapidly. At  $t = 40$  s, DAM is almost the same as  $t = 0$  s, with only slight activation due to permanent damage. During the whole observation period of 40 s, there is no propagation and change in fluorescence intensity detectable in confocal microscopy. Relating to the propagation behavior at larger strain, we can attribute these transient dynamics to undetectable damage/propagation below our resolution.

For TN, because of the self-stabilization mechanism at fixed displacement, MSDWS does not provide more information than DIC shown in Fig. 4.8. No transient dynamics change is detected during the whole experiment, confirming our conclusion that the tendency of further damage or propagation is constrained in TN, with a more sensitive detection by MSDWS.

---

Chapter 5 Heterogeneous creasing and swelling in  
constrained hydrogel film

## 5 Heterogeneous creasing and swelling in constrained hydrogel film

Jianzhu Ju <sup>a</sup>, Ken Sekimoto <sup>b,c</sup>, Luca Cipelletti <sup>d,e</sup>, Costantino Creton <sup>a,f</sup>, Tetsuharu Narita <sup>\*,a,f</sup>

<sup>a</sup> Sciences et Ingénierie de la Matière Molle, CNRS UMR 7615, ESPCI Paris, PSL Université, Paris, France

<sup>b</sup> Gulliver, CNRS-UMR7083, ESPCI, 75231 Paris, France

<sup>c</sup> Matières et Systèmes Complexes, CNRS-UMR7057, Université Paris-Diderot, 75205 Paris, France

<sup>d</sup> Laboratoire Charles Coulomb (L2C), University of Montpellier, CNRS, Montpellier, France

<sup>e</sup> Institut Universitaire de France

<sup>f</sup> Global Station for Soft Matter, Global Institution for Collaborative Research and Education, Hokkaido University, Sapporo, Japan

### Abstract

Surface creasing is a common occurrence in gels under strong enough compression. The transition from smooth to creased surface has been well-studied in equilibrium condition and applied to achieve stimuli-responsive properties. Classical predictions of the creased state, assuming the gel is at equilibrium and homogeneous, are generally satisfactory, while the transient behavior in swelling gel is often far from equilibrium and is commonly heterogeneous. Short time response is essential for the materials in dynamic environments, but so far unreported and largely unknown due to limited resolution. Here, spatially resolved multi-speckle diffusing wave spectroscopy (MSDWS) with sub-microsecond time resolution is used to measure the spatially dependent swelling and creasing of a constrained poly(vinyl alcohol) (PVA) chemical gel in salt solutions of varying concentrations. Our high speed imaging by MSDWS shows that the swelling

---

\*correspondence authors: [tetsuharu.narita@espci.fr](mailto:tetsuharu.narita@espci.fr)

behavior and mechanical response can be highly heterogeneous in time and space, detectable at thousands of seconds before corresponding creasing transition. This unprecedented visualization of the heterogeneous and time-dependent behavior beyond equilibrium morphological changes unveils the full complexity of the transient material responses after exposure to external stimuli and could provide keys to understand the formation mechanism of metastable states in dynamic processes.

## 5.1 Introduction

When a gel is under strong enough compression, periodical surface creasing (singular regions formed in a sharp folding) is commonly generated as the result of buckling instabilities, as schematically shown in Fig. 5.1(a).<sup>1,2</sup> Similar phenomenon can be observed in lots of natural living creatures with very different scales, as seen in Fig. 5.2 (b).<sup>3</sup> The mathematical significance of the mechanical instability induced pattern has attracted many theoretical and experimental investigations aiming at understanding its topological nature<sup>3,4</sup> and mechanical origins.<sup>2,5-7</sup> Recently, the stimuli-responsive nature of surface buckling has been used advantageously to design tunable surface morphology and property.<sup>8-10</sup> As creasing can be well controlled by different stimuli such as temperature<sup>8,11</sup>, external deformation<sup>6,12</sup> and pH<sup>13</sup>, the practical performance of the functionalized surface pattern is essentially limited by the time scale of the dynamic response when exposed to external stimuli.<sup>14,15</sup> While for the creasing behavior in a static condition equilibrium models have successfully described the critical nucleation condition<sup>16,17</sup> and growth kinetics of creasing<sup>18,19</sup>, there are many open questions concerning the transient behavior during the creasing transition; in particular, the possible existence and life time of metastable states may be important for the design of properties and practical application of the materials.

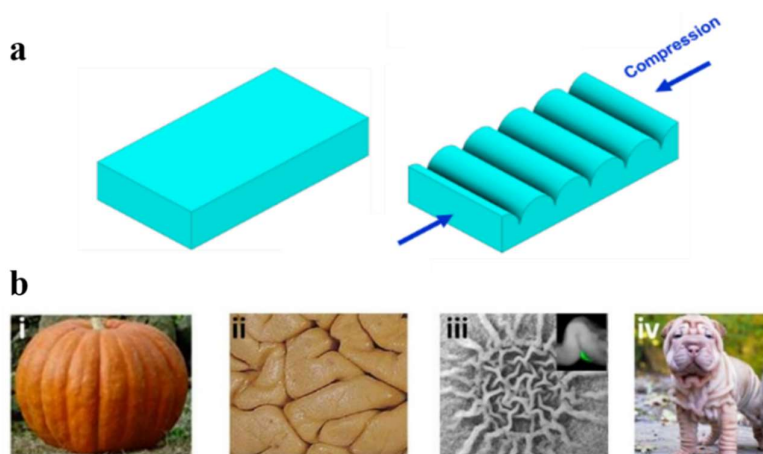


*Fig. 5.1 (a) Schematic of surface creasing in a compressed gel. (b) Surface buckling instability in living creatures.*

In a well-defined condition where the swollen gel film adheres to a rigid substrate, lateral deformation is limited by the substrate so that swelling leads to an equibiaxial compression, which commonly causes surface creasing.<sup>2,17</sup> Equilibrium models typically assume that the gel remains homogeneous and at mechanical equilibrium without stress gradients ( $\partial\sigma/\partial x = 0$ ).<sup>20,21</sup> With measurements of the crease morphology at the swelling equilibrium, the critical creasing condition can be related to the equilibrium swelling ratio  $\alpha_\infty$  (ratio of final and initial weight of the gel).<sup>5,17,22</sup> For creases generated during transient swelling, i.e. well before reaching  $\alpha_\infty$ ,<sup>2,18,23-25</sup> the nucleation and growth of creases is considered to depend on swelling kinetics, which is only governed by cooperative diffusion of water.<sup>18,19,26</sup>

While at equilibrium, experiments are in agreement with both theoretical analysis<sup>11,18,22</sup> and simulations<sup>1,5</sup>, the transient state before reaching equilibrium is rarely discussed. Remarkably, it has been reported that surface creasing is a subcritical process where the critical condition can deviate dramatically from the equilibrium condition due to energy barriers,<sup>27,28</sup> such as surface energy<sup>5,11</sup>, inelasticity<sup>27,29</sup> and interactions with the substrate<sup>30</sup>. At the onset of creasing, the selective folding of the surface indicates the existence of the structural frustration and heterogeneity before macroscopic creasing sets in, where local stability is sacrificed to benefit global stability. During the transient metastable state, the nucleation of creasing and swelling kinetics cannot be simply predicted by the quasi-static models.<sup>23,31,32</sup> The swelling and creasing kinetics are controlled by the equilibrium final state ( $\alpha_\infty$ ), which itself changes with compression level.<sup>21,33</sup> To describe the creasing transition in a modified model that includes heterogeneity and transient kinetics during creasing, a method with both spatial and temporal resolution is required.

As an extended method of dynamic light scattering, multi-speckle diffusing wave spectroscopy (MSDWS)<sup>34,35</sup> detects the decorrelation of light multiply scattered by a small amount of probe particles embedded in the sample, providing a good tool to observe spatially and temporally resolved microscopic response during dynamic transitions.<sup>36,37</sup> As a first step, a relative simple condition is studied, where creasing is induced during the one-dimensional (1D) swelling of a constrained hydrogel before reaching swelling equilibrium. A common strategy to tune the swelling ratio and kinetics is to adjust the cross-linker concentration, while it inevitably also changes significantly the initial elastic

modulus,<sup>17,22</sup> modifying an important system parameter.<sup>22,38</sup> In this work, swelling is induced and tuned by the introduction of charges in a neutral chemical gel by complexation. In-situ measurement with MSDWS shows that creasing process in dynamic swelling contains a subcritical nucleation period where swelling and creasing is spatially heterogeneous and deviates from kinetics described by diffusion equation, showing the existence of long-lived metastable states. Contrary to common knowledge, rich heterogeneous behaviors happen at different temporal/spatial scales, both before and during creasing, which cannot be detected with ordinary method. Fast dynamics measurement by MSDWS supplements the transient behavior during the generation of responsive surface pattern, which also provides a tool for the investigation of general dynamic process.

## 5.2 Material and methods

### 5.2.1 Gel preparation and swelling

We use a well-known system comprising poly(vinyl alcohol) (PVA) and borate ions (generated by dissolution of sodium tetraborate, borax), and different borax concentrations ( $C_b$ ) are applied to tune the swelling kinetics and to induce a large increase in the equilibrium swelling ratio.<sup>39,40</sup> PVA with weight-averaged molecular weight of 89 000–98 000 g/mol and glutaraldehyde (GA) cross-linker were purchased from Aldrich. PVA powder was dissolved in deionized water at 90 °C and stirred over 10 hours at a concentration of 8.8 wt%, as a stock solution. A chemically cross-linked PVA hydrogel was prepared in an aqueous mixture with PVA (4.4 %), GA (5 mM), and hydrochloric acid (HCl, 0.05 mM). Prior to the gelation, polystyrene nanoparticles (from Micromod, diameter: 500 nm, concentration: 1 %) were added as probe for MSDWS measurements.

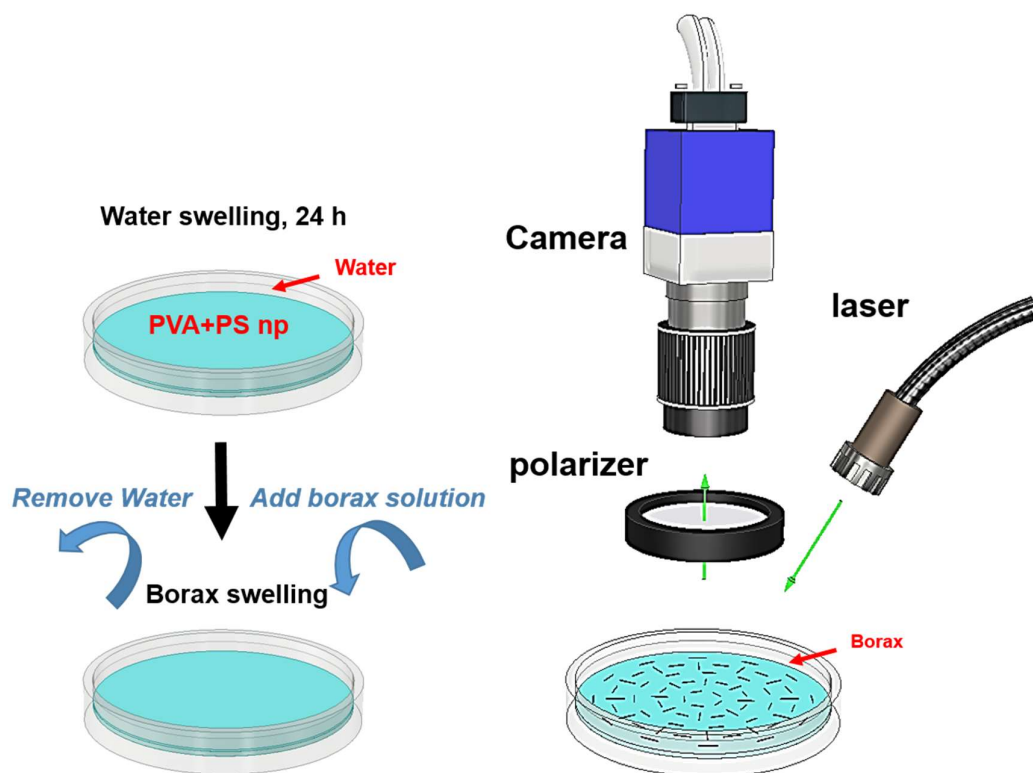


Fig. 5.2 Sample preparation and in-situ measurement of constrained swelling.



The preparation and measurement process are shown in Fig. 5.2. 4 ml of solution before chemical cross-linking was poured into a round plastic petri dish with a radius of 55 mm, giving a solution thickness of 1.68 mm. The solution was then sealed for 10 h for the PVA chemical cross-linking to occur. Then the chemical gel was washed in pure water for 24 h to remove the HCl. HCl acts as a catalyst for chemical cross-linking but cannot coexist with  $B(OH)_4^-$ .<sup>41</sup> During the washing step, the PVA gel slightly swells (to  $\alpha = 1.1$  and  $H = 1.85$  mm) while no surface morphology change was observed. In order to further swell the gel and induce the surface morphology change, the gel was immersed in a solution of borax (sodium tetraborate, from Aldrich) with different concentrations (0.2 ~ 10 mM). Borate ions diffuse into the gel and make a didiol complex with the hydroxyl groups on the PVA chains. The same molarity of sodium ions as counterions also diffuses into the gel for electroneutrality, inducing the gel swelling due to the osmotic pressure. The thickness of the gel ( $H=1.85$  mm) is much smaller than its radius (55 mm) and the gel adheres to the surface of the plastic petri dish, thus the gel swelling is one dimensional, along the thickness direction. Swelling ratios  $\alpha$  can be measured from the ratio of measured weight  $m$  and initial weight  $m_0$ , which is also the thickness ratio ( $\alpha = \frac{m}{m_0} = \frac{H}{H_0}$ ).

## 5.2.2 Data collection and processing

### 5.2.2.1 Image collection

MSDWS was performed during the complexation and swelling of the chemical gel. The whole gel surface was illuminated homogeneously with a divergent laser beam with a wavelength of 532 nm, as shown in Fig. 5.2. Speckle images were collected by a CMOS camera (BASLER acA2000-340km) equipped with a polarizer. The polarizer axis was oriented so as to reject the singly scattered light. Time resolution was set in different scales from 5 to 300 ms and the pixel size corresponded to 32  $\mu\text{m}/\text{pixel}$  in the sample, with image size of 2048x1088 pixels. The exposure time of a raw image was 3 ms to optimize the time resolution and speckle appearance. For the observation of the fast dynamics at the scale of around 0.1 ms, a fast camera (Photron FASTCAM SA3) was used with a frame rate of 6000 frames per second and a pixel size of 125  $\mu\text{m}/\text{pixel}$  in the sample, with image size of 512  $\times$  512 pixels.

### 5.2.2.2 Fitting of the autocorrelation function

In the backscattering geometry, MSDWS analyzes the temporal fluctuations of the backscattered light. To extract the spatial and temporal dynamics information during the swelling, a spatially and temporally resolved intensity autocorrelation function  $C(\vec{r}, t, \tau)$  is calculated:

$$C(\vec{r}, t, \tau) = \frac{\langle I_p(t)I_p(t+\tau) \rangle_{\vec{r}}}{\langle I_p(t) \rangle_{\vec{r}} \langle I_p(t+\tau) \rangle_{\vec{r}}} - 1 \quad 5.1$$

where  $I_p$  is the intensity of the  $p$ -th pixel, and  $\langle \dots \rangle_{\vec{r}}$  designates an average over pixels belonging to a small region centered around position  $\vec{r}$ .  $t$  is the time after swelling and  $\tau$  is the time delay. At fixed  $t$  and  $\vec{r}$ , the autocorrelation function can be expressed in an exponential form as a function of  $\tau$ :<sup>42,43</sup>

$$C(\tau) = A \exp \left( -2\gamma \sqrt{\left( \frac{\tau}{\tau_0} \right)^2 + a} \right) + B \quad 5.2$$

$\gamma$  is a coefficient depending on the polarization condition of the incident/detected light. In our experiments, a polarizer is applied to remove the singly scattered light so that we used  $\gamma = 2.7$ .<sup>44,45</sup>  $a$  is determined by the ratio between the transport mean free path  $l^*$ <sup>34</sup> and gel thickness.<sup>42,43</sup> By using the measurement of a slower swelling as a reference,  $a$  is set to 0.015.  $\tau_0(t)$  corresponds to the time over which the probe particles are displaced by a distance of the order of 50 nm ( $1/k$ ).  $k$  is the wave vector of the incident light ( $k = 2\pi n/\lambda$ ,  $\lambda = 532$  nm,  $n = 1.4$  is the index of refraction).<sup>46</sup>

The measured dynamics probed by the decorrelation of the backscattered light can be due to a number of different mechanisms.<sup>47,48</sup> The affine deformation field during swelling is expected to result in microscopic ballistic motion<sup>45,49</sup> while the disturbance due to compression and local heterogeneity may lead to an additional non-affine contribution to the displacement of the particles<sup>47,48,50,51</sup>. In the case where the time scales of different contributions overlap with each other, the analysis becomes rather complex.<sup>47,48</sup> Fortunately, although the time scale of additional non-affine contributions is unknown, the relationship between the time scale of the ballistic dynamics and the affine deformation rate is well studied.<sup>45,48</sup> For a purely affine deformation with no additional dynamics, the autocorrelation function can be related to the strain field by:<sup>42,43</sup>

$$C(\tau) = A \exp\left(-2\gamma\sqrt{3k^2l^{*2}f[U(\tau)] + a}\right) + B \quad 5.3$$

where  $f[U(\tau)]$  is a function of the deformation tensor  $U$ :  $f[U] = [Tr^2(U) + 2Tr(U^2)]/15$ . For 1D swelling under lateral confinement one has:

$$U(\tau) = \begin{bmatrix} 0 & 0 & 0 \\ 0 & 0 & 0 \\ 0 & 0 & \dot{\alpha}_{DWS}\tau \end{bmatrix} \quad 5.4$$

with  $\dot{\alpha}_{DWS}$  is the swelling rate  $\left(\frac{\partial\alpha}{\partial t}\right)$  measured by MSDWS. Hence,  $f[U] = (\dot{\alpha}_{DWS}\tau)^2/5$ ;<sup>45</sup> inserting  $\tau = \tau_0 = 1/\nu_0$  in the above equations, the relationship between  $\dot{\alpha}_{DWS}$  and  $\nu_0$  is found to be:

$$\dot{\alpha}_{DWS}(t) = \sqrt{\frac{5}{3}} \frac{\nu_0}{kl^*(t)} \quad 5.5$$

The corresponding scale of  $\nu_0$  associated with swelling then can be estimated from theoretical swelling kinetics by diffusion equation, using  $\alpha_\infty$  from mass measurement (Fig. 5.1(c)). The swelling rate  $\dot{\alpha}$  is proportional to  $\nu_0/l^*$ , where  $l^*$  has initial value  $l_0^*$  around 0.2 mm at the studied condition.<sup>52</sup> During swelling,  $l^*$  increases because the volume fraction of the tracer particles decreases. For 1D swelling, the volume fraction is inversely proportional to  $\alpha$ , such that  $l^*(t) \approx \alpha l_0^*$ . MSDWS provides the averaged dynamics in the detection thickness  $L$  (a few  $l^*$ ), which needs to be experimentally determined. To calculate the approximate range of  $\nu_0$  and distinguish the time scales of different contributions to observed dynamics,  $L$  is set to be 1 mm. In the time scale in the experiments (10000 s), the cooperative diffusion length ( $\sqrt{2D_{co}t}$ , cooperative diffusion coefficient  $D_{co}$  around  $2.2 \times 10^{-7} \text{ cm}^2/\text{s}^2$ ) is smaller than  $L$ , so that the increase of the swelling ratio  $(\alpha - 1)$  is proportional to  $t^{0.5}$ ;<sup>20,25</sup>

$$\frac{\alpha-1}{\alpha_\infty-1} = \frac{2\sqrt{D_{co}t}}{L\sqrt{\pi}} \quad 5.6$$

One thus has:

$$\dot{\alpha} = \frac{(\alpha_\infty-1)\sqrt{D_{co}}}{L\sqrt{\pi t}} \quad 5.7$$

In the experimental scale from 100 s (after initial spreading and wetting on the surface) to 10000 s,  $\dot{\alpha}$  varies from  $3 \times 10^{-4} \text{ s}^{-1}$  to  $3 \times 10^{-5} \text{ s}^{-1}$ . The order of magnitude of  $v_0$  can thus be applied as an indicator to distinguish different contributions to dynamics. Considering the change of  $\alpha$  from 1 to 2.2,  $v_0$  range due to the affine deformation is found to vary approximately from 0.01 to  $10 \text{ s}^{-1}$ .

### .5.2.2.3 Time-averaged correlation maps

For the visualization of the spatial heterogeneity of the dynamics during swelling, spatially-resolved correlation functions  $C(\vec{r}, t)_\tau$  were calculated as the function of position  $\vec{r}$  and time, with a fixed time interval  $\tau$ . Here,  $\vec{r}$  is the center of a region of interest (ROI) size of 6x6 pixels.  $C(\vec{r}, t)_\tau$  is converted to a grey scale intensity and shown as a dynamic activity map.<sup>35,37,49</sup> The faster the local dynamics, the lower the correlation function at a fixed  $\tau$ . Hence, darker shades in the activity maps correspond to regions with faster dynamics.

To separate the fast dynamics from the characterization of longer time scales, time-averaging is applied using the following equations:

$$\overline{C(\vec{r}, t, \tau)} = \frac{\langle \overline{I_t I_{t+\tau}} \rangle_{\vec{r}}}{\langle \overline{I_t} \rangle_{\vec{r}} \langle \overline{I_{t+\tau}} \rangle_{\vec{r}}} - 1 \quad 5.8$$

where:

$$\overline{I_t} = \sum_{n=-N}^{n=N} I_{t+nT} \quad (T > 2\tau) \quad 5.9$$

The time-averaged autocorrelation function  $\overline{C(\vec{r}, t)_\tau}$  is calculated with time averaged intensity with interval  $T$  longer than the fast dynamics time scale ( $\tau_0 < 20 \text{ ms}$ ). The ensemble averaging correlation is made between time-averaged intensity instead of ensemble time- and space- averaging, which would be too costly computationally. Here  $\tau$ ,  $T$  and  $N$  are chosen 0.1 s, 0.4 s and 25, for Fig. 5.4 and 6, and 1 s, 4 s, and 10 for Fig. 5.5, respectively.

### 5.3 Morphological observation

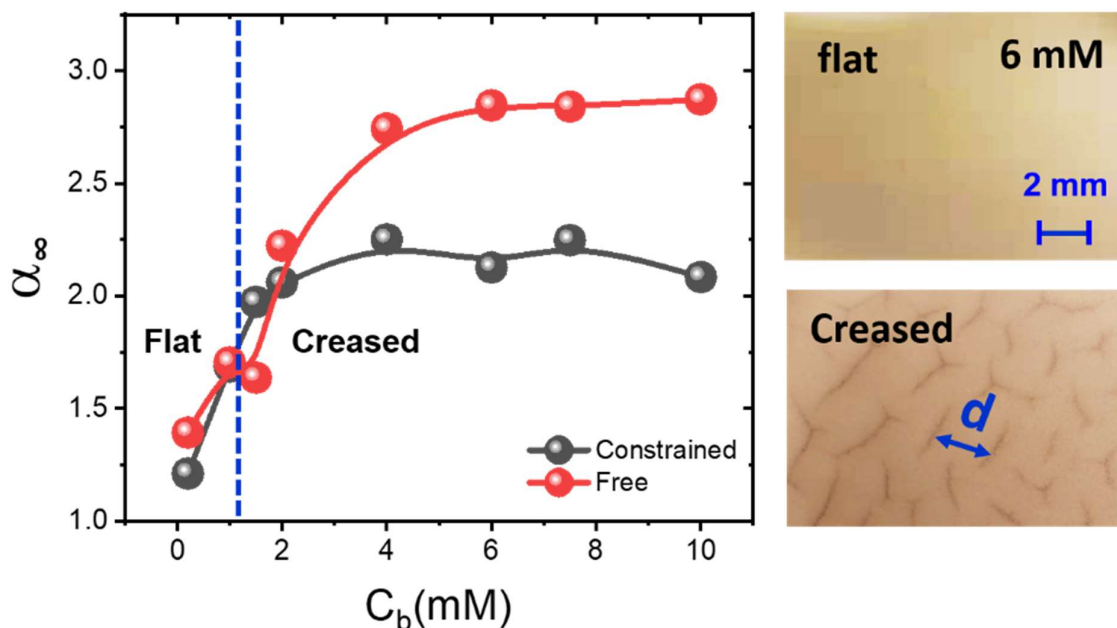


Fig. 5.3 Equilibrium swelling ratio  $\alpha_\infty$  in constrained and free swelling conditions, respectively. Creasing occurs for  $C_b \geq 1.5$  mM. Inserted: Magnified view of the sample with  $C_b = 6$  mM, before and after 2 days of swelling, respectively.

The equilibrium swelling ratios  $\alpha_\infty$  of the constrained (1D swelling) and free (3D swelling) gels are compared in Fig. 5.3.  $\alpha_\infty$  increases with  $C_b$  and reaches a plateau for  $C_b > 2$  mM, whose value for the constrained gels ( $\alpha_\infty \approx 2.2$ ) is lower than that of the free-swelling gels ( $\alpha_\infty \approx 3$ ). In constrained gels, periodically distributed streak-like creases can be observed all over the sample surface for  $C_b \geq 1.5$  mM (see enlarged image with  $C_b = 6$  mM in Fig. 5.3, after 2 days). During the swelling process, sample is illuminated by non-polarized white light and surface images are collected with a CMOS camera. Images are subtracted by the initial image right after swelling to visualize better the creases. Creased region with the gel folding downwards reflects more light, so that the creases are given by the bright part, as shown in Fig. 5.4(a). Detectable creases appear between 600 and 800 s for  $C_b = 4$  mM, and between 90 and 300 s for  $C_b = 10$  mM. The crease distribution

is not homogeneous at the beginning, after which heterogeneous pattern gradually disappears after nucleation and the increase of crease size over time can be observed. The growth of the surface patterns can be characterized by the characteristic length  $d$ ,<sup>18,22</sup> defined as the average distance between creases.  $d$  is estimated by 2D FFT processing of the images (details are provided in supporting information 5.7.2) and plotted in Fig. 5.4(b). Different growth kinetics with different  $C_b$  is observed, while the final length is similar, around 2 mm.  $d$  is in the same order of sample thickness and matches well with the results that similar  $\alpha_\infty$  value is measured at different  $C_b$  (Fig. 5.3). This is in agreement with previously reported observations.<sup>18,22</sup>

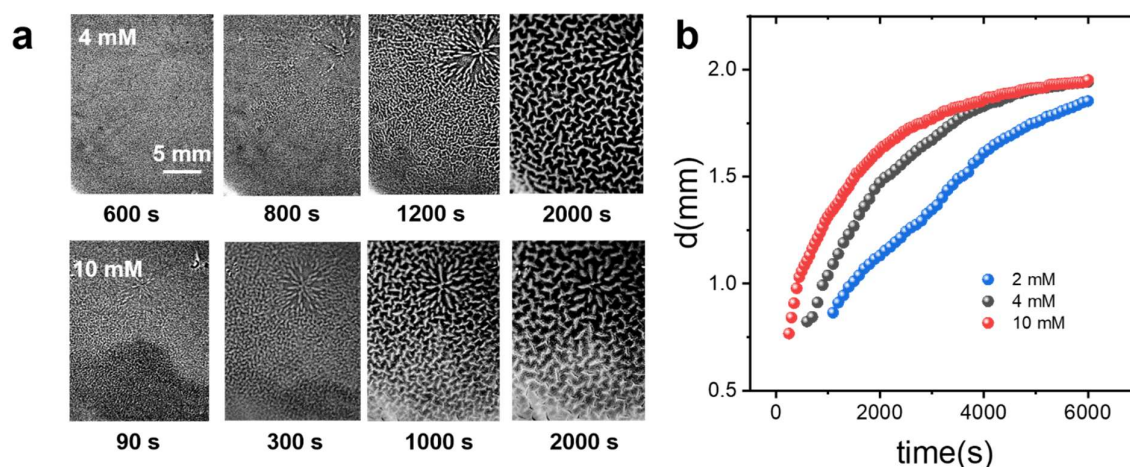


Fig. 5.4 (a) Images of gel surface taken at different swelling times (top row:  $C_b = 4$  mM; bottom row:  $C_b = 10$  mM). (b) Crease wavelength  $d$  for different  $C_b$  as a function of time.

Remarkably, creasing can here only be observable after a period of the order of 1000 s, even the surface of the gel immediately reaches the maximal value  $\alpha_\infty$  after being exposed to the borax solutions<sup>20,25</sup>. As creasing is eventually observed with homogeneous  $\alpha_\infty$ , so that we have critical swelling ratio  $\alpha_c < \alpha_\infty$ .<sup>11,17</sup> For the surface layer, following the equilibrium analysis, creasing should be observable immediately after immersing in the solvent. The existence of this  $C_b$ -dependent induction period shows the transient  $\alpha_c$  differs from the equilibrium value and gel is in subcritical condition before creasing.<sup>5</sup>

## 5.4 MSDWS unveils multi-scale dynamics

The results in section 5.3 confirm that our experiments can characterize morphologically the nucleation and growth of creases during the swelling of a PVA chemical gel, finding features consistent with previous works.<sup>5,17,18</sup> Next, we show that high-resolution MSDWS allows also for the spatial mapping of the microscopic fast dynamics, where transient dynamic behavior in short time scale is highly heterogeneous and deviate from existing models for swelling and creasing.

After illuminated by expanded laser, dynamic intensity of the light backscattered by a small amount of probe particles dispersed in the gel provides the information of network dynamics. By fitting the ensemble-averaged autocorrelation function, we obtained the characteristic time  $\tau_0(t)$  of the decay of the scattered intensity autocorrelation function. The characteristic decorrelation rate  $\nu_0=1/\tau_0$  is used here to quantify the time scale of the dynamics and a larger value of  $\nu_0$  corresponds to faster dynamics. Using classical macroscopic analysis methods where swelling is assumed to be governed by cooperative diffusion, the corresponding value of  $\nu_0$  contributed by affined deformation can be estimated to be in the range 0.01 to 10  $s^{-1}$  in the experimental condition.

### 5.4.1 Fast dynamics beyond swelling kinetics

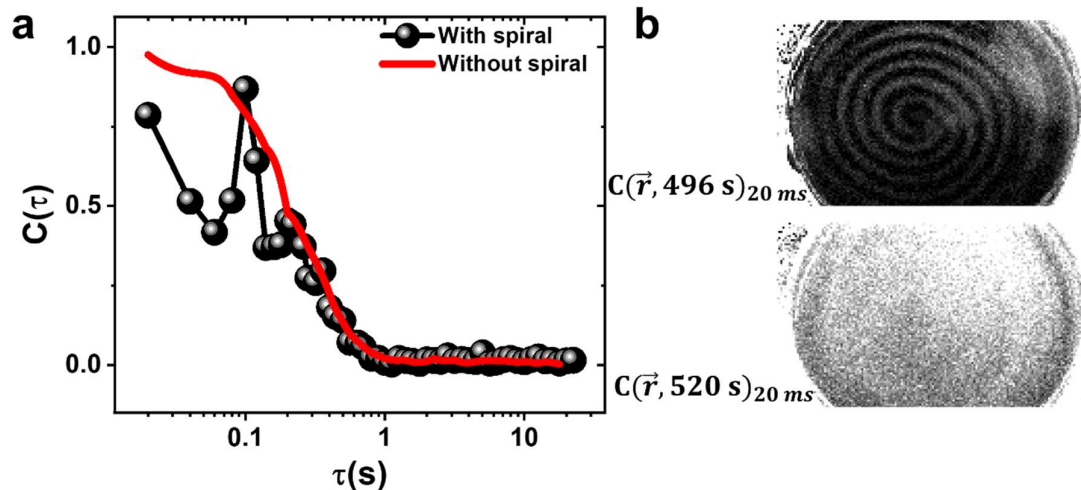


Fig. 5.5 (a) Autocorrelation function averaged over the whole surface with and without spiral events, respectively. The two curves were taken at 496 s (with spiral) and 520 s (without

*spiral), respectively. (b) Dynamic activity map ( $C(\vec{r}, 496 \text{ s})_{20 \text{ ms}}$ ) and ( $C(\vec{r}, 520 \text{ s})_{20 \text{ ms}}$ ).*

The time scale of the global dynamics are described by  $\nu_0$  averaged over the whole gel surface. From these global dynamics measurements, the fitted  $\nu_0$  values range from 0.01 to  $2 \text{ s}^{-1}$ , corresponding to dynamics dominated by the affine deformation associated with swelling. However, at time scales much faster than that of swelling, a different dynamics response is observed. Dynamic activity maps are calculated to visualize the spatial distribution of the dynamics and a dark intensity indicates faster dynamics. In the dynamic activity map ( $C(\vec{r}, t)_{20 \text{ ms}}$ ), a spiral shaped pattern is randomly observed, causing a drop in the correlation value averaged over the whole surface (Fig. 5.5 (a) and (b)). Once the spiral disappears, the decorrelation recovers a value consistent with that seen when no spirals are present. This transient spiral pattern can be observed either before or after the optical observation of creasing, starting from the first immersion in the swelling fluid. Locally, a full decorrelation can be observed at the fastest time interval  $\tau = 5 \text{ ms}$  (black region in the maps) indicating that  $\nu_0 \gg 200 \text{ s}^{-1}$ , which cannot be attributed to the affine deformation associated with swelling. The change in the fast dynamics distribution is visualized by a high-speed camera with a frame frequency of 6000 frame/s for the case of swelling in the round container and results are shown in supporting information 5.7.3 (Fig. 5.S3). We discovered that the high dynamics region in the spiral was rotating with a speed of around 25 cycle/s without radial propagation. The pattern motion and change in intensity can be observed clearly in movie S1 (Movie S1 available upon request). Interestingly, when the same constrained swelling experiments are performed in containers with different geometries, a clear dependence of the fast transient pattern on the boundary condition was observed (Fig. 5.6). For hexagon and triangle containers (Fig. 5.6(b) and (c)), isolated spots are generated with a distance around 10 mm from each other. For an elliptical container (Fig. 5.6(d)), the pattern loses its symmetry compared to the round container in (Fig. 5.6(a)) and shows multiple targets. Comparing square (Fig. 5.6(e)) and rectangular (Fig. 5.6(f)) containers, it can be observed that the streaks can only be generated parallel to the length direction in the rectangular container.



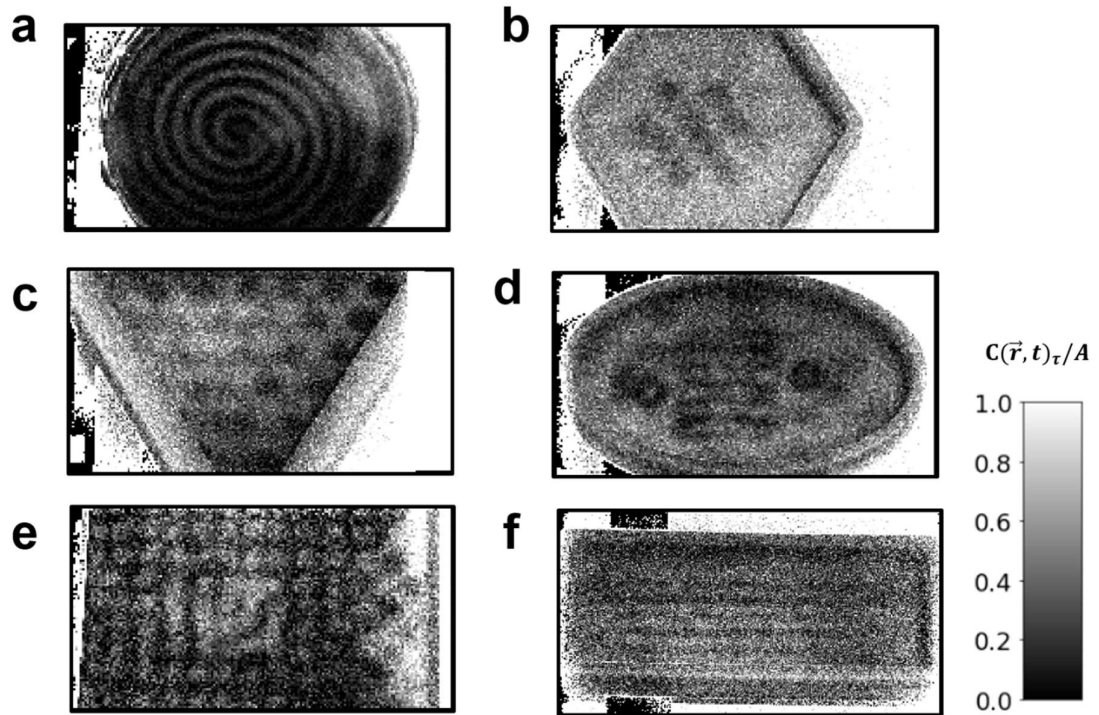


Fig. 5.6 Dynamic activity map for containers with different geometries are shown in: round (a), hexagon (b), equilateral triangle (c), ellipse (d), square (e) and rectangle (f). Thicknesses of gels are around 2 mm for all the containers. Correlation values are normalized by the fitting parameter  $A$ , as indicated in the greyscale bar.

The reversibility and geometry dependence of the patterns strongly suggests an elastic instability. In the constrained swelling geometry, compression and energy release may produce a self-oscillation state, which is similar to what was observed in Faraday experiments where capillary spiral waves can be induced by an oscillating gravity field.<sup>53</sup> The appearance of these patterns before creasing clearly indicates that significant compressive stresses are generated even before macroscopic creasing occurs. The observed dynamics are the result of the overlapping between the fast heterogeneous dynamics and the dynamics due to swelling occurring at longer time scales. Transient decorrelation is much faster than the time scale of the decorrelation due to swelling and only observable in a small part of our collected data: it contributes strong high-frequency fluctuations but does not influence the fitting of  $\nu_0$  and the dynamics visualization at a longer time scale.

#### 5.4.2 Spatially and temporally heterogeneous swelling kinetics

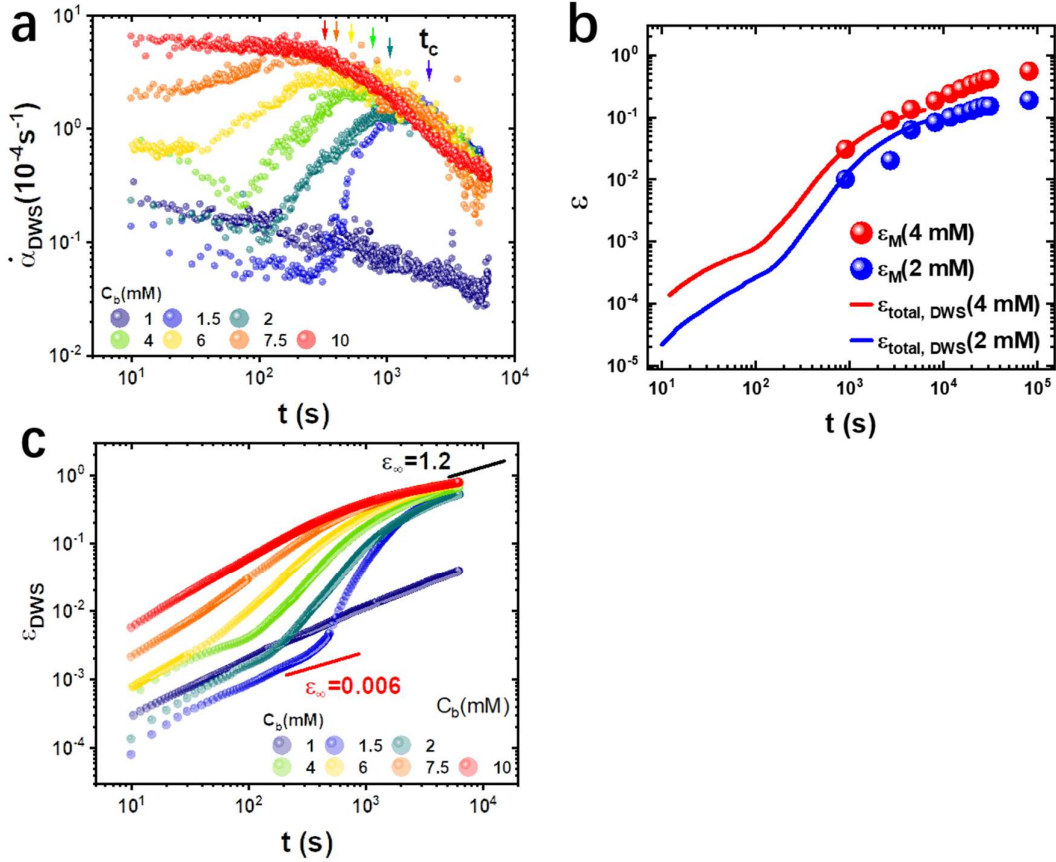


Fig. 5.7 (a) Global  $\alpha_{DWS}$  as a function of time measured during swelling in solutions with different  $C_b$ . Peak time/creasing time  $t_c$  are indicated by arrows. (b) Increase of swelling ratio ( $\epsilon$ ) of the whole gel measured by mass ( $\alpha_M$ ) and calculated from DWS ( $\alpha_{total,DWS}$ ), at  $C_b = 2$  and 4 mM. (c)  $\epsilon_{DWS}$  as a function of time for creased gels.

In addition to mass measurement of swelling ratio (Fig. 5.3), temporally and spatially resolved swelling kinetics can be achieved by MSDWS, with excellent resolution. Based on previous work<sup>5,20,25,54</sup> after macroscopic creasing occurs, the gel reaches a quasi-static state and the average swelling ratio can be described by classical 1D swelling models based on the diffusion equation:

$$\epsilon = \frac{2\sqrt{D_{co}t}}{T\sqrt{\pi}} \epsilon_\infty \quad 5.10$$

where  $T$  is the initial thickness of the reference layer, which is detection length  $L$  for MSDWS experiments and is  $H_0$  (initial gel thickness, 1.85 mm) for the mass measurements. Swelling ratio from DWS  $\epsilon_{DWS}$  is proportional to that from mass

measurement  $\varepsilon_M$  and  $L$  is in the scale of hundreds of microns, which needs to be experimentally determined.  $D_{co}$  is the cooperative diffusion coefficient, around  $2.2 \times 10^{-7}$  cm<sup>2</sup>/s in the studied condition.<sup>52</sup>  $t$  is the time after the onset of swelling. Note that here we use the increase of swelling ratio  $\varepsilon = \alpha - 1$ , for simplicity.  $\varepsilon(t)$  is proportional to equilibrium swelling  $\varepsilon_\infty$  ( $\varepsilon_\infty = \alpha_\infty - 1$ ), the final state of the swelling.  $\varepsilon_\infty$  indicates the scale of swelling kinetics, is applied as a characteristic rate for comparison swelling kinetics at different stage.

The global swelling rate  $\dot{\alpha}_{DWS}$  for different  $C_b$  is directly calculated from MSDWS and shown in Fig. 5.7(a), as a function of  $t$ . For  $C_b < 1.5$  mM,  $\dot{\alpha}_{DWS}$  has a very low value around  $10^{-5}$  s<sup>-1</sup> and slowly decreases with time. In this regime, no significant  $C_b$  dependence was observed. At  $C_b = 1.5$  mM where creasing is induced, we found a different behavior.  $\dot{\alpha}_{DWS}$  increases with  $t$  after an initial plateau around 500 s, and starts to drop again for  $t > 2000$  s. The same behaviors were observed for all the higher  $C_b$ , and the increase rate  $\dot{\alpha}$  before dropping increased with  $C_b$ . Images are averaged over a time interval longer than the decorrelation time of the speckle intensity (as seen in supporting information 5.7.1) to distinguish the surface morphology from speckled appearance, and compared with transition of  $\dot{\alpha}_{DWS}$ . Interestingly, we find that for all  $C_b$  above 1.5 mM in the time range where  $\dot{\alpha}_{DWS}$  peaks and decreases later, creasing becomes homogeneously distributed. The transition time  $t_h$  ranges from around 360 s ( $C_b=10$  mM) to 2000 s ( $C_b=1.5$  mM), as indicated in Fig. 5.7 (a).

Swelling ratio can be obtained by the time integration of  $\dot{\alpha}_{DWS}$ :

$$\varepsilon_{DWS}(\vec{r}, t) = \int_0^t \dot{\alpha}_{DWS}(\vec{r}, T) dT \quad 5.11$$

By imposing that the spatially averaged  $\varepsilon_{DWS}$  superimpose to the  $\varepsilon_M$  obtained from mass measurement, we find an estimated value of  $L \approx 0.4$  mm. With this value of  $L$ , we find an excellent agreement between the increase of swelling ratio of the whole gel  $\varepsilon_{total,DWS}$  calculated from MSDWS ( $\varepsilon_{total,DWS} = \frac{L}{H} \varepsilon_{DWS}$ ) and  $\varepsilon_M$  throughout the whole swelling processes (Fig. 5.7 (b)), confirming that MSDWS measurements allow us to precisely quantify swelling. Importantly, MSDWS has an obvious advantage over macroscopic mass measurements, in that it allows for determining the spatially resolved swelling evolution without perturbing the sample.

When the global swelling ratios  $\varepsilon_{DWS}$  for all  $C_b$  are logarithmically plotted (Fig. 5.7 (c)), it is clear that the swelling kinetics cannot be simply described by the diffusion model. The initial growth of  $\varepsilon_{DWS}$  approximately follows  $\varepsilon_{DWS} \propto t^{0.5}$  for all  $C_b$ . However, when we try to describe the swelling kinetics with the diffusion equation, the  $\varepsilon_\infty$  value fitted from these early stages is found to range from around 0.006 (1.5 mM) to 0.05 (7.5 mM), much smaller than the actual equilibrium value ( $\approx 1.2$ ) after creasing (Fig. 5.3). For  $C_b < 1.5$  mM, the swelling rate follows the same time dependence until the end of the measurement period. For higher  $C_b$  where creasing is observed,  $\varepsilon_{DWS}$  accelerates with respect to its initial behavior ( $\varepsilon_{DWS} \propto t^\beta$ ,  $\beta > 0.5$ ), corresponding to the observed increase in  $\dot{\varepsilon}_{DWS}$  in Fig. 5.7 (a). During homogeneous creasing (after  $t_h$ ), the swelling ratios approach the same asymptote again, where  $\varepsilon_{DWS}$  is proportional to  $t^{0.5}$  and the values of fitted  $\varepsilon_\infty$  after creasing increase to around 1.2 for all  $C_b$ , equal to the equilibrium value. It can be inferred that the initial swelling is highly suppressed by compression with a smaller  $\varepsilon_\infty$  than the eventual creased state, which is at equilibrium. In both flat state and homogeneously creased state after  $t_h$ ,  $\varepsilon_{DWS} \propto t^{0.5}$  can be described by the diffusion model, but with different values of  $\varepsilon_\infty$  ( $< 0.05$  and  $1.2$ , respectively). The deviation from diffusion model before creasing indicates that swelling kinetics is also coupled to creasing transition. From the comparison of free and constrained swelling (Fig. 5.3 and previously reported results<sup>21,33</sup>),  $\varepsilon_\infty$  depends strongly on the confinement condition. It is reasonable to believe that  $\varepsilon_\infty$  increases after creasing where the compressive stresses can be released by the creasing motion. However, the increase of  $\varepsilon_\infty$  shows the self-acceleration of the swelling kinetics and a spontaneous breaking of metastable equilibrium is expected during the transition period (ranging from 150 to 1000 s at different  $C_b$ ), whose sign should be detectable by MSDWS.

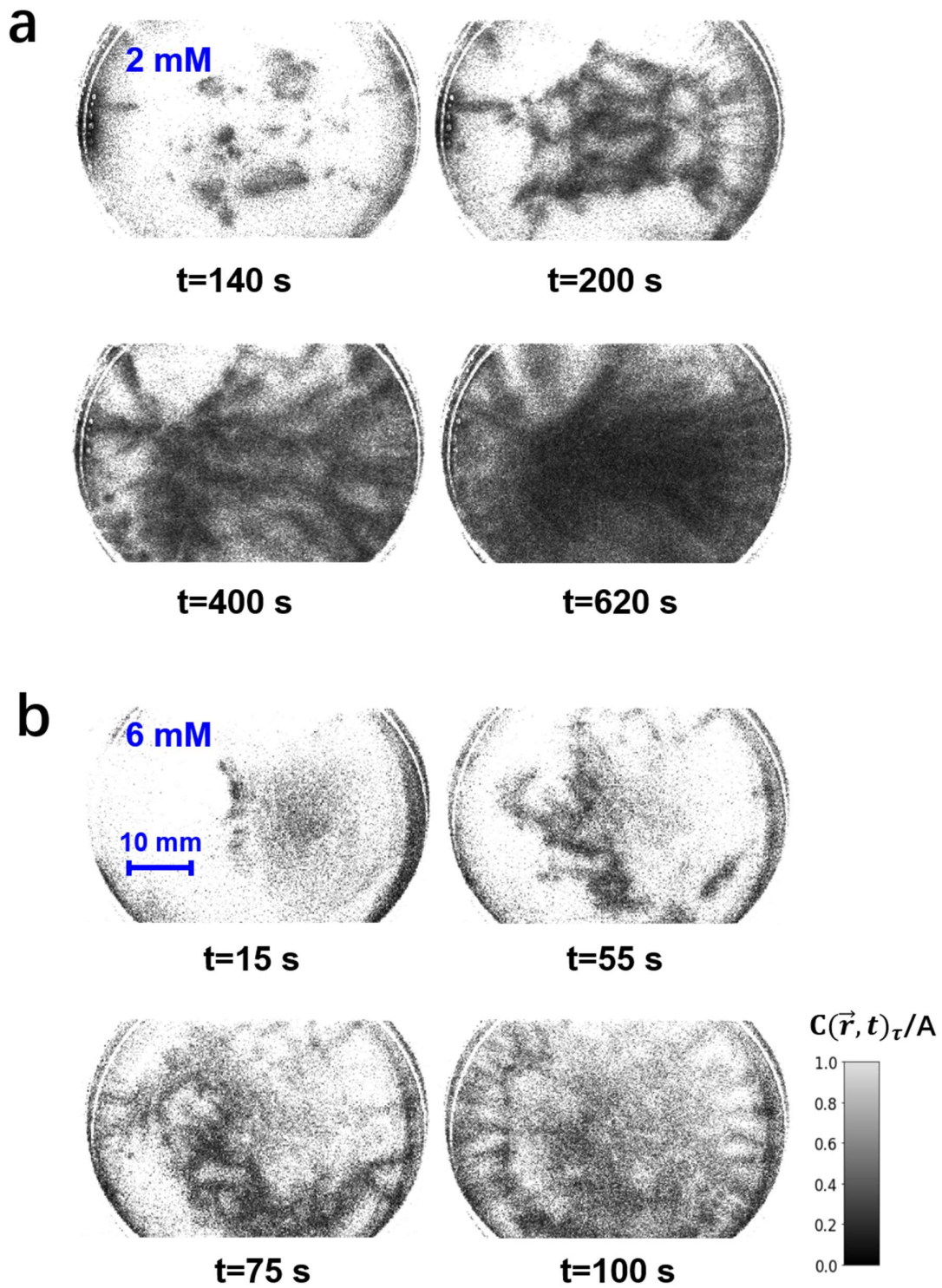


Fig. 5.8 Time-averaged correlation maps before creasing, with  $\tau = 0.1$  s at (a)  $C_b = 2$  and (b) 6 mM.

Time-averaged correlation maps  $\overline{C(\vec{r}, t)_\tau}$  are calculated to characterize the spatial

heterogeneity of swelling, where only the differences in the dynamics occurring over the time scale of the relaxation of correlation functions due to affine deformation are shown. As seen in the  $\overline{C(\vec{r}, t)}_{0.1s}$  maps of Fig. 5.8, initial dynamics is homogeneous over the whole sample. During the time interval where the global  $\dot{\alpha}_{DWS}$  increases (before 1100 s for 2mM (Fig. 5.8(a)) and before 500 s for 6mM (Fig. 5.8(b))), there are some signs of nucleation of regions with swelling faster than the global  $\dot{\alpha}_{DWS}$ . The onset of the heterogeneous swelling results in the accelerated swelling in Fig. 5.7(c). Measurements with smaller field and better resolution (20  $\mu\text{m}/\text{pixel}$ ) are performed to visualize the detailed information in  $\overline{C(\vec{r}, t)}_{\tau}$  for  $C_b=6$  mM, in a separate experiment. Image acquisition is switched between white light illumination (for crease visualization) and laser illumination (for dynamics measurement) to relate swelling rate and creasing morphology with small initial size upon nucleation. In Fig. 5.9(a), at 360 s, the heterogeneous nucleation of creasing can be observed, while the branches of growth matches well with pattern of  $\overline{C(\vec{r}, t)}_{1s}$  in Fig. 5.9(b). The growth of region with fast dynamics can be observed, similar to Fig. 5.6. It can be noticed that the diffusive patterns are actually formed by the scattered spots (diameter around 0.2 mm) and their surrounding regions, with faster swelling rate. This indicates that the growing region in Fig. 5.8 corresponds to the onset of creases with small initial size. The folding motion during creasing results in a local fluctuation of swelling rate, in the form of spot pattern in  $\overline{C(\vec{r}, t)}_{\tau}$ .

Based on results in Fig. 5.8 and 9, we discover that the unusual jump of the extrapolated final state (fitted  $\varepsilon_{\infty}$  from below 0.05 to 1.2 in Fig. 5.7 (c)) is achieved via an intermediate heterogeneous creasing and swelling stage. In this transition period, the overall swelling rate is even faster than that close to the equilibrium state after creasing. This can be caused by two effects: (a) the process of breaking the confinement and releasing the accumulated elastic energy in compressed flat state can contribute to this faster swelling rate. (b) Heterogeneous swelling indicates a locally less-constrained swelling mode, whose final  $\alpha_{\infty}$  can be much larger than that in constrained state.

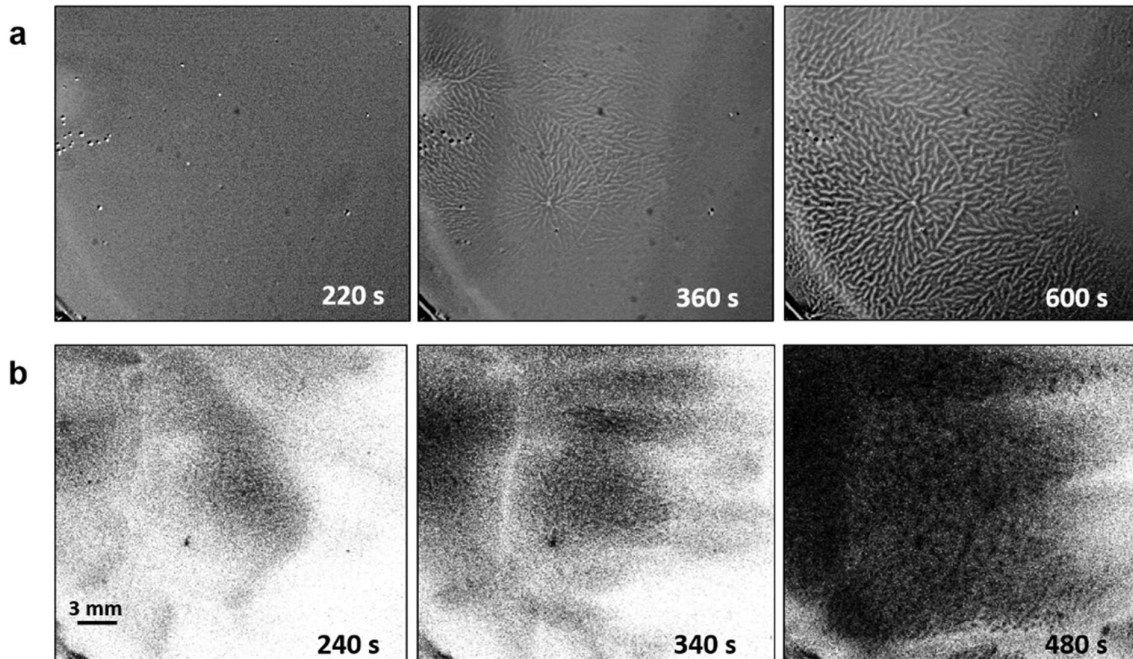


Fig. 5.9 (a) Crease images (with white light illumination) at different time after swelling. (b) Time-averaged correlation maps  $\overline{C(\vec{r}, t)}_{1s}$  for  $C_b=6$  mM. in the same region of (a).

After the onset of creasing, the growth of the surface patterns can be observed with increasing distance between creases, as a result of further swelling. During homogeneous creasing, spots are distributed homogeneously, too, as seen in Fig. 5.10. Interestingly, each spot exhibits a flickering (around 100 s) of the transient activity (Fig. 5.11), as shown for one representative high dynamics spot. The active phase of each spot occurs at different times and the whole dynamic map exhibits flickering high dynamics spots at different locations (movie S2, 25 ×).

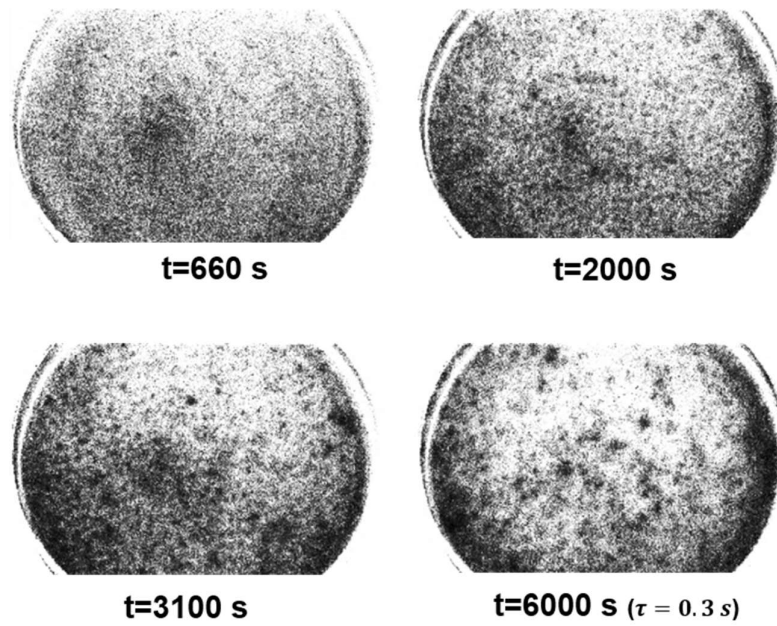


Fig. 5.10 Time-averaged correlation maps after creasing for  $C_b=6 \text{ mM}$ .

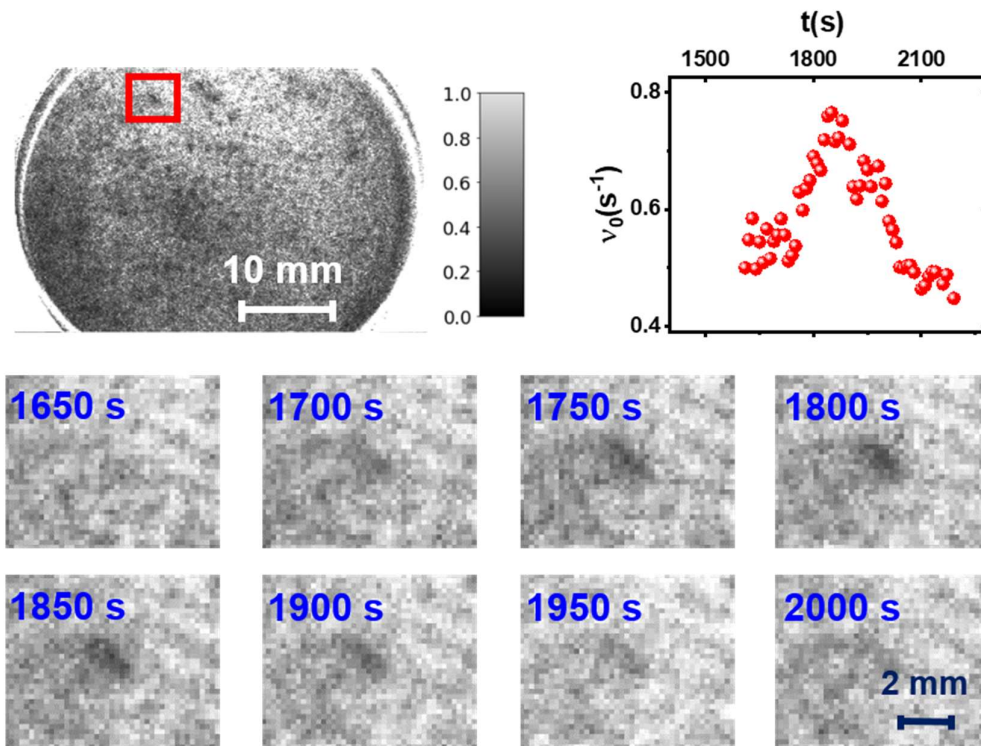


Fig. 5.11 Spot patterns and local changes of one spot ( $C_b = 6 \text{ mM}$ ,  $\tau = 0.1 \text{ s}$ ) in time-averaged correlation maps around  $t = 1800 \text{ s}$ .



Dynamic spots are accumulated and compared with crease patterns in Fig. 5.12. The high dynamics spots and the creases are spatially related and that the high dynamics spots correspond to the gap between the creases. Spot pattern shows the similar length scale as creases, confirmed by 2D-FFT processing (Fig. 5. S2). This further confirms the results in Fig. 5.9, and the folding and rearrangement of creases both lead to local fluctuation of swelling rate. More importantly, the fluctuation of spot pattern, corresponding to local adjustment of crease distribution, indicates that the growing creases are still spatially heterogeneous, even when their distribution is already homogeneous.

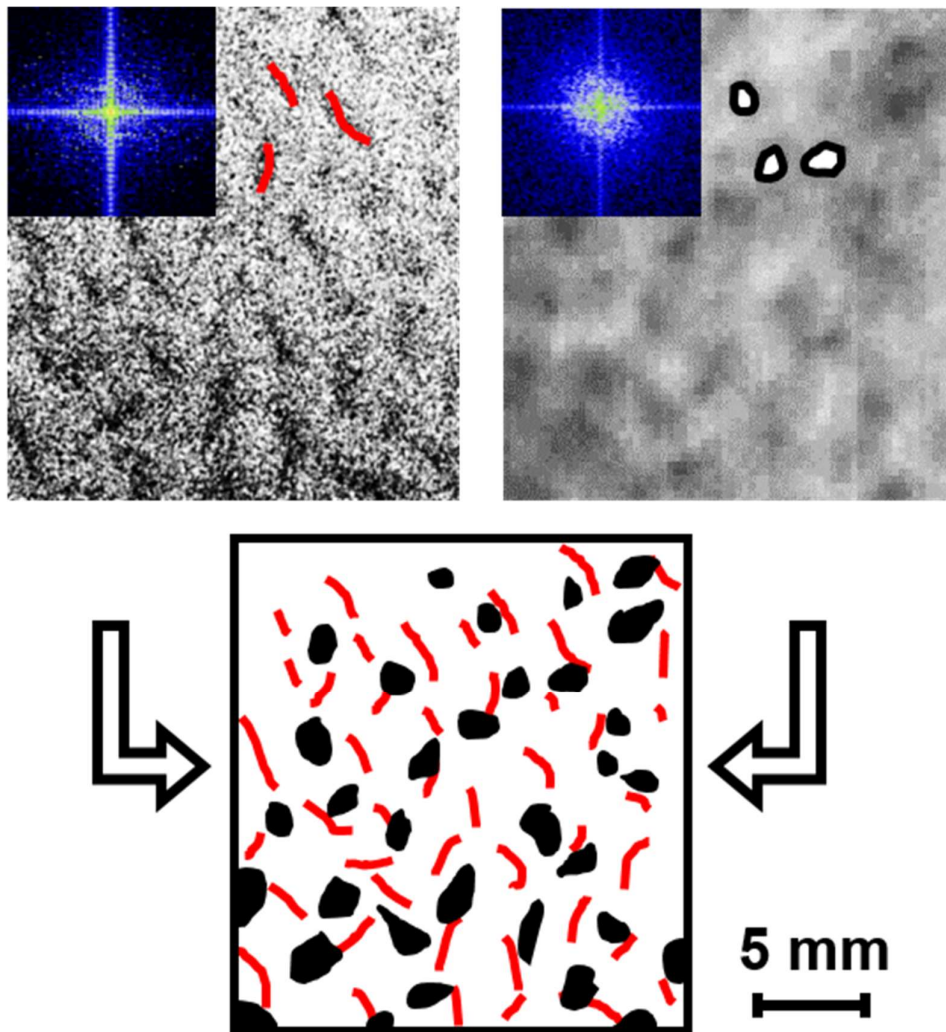


Fig. 5.12 Surface image (top, left) and corresponding cumulated dynamics map (top, right) at  $t = 5600$  s. 2D-FFT results are inserted in the images. The locations of the creases and spot pattern are indicated in the same image (bottom).

## 5.5 Conclusions

This work applies MSDWS to the measurements of spatio-temporal transitions in dynamics in a complex system, where we almost push the application to its limit, with time resolution around 0.1 ms and spatial resolution around 100  $\mu\text{m}$ . Due to the lack of characterization methods, such transient behavior has not been reported so far and point to the existence of metastable states. We discovered that the initial behavior is rather complex that deviates from existing models considering only diffusion kinetics. In addition to the well-known result that creasing nucleation and growth is governed by the swelling,<sup>5,17</sup> we discovered that the swelling kinetics is conversely influenced by the creasing transition. The interaction between compression and surface instability results in an unusual heterogeneous swelling and creasing (Fig. 5.7), even though gel is initially homogeneous in plane. In fact, considering limited diffusion kinetics, the effect of heterogeneous swelling should commonly exist in transient swelling, but observed here for the first time. Our work shows a convenient tool to visualize and quantify the dynamic behaviors in poroelastic materials. Even after creasing becomes visible, where global swelling kinetics coincides with equilibrium models by diffusion equation, the adjustment events during growth of the crease structure also results in a spatially and temporally heterogeneous swelling events between the creases. In the practical application of surface patterns generated in a similar dynamic condition, the time scale for the delayed nucleation and post-stabilization of the pattern can be evaluated with the tool provided in this work.

In summary, in-situ measurements of surface creasing during swelling provides the dynamic response and detects rich heterogeneous behaviors in well-controlled conditions. With these high temporal resolution methods, transient behaviors and the existence of metastable states can be experimentally characterized and unveils how such large instabilities that in principle may have large activation energies can occur kinetically by a sum of smaller steps with a much lower activation barrier. Such a stepwise process of the onset of instabilities may be more widespread than gel swelling and the knowledge of the intermediate steps may lead to more realistic modeling and prediction of the kinetics of the transition and help the design of a new generation of knowledge based responsive materials.

## 5.6 Reference

- 1 Liu, Q., Ouchi, T., Jin, L., Hayward, R. & Suo, Z. Elastocapillary Crease. *Phys Rev Lett* **122**, 098003, doi:10.1103/PhysRevLett.122.098003 (2019).
- 2 Tanaka, T. *et al.* Mechanical instability of gels at the phase transition. *Nature* **325**, 796 (1987).
- 3 Wang, Q. & Zhao, X. A three-dimensional phase diagram of growth-induced surface instabilities. *Scientific reports* **5**, 1-10 (2015).
- 4 Arifuzzaman, M. *et al.* Geometric and Edge Effects on Swelling-Induced Ordered Structure Formation in Polyelectrolyte Hydrogels. *Macromolecules* **46**, 9083-9090, doi:10.1021/ma401773w (2013).
- 5 Chen, D., Cai, S., Suo, Z. & Hayward, R. C. Surface energy as a barrier to creasing of elastomer films: an elastic analogy to classical nucleation. *Phys Rev Lett* **109**, 038001, doi:10.1103/PhysRevLett.109.038001 (2012).
- 6 Hong, W., Zhao, X. & Suo, Z. Formation of creases on the surfaces of elastomers and gels. *Applied Physics Letters* **95**, 111901 (2009).
- 7 Ciarletta, P. Matched asymptotic solution for crease nucleation in soft solids. *Nature communications* **9**, 1-7 (2018).
- 8 Kim, J., Yoon, J. & Hayward, R. C. Dynamic display of biomolecular patterns through an elastic creasing instability of stimuli-responsive hydrogels. *Nat Mater* **9**, 159-164, doi:10.1038/nmat2606 (2010).
- 9 Kim, H. S. & Crosby, A. J. Solvent-responsive surface via wrinkling instability. *Adv Mater* **23**, 4188-4192, doi:10.1002/adma.201101477 (2011).
- 10 Yang, S., Khare, K. & Lin, P.-C. Harnessing Surface Wrinkle Patterns in Soft Matter. *Advanced Functional Materials* **20**, 2550-2564, doi:10.1002/adfm.201000034 (2010).
- 11 Yoon, J., Kim, J. & Hayward, R. C. Nucleation, growth, and hysteresis of surface creases on swelled polymer gels. *Soft Matter* **6**, doi:10.1039/c0sm00372g (2010).
- 12 Xu, B., Chen, D. & Hayward, R. C. Mechanically gated electrical switches by creasing of patterned metal/elastomer bilayer films. *Advanced Materials* **26**, 4381-4385 (2014).
- 13 Zalachas, N., Cai, S., Suo, Z. & Lapusta, Y. Crease in a ring of a pH-sensitive hydrogel swelling under constraint. *International Journal of Solids and Structures* **50**, 920-927 (2013).
- 14 Wu, K. *et al.* Harnessing Dynamic Wrinkling Surfaces for Smart Displays. *Nano Letters* **20**, 4129-4135 (2020).
- 15 Li, F., Hou, H., Yin, J. & Jiang, X. Near-infrared light-responsive dynamic wrinkle patterns. *Science advances* **4**, eaar5762 (2018).
- 16 Biot, M. A. Surface instability of rubber in compression. *Applied Scientific Research, Section A* **12**, 168-182 (1963).
- 17 Trujillo, V., Kim, J. & Hayward, R. C. Creasing instability of surface-attached hydrogels. *Soft Matter* **4**, doi:10.1039/b713263h (2008).
- 18 Tanaka, H., Tomita, H., Takasu, A., Hayashi, T. & Nishi, T. Morphological and kinetic evolution of surface patterns in gels during the swelling process: Evidence of dynamic pattern ordering. *Physical review letters* **68**, 2794 (1992).
- 19 Tanaka, T. *et al.* Mechanical instability of gels at the phase transition. *Nature* **325**, 796-798 (1987).
- 20 Yoon, J., Cai, S., Suo, Z. & Hayward, R. C. Poroelastic swelling kinetics of thin

- hydrogel layers: comparison of theory and experiment. *Soft Matter* **6**, doi:10.1039/c0sm00434k (2010).
- 21 Bouklas, N. & Huang, R. Swelling kinetics of polymer gels: comparison of linear and nonlinear theories. *Soft Matter* **8**, 8194-8203 (2012).
- 22 Guvendiren, M., Burdick, J. A. & Yang, S. Kinetic study of swelling-induced surface pattern formation and ordering in hydrogel films with depth-wise crosslinking gradient. *Soft Matter* **6**, doi:10.1039/b927374c (2010).
- 23 Toh, W., Ding, Z., Yong Ng, T. & Liu, Z. Wrinkling of a polymeric gel during transient swelling. *Journal of Applied Mechanics* **82** (2015).
- 24 Ilseng, A., Prot, V., Skallerud, B. H. & Stokke, B. T. Buckling initiation in layered hydrogels during transient swelling. *Journal of the Mechanics and Physics of Solids* **128**, 219-238 (2019).
- 25 Doi, M. Gel dynamics. *Journal of the Physical Society of Japan* **78**, 052001 (2009).
- 26 Tanaka, T. & Fillmore, D. J. Kinetics of swelling of gels. *The Journal of Chemical Physics* **70**, 1214-1218 (1979).
- 27 Hohlfeld, E. & Mahadevan, L. Unfolding the sulcus. *Physical review letters* **106**, 105702 (2011).
- 28 Hohlfeld, E. & Mahadevan, L. Scale and nature of sulcification patterns. *Physical review letters* **109**, 025701 (2012).
- 29 Yang, J., Illeperuma, W. & Suo, Z. Inelasticity increases the critical strain for the onset of creases on hydrogels. *Extreme Mechanics Letters* **40**, 100966 (2020).
- 30 Chen, D., Jin, L., Suo, Z. & Hayward, R. C. Controlled formation and disappearance of creases. *Mater. Horiz.* **1**, 207-213, doi:10.1039/c3mh00107e (2014).
- 31 Takahashi, R. *et al.* Coupled instabilities of surface crease and bulk bending during fast free swelling of hydrogels. *Soft Matter* **12**, 5081-5088 (2016).
- 32 Curatolo, M., Nardinocchi, P., Puntel, E. & Teresi, L. Transient instabilities in the swelling dynamics of a hydrogel sphere. *Journal of Applied Physics* **122**, 145109 (2017).
- 33 Marcombe, R. *et al.* A theory of constrained swelling of a pH-sensitive hydrogel. *Soft Matter* **6**, 784-793 (2010).
- 34 Pine, D. J., Weitz, D. A., Zhu, J. X. & Herbolzheimer, E. Diffusing-wave spectroscopy: dynamic light scattering in the multiple scattering limit. *Journal de Physique* **51**, 2101-2127, doi:10.1051/jphys:0199000510180210100 (1990).
- 35 Duri, A., Sessoms, D. A., Trappe, V. & Cipelletti, L. Resolving long-range spatial correlations in jammed colloidal systems using photon correlation imaging. *Physical review letters* **102**, 085702 (2009).
- 36 Aime, S., Ramos, L. & Cipelletti, L. Microscopic dynamics and failure precursors of a gel under mechanical load. *Proc Natl Acad Sci U S A* **115**, 3587-3592, doi:10.1073/pnas.1717403115 (2018).
- 37 Amon, A., Nguyen, V. B., Bruand, A., Crassous, J. & Clement, E. Hot spots in an athermal system. *Phys Rev Lett* **108**, 135502, doi:10.1103/PhysRevLett.108.135502 (2012).
- 38 Kang, M. K. & Huang, R. Swell-induced surface instability of confined hydrogel layers on substrates. *Journal of the Mechanics and Physics of Solids* **58**, 1582-1598 (2010).
- 39 Zhao, J., Mayumi, K., Creton, C. & Narita, T. Rheological properties of tough hydrogels based on an associating polymer with permanent and transient crosslinks: Effects of crosslinking density. *Journal of Rheology* **61**, 1371-1383 (2017).

- 40 Shibayama, M., Takeuchi, T. & Nomura, S. Swelling/shrinking and dynamic light scattering studies on chemically cross-linked poly (vinyl alcohol) gels in the presence of borate ions. *Macromolecules* **27**, 5350-5358 (1994).
- 41 Luo, W. *et al.* Surfactant-free CO<sub>2</sub>-in-water emulsion-templated poly (vinyl alcohol)(PVA) hydrogels. *Polymer* **61**, 183-191 (2015).
- 42 Cardinaux, F., Cipolletti, L., Scheffold, F. & Schurtenberger, P. Microrheology of giant-micelle solutions. *EPL (Europhysics Letters)* **57**, 738 (2002).
- 43 Weitz, D. & Pine, D. in *Dynamic light scattering: The method and some applications* 652-720 (Oxford University Press, 1993).
- 44 MacKintosh, F. C., Zhu, J.-X., Pine, D. & Weitz, D. Polarization memory of multiply scattered light. *Physical Review B* **40**, 9342 (1989).
- 45 Nagazi, M.-Y. *et al.* Space-resolved diffusing wave spectroscopy measurements of the macroscopic deformation and the microscopic dynamics in tensile strain tests. *Optics and Lasers in Engineering* **88**, 5-12 (2017).
- 46 Xia, W. *et al.* Poly (vinyl alcohol) gels as photoacoustic breast phantoms revisited. *Journal of biomedical optics* **16**, 075002 (2011).
- 47 Wu, X., Pine, D., Chaikin, P., Huang, J. & Weitz, D. Diffusing-wave spectroscopy in a shear flow. *JOSA B* **7**, 15-20 (1990).
- 48 Amon, A., Mikhailovskaya, A. & Crassous, J. Spatially resolved measurements of micro-deformations in granular materials using diffusing wave spectroscopy. *Rev Sci Instrum* **88**, 051804, doi:10.1063/1.4983048 (2017).
- 49 van der Kooij, H. M. *et al.* Laser Speckle Strain Imaging reveals the origin of delayed fracture in a soft solid. *Science advances* **4**, eaar1926 (2018).
- 50 van der Kooij, H. M., Susa, A., Garcia, S. J., van der Zwaag, S. & Sprakel, J. Imaging the Molecular Motions of Autonomous Repair in a Self-Healing Polymer. *Adv Mater* **29**, doi:10.1002/adma.201701017 (2017).
- 51 Verho, T., Karppinen, P., Groschel, A. H. & Ikkala, O. Imaging Inelastic Fracture Processes in Biomimetic Nanocomposites and Nacre by Laser Speckle for Better Toughness. *Adv Sci (Weinh)* **5**, 1700635, doi:10.1002/advs.201700635 (2018).
- 52 Narita, T., Mayumi, K., Ducouret, G. & Hébraud, P. Viscoelastic properties of poly (vinyl alcohol) hydrogels having permanent and transient cross-links studied by microrheology, classical rheometry, and dynamic light scattering. *Macromolecules* **46**, 4174-4183 (2013).
- 53 Kiyashko, S., Korzinov, L., Rabinovich, M. & Tsimring, L. S. Rotating spirals in a Faraday experiment. *Physical Review E* **54**, 5037 (1996).
- 54 Peters, A. & Candau, S. Kinetics of swelling of spherical and cylindrical gels. *Macromolecules* **21**, 2278-2282 (1988).
- 55 Lynch, S. in *Dynamical Systems with Applications using Python* 471-489 (Springer, 2018).

## 5.7 Supporting information

### 5.7.1 Processing of raw speckle images

Examples of raw speckle images are shown in Fig. 5.S1 (a), the first one of which is collected at 3000 s for a borax concentration ( $C_b$ ) of 6 mM. Even though creases have already been generated, the morphology feature is barely observable in the speckle images. The intensity difference due to a height difference due to surface features is hidden by the fluctuating intensity of speckles generated by the laser illumination. It has been checked that up to 2 h the creases do not contribute to the autocorrelation function. MSDWS characterization is still valid since the height difference due to creasing and swelling is negligible ( $\sim 1$  mm), compared to the distance from the camera to the sample surface ( $\sim 20$  cm). To detect the change in surface morphology, a series of raw images are averaged with a time interval  $\Delta t(t)$  larger than  $\tau_0(t)$  so that the speckles are smeared out by the averaging of uncorrelated images. The raw image right after adding the borax solution is used as a background to highlight the crease structure, as seen in Fig. 5.S1 (b). With this method, both space resolved dynamics and surface morphology can be observed simultaneously with no need of a separate imaging of the gel surface. However, at the early stage of creasing, the initial size and depth is too small to be measured this way, so that white illumination is still applied (Fig. 5.9(a)), with exposure time of 1 ms.

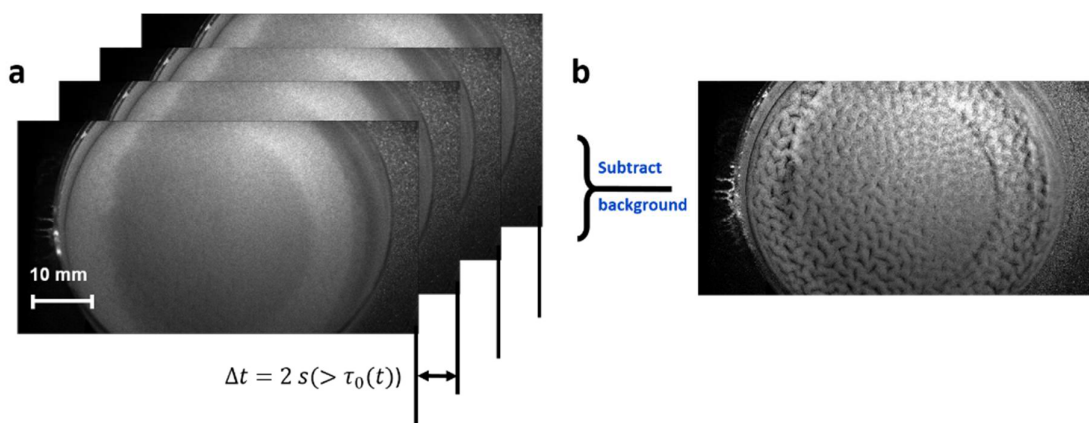


Fig. 5.S1 Series of raw images where surface feature is hidden by speckle fluctuation. (b) Surface images from averaging with time interval over  $\tau_0(t)$ .

## 5.7.2 2D Fourier Transform processing of the images

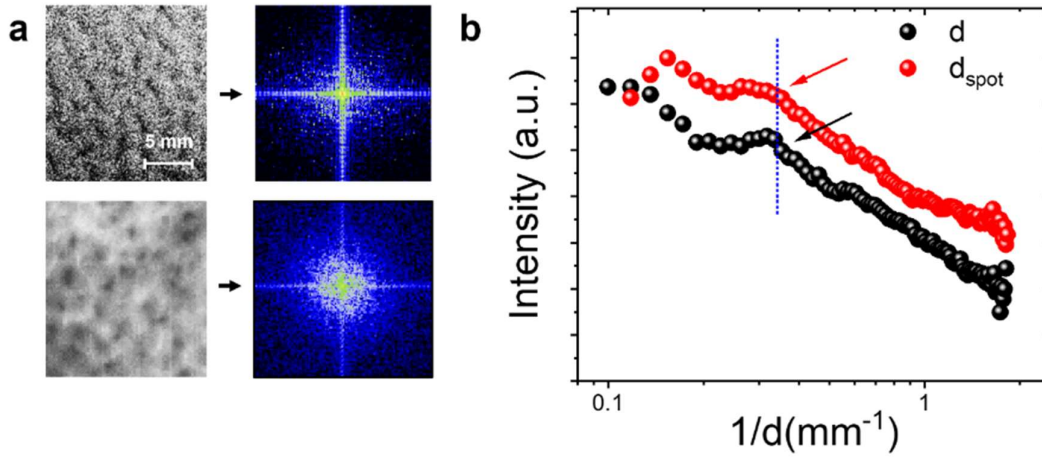


Fig. 5.S2 Images (surface images and accumulated map) and corresponding 2D-FFT results at  $t=5600$ . (b) 1D intensity results of  $F(1/d)$ .

The characteristic length of the image features (spots in accumulated maps and creases in surface images) can be obtained by Two-Dimensional Discrete Fourier Transform (2D-DFT):<sup>55</sup>

$$F(u, v) = \sum_0^{M-1} \sum_0^{N-1} I(x, y) e^{-j2\pi(\frac{ux}{M} + \frac{vy}{N})} \quad 1$$

$I(x, y)$  is the corresponding intensity value for each pixel in the time-averaged correlation maps and surface images. The fast algorithm for computing 2D-DFT, Two-Dimensional Fast Fourier Transform (2D-FFT) is carried out with the optimized library NumPy in Python. After shifting the zeroth frequency to the center, a halo can be observed in  $F(u, v)$  (as seen in Fig. 5.S2(a)), which corresponds to the mean period in the original images, i.e. a characteristic length. Considering the results to be isotropic,  $F(u, v)$  is azimuthally integrated to obtain a one-dimensional  $F(1/d)$  so that the characteristic length can be visualized and compared as seen in Fig. 5.S2(b). A peak was observed at the same value around  $0.35 \text{ mm}^{-1}$  for both images in 1D intensity results, which corresponds to an average size of the crease as well as to the dynamic spot,  $d_{spot} \approx d = 2.8 \text{ mm}$ . By checking  $d$  and  $d_{spot}$  values at different times, it has been confirmed that they have a similar value so that the characteristic length scale of the creases and that of the high dynamics spots are spatially related.

### 5.7.3 Rotation of spiral pattern in round container

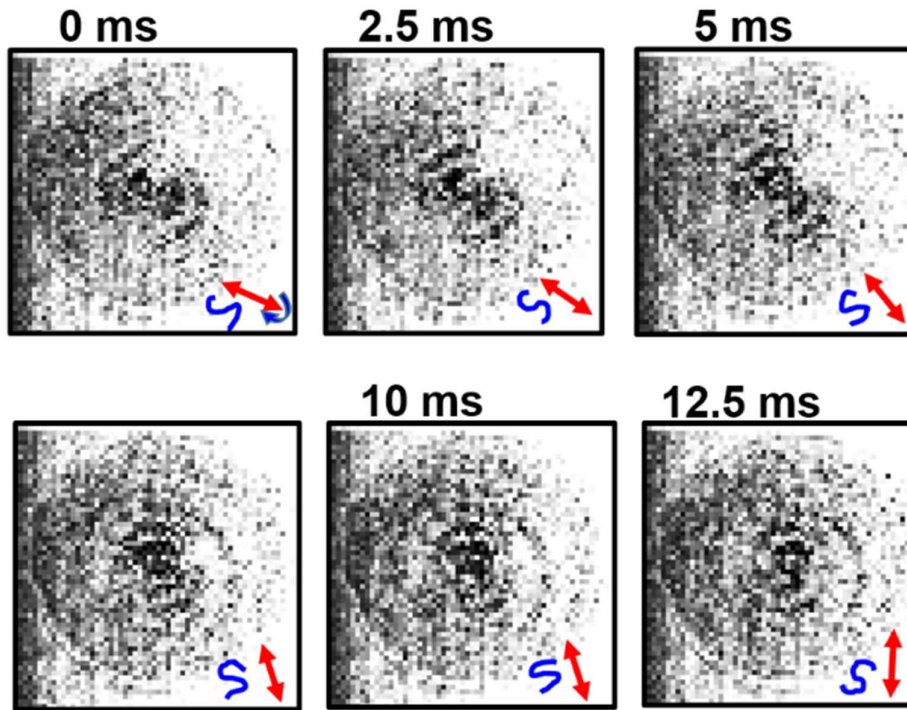


Fig. 5.S3 Fast patterns  $C(\vec{r}, t)_{20\text{ ms}}$  with a high time resolution ( $1/6000\text{ s}$ ). The rotation direction is indicated by a red arrow in the direction of the axis of the “S” shape pattern in the center.

The evolution of the patterns of  $C(\vec{r}, t)_{20\text{ ms}}$  within 20 ms are shown in Fig. 5.S3. Using the fast camera, we discovered that the high dynamics region in the spiral was rotating with a speed of around 25 cycle/s without radial propagation, showing the motion as a standing spiral-shaped wave. The pattern motion and change in intensity can be observed clearly in movie S1. The spiral patterns have a lifetime around 50 ms and a period (average time between two consecutive spirals) around 300 ms, so that spirals are seen over around 1/6 of the observation time window.

### 5.7.4 Supporting videos (available upon request)

Movie S1: Spiral pattern. Playback speed 1/200×.

Movie S2: Spot pattern. Playback speed 25×.



---

## Chapter 6 Conclusion and perspective

## 6 Conclusion and perspective

### 6.1 General conclusion

Fracture of material is a macroscopic behavior, which typically takes place by nucleation and growth of localized cracks and results in the decrease of remote stress in the mechanical response. A critical condition argument is widely applied in fracture mechanics, that the fracture energy  $\Gamma$  is defined as equal to the critical value of the strain energy release rate  $G_c$ , where the crack begins to propagate from a preexisting notch. Theoretical analysis and experimental observations based on these models treat fracture as a sudden event, simply considering fracture as a change of macroscopic geometry. However, with the development of detection methods, abundant structural and mechanical changes before a macroscopic transition occurs have been discovered and invalidate the existing simple models, such as strain localization,<sup>1</sup> large-scale molecular bonds breaking<sup>2,3</sup> and strain induced crystallization<sup>4,5</sup> around a localized geometry. These “subtle” changes are directly related to fracture, and the investigation of these local events can help us to understand fracture mechanisms and to optimize fracture resistance. Furthermore, the in-situ observation of these events can be designed to be used in real time in a non-destructive way to estimate the life time or prevent failure of the materials. We focus in this thesis on characterization of microscopic and mesoscopic behavior before fracture, namely “fracture precursors”, which can take place a long time (even hours) before the ordinary detection of crack propagation.

#### 6.1.1 Optical methods for fracture characterization

To quantitatively measure the time-dependent behavior, we developed different optical techniques and combined them with mechanical testing set-ups designed to study the fracture of elastomers. Several methods are applied in this thesis:

1. Multiple speckle diffusing wave spectroscopy (MSDWS). By measuring the decorrelation profile of multiply scattered light intensity from the probes in the materials, deformation rate can be measured with excellent time and strain rate resolution. We applied MSDWS to measure the transient change in deformation rate heterogeneity before crack propagation and other macroscopic transitions.

2. Confocal microscopy. We used confocal microscopy to visualize the 3D damage distributed around the opened crack induced during the crack opening and to understand material behaviors at the molecular level. Mechanophore molecules are used as labels and incorporated as crosslinkers in the elastomer network (PDMS and acrylates elastomers), and fluorescence emission upon their rupture was measured with micron resolution.
3. Digital image correlation (DIC). DIC is a well-established method to measure fields of small displacements with sub-pixel resolution. With the displacement of the regions containing speckles (prepared by spray painting) from the reference image, the deformation tensor can be calculated. We found that MSDWS has superior time and displacement (of the tracer/probe) resolution over DIC, while DIC gives directly deformation tensor and is more universal for measurements in different geometry and conditions. DIC was mainly used as a supplementary method to provide spatially resolved mechanical response.
4. Direct imaging and digital image processing. With ordinary imaging, morphological differences and changes can be directly visualized. Grey scale values of digital images can be further processed to optimize and quantify the relevant parameters.

### 6.1.2 Deformation heterogeneity as a sign of microscopic damage before fracture

We characterized the fracture behavior in a model commercial elastomer: PDMS. The PDMS (Sylgard 184) we chose is brittle for an elastomer (with a nominal fracture strain  $\varepsilon_N < 0.25$ ) where a crack propagates rapidly at the critical fracture strain. With the combination of MSDWS and confocal microscopy, we detected subtle changes beyond force measurement and crack observation. At relatively long time scales ( $\Delta t \sim 10$  min/ $\Delta\varepsilon_N \sim 0.02$  for continuous stretching and 1 h for fixed strain) before the onset of a detectable propagation, the acceleration of damage accumulation around the crack tip was already observed. Simultaneously with the damage acceleration, an increase in heterogeneity of strain rate was observed by MSDWS far away from the tip ( $\sim$ cm). Although the mechanophore-based mapping of damage distribution is powerful,

visualizing bond scission directly requires both labeling the sample with a mechanophore, which is an additional chemical modification, and high resolution confocal optics. Our discovery that this time dependent molecular damage under load also causes a large scale ( $\sim\text{cm}^2$ ) gradient in deformation rate significantly before fracture is important, since such an observation only requires a relatively common laser and acquisition camera and no chemical labeling. Based on the results, the measurement of changes in heterogeneous deformation rate provides a sensitive detection of fracture precursors, long before microscopic events become critical.

### 6.1.3 Enhancement mechanism of fracture toughness in multiple network elastomers

Multiple network elastomer refers to a series of soft materials that are not only highly stretchable, but also have an excellent fracture toughness. As their mechanical strength and fracture resistance is largely improved, the enhancement mechanism of mechanical property is less understood. To better understand the energy dissipation mechanism due to the breaking of the sacrificial network and how it works around the crack, we developed a 3D visualization method of the damage occurring in multiple networks having their sacrificial network labeled with mechanophores. Damage mapping, together with deformation rate mapping of the whole sample by DIC, shows that multiple network elastomers have a responsive protection against flaws, that deformation localization can be suppressed by a self-strengthening mechanism, benefiting from the strain hardening of filler network. Multiple network elastomers also show an increased resistance to delayed fracture at fixed strain, and the kinetics of the damage accumulation and crack deformation indicate that a self-stabilization mechanism exists in the damaged region under load, which avoids macroscopic fracture over long waiting time.

### 6.1.4 Application of MSDWS to heterogeneous systems

Besides the study of crack propagation, we also developed the application of MSDWS and used it for other systems in this thesis. Taking advantages of its excellent time- and strain rate- sensitivity, we successfully investigated the subtle heterogeneities and time dependent response in several systems.

For example, in Chapter 2, the debonding interface of commercial pressure sensitive adhesive tapes under constant applied shear was observed with MSDWS. Although the strain/stress concentration at the interface has been theoretically predicted, it is directly visualized for the first time with experimental methods. Furthermore, we detected the increase in strain rate heterogeneity a long time before debonding occurs, and we explore the possibility to optically predict adhesive debonding. In Chapter 5, we applied MSDWS to the dynamics of swelling of a constrained hydrogel. Coupling with surface creasing due to elastics instability, the swelling kinetics deviates from the behavior predicted by classical models focusing on thermodynamics, and is spatially heterogeneous.

Based on our progress in the thesis, we show that MSDWS is a powerful tool to study the transient and heterogeneous behavior in polymer network systems.

## 6.2 Perspective

Combining optical characterization, simulation and theoretical analysis, we improved our understanding on the subtle behavior occurring before fracture in soft polymer networks. This work can be further expanded in several aspects:

### 6.2.1 Synchronized and responsive controlling

**Synchronized control:** Different measurements, even though they were performed simultaneously, are controlled separately in this thesis. For the time scale (1 ~ 10000 s) relevant in our study, the time delay due to the separate controlling is not critical, while it can be important for applications in real-time detection of fast failure behavior. Synchronized control (e.g. by LabVIEW programming) can improve the performance of the methods shown in this thesis.

**Responsive control:** As we focus on dynamic characterizations, material parameters are changing over time, and the measurement conditions also vary at different stages during the experiments. In forthcoming work, this could be optimized by adjusting experimental parameters in-situ from a feed-back loop. For example, the thickness change during uniaxial extension is around 0.1 mm and the absorption is renormalized by using a bulk region as a reference. The surface displacement can be measured easily with laser detection and the drifts can be sent to confocal microscopy software to adjust the

detection depth for the next scan.

## 6.2.2 Better understanding and application of MSDWS

In this thesis, we intensively used MSDWS but mainly focused on its use to measure strain rate. As it gives a sensitive motion measurement, MSDWS has been reported to be able to measure an abundant variety of dynamics behaviors, such as molecular mobility<sup>6</sup> and cluster rearrangement.<sup>7</sup> It was also pointed out that by careful examination of the autocorrelation function, different contributions of dynamics can be distinguished and characterized.<sup>7-9</sup>

For the investigation of the fracture behavior, we chose parameters in a range where the contribution of strain rate to the autocorrelation function is dominating. Future work can further analyze the profile of the autocorrelation function to extract more information on the actual fluctuations of the molecules reflected by the motions of probe particles.

## 6.2.3 Improving failure prediction with machine learning

We have explored the microscopic changes long before macroscopic fracture in different materials. Qualitative models have been proposed and discussed in this thesis, but the full understanding of the relationship between the dynamic precursors and the macroscopic transition requires further investigation and development of multi-scale models. On the other hand, even though not theoretically understood, the response of a specific material can be analyzed, which is important for the practical application of the techniques.

Since the details of the fracture mechanism can be different among different materials, it is almost impossible to theoretically predict a macroscopic failure. However, taking advantages of the development of machine learning methods, the quantitative measurement by the methods in our work can be better analyzed. In the future work, a strategy can be applied that after enough samples are tested until broken under interested loading geometry, the relationship between precursor (size and time scale of the dynamics heterogeneity, pattern growth kinetics, etc.), loading information and propagation behavior can be obtained. After building the empirical relationship between precursor and fracture by machine learning, the macroscopic transition can be predicted and prevented without knowing the material itself.

### 6.3 Reference

- 1 Luo, F. *et al.* Crack Blunting and Advancing Behaviors of Tough and Self-healing Polyampholyte Hydrogel. *Macromolecules* **47**, 6037-6046, doi:10.1021/ma5009447 (2014).
- 2 Ducrot, E., Chen, Y. L., Bulters, M., Sijbesma, R. P. & Creton, C. Toughening Elastomers with Sacrificial Bonds and Watching Them Break. *Science* **344**, 186-189, doi:10.1126/science.1248494 (2014).
- 3 Millereau, P. *et al.* Mechanics of elastomeric molecular composites. *Proceedings of the National Academy of Sciences* **115**, 9110-9115 (2018).
- 4 Zhang, H. *et al.* Strain induced nanocavitation and crystallization in natural rubber probed by real time small and wide angle X-ray scattering. *Journal of Polymer Science Part B: Polymer Physics* **51**, 1125-1138 (2013).
- 5 Marano, C., Boggio, M., Cazzoni, E. & Rink, M. Fracture phenomenology and toughness of filled natural rubber compounds via the pure shear test specimen. *Rubber Chemistry and Technology* **87**, 501-515 (2014).
- 6 van der Kooij, H. M., Susa, A., Garcia, S. J., van der Zwaag, S. & Sprakel, J. Imaging the Molecular Motions of Autonomous Repair in a Self-Healing Polymer. *Adv Mater* **29**, doi:10.1002/adma.201701017 (2017).
- 7 Aime, S., Ramos, L. & Cipelletti, L. Microscopic dynamics and failure precursors of a gel under mechanical load. *Proc Natl Acad Sci U S A* **115**, 3587-3592, doi:10.1073/pnas.1717403115 (2018).
- 8 Amon, A., Mikhailovskaya, A. & Crassous, J. Spatially resolved measurements of micro-deformations in granular materials using diffusing wave spectroscopy. *Rev Sci Instrum* **88**, 051804, doi:10.1063/1.4983048 (2017).
- 9 Cipelletti, L., Brambilla, G., Maccarrone, S. & Caroff, S. Simultaneous measurement of the microscopic dynamics and the mesoscopic displacement field in soft systems by speckle imaging. *Opt Express* **21**, 22353-22366, doi:10.1364/OE.21.022353 (2013).

## Appendix

During my PhD, I collaborated with other colleagues, where I collected and analyzed x-ray scattering data during the deformation and fracture of thermoplastic elastomers (TPE). TPE are advanced material that combine high elasticity and processability at high temperature. Crosslinking relies on physical associations and microphase separation only, so that mechanical properties of these elastomers depend strongly on temperature and show a unique behavior compared to ordinary elastomers. As the mechanical properties of TPE are related to their structural transitions during deformation, it is important to understand the coupling between change in structure and changes in properties.

The combination of X-ray scattering and mechanical testing is applied to characterize the structural transition, related to the macroscopic deformation. Since this part of my work is not related to the main content of the thesis and yet I am the co-author in the published papers based on it, I attach the published papers here as appendix.

- (1) Sbrescia, S., **Ju, J.**, Engels, T., Van Ruymbeke, E., & Seitz, M. (2021). Morphological origins of temperature and rate dependent mechanical properties of model soft thermoplastic elastomers. *Journal of Polymer Science*, 59(6), 477-493.
- (2) Scetta, G., **Ju, J.**, Selles, N., Heuillet, P., Ciccotti, M., & Creton, C. (2021). Strain induced strengthening of soft thermoplastic polyurethanes under cyclic deformation. *Journal of Polymer Science*, 59(8), 685-696.
- (3) Scetta, G., Euchler, E., **Ju, J.**, Selles, N., Heuillet, P., Ciccotti, M., & Creton, C. (2021). Self-Organization at the Crack Tip of Fatigue-Resistant Thermoplastic Polyurethane Elastomers. *Macromolecules*.



## Self-Organization at the Crack Tip of Fatigue-Resistant Thermoplastic Polyurethane Elastomers

Giorgia Scetta, Eric Euchler, Jianzhu Ju, Nathan Selles, Patrick Heuillet, Matteo Ciccotti,\* and Costantino Creton\*

Cite This: *Macromolecules* 2021, 54, 8726–8737

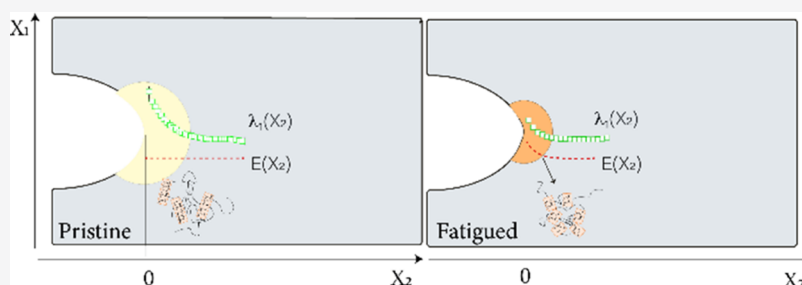
Read Online

ACCESS |

Metrics & More

Article Recommendations

Supporting Information



**ABSTRACT:** Despite their technological relevance, the resistance of soft thermoplastic polyurethanes (TPU) to crack propagation in cyclic fatigue has never been investigated in detail. In particular, a clear shortcoming in the literature for this class of materials is the lack of connection between the cyclic fatigue resistance and the large strain behavior that has a fundamental role in defining the material's resistance to crack propagation. We demonstrate here for the first time that when the strain-induced stiffening mechanism of TPU (already observed for large deformation) is combined with the presence of the nonhomogeneous strain, as in the case of cyclic fatigue, it produces a selective reinforcement in the crack tip area, which is the key to explain the remarkable cyclic fatigue resistance of TPU. Using commercial TPU with similar modulus ( $\sim 8$  MPa) but different large strain behavior, we show that the described mechanism stems from the multiphase nature of TPU and it is not necessarily linked to a specific large strain property as the case of TPU, which undergoes strain-induced crystallization.

### INTRODUCTION

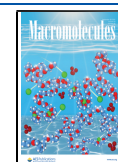
Thermoplastic polyurethanes (TPU) are segmented multi-block copolymers characterized by alternating blocks of soft segments (SS) and hard segments (HS). The former are composed of long and flexible polyester or polyether chains that ensure high deformability, while the latter consist of urethane-rich hard segments. The TPU typically self-organize in hard domains (HD), which are generated from the lateral stacking of HS through physical interactions and hydrogen bonding. They generally have dimensions of tens of nanometers,<sup>1,2</sup> comparable to that of common reinforcing fillers used in rubbers. TPU can be produced in different grades with Young's moduli  $E$  ranging from a few MPa to 1.000 MPa. Among those, soft TPU ( $E < 10$  MPa), where the flexible chains represent the majority of the material and are physically cross-linked by the HD, generally show high elasticity and excellent abrasion resistance at ambient temperatures. Despite their high price, soft TPU have already found many applications in fields as sportswear and footwear and are gaining increasing industrial attention as recyclable alternative to replace classical filled and vulcanized rubber in structural applications such as cables, dampers, and belts. One of the most desirable properties in this kind of structural applications

is the ability to sustain a large number of cyclic loadings at low stress levels without hazardous rupture of the material. In other words, they must have an appreciable cyclic fatigue resistance.

In a previous paper,<sup>3</sup> we proposed a method to probe the cyclic fatigue resistance of soft TPU based on the classic fracture mechanics approach, originally developed for chemically cross-linked rubbers. We highlighted that during cyclic deformation, TPU experience a shake down<sup>4</sup> and stabilization of the stress–stretch curve. Provided that the loading and unloading cycles are conveniently adapted to tackle the effects of plastic creep, the crack propagation process in standard notched pure-shear samples can be robustly expressed as crack propagation per cycle  $dc/dn$  as a function of applied energy release rate  $G$ . These preliminary results confirmed the very high resistance of soft TPU to crack propagation under cyclic fatigue conditions even for large applied strains. To date, a

Received: April 28, 2021

Published: September 16, 2021



clear shortcoming in the literature for this class of materials comes from the lack of connection between the cyclic fatigue resistance and the large strain behavior that has a fundamental role in defining the material's resistance to crack propagation. Although the typical range of bulk strain used in fatigue experiments is generally considerably lower than the strain at break in uniaxial tests, the presence of the crack induces significantly larger local strains at the crack tip.<sup>5,6</sup> This strain concentration is particularly important for TPU since their structure, and hence the mechanical response, evolves with applied strain.<sup>1,7–11</sup> However, previous studies on the structural evolution of hard domains with applied strain only focused on uniaxial tension samples and did not include the effect of local singularities generated by defects or notches as is the case for fatigue fracture. Indeed, as proved by Mzabi et al.<sup>5</sup> in filled and cross-linked styrene-butadiene rubber (SBR), the presence of a loaded crack generates a local strain gradient at the crack tip, the amplitude of which depends on external loading and on material's characteristics. To the best of our knowledge, a comprehensive characterization of the local morphology induced at the crack tip during a cyclic fatigue experiment, and the discussion of its effects on the crack propagation rate for soft TPU has never been carried out.

To understand the effect of a loaded crack on local structural modifications, it is useful to briefly recall some key results obtained in the uniaxial extension of TPU.<sup>7,9–16</sup> Bonart<sup>1</sup> was among the first authors to investigate the deformation behavior of TPU using small- and wide-angle X-ray scattering, SAXS, and WAXS, respectively. He proposed that, for moderate levels of stretch ( $\lambda < 3$ ), the progressive alignment of the SS along the tensile direction exerts a torque on the HD. As a result, the HD tend to orient in a transversal direction relative to the applied load. In a TPU with a low percentage of HS, further elongation generally corresponds to a reorganization of HD and alignment along the loading direction. This process, defined as “restructuring of the cross-linking” by Ishihara,<sup>12</sup> consists of breaking and re-forming hydrogen bonds to realign the hard segments. An excellent summary on X-ray investigations in deformed TPU with low HS content (weight percentage about 12%) was provided by Yeh and co-workers.<sup>7</sup>

In this work, we tested the cyclic fatigue resistance of two TPU which share very similar small strain properties but present completely different large strain behavior in uniaxial tension at ambient temperature: TPU\_XTAL which displays a marked strain-hardening partially due to strain-induced crystallization (SIC) and TPU\_SOFT, which has higher extensibility and barely visible strain-hardening before rupture. In addition to the fatigue experiments, expressed by  $dc/dn$  vs  $G$  and uniaxial step-cycle tests, we used two additional techniques to characterize the differences between the bulk and at the crack tip as the sample is experiencing loading cycles in fatigue: digital image correlation (DIC) to characterize the strain field near the crack tip and spatially resolved in situ X-ray wide- and small-angle scattering analysis (WAXS, SAXS) to detect structural changes with the number of cycles both in the bulk and near the tip.

## MATERIALS AND METHODS

**Materials.** The used TPU are commercial polyester-based polyurethane multiblock copolymers produced by BASF, Elastollan series, with the trade names: S65A 12P and LP9277 10, respectively, denoted as TPU\_XTAL and TPU\_SOFT based on their large strain

behavior under uniaxial conditions. The materials were kindly provided by BASF.

Dog-bone samples had a cross section of 2 mm × 4 mm and were cut along the injection direction from a 2 mm thick square-plate injection molded by the Laboratoire de Recherche et Contrôle des Caoutchoucs et Plastiques (LRCCP). The injection conditions are reported in Figure S1 and Table S1. The pure-shear geometry is generally used in cyclic fatigue experiments because the energy release rate  $G$  can be easily calculated and is independent of crack length.<sup>17</sup> All pure-shear samples were pre-notched using a fresh razor blade with a 20 mm cut. The chemical composition of both TPU is not available since they are commercial products. The number-average molecular weight  $M_n$  and weight-average molecular weight  $M_w$  of TPU\_XTAL after injection are 47 and 61 kg/mol, respectively, and were obtained by gel permeation chromatography (GPC). The values of absolute molecular weights were extracted from refractive index and light scattering signals, using a measured  $dn/dc$  value of 0.11 mL·g<sup>-1</sup> for the TPU. Fourier transform infrared (FTIR) spectroscopy was used for structural analysis of the polymers. Only in the case of TPU\_SOFT, it revealed an absorbance peak around 1640 cm<sup>-1</sup>, which may be consistent with the presence of bidentate urea. The latter is generally associated with stronger interactions than simple hydrogen bonding in HD<sup>18</sup> and may explain the poor solubility of TPU\_SOFT suggesting a stronger interdomain stability.

**Step-Strain Cyclic Tests.** The dog-bone-shaped samples were strongly fixed between mechanical clamps since TPU are very tough. An optical detection system was used to measure the local stretch in the gauge area of the sample and to check the absence of slippage from the clamps during the test. The samples were loaded under uniaxial conditions at the stretch rate of  $\dot{\lambda} = 4$  s<sup>-1</sup>. The loading was performed in a stepwise mode: 10 cycles were performed for each increasing value of maximum applied stretch  $\lambda_k$  for both TPU. The stress was reduced to  $\sigma = 0$  between two successive steps to prevent buckling. The mechanical quantities strain  $\varepsilon$ , stretch  $\lambda$ , Hencky strain  $h$ , nominal stress  $\sigma$ , and true stress  $T$  are defined as below.

$$\varepsilon = \frac{l - l_0}{l_0} \lambda = \frac{l}{l_0} h = \int dl = \int_{l_0}^l \frac{1}{l} dl = \ln(\lambda) \sigma = \frac{F}{A_0} T = \sigma \cdot (1 + \varepsilon)$$

Here,  $l_0$  and  $l$  indicate the initial length and instantaneous length, respectively;  $A_0$  is the initial cross-sectional area; and  $F$  is the measured force.

**WAXS and SAXS Characterization.** In situ WAXS and SAXS experiments were carried out under two conditions: on relaxed samples ( $\lambda = 1$ ) and on strained samples ( $\lambda = 2.5$ ). The first set of experiments ( $\lambda = 1$ ) was carried out on a GANESHA 300XL+ system from JJ X-ray 1 in the X-ray lab at DSM Materials Science Center in the Netherlands. The in situ experiments on strained samples ( $\lambda = 2.5$ ) were carried out at the PETRA III beamline P03 at Deutsches Elektronen-Synchrotron (DESY) in Hamburg. The technical details of the scattering experiments are summarized in Table 1.

The two-dimensional (2D) scattering data were integrated using the software tool FIT-2D.<sup>19</sup> All data were corrected by subtracting background scattering. In situ WAXS and SAXS experiments were

**Table 1. Parameters of X-ray Experiments**

facility	DESY, Petra III	DSM resolve
energy	13 keV	8.4 keV
wavelength ( $\nu$ )	0.096 nm	0.15 nm
beam size	22 × 16 $\mu\text{m}^2$	300 × 300 $\mu\text{m}^2$ (SAXS) 700 × 700 $\mu\text{m}^2$ (WAXD)
step width	100 $\mu\text{m}$	
distance from detector		
SAXS	4050 mm	1465 mm
WAXS	171 mm	120 mm
image resolution	172 × 172 pixel	172 × 172 pixel

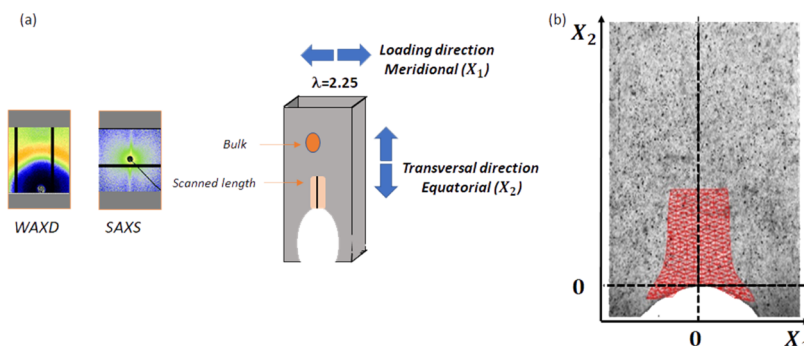


**Figure 1.** Sketch of the experimental setup for WAXD and SAXS in situ experiments (a). Example of open crack profile and deformed mesh obtained from DIC analysis (b).  $X_1$  and  $X_2$  indicate the directions parallel (meridional) and perpendicular (equatorial) to the applied load, respectively.

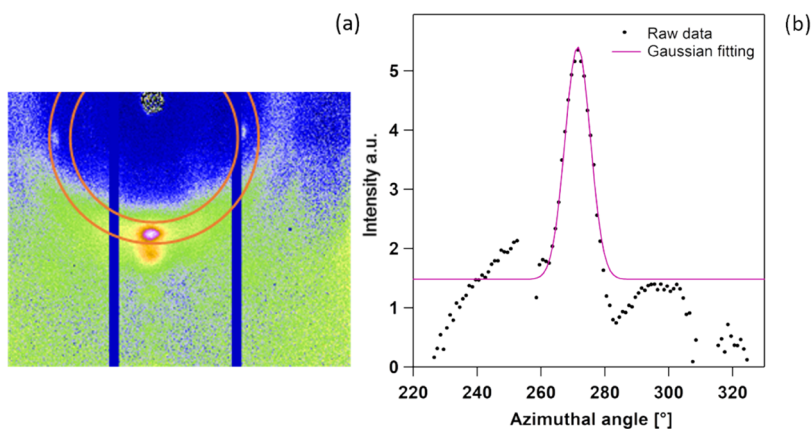


**Figure 2.** Example of azimuthal integration to evaluate the orientation factor (a). Example of Gaussian fitting of azimuthal one-dimensional (1D) profile to evaluate the FWHM (b).

carried out for two sets of samples: samples that were pre-fatigued and pristine samples. All of them contained a notch. For in situ experiments, the notched pure-shear specimens were stretched in a displacement-controlled mode up to  $\lambda = 2.25$ , then 2D WAXS and SAXS scans were performed along the entire sample's length parallel to the crack and in front of it. The position of the first point (the actual crack tip) has an uncertainty of  $\pm 100 \mu\text{m}$ , i.e., the step width between each successive scan. Figure 1a reports a schematic of the in situ scattering experimental setup. Figure 1b is an example of the crack profile of the loaded sample and shows the deformed mesh used to evaluate the local strain at the crack tip. The axes  $X_1$  and  $X_2$  correspond to the direction parallel (meridional) and perpendicular (equatorial) to the applied load.

**WAXS Analysis.** The 2D WAXS pattern was circularly integrated. Peaks in the  $2\theta$  range between  $12$  and  $20^\circ$  were deconvoluted using Gaussian/Lorentzian peak fitting routines. The crystalline fraction  $\chi_c$  was evaluated classically as the ratio between the total area of crystalline peaks  $I_{cr}$  and the total area (crystalline and amorphous:  $I_{cr} + I_{am}$ ) underneath the diffraction profile as

$$\chi_c = \int_{2\theta} \frac{I_{cr}}{I_{cr} + I_{am}}$$

Azimuthal integration was performed on the most prominent peak as indicated in Figure 2a. The obtained peak was then fitted with a Gaussian function to calculate the full width at half-maximum (FWHM) as in Figure 2b. The value of FWHM is indicative of the variability of the lattice parameter around its average value and it is an indication of the level of disorder of the structure. A high value of FWHM indicates less order in the crystal phase.

**SAXS Analysis.** SAXS data are expressed in terms of intensity as a function of wave vector  $q = \frac{4\pi \sin \theta}{\lambda}$ , where  $2\theta$  is the scattering angle

and  $\lambda$  is the wavelength. The long period  $L$  represents the recurrent spacing periodicity between hard domains,<sup>1</sup> and it was calculated as  $L = \frac{2\pi}{q^*}$ , where  $q^*$  represents the center of the Gaussian fitting of the peak in the 1D SAXS profile.

**Cyclic Fatigue Experiments.** Fatigue results are generally expressed in terms of crack propagation per cycle  $dc/dn$  vs  $G$ . All of the experiments were carried out on pure-shear samples following the procedure developed for TPU by Scetta et al. in a previous paper.<sup>3</sup> The curve  $G(\lambda_{max})$  was evaluated on un-notched pure-shear samples by applying sinusoidal cycles between  $\sigma_{min} = 0$  and an increasing value of the maximum stretch  $\lambda_{max}$  at the frequency of 10 Hz. Under cyclic conditions, the stress–stretch curve of TPU shows a very marked stress softening and some residual strain that eventually stabilizes between 5000 and 10 000 cycles. This effect is known as shake down.<sup>4</sup> We used the stress–stretch curve at 10 000 cycles to evaluate  $G(\lambda_{max})$  as  $G = HW_{PS}(\lambda_{max})$ , where  $H$  is the unstrained height of the pure-shear sample and  $W_{PS}$  is the strain energy density as a function of the maximum applied stretch  $\lambda_{max}$  in the pure-shear geometry.<sup>17</sup> To evaluate the crack propagation per cycle, a single long notch of 22 mm was cut on pristine samples. Each notched sample was strained between  $\sigma_{min} = 0$  and  $\lambda_{max}$  for a minimum of 36 000 cycles. During the test, the extension of the crack was monitored using a digital camera (BAUMER VCXU-32M) with a resolution of 3.1 Megapixel equipped with a macro-objective resulting in a pixel size of  $38 \mu\text{m}$ . The crack propagation rate stabilizes after 5000–10 000 cycles and then we evaluated  $dc/dn$ .

**Digital Image Correlation (DIC).** DIC is a technique that allows measuring displacement fields by matching a reference with a deformed image. Here, the Correli-LMT software,<sup>20</sup> which represents the displacement field by the same kind of mesh as in finite element methods, was used. The final displacement is evaluated using an

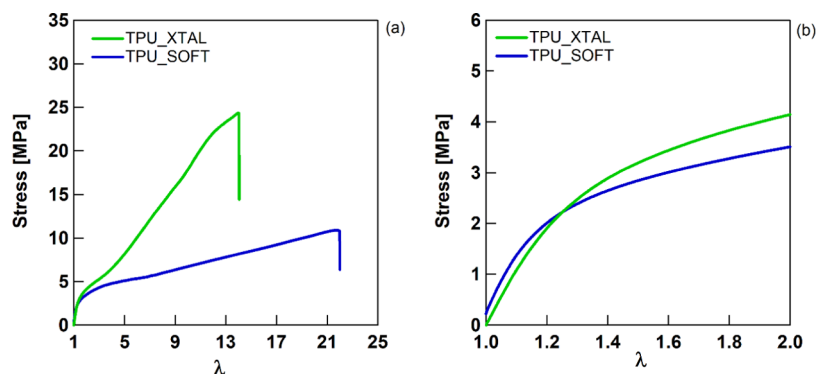


**Figure 3.** Uniaxial nominal stress–stretch curve of TPU\_XTAL and TPU\_SOFT at 23 °C (a). Zoom on the small stretch region (b).

algorithm that minimizes the difference in the gray levels between the matched images, while imposing some level of regularity to the solutions.

The objective adopted for this analysis corresponds to a pixel size of 7  $\mu\text{m}$  and the mesh size was  $x$  chosen as 16 pixels. Under this condition, the spatial resolution of the DIC analysis (minimum distance between two adjacent estimates of displacement) was 112  $\mu\text{m}$ . Since the datapoint associated by convention with a distance of 0 mm from the crack tip is indeed the closest available point, this spatial resolution should also be considered as an uncertainty on the distance of such point from the crack tip. The samples were uniformly backlit. A random speckle texture was obtained by black ink spraying, a method which provides a good contrast with the sample surface (either white or transparent). For each DIC characterization, a set of 40–60 images was acquired between  $\sigma_{\text{min}} = 0$  and  $\lambda_{\text{max}}$ . To minimize the alteration of the gray levels by the large applied strains during DIC, the correlation procedure was first performed between each couple of subsequent images starting from the unloaded condition up to the maximum strain. Then, the total displacement for each  $\lambda$  was evaluated by progressively adding the differential displacement fields of each step. The total displacement field was then used to evaluate the local strain field following the same procedure as in Mzabi et al.<sup>21</sup>

## RESULTS

**Tensile Tests.** Figure 3a reports the stress–stretch curve in uniaxial tension at 23 °C and highlights the main differences in large strain behavior between TPU\_XTAL and TPU\_SOFT. Both TPU are characterized by a high extensibility at failure (more than 1000%) and, after an initial linear elastic regime that only lasts a few percent strain, they soften as displayed in Figure 3b. In the case of TPU\_XTAL, this is rapidly followed by a marked strain hardening, which is much less pronounced in TPU\_SOFT. Table 2 reports the elastic moduli as well as the stress and stretch at break for both TPU.

**Cyclic Fatigue.** Figure 4a shows the values of  $dc/dn$  in the steady-state regime as a function of  $G$  for both TPU. The threshold values,  $G_t$ , indicated in the picture, are conventionally evaluated using the same procedure adopted in our previous paper<sup>3</sup> and correspond to the minimum value of  $G$

**Table 2.** Tangent Modulus ( $E$ ), Maximum Stretch ( $\lambda_b$ ), and Maximum Nominal Stress ( $\sigma_b$ ) at Break for TPU\_XTAL and TPU\_SOFT at 23 °C

name	$E$ [MPa]	$\lambda$	$\sigma_b$ [MPa]
TPU_XTAL	8.7	15.4	25.1
	$\pm 0.1$	$\pm 1.2$	$\pm 1.3$
TPU_SOFT	7.8	19.1	11.5
	$\pm 0.1$	$\pm 2.8$	$\pm 0.8$

below which during a single fatigue experiment lasting 36 000 cycles and with the resolution of our optical system (38  $\mu\text{m}$ ), we could not detect any crack propagation. Under this condition, the minimum detectable crack growth per cycle was equal to:  $\frac{38\text{m}}{36\,000\text{ cycles}} \sim 1\text{ nm/cycle}$ . Using this definition, the values of  $G_t$  were found to be  $\sim 3$  and  $\sim 5\text{ kJ/m}^2$  for TPU\_SOFT and TPU\_XTAL, respectively. We underline that this is not a physical value of  $G_t$ , but it depends on the experimental system, and we cannot exclude that higher resolution and/or longer testing may lead to a lower value of  $G_t$ . Nevertheless, in classical rubbers, the average threshold  $G_t$  is typically found between 40 and 100  $\text{J/m}^2$ ,<sup>2,22,23</sup> well below those obtained for TPU, which present a fatigue threshold (and the corresponding stretch  $\lambda$ ) more than 1 order of magnitude larger. Above the threshold,  $dc/dn$  of TPU\_XTAL increases as a power law  $\approx G^{2.7}$ . This behavior is similar to that found in several elastomeric systems, where the exponent  $n$  varies between 1 and 4.<sup>24</sup> On the other hand, TPU\_SOFT has a rapid transition between a very slow- or almost not propagating regime to a fast-propagating regime, where the values of  $dc/dn$  are only weakly dependent on  $G$  and are higher than that for TPU\_XTAL at comparable  $G$ . The toughness, generally defined as a critical value  $G_c$  or  $\Gamma$  above which the crack propagates so fast that the sample breaks in a few cycles,<sup>25</sup> must be above 20  $\text{kJ/m}^2$  in both TPU since this unstable regime was not observed. For comparison, for a typical filled natural rubber with similar linear modulus, the average value of toughness is generally below 10  $\text{kJ/m}^2$ .<sup>25</sup> Overall, both TPU have a higher fatigue resistance than classical filled elastomers at the same applied  $G$  and require a much higher strain to propagate the crack during cyclic fatigue. Figure 4b reports an equivalent representation in terms of  $dc/dn$  vs the maximum stretch  $\lambda_{\text{max}}$  which demonstrates the extremely large strain required to propagate a crack in cyclic fatigue for TPU. Interestingly, comparable values of  $dc/dn$  for a similarly high value of  $\lambda_{\text{max}}$  were reported by Li et al.<sup>26</sup> in a hydrogel material, which, similarly to TPU, presents a multiphase morphology. They showed that highly fatigue resistance hydrogels containing a reinforcing hard phase at the 100 nm scale, much larger than the characteristic size of the polymer network defined as the characteristic distance between cross-links (10 nm), can be deformed at  $\lambda_{\text{max}} > 1$  for thousands of cycles without initiating a catastrophic propagation of the crack. In those systems, the maximum stretch is a critical parameter in determining the resistance of the material against fatigue.

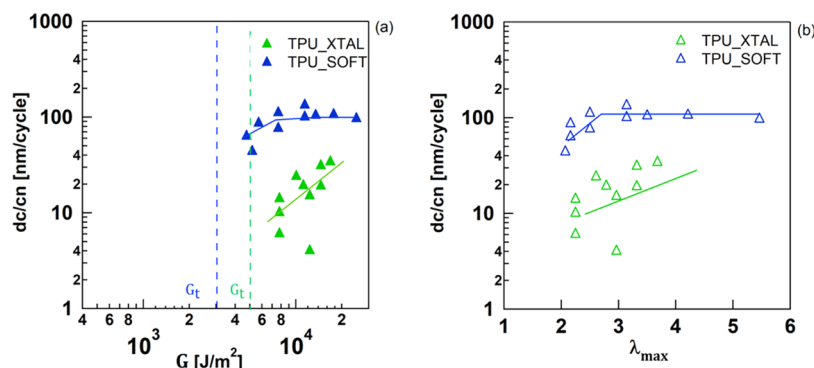


**Figure 4.** Crack growth rate per cycle as a function of the applied release rate  $G$  (a) and applied stretch  $\lambda_{\max}$  (b) for TPU\_XTAL and TPU\_SOFT at 23 °C.

### Stiffening Effect in Cycles of Uniaxial Deformation.

Characterizing the large strain cyclic behavior is fundamental to better understand the fatigue resistance of TPU. In cyclic fatigue, the crack propagates at levels of bulk applied stretch considerably lower than the strain at break in quasi-static extension. Despite that, close to the crack tip, the local strain is higher than in the bulk because of the stress and strain concentration induced by the crack. The history of a material point being approached by the propagating crack during cyclic fatigue can be simplistically represented by step-strain cyclic experiments up to rupture. In a previous paper,<sup>27</sup> we performed cyclic uniaxial loading at increasing values of maximum stretch for the same TPU used in this work. We demonstrated that the dissipative behavior in the uniaxial extension of TPU\_SOFT and TPU\_XTAL is qualitatively very similar and cannot thus explain in any obvious way the considerably higher fatigue resistance of TPU\_XTAL. As explained in our previous work,<sup>27</sup> during the cyclic experiments, the stress–strain response of the material is permanently affected by the maximum applied strain and it does not follow the classical trend observed in cross-linked elastomers. We confirmed this result with two different indicators both at large and small strain, and in Figure 5, we

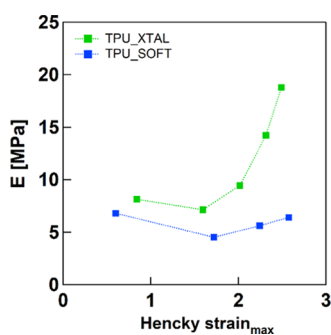


**Figure 5.** Tangent modulus  $E$  vs maximum Hencky strain for both TPU at 23 °C.

report the evolution of the tangent modulus  $E$  (calculated at low strain) with  $\lambda_c$  as often done to estimate damage in elastomers. For both TPU,  $E$  first decreases, as commonly observed in filled elastomers,<sup>28</sup> and above a critical strain, it increases again achieving the same or higher value than the pristine sample. Overall, these results indicate a permanent stiffening effect, which combined with a residual deformation strongly suggests a strain-induced modification in the TPU

microstructure. Figure 5 also shows that the stiffening effect in TPU\_XTAL, which can crystallize under strain, is considerably more pronounced than in TPU\_SOFT for all values of applied maximum stretch. To understand the role of the increase of the elastic modulus with applied strain in TPU under cyclic fatigue, we carried out a complete evaluation of the strain field and of the reorganization of the microstructure at the crack tip before and after fatigue cycling in TPU\_XTAL and TPU\_SOFT.

**Local Strain Gradient in TPU before and after Fatigue.** Figure 6 reports the value of the local stretch  $\lambda_1$  in the loading direction calculated at different distances from the crack tip for both TPU by DIC. Two sets of samples were used: pristine and fatigued. Pristine samples were directly strained at  $\lambda_{\max} = 2.25$ , while fatigued samples were previously cycled for 36 000 cycles and then monotonically strained at the same value of  $\lambda_{\max}$ .

For comparable distances from the crack tip, the value of vertical strain  $\lambda_1$  of the fatigued sample is lower than that of its pristine counterpart in both TPU. However, in the case of TPU\_XTAL, the strain localization is much less pronounced after fatigue and only involves a smaller area around the crack ( $\approx 1000 \mu\text{m}$ ), compared to TPU\_SOFT ( $>2000 \mu\text{m}$ ). This result is consistent with the more pronounced cyclic strain-stiffening effect of TPU\_XTAL reported in Figure 5. At the beginning of the test, the action of repeated cycles at the same value of  $\lambda_{\max}$  gradually modifies the local response of the material, which eventually becomes stiffer and less stretchable at the crack tip explaining the lower values of  $\lambda_1$  in fatigued samples. This effect is also accompanied by an overall induced uniformization of the strain gradient after fatigue as shown in Figure 7, which reports the strain distribution of  $\lambda_1$  along the direction  $X_1$ , parallel to the applied load, in the close vicinity of the crack tip. An additional remark must be made concerning the value of  $\lambda_{\max}$  in fatigued samples. As shown in our previous work,<sup>3,27</sup> TPU generally present some residual strain when cyclically loaded in uniaxial tension. The latter implies that the actual length  $l_0^{\text{fatigued}}$  of unloaded samples after fatigue is longer than the original in pristine sample  $l_0$ , which we used to evaluate  $\lambda_{\max}$ . Therefore, the real stretch experienced by the material is lower than  $\lambda_{\max}$ . This effect is visible in Figure 6 for both TPU, where, for large distances from the crack tip, the value of  $\lambda_1$  at the plateau (which corresponds to the macroscopic applied  $\lambda_{\max}$ ) is slightly higher in pristine than in fatigued sample. This effect is however barely distinguishable and cannot explain the remarkable reduction of the strain singularity after fatigue.

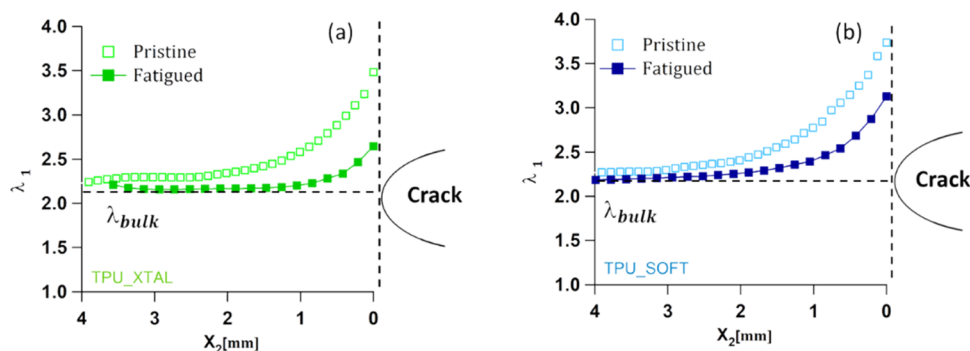


**Figure 6.** Maximum stretch in the loading direction  $\lambda_1$  as a function of the distance from the open crack tip evaluated for TPU\_XTAL (a) and TPU\_SOFT (b), both pristine and after being fatigued for 36 000 cycles at  $\lambda_{max} = 2.25$ .

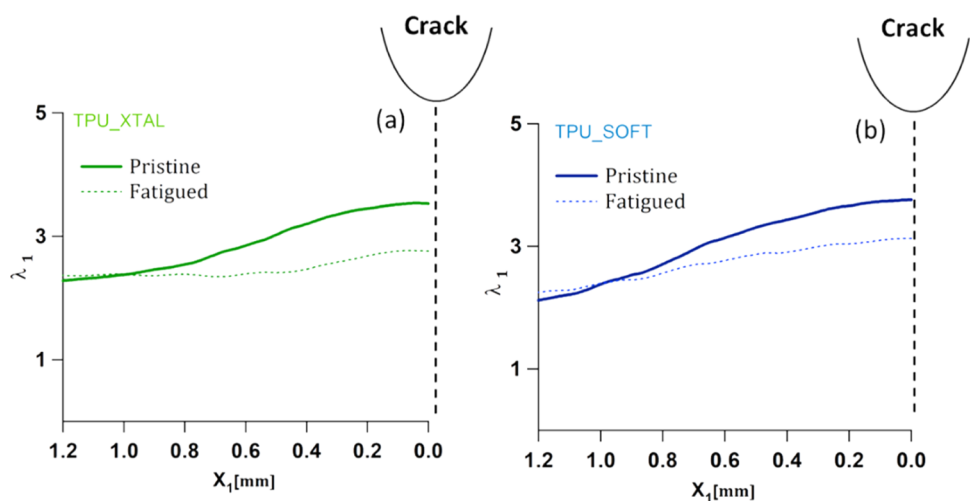


**Figure 7.** Distribution of the maximum  $\lambda_1$  at the crack tip along the loading direction  $X_1$  for pristine and fatigued TPU\_XTAL (a) and TPU\_SOFT (b).

**Effect of the Strain Gradient on the Microstructure in Pristine and Fatigued TPU.** As previously explained, the mechanical properties of TPU are intrinsically related to the hard–soft domains organization. The natural physical explanation for the overall reduction in the intensity of the strain singularity in the crack tip zone in fatigued TPU must be found in the peculiar microstructural rearrangements induced by cyclic loading.

In situ WAXS and SAXS experiments were carried out at different distances from the crack tip on notched pure-shear samples of TPU\_XTAL and TPU\_SOFT loaded at  $\lambda_{max} = 2.25$  as detailed in the **Materials and Methods** section. Also, in this structural analysis, two sets of samples were used: pristine and fatigued as already described for the analysis by DIC. We first discuss notched pristine samples loaded to  $\lambda_{max} = 2.25$ . **Figure 8a** shows representative WAXS and SAXS 2D patterns at two different sample locations, far away (bulk) and very close to the crack tip, obtained for pristine TPU\_XTAL (the corresponding images for TPU\_SOFT are reported in **Figure S2**). A first qualitative analysis of the 2D patterns reveals two important phenomena: (i) the development of a strain-induced anisotropy both in the bulk and in the crack tip zone and (ii) the change in the structure of the material as the local strain gradient develops. More specifically:

- (i) The anisotropic character of strained TPU\_XTAL is visible in all diffraction patterns. The darker area along the meridional direction in the circular 2D WAXS

images indicates that the amorphous SS gradually orient toward the loading direction.<sup>7</sup> Additionally, the presence of two meridional sharp reflections (or lobes) in the SAXS images indicates the preferential tilting of the HD along the meridional (loading direction) axis.<sup>7,9,10,29</sup>

- (ii) The dissimilar morphology developed as the strain gradient increases is demonstrated by the different patterns observed in the bulk and in the crack tip region. In the 2D SAXS patterns corresponding to the crack tip area, the two meridional lobes are clearly less intense, while a new equatorial sharp streak appears. The appearance of the streak can be associated with either the presence of voids<sup>30,31</sup> or a fibrillar morphology<sup>32</sup> and is frequently found in TPU deformed in large strains.<sup>7–10,14,29</sup> This feature stems from the destruction of HD in favor of rod-like soft domains composed of both elongated SS and HS in the most strained region at the crack tip. A similar behavior was also observed in TPU\_SOFT (**Figure S2**). The 1D WAXS integrated profiles for TPU\_XTAL and TPU\_SOFT are reported in **Figure 8b,c**. In the case of TPU\_XTAL (**Figure 8b**), the 1D WAXS profile close to the crack tip shows the presence of two main crystalline peaks, absent in the bulk, indicating the presence of well-oriented strain-induced crystallization (SIC)<sup>29,33</sup> in the higher stretched area (see DIC data in **Figure 6**). On the other hand, crystalline peaks are clearly detected in the bulk and still

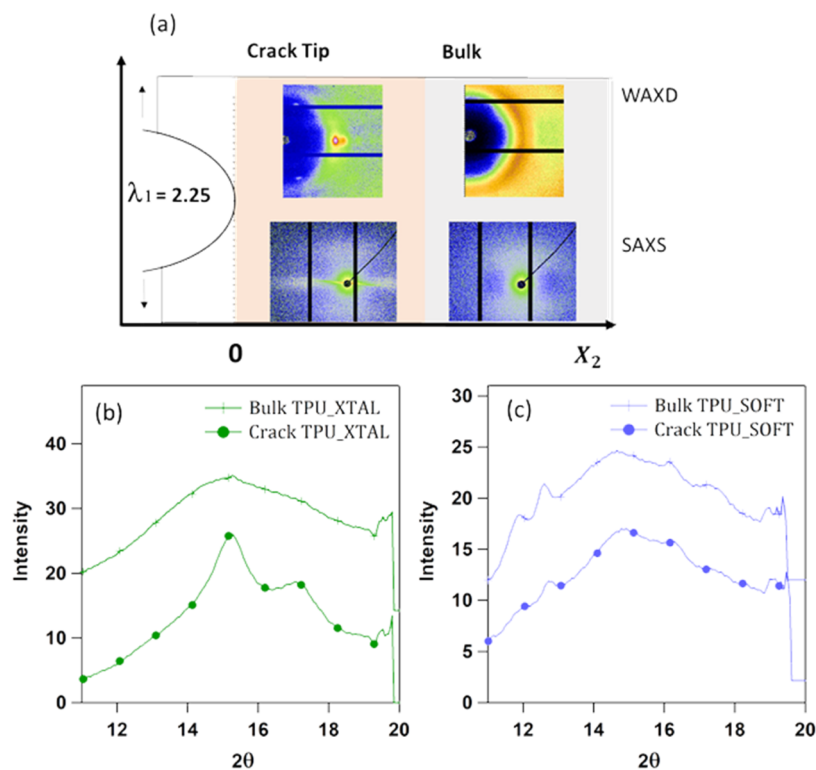


**Figure 8.** Representative in situ WAXD and SAXS 2D pattern for TPU\_XTAL close and far from the open crack for pristine sample monotonically strained at  $\lambda_{\max} = 2.25$  (a). Integrated 1D profile of WAXS crystalline peak in TPU\_XTAL (b) and TPU\_SOFT (c) obtained for the crack tip and the bulk area at  $\lambda_{\max} = 2.25$ .

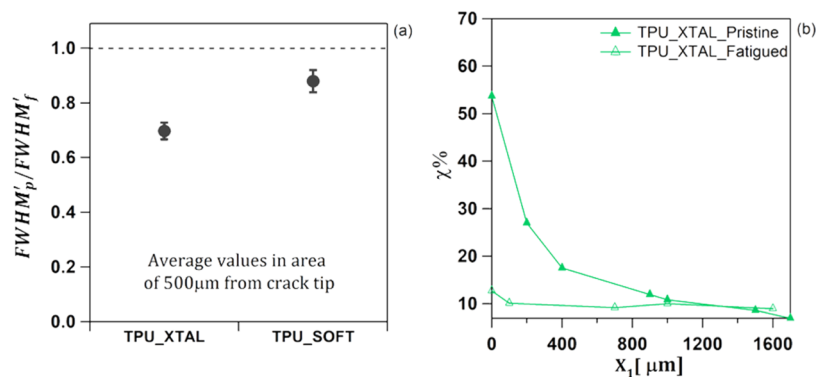


**Figure 9.** Values of averaged FWHM ratio between pristine and fatigued sample (a) and crystalline fraction in TPU\_XTAL at increasing distance from the crack for pristine and fatigued sample (b) monotonically strained at  $\lambda_{\max} = 2.25$ .

visible close to the crack tip for TPU\_SOFT in the 1D WAXS profile of Figure 8c. The position of these peaks corresponds to those of the crystallized butadiene terephthalate<sup>29</sup> (PBT) sequence probably present as a comonomer in TPU\_SOFT. This is however a hard segment (crystalline in the absence of strain) becoming less crystalline with strain.

To evaluate how the effect of several cycles affects the local structure evolution in TPU, we now compare the X-ray scattering results obtained at a similar distance from the crack tip for pristine and fatigued samples of TPU strained at  $\lambda_{\max} \approx 2.25$ . Consistent with the DIC results of Figure 6, we find that the level of orientation and crystallinity is lower for fatigued samples than for pristine ones. Figure 9a shows in particular the ratio between peak widths  $FWHM_p$  and  $FWHM_f$ , where  $FWHM'$  indicates the averaged FWHM values of the peak

integrated along the azimuthal direction (as indicated in the Materials and Methods section) in the region within  $500 \mu\text{m}$  of the crack tip and the subscripts p and f stand for the pristine and fatigued sample, respectively. Values lower than unity indicate that the quality of the crystal orientation in the pristine sample is higher than that for the fatigued sample, at a comparable distance from the crack tip. This implies that the crystallites that were either produced during strain (TPU\_XTAL) or originally present in the hard domains (TPU\_SOFT) become fragmented and less oriented during fatigue. In the case of TPU\_XTAL, we can also extract the crystalline fraction  $\chi$ , at different distances from the crack tip for both pristine and fatigued samples (Figure 9b). It is striking to see that while strain-induced crystallization is very active in pristine samples ( $\chi$  gradually increases when approaching the crack tip), the degree of crystallinity at the crack tip almost completely

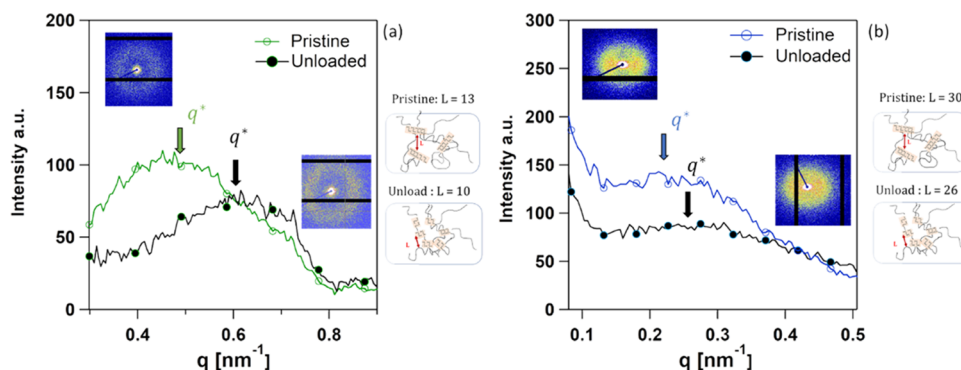


**Figure 10.** Two-dimensional SAXS images and the corresponding 1D profile for pristine and unloaded fatigued (after 36 000 cycles) TPU\_XTAL (a) and TPU\_SOFT (b). The schematics show the decrease of  $L$  and the fragmentation of the HD structure before and after fatigue testing (not all soft segments are represented for clarity). The X-ray patterns were collected at DSM, the Netherlands.

disappears in fatigued samples (Figure 9b). After being fatigued, both TPU\_SOFT and TPU\_XTAL are less oriented and, in the case of TPU\_XTAL, show less strain-induced crystallinity when stretched again. This reduced ability of the cycled sample to orient and crystallize under stretch is somewhat counterintuitive, considering the remarkable fatigue resistance showed by both TPU, and especially by TPU\_XTAL. Since the fraction of strain-induced crystallites increases with the applied strain,<sup>34</sup> we believe that the lower crystalline fraction found in fatigued sample is a direct consequence of the reduced strain concentration (and therefore a lower value of maximum strain) generated at the crack tip during cyclic fatigue.

**Permanent Modification of the Microstructure Induced by Strain History.** In the previous section, we showed that loading cycles induce some reorganization of the original two-phase structure of TPU when stretched at the same value of  $\lambda_{\max} = 2.25$ . We now investigate whether the original morphology is completely recovered when the sample is unloaded. To understand which changes are permanent after the removal of the external load, we compare the scattering patterns of TPU in its relaxed state ( $\lambda = 1$ ) for pristine and fatigued sample with those obtained at  $\lambda_{\max} = 2.25$ . Figure 10 shows 2D SAXS images and the corresponding 1D scattering profiles for TPU\_XTAL (a) and TPU\_SOFT (b). In both cases, the 1D scattering profile is shifted at higher  $q$  for the unloaded fatigued sample; therefore, the interdomain distance  $L$  related to the periodicity of the hard and soft phases reduces slightly for unloaded fatigued sample. The decrease of  $L$  can be interpreted as permanent fragmentation of HD in smaller units during the fatigue experiment<sup>10</sup> as shown in Figure 10a,b for TPU\_XTAL and TPU\_SOFT, respectively. It is worthy to remark that the SAXS analysis for the unloaded sample was performed around 30 days after the sample was fatigued. This led us to believe that such fragmentation is not easy to recover at ambient temperature even for materials that present some relaxation effects as physical cross-linked TPU.

The fragmentation of HD is not the only permanent effect induced by cyclic loading on TPU. In the case of TPU\_XTAL, the new crystalline phase formed near the crack tip during cycling is partially retained after fatigue as shown by the differential scanning calorimetry (DSC) thermograms comparing pristine TPU\_XTAL and a pure-shear sample that was previously fatigued (Figure 11). As also reported by other authors,<sup>35</sup> the endothermic peak ( $T_{\text{m,SIC}}$ ) absent in the pristine sample is associated with a new crystalline phase

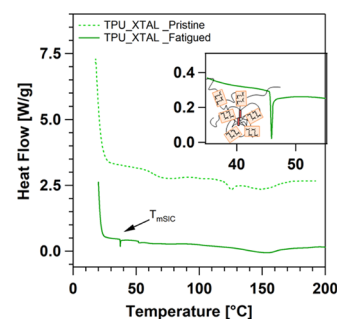


**Figure 11.** DSC thermogram for TPU\_XTAL: pristine and fatigued sample. The inset is a magnification of the endothermic peak in the fatigued sample corresponding to the melt of crystallites schematically represented as red bars.

generated during loading, which persists after the removal of the load (red bars in the schematic of Figure 11).

## DISCUSSION

**Model To Explain the Strain-Induced Reinforcement in TPU.** In strained TPU containing an initial crack, the strain singularity along the crack direction  $X_2$ , expressed as the stretch field  $\lambda_1(X_2)$  evaluated at different distances  $X_2$  ahead of the crack tip, is accompanied by a progressive change in the microstructure as proved by X-ray analysis. The changes in local microstructure with applied uniaxial strain in TPU have been investigated in-depth in the past for homogeneously strained samples.<sup>7,10,11,13,14,29,33,36</sup> Different authors showed that some of those changes are permanent and that the unloaded material does not completely recover its original state,<sup>10,16,29</sup> but, depending on the maximum experienced strain, the polymer retains a certain degree of anisotropy or strain-induced crystallites as shown by the DSC analysis in Figure 11. In particular, for TPU made from SS able to crystallize under strain, the formation of new crystalline domains, which are persistent after unloading, may be responsible for the strengthening of the material with increasing strain. In our case, the modulus of both TPU increases with applied strain, but X-ray analysis shows that only TPU\_XTAL crystallizes under strain. This indicates that the strengthening effect induced by the strain is not uniquely related to the formation of a crystalline phase, but is a general property due to the self-organized structure of TPU in soft and hard domains. We believe that the permanent reorganization of the two-phase microstructure in TPU induces stiffening of the



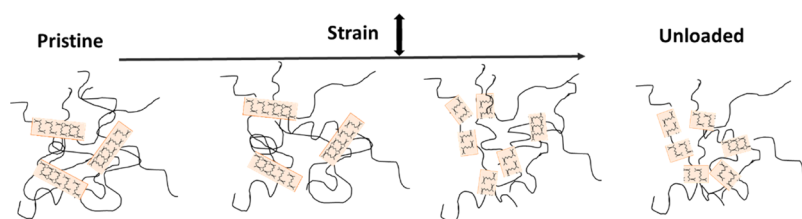


**Figure 12.** Sketch of the effect of elongation on HD restructuration.

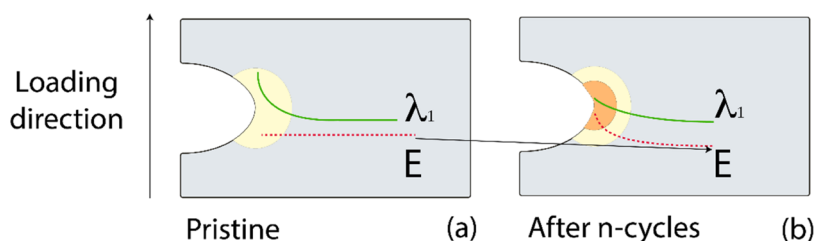


**Figure 13.** Sketch of the spatial evolution of the tangent modulus  $E$  and strain  $\lambda_1$  for pristine and fatigued TPU. In a notched and loaded pristine TPU,  $E$  is constant and a strain gradient is induced by the presence of the crack in the neighboring area (a). After thousands of cycles, the reorganization at the crack tip generates a hard core with a higher local modulus than the bulk, which strengthens the crack tip reducing the strain field compared to the loaded pristine sample (b).

material through two main possible mechanisms, which in some cases can act simultaneously:

- (1) Above a certain value of  $\lambda_{\max}$ , the original HD are fragmented into smaller units and this new structure partially persists after the removal of the strain (as suggested by the decrease of the long period for strained TPU (Figure 10)). The fragmentation of HD may contribute to the increase in stiffness in two different and complementary ways:
  - (A) Filler-like effect of HD. In a homogeneously stretched sample at the same “filler volume fraction”, these smaller and probably well-dispersed HD contribute more to the modulus in analogy with a nanoparticle effect.
  - (B) Physical cross-linking effect of HD. In classical cross-linked elastomers, the elastic modulus is defined by the number of elastically active chains per unit volume. In pristine TPU, we can consider that not all of the polymer chains are elastically active and some of them are coiled in closed loops. When HD are fragmented in smaller units, some elastic chains can be released from their original conformation as schematically shown in Figure 12. In this case, although the density of elastic soft segment chains remains unchanged, the number of elastically active ones can increase causing an increase of the modulus. The reloaded sample thus shows both an increase in tangent modulus and a decrease in the stretch at break with applied strain as shown in our previous paper.<sup>27</sup>
- (2) In this new reconfiguration of HD, some soft chains, which were highly elongated during the deformation of the sample, may be prevented from recovering their original configuration, thus remaining partially elongated in the unloaded sample explaining the presence of residual crystallinity in TPU\_XTAL. This residual crystalline phase acts as additional hard domains as suggested by the larger increase of  $E$  (and reduction of  $\lambda_1$ ) in TPU\_XTAL. This leads to a further increase of the fatigue resistance compared to noncrystallizing TPU,

but it is not a necessary condition for strain-induced reinforcement of TPU.

**Effects Related to the Presence of a Crack in Cyclic Deformation.** Previous investigations on the structural evolution of soft TPU with applied strain mainly focused on homogeneously strained materials and sometimes discussed a remarkable strain-stiffening after elongation.<sup>10</sup> To the best of our knowledge, the effect of the presence of a crack and its associated strain localization has never been investigated in this context. In Figure 6, we have shown that the presence of a strain gradient at the crack tip causes a corresponding spatial gradient in the structural reorganization within the TPU, thus affecting the local mechanical response to the applied strain. Intriguingly, we also observed that the repetition of several loading cycles (at the same bulk  $\lambda_{\max}$ ) leads to a decrease of the strain-induced anisotropy and crystallinity fraction (in TPU\_XTAL) in the crack tip region and, in general, to a decrease in the sharpness of the structural gradient. We infer that the less oriented structure created by cyclic fatigue at the crack tip, compared to their pristine counterpart, is associated with a reduction of the severity of the strain concentration at the crack tip with number of cycles. Obviously, in cyclic fatigue, the strain experienced in the bulk is lower than that close to the crack tip, which in turn controls the crack propagation rate. This difference in strain generates a spatially heterogeneous structure consisting of the region far from the crack, which is deformed at below  $\lambda_c$  (and similarly to classical elastomers has tangent modulus  $E$  lower than the pristine material, see Figure 5) and a stiffer core in the crack tip region, where the strain eventually may become large enough to overcome the critical  $\lambda_c$  generating an increase in  $E$ , which locally becomes equal to (TPU\_SOFT) or higher (TPU\_XTAL) than the pristine one. This difference in stiffness produced by the spatial-dependent restructuration of hard domains can be consequently interpreted as a sort of protecting mechanism, which, after a short transitory, shields the crack tip from achieving a very large strain, which may produce the rupture of material and therefore is correlated to crack propagation. Because of the stiffened core, the material

far from the crack in the fatigued TPU must deform more to reach the same local strain around the crack tip compared to the pristine sample and results in a decrease in the severity of the strain concentration at the crack tip as visible in Figures 6 and 7. The proposed scenario is schematically shown in Figure 13 and is consistent with the lower crystallinity observed in TPU\_XTAL after fatigue.

Noteworthy, the equatorial streak that we observed in the SAXS 2D pattern for the area close to the crack tip (Figure 8) above a characteristic stretch ( $\lambda_{\max} > 2.25$ ) is characteristically seen by X-ray scattering in several TPU<sup>1,7,8,10</sup> and was associated with the presence of either fibrillar structures or voids, which could be seen as a signature of certain damage produced in the system. For moderate applied macroscopic strains, this streak is only visible in the crack tip regime. However, when the whole sample is strained above this stretch threshold, some structural damage can take place in the bulk causing a ruin of the sample.

**Effect of Crack Tip Stiffening on the Energy Available for Crack Propagation in Fatigue.** We should finally discuss how the local spatial reorganization is related to the energy available for crack advance in cyclic fatigue. Mzabi et al.<sup>5</sup> proposed the concept of local energy release rate  $g_{\text{local}}$  indicating the locally stored elastic energy available for crack propagation in different SBR. They considered the highly strained zone at the crack tip as homogeneously strained at  $\epsilon_{\text{max}11}$  (corresponding to the maximum strain detected by DIC).  $g_{\text{local}}$  was estimated as follows

$$g_{\text{local}} = W(\epsilon_{\text{max}})h_0$$

where  $\epsilon_{\text{max}}$  is the maximum strain calculated with DIC at the crack tip,  $W(\epsilon_{\text{max}})$  indicates the elastic strain energy  $W(\epsilon_{\text{max}}) = \int_0^{\epsilon_{\text{max}}} \alpha d\epsilon$  obtained from the uniaxial tension curve, and  $h_0$  is the size of the strain concentration region in the loading direction. In that paper, they show that different SBR, differing by almost 2 orders of magnitude in terms of  $dc/dn$  vs  $G$ , fall on a master curve when  $dc/dn$  is plotted against  $g_{\text{local}}$ . In particular, the highest fatigue-resistant SBR presents both a lower level of local strain at the crack tip and less elastic energy available at the crack tip ( $g_{\text{local}}$ ) for the same value of applied  $G$ . We decided to apply the proposed method<sup>3</sup> to calculate the local energy available at the crack tip  $g_{\text{local}}$  in the pristine and fatigued TPU loaded at  $\lambda_{\max} = 2.25$ . According to Mzabi et al.,<sup>5</sup>  $h_0$  corresponds to the portion of the material in the loading direction where  $\epsilon_{\text{max}} > 0.95\epsilon_{11}$  and was calculated from the data of Figure 7. We used the 1st and 10th cycles to evaluate  $W(\epsilon_{\text{max}})$  (and therefore  $g_{\text{local}}$ ) in pristine and fatigued samples, respectively. The choice of using the 10th cycle of the sample under uniaxial loading to evaluate  $g_{\text{local}}$  for the fatigued sample is justified by the fact that the major changes in the cyclic stress–strain curve of the TPU take place at the beginning of the test. All of the values are reported in Table 3. Noteworthy, in the case of the fatigued sample,  $g_{\text{local}}$  provides only an upper bound value of the strain energy density experienced by the material at the crack tip. Indeed, as discussed in our previous paper, during cyclic loading, the strain energy  $G$  reduces with number of cycles. The most dramatic drop in  $G$  vs cycle occurs within the first cycles and then gradually achieves a steady state after some thousands of cycles. For the same maximum applied strain, pristine TPU\_SOFT, which has a lower fatigue resistance than TPU\_XTAL, has higher values of  $g_{\text{local}}$ . Moreover, the

**Table 3.**  $\epsilon_{\text{max}11}$ ,  $h_0$ ,  $W(\epsilon_{\text{max}})$ , and  $g_{\text{local}}$  for TPU\_SOFT and TPU\_XTAL for Pristine (P) and Fatigued (F) Sample Strained at  $\lambda_{\max} = 2.25$  Corresponding to Steady State  $G$  of 5600 and 7800 [J/m<sup>2</sup>], Respectively

	$G$ [J/m <sup>2</sup> ]	$\epsilon_{\text{max}11}$	$h_0$ [mm]	$W(\epsilon_{\text{max}})$ [MJ/m <sup>3</sup> ]	$g_{\text{local}}$ [J/m <sup>2</sup> ]
TPU_SOFT_P		2.8	0.58	3.69	2143
TPU_SOFT_F	5600	2.13	0.78	1.68	1316
TPU_XTAL_P		2.53	0.56	3.62	2028
TPU_XTAL_F	7800	1.7	0.28	2.39	671

measured  $g_{\text{local}}$  in fatigued samples is always lower than that measured in the pristine counterpart, and the drop is considerably more pronounced in TPU\_XTAL (which presented the lowest values of  $\lambda_1$  ( $X_2$ ) measured in DIC after fatigue in all of the area around the crack tip (Figure 6)). This result is in agreement with the suggestion of Mzabi et al. that the crack propagation resistance does depend on the strain energy available within the highly strained region at the crack tip. In the case of TPU\_XTAL, the ability of crystallization under strain and the corresponding remarkable increase in the modulus with applied stretch not only reduces the local strain but also the elastic energy available to propagate the crack compared to TPU\_SOFT (where SIC is absent and the only strengthening mechanism at the crack tip is the fragmentation of HD). Differently from SBR and other typical vulcanized elastomers, the peculiar feature of the TPU is their ability to maintain an excellent reversible elasticity in the bulk (necessary for applications), while retaining the ability to plastically deform at high strain to reduce the severity of the strain concentration at the crack tip. A similar mechanism has been recently shown for polyampholyte hydrogels, where a strain-dependent structural change is also active.<sup>26</sup>

## CONCLUSIONS

The cyclic fatigue behavior and structural evolution of notched samples of two commercial soft TPU with nearly identical small strain moduli but different large strain behavior have been investigated at room temperature in the pure-shear geometry<sup>3</sup> and reported as  $dc/dn$  vs  $G$ . For both TPU, the presence of a strain gradient in an area close to the loaded crack was shown to generate a self-strengthening nonuniform spatial organization of the TPU microstructure above a threshold value of strain. The more highly strained region at the crack tip becomes stiffer than the bulk, reducing the intensity of the strain concentration and the elastic energy available at the crack tip. As a result of this weak strain concentration, the crack propagation resistance in TPU is markedly increased compared to classical vulcanized elastomers. Furthermore, the presence of strain-induced crystallization in one of the TPU improves the cyclic fatigue resistance by reinforcing the crack tip in a similar way to that in stretched natural rubbers with the main difference that the phenomenon in TPU is not completely reversible and some residual crystals are still visible in unloaded TPU. Defining a local elastic strain energy  $g_{\text{local}}$  based on the methodology of Mzabi et al., we further show that a lower  $g_{\text{local}}$  leads to a lower value of  $dc/dn$  at the same applied  $\lambda$ .

However, when  $\lambda_{\text{max}}$  exceeds a critical value of stretch, the HD restructuring and some damage (suggested by the equatorial streak) start to occur within the whole sample and no longer selectively at the crack tip. Under those loading

conditions, the entire material would experience a strain-induced stiffening effect without the formation of a hard core protecting the crack tip leading to a higher crack propagation rate.

Our study clearly shows that this self-strengthening mechanism due to localized crack tip plasticity is active in commercial TPU and is responsible for their remarkable enhanced fatigue resistance at high strains. Interestingly, the value of such a localized stiffening mechanism may be more general and a similar localized strengthening has been observed for microphase-separated polyampholyte hydrogels.<sup>26</sup>

## ■ ASSOCIATED CONTENT

### SI Supporting Information

The Supporting Information is available free of charge at <https://pubs.acs.org/doi/10.1021/acs.macromol.1c00934>.

Additional details on the injection process and in situ 2D X-ray image of TPU\_SOFT (PDF)

## ■ AUTHOR INFORMATION

### Corresponding Authors

**Matteo Ciccotti** – *Sciences et Ingénierie de la Matière Molle, ESPCI Paris, Université PSL, CNRS, Sorbonne Université, 75005 Paris, France*; Email: [matteo.ciccotti@espci.psl.eu](mailto:matteo.ciccotti@espci.psl.eu)

**Costantino Creton** – *Sciences et Ingénierie de la Matière Molle, ESPCI Paris, Université PSL, CNRS, Sorbonne Université, 75005 Paris, France*; [orcid.org/0000-0002-0177-9680](https://orcid.org/0000-0002-0177-9680); Email: [costantino.creton@espci.psl.eu](mailto:costantino.creton@espci.psl.eu)

### Authors

**Giorgia Scetta** – *Sciences et Ingénierie de la Matière Molle, ESPCI Paris, Université PSL, CNRS, Sorbonne Université, 75005 Paris, France*; [orcid.org/0000-0002-5757-203X](https://orcid.org/0000-0002-5757-203X)

**Eric Euchler** – *Leibniz-Institut für Polymerforschung Dresden e.V., 01069 Dresden, Germany*

**Jianzhu Ju** – *Sciences et Ingénierie de la Matière Molle, ESPCI Paris, Université PSL, CNRS, Sorbonne Université, 75005 Paris, France*

**Nathan Selles** – *Laboratoire de Recherches et de Contrôle du Caoutchouc et des Plastiques, 94408 Vitry-sur-Seine, France*

**Patrick Heuillet** – *Laboratoire de Recherches et de Contrôle du Caoutchouc et des Plastiques, 94408 Vitry-sur-Seine, France*

Complete contact information is available at: <https://pubs.acs.org/doi/10.1021/acs.macromol.1c00934>

### Notes

The authors declare no competing financial interest.

## ■ ACKNOWLEDGMENTS

The PhD work of Giorgia Scetta was jointly funded by the French ANRT and the LRCCP. The authors are grateful to Dr. Matthias Schwartzkopf for the access to P03 DESY beamline and to Dr. Dario Cavallo for his support on the interpretation of X-ray data. They are indebted to Dr. Matthias Gerst, Dr. Elke Marten, and Mr. Stephan Dohmen from BASF AG for kindly providing the TPU samples. They also thank Stephane Delaunay for injecting the samples and Mohamed Hanafi for the chemical characterization. Costantino Creton has received funding from the European Research Council (ERC) under the European Union's Horizon 2020 research and innovation program under grant agreement AdG No 695351.

## ■ REFERENCES

- (1) Bonart, R. X-Ray Investigations Concerning the Physical Structure of Cross-Linking in Segmented Urethane Elastomers. *J. Macromol. Sci., Part B: Phys.* **1968**, *2*, 115–138.
- (2) Petrović, Z. S.; Ferguson, J. Polyurethane Elastomers. *Prog. Polym. Sci.* **1991**, *16*, 695–836.
- (3) Scetta, G.; Selles, N.; Heuillet, P.; Ciccotti, M.; Creton, C. Cyclic Fatigue Failure of TPU Using a Crack Propagation Approach. *Polym. Test.* **2021**, *97*, No. 107140.
- (4) Bai, R.; Yang, J.; Suo, Z. Fatigue of Hydrogels. *Eur. J. Mech. A/Solids* **2019**, *74*, 337–370.
- (5) Mzabi, S.; Berghezan, D.; Roux, S.; Hild, F.; Creton, C. A Critical Local Energy Release Rate Criterion for Fatigue Fracture of Elastomers. *J. Polym. Sci. Part B Polym. Phys.* **2011**, *49*, 1518–1524.
- (6) Martinez, J. R. S.; Toussaint, E.; Balandraud, X.; Le, J.; Berghezan, D.; Martinez, J. R. S.; Toussaint, E.; Balandraud, X.; Cam, J. Le.; Heat, D. B. Heat and Strain Measurements at the Crack Tip of Filled Rubber under Cyclic Loadings Using Full-Field Techniques. In *Mechanics of Materials*; Elsevier, 2015; Vol. 81, pp 62–71.
- (7) Yeh, F.; Hsiao, B. S.; Sauer, B. B.; Michel, S.; Siesler, H. W. In-Situ Studies of Structure Development during Deformation of a Segmented Poly(Urethane-Urea) Elastomer. *Macromolecules* **2003**, *36*, 1940–1954.
- (8) Rahmawati, R.; Masuda, S.; Cheng, C. H.; Nagano, C.; Nozaki, S.; Kamitani, K.; Kojio, K.; Takahara, A.; Shinohara, N.; Mita, K.; Uchida, K.; Yamasaki, S. Investigation of Deformation Behavior of Thiourethane Elastomers Using In Situ X-Ray Scattering, Diffraction, and Absorption Methods. *Macromolecules* **2019**, *52*, 6825–6833.
- (9) Kojio, K.; Matsuo, K.; Motokucho, S.; Yoshinaga, K.; Shimodaira, Y.; Kimura, K. Simultaneous Small-Angle X-Ray Scattering/Wide-Angle X-Ray Diffraction Study of the Microdomain Structure of Polyurethane Elastomers during Mechanical Deformation. *Polym. J.* **2011**, *43*, 692–699.
- (10) Koerner, H.; Kelley, J. J.; Vaia, R. A. Transient Microstructure of Low Hard Segment Thermoplastic Polyurethane under Uniaxial Deformation. *Macromolecules* **2008**, *41*, 4709–4716.
- (11) Blundell, D. J.; Eeckhaut, G.; Fuller, W.; Mahendrasingam, A.; Martin, C. Real Time SAXS / Stress – Strain Studies of Thermoplastic Polyurethanes at Large Strains. *Polymer* **2002**, *43*, 5197–5207.
- (12) Ishihara, H.; Kimura, I.; Yoshihara, N. Studies on Segmented Polyurethane-Urea Elastomers: Structure of Segmented Polyurethane-Urea Based on Poly(Tetramethylene Glycol), 4,4'-Diphenylmethane Diisocyanate, and 4,4'-Diaminodiphenylmethane. *J. Macromol. Sci., Part B: Phys.* **1983**, *22*, 713–733.
- (13) Van Bogart, J. W. C.; Lilaonitkul, A.; Cooper, S. L. Morphology and Properties of Segmented Copolymers. In *Multiphase Polymers*; Cooper, S. L.; Gerald, M. E., Eds.; American Chemical Society, 1979; pp 3–30.
- (14) Waletzko, R. S.; Korley, L. T. J.; Pate, B. D.; Thomas, E. L.; Hammond, P. T. Role of Increased Crystallinity in Deformation-Induced Structure of Segmented Thermoplastic Polyurethane Elastomers with PEO and PEO-PPO-PEO Soft Segments and HDI Hard Segments. *Macromolecules* **2009**, *42*, 2041–2053.
- (15) Zhu, P.; Dong, X.; Wang, D. Strain-Induced Crystallization of Segmented Copolymers: Deviation from the Classic Deformation Mechanism. *Macromolecules* **2017**, *50*, 3911–3921.
- (16) Toki, S.; Hsiao, B. S.; Kohjiya, S.; Tosaka, M.; Tsou, A. H.; Datta, S. Synchrotron X-Ray Studies of Vulcanized Rubbers and Thermoplastic Elastomers. *Rubber Chem. Technol.* **2006**, *79*, 460–488.
- (17) Rivlin, R. S.; Thomas, A. G. Rupture of Rubber. I. Characteristic Energy for Tearing. *J. Polym. Sci.* **1953**, *10*, 291–318.
- (18) Mattia, J.; Painter, P. A Comparison of Hydrogen Bonding and Order in a Polyurethane and Poly(Urethane-Urea) and Their Blends with Poly(Ethylene Glycol). *Macromolecules* **2007**, *40*, 1546–1554.
- (19) Hammersley, A. P. "FIT2D" <http://www.esrf.eu/computing/scientific/FIT2D/> (accessed March 15, 2021).

(20) ENS. Digital image correlation which revolutionizing the domain of mechanical tests <https://www.correli-stc.com/> (accessed April 15, 2021).

(21) Mzabi, S. Caractérisation et Analyse Des Mécanismes de Fracture En Fatigue Des Élastomères Chargés. PhD Thesis, 2010.

(22) Bhowmick, A. K. Threshold Fracture of Elastomers. *J. Macromol. Sci., Polym. Rev.* **1988**, *28*, 339–370.

(23) Lake, G. J.; Lindley, P. B. Mechanical Fatigue Limit for Rubber. *Rubber Chem. Technol.* **1966**, *39*, 348–364.

(24) Mars, W.; Fatemi, a. A Literature Survey on Fatigue Analysis Approaches for Rubber. *Int. J. Fatigue* **2002**, *24*, 949–961.

(25) Lake, G. J.; Lindley, P. B. Cut Growth and Fatigue of Rubbers. *J. Appl. Polym. Sci.* **1964**, *455*, 292–300.

(26) Li, X.; Cui, K.; Sun, T. L.; Meng, L.; Yu, C.; Li, L.; Creton, C.; Kurokawa, T.; Gong, J. P. Mesoscale Bicontinuous Networks in Self-Healing Hydrogels Delay Fatigue Fracture. *Proc. Natl. Acad. Sci. U.S.A.* **2020**, *117*, 7606–7612.

(27) Scetta, G.; Ju, J.; Selles, N.; Heuillet, P.; Ciccotti, M.; Creton, C. Strain Induced Strengthening of Soft Thermoplastic Polyurethanes Under Cyclic Deformation. *J. Polym. Sci.* **2021**, *1*, 685–696.

(28) Merckel, Y.; Diani, J.; Brieu, M.; Gilormini, P.; Caillard, J. Characterization of the Mullins Effect of Carbon-Black Filled Rubbers. *Rubber Chem. Technol.* **2011**, *84*, 402–414.

(29) Zhu, P.; Zhou, C.; Dong, X.; Sauer, B. B.; Lai, Y.; Wang, D. The Segmental Responses to Orientation and Relaxation of Thermoplastic Poly(Ether-Ester) Elastomer during Cyclic Deformation: An in-Situ WAXD/SAXS Study. *Polymer* **2020**, *188*, No. 122120.

(30) Statton, W. O. Microvoids in Fibers as Studied by Small-Angle Scattering of x-Rays. *J. Polym. Sci.* **1962**, *58*, 205–220.

(31) Zhang, H.; Scholz, A. K.; De Crevoisier, J.; Berghezan, D.; Narayanan, T.; Kramer, E. J.; Creton, C. Nanocavitation around a Crack Tip in a Soft Nanocomposite: A Scanning Microbeam Small Angle X-Ray Scattering Study. *J. Polym. Sci., Part B: Polym. Phys.* **2015**, *53*, 422–429.

(32) Stribeck, N.; Sapoundjieva, D.; Denchev, Z.; Apostolov, A. A.; Zachmann, H. G.; Stamm, M.; Fakirov, S. Deformation Behavior of Poly(Ether Ester) Copolymer as Revealed by Small- and Wide-Angle Scattering of X-Ray Radiation from Synchrotron. *Macromolecules* **1997**, *30*, 1329–1339.

(33) Toki, S.; Sics, I.; Hsiao, B. S.; Murakami, S.; Tosaka, M.; Poompradub, S.; Kohjiya, S.; Ikeda, Y. Structural Developments in Synthetic Rubbers during Uniaxial Deformation by In Situ Synchrotron X-Ray Diffraction. *J. Polym. Sci., Part B: Polym. Phys.* **2004**, *42*, 956–964.

(34) Demassieux, Q.; Berghezan, D.; Cantournet, S.; Proudhon, H.; Creton, C. Temperature and Aging Dependence of Strain-Induced Crystallization and Cavitation in Highly Crosslinked and Filled Natural Rubber. *J. Polym. Sci., Part B: Polym. Phys.* **2019**, *57*, 780–793.

(35) Candau, N.; Stoclet, G.; Tahon, J. F.; Demongeot, A.; Yilgor, E.; Yilgor, I.; Menciloglu, Y. Z.; Oguz, O. Mechanical Reinforcement and Memory Effect of Strain-Induced Soft Segment Crystals in Thermoplastic Polyurethane-Urea Elastomers. *Polymer* **2021**, *223*, No. 123708.

(36) Kimura, I.; Ishihara, H.; Ono, H.; Yoshihara, N.; Nomura, S.; Kawai, H. Morphology and Deformation Mechanism of Segmented Poly(Urethaneureas) in Relation to Spherulitic Crystalline Textures. *Macromolecules* **1974**, *7*, 355–363.

## ORIGINAL ARTICLE

# Morphological origins of temperature and rate dependent mechanical properties of model soft thermoplastic elastomers

Simone Sbrescia<sup>1</sup>  | Jianzhu Ju<sup>2</sup> | Tom Engels<sup>1</sup>  |  
Evelyne Van Ruymbeke<sup>3</sup>  | Michelle Seitz<sup>1</sup> 

<sup>1</sup>Materials Science Center, DSM, Geleen, The Netherlands

<sup>2</sup>Laboratoire Sciences et Ingénierie de la Matière Molle, ESPCI Paris, PSL University, CNRS, Sorbonne Université, Paris, France

<sup>3</sup>Bio and Soft Matter Division (BSMA), Institute of Condensed Matter and Nanosciences (IMCN), Université Catholique de Louvain, Louvain-la-Neuve, Belgium

## Correspondence

Michelle Seitz, Materials Science Center, DSM, Urmonderbaan, 6167 RD Geleen, The Netherlands.

Email: michelle.seitz@dsm.com

## Funding information

H2020 Marie Skłodowska-Curie Actions, Grant/Award Number: 765811

## Abstract

Thermoplastic elastomers (TPEs) combine high elasticity with melt processability due to their structural features being based on physical associations rather than chemical crosslinking. Their mechanical properties are governed by the interplay of the different dynamics present in the system (i.e., hard block associations and soft block mobility) combined with their morphology. Irrespective of their exact chemical structure or type of association (crystals, hydrogen bonds, or glassy domains), many soft TPEs show a reduction in toughness at elevated temperatures. In this study, we investigate the high-temperature mechanical properties of a model series of industrially relevant TPEs via systematically varying composition and molecular weight. The results show an increase in temperature resistance and in large-strain stress response as chain length increases. We underline the key parameters that influence the mechanical behavior and explain the observed effect of molecular weight on both the temperature- and rate-dependent large-strain response. A physical network-based model is presented that can explain the experimental findings assuming an improved network connectivity and extended lifetime of the entangled segments with increasing molecular weight.

## KEYWORDS

morphology, network connectivity, strain recovery, thermomechanical property, thermoplastic elastomer

## 1 | INTRODUCTION

Balancing high performance and recyclability with polymeric materials is a challenge. Rubbers with permanent chemical crosslinks are widely used because of their high flexibility, creep and chemical resistance as well as broad temperature range of use. However, they cannot be reshaped and reused. Replacing chemical crosslinks with non-permanent, physical associations enables both melt processing and recycling. Thermoplastic elastomers

(TPEs) offer an alternative to rubbers as they are crosslinked via physical associations and trapped entanglements that lead to high elasticity coupled with melt processability.<sup>1</sup> They are widely used in applications such as automotive ducts, shoes, and medical devices. However, TPEs are not yet able to replace cross-linked rubbers in all applications, as they generally have lower creep resistance and do not reach the same low-end values for the modulus.<sup>1</sup> Some common examples of TPEs are segmented copolymers with associating blocks of

polyesters,<sup>1–6</sup> polyamides,<sup>1,7,8</sup> and polyurethanes.<sup>9–11</sup> They all share the feature of having a low glass transition ( $T_g$ ) of the soft blocks (SBs) combined with physically associating hard blocks (HBs). Their mechanical properties are governed by the interplay of the different dynamics present in the system (e.g., hard block associations and soft block mobility) as well as by their morphology, that is, the physical arrangement of the polymer chains.<sup>1–7,9,10,12–18</sup>

For TPEs where the elasticity stems from crystallizing HBs, the initial morphology develops upon cooling from the melt during which crystallization and phase separation occur. Typically, the assumption of only two dominant phases (soft amorphous and hard crystalline) is taken to simplify the interpretation of the mechanical results.<sup>4</sup> Depending on the specific TPE, the fraction of associated HB can range from 20 to 80%.<sup>19</sup> Additionally the low  $T_g$  SB-rich phase may also be partially crystallized at lower temperatures. For many TPEs the morphology and, in consequence, mechanical properties evolve with deformation. Upon deformation, the initial crystal network breaks up into smaller domains that act as physical crosslinks. The microstructure evolution upon deformation at room temperature has been extensively studied for TPEs based on urethanes and esters (TPUs and TPE-Es respectively).<sup>2,7,8,18,20–24</sup> Complicating our further understanding is that their dynamics are strongly influenced by temperature, deformation and, for some chemistries, by strain induced crystallization of the initially mobile soft blocks.<sup>4,8,13,24</sup>

Previous studies mainly focused on the linear properties of TPE-Es with HB contents  $>40$  wt%.<sup>4,5,13,14</sup> The effects of the composition (SB/HB ratio) on the initial morphology and of the length of the individual blocks have been explored, showing increasing elastic modulus and melting temperature with increasing HB content. Systems with lower modulus and less temperature dependent rubber plateaus have been enabled by synthetic advances allowing mono-disperse hard blocks.<sup>10,18,25</sup> However, most commercial TPU or TPE-E systems are based on polydisperse hard blocks.

Compared to rubber with permanent crosslinks, a major drawback of many TPEs based on multiblock copolymers with  $<50$  wt% HB is a large reduction in toughness at higher temperatures, independent of their exact chemical structure, type of association, or block polydispersity.<sup>18,26,27</sup> This is a significant limitation in reaching low modulus, melt processible rubber alternatives with sufficiently broad temperature use range.

A few studies on TPE-Es and TPUs report mechanical data in the non-linear, large-strain regime.<sup>13,25–28</sup> Currently lacking in the literature is a systematic study on the effects of the molecular weight (Mw) on the

mechanical properties as a function of temperature and strain-rate. To our knowledge, there are no studies combining both composition and temperature effects of TPE-Es. While there are a few observations,<sup>25,27</sup> there is no systematic description of the influence of the Mw on the mechanical properties.

To gain insight into the key parameters that influence the mechanical behavior at different stages of deformation, we use combination of mechanical testing and morphology characterization to study the influence of composition (SB/HB ratio), temperature, and Mw for a series of model polyether-ester block copolymers. We emphasize here that despite the relatively small range in Mw among the studied samples, the effects on the high-strain mechanics are surprisingly large. Building upon the work of Aime et al.<sup>27</sup> that explored the temperature dependent ultimate failure of soft-TPEs, we focus on what controls the level of stress at different temperatures and strain-rates. The aim is to present a qualitative physical model that is able to explain the observations collected experimentally, taking into account the presence of both crystalline HBs and entanglements as stress bearing units as well as their time-temperature dependent kinetics.

This paper begins with a description of the model TPE-E systems' chemistry and composition. We then present the morphology of the system and how it evolves upon deformation, describing the linear and nonlinear mechanical properties focusing on the effects of composition, temperature, Mw and morphology evolution. Next, we present a first order physical picture that allows us to interpret the experimental results in light of local morphology and network connectivity and that is consistent with previous observations of similar materials. This picture is finally supported and enriched by a simple model that focuses on the Mw and rate effects and illustrates how dangling end disentanglement time influences the stress level. We end by drawing generic conclusions on the deformation mechanism of these model TPE-E that can be applied to a broad range of soft, segmented copolymer systems.

## 2 | EXPERIMENTAL

### 2.1 | Materials

We use as a model system a poly(ether-ester) block-copolymer based on polybutylene terephthalate (PBT) as HB, and poly(tetramethylene oxide) (PTMO) as SB obtained via transesterification followed by polycondensation of dimethyl terephthalate (DMT), 1,4-butanediol (BDO) and PTMO diol. Details on the synthesis

procedure have been previously described.<sup>4</sup> After polymerization, the material is extruded and pelletized into granules.

The three different compositions studied here are reported in Table 1. The soft blocks used had either a number average molecular weight,  $M_{n,SB}$ , of 2 or 3 kg/mol and they have a polydispersity index (PDI) of  $\sim 2$ . Materials are denoted by the wt% and length of PTMO used followed by the total  $M_n$  of the block-copolymer, for example, 60\_PTMO2k\_25 is a polymer with total  $M_n$  of 25 kg/mol made with 60 wt% of PTMO with  $M_{n,SB}$  of 2 kg/mol. Different Mw are obtained via solid state post condensation (SSPC) for different times (0,4,6,9,12 h) under dry nitrogen atmosphere at 180°C. For simplicity we refer to the amount of soft block in the system as the wt% of PTMO ( $SB_{wt}$ ) used in the polymerization and the amount of hardblock as the wt fraction of PBT in the system ( $HB_{wt}$ ). It should be noted that the PTMO diols can be connected by a single DMT or by short DMT-BDO repeats that may not crystallize and thus act as chain extenders for the PTMO segments. It also follows that not all the DMT ends up in the HBs and  $HB_{wt} \neq 1 - SB_{wt}/100$ . We will simply refer to the segments comprising SBs and non-crystallized HBs as soft segments. By assuming random copolymerization of the components and calculating the molar fraction of PBT after polymerization,  $x_{PBT}$ , we can determine the average length of a

HB,  $\langle L_n \rangle$ , expressed in terms of PBT repeat units, as follow:<sup>15</sup>

$$\langle L_n \rangle = \frac{1}{1 - x_{PBT}}, \quad (1)$$

Equation 1 can be easily obtained from the definition of degree of polymerization, noting that for this system  $x_{PBT}$  can be approximated to the propagation probability. This allows us to estimate the average number of HB per chain,

$$\langle N \rangle = \frac{M_n HB_{wt}}{\langle L_n \rangle M_{0,PBT}} \quad (2)$$

where  $M_{0,PBT} = 0.22$  kg/mol is the weight of a single PBT unit. Since not all the HBs in the chain crystallize upon cooling from the melt, we estimate the number of the ones that crystallize as follow:

$$\langle N_{crys} \rangle = \langle N \rangle X_{PBT}/100 \quad (3)$$

where  $X_{PBT}$  is the percentage of PBT that crystallizes. For clarity, we report the structural parameters in Table 1. From the values of  $X$  and the densities of the various phases, 0.98, 1.28, and 1.40 g/cm<sup>3</sup>,<sup>29,30</sup> respectively, for amorphous PTHF, amorphous PBT, and crystalline PBT

**TABLE 1** Structural parameters

Sample	SB <sub>wt</sub> (%)	M <sub>n,SB</sub> (kg/mol) <sup>a</sup>	T <sub>m</sub> peak (°C) <sup>b</sup>	X(X <sub>PBT</sub> ) (%) <sup>c</sup>	⟨L <sub>n</sub> ⟩ (#) <sup>d</sup>	⟨N⟩ (#) <sup>e</sup>	⟨N <sub>crys</sub> ⟩ (#) <sup>f</sup>	M <sub>n</sub> (kg/mol) <sup>g</sup>	M <sub>w</sub> (kg/mol) <sup>h</sup>
60_PTMO2k	60	2	200	17 (47)	6.5	6.2	2.9	24.6	49.0
						7.5	3.5	29.4	59.1
						8.1	3.8	31.9	62.1
						8.7	4.1	34.2	67.0
						11.1	5.2	43.9	88.0
						12.7	6.0	50.2	100.0
70_PTMO2k	70	2	175	9 (35)	4.5	7.3	2.6	27.2	52.9
						8.9	3.2	33.1	66.3
						10.1	3.6	37.6	73.0
						10.3	3.7	38.5	76.0
						13.6	4.8	50.6	100.0
						18.0	6.4	67.0	124.0
75_PTMO3k	75	3	180	8.5 (29)	5	8.6	2.5	32.3	65.6

<sup>a</sup>M<sub>n</sub> of the PTMO diol.

<sup>b</sup>PBT melting peak maximum extracted from DSC.

<sup>c</sup>Degree of crystallinity per total sample weight calculated from DSC for the non-SSPCed samples. In brackets, the percentage of crystalline PBT.

<sup>d</sup>Average sequence length of the PBT segments.

<sup>e</sup>Average number of HBs per chain.

<sup>f</sup>Average number of crystallized HBs per chain.

<sup>g</sup>PDI = M<sub>w</sub>/M<sub>n</sub>  $\sim 2$  for all the samples.

<sup>h</sup>M<sub>w</sub> weight average molecular weight.

it is possible to estimate the volume percentage of crystallites: 13.7%, 7.0%, and 6.5% respectively for 60\_PTMO2k, 70\_PTMO2k and 75\_PTMO3k.

As not all the HB crystallize, the possibility of glassy HB domains arises; indeed, this is argued in similar systems.<sup>19</sup> However, previous studies show that for system similar to ours, i.e. with a limited amount of PBT HB, no glassy HB domains are detected.<sup>4,5,13</sup>

## 2.2 | Sample preparation

Granulates are compression molded into either 200  $\mu\text{m}$  or 1 mm thick sheets under vacuum at 230°C and allowed to equilibrate for a few minutes at this temperature before being rapidly cooled to room temperature by cooling the press by an internal water circulation system. To define the thickness, Teflon sheets are used as molds, sandwiched between two more Teflon sheets to prevent sticking to the metal plates. The cooling rate was approximately 40°C/min, though not constant during the entire cooling time. Due to practical equipment issues, some samples are cooled down from the melt at a constant rate of 20°C/min. To differentiate these samples from the one cooled down with a faster rate, a “\*” is placed at the end of their denomination. However, previously collected data (not shown) suggested no appreciable effects of cooling rate on the mechanics at temperatures ranging from room temperature (RT) to 100°C for these samples. Example cooling curves are shown in Appendix S1.

## 2.3 | Methods

Tensile bars of ISO 527/5A standard shape are punched out from the 200  $\mu\text{m}$  films and tested on a standard Zwick Roell (Germany) 1474–2 Universal tensile testing machine equipped with an air circulation oven for samples at temperatures higher than room temperature and on a Zwick Roell 1455 for the tests at room temperature. Engineering strain is determined using an optical extensometer for increased accuracy, especially in the high strain regime, where strain-hardening and some slippage from the grips are likely to occur. Furthermore, for the tests at room temperature, pneumatic grips are used to further decrease slippage. For all the tests at high temperatures, the samples are equilibrated at target temperature for 10 min before the test starts. Temperatures are indicated where appropriate in the respective figures and/or captions.

### 2.3.1 | Tensile tests

During the tensile tests, samples are subsequently stretched at a constant cross-head speed until failure. A

preload of 0.05 N (ca. 0.06 MPa) is applied before starting. The elastic modulus is calculated at a strain rate of 1 mm/min between 0.05 and 1% of strain. The cross-head speed outside the modulus determination strain is increased to between 5 and 500 mm/min, corresponding to strain rates,  $\dot{\epsilon}$ , ranging from 0.0017 to 0.17 s<sup>-1</sup>. The engineering stress and strain curves are plotted to allow for a direct comparison with previous studies on similar materials. Additionally, particularly in the conditions where strain induced crystallization occurs, the assumption of constant volume during deformation might not be correct, which makes it not possible to estimate the true stress.

### 2.3.2 | Cyclic tensile tests

The cross-head speed for the cyclic tests is set to 50 mm/min (0.017 s<sup>-1</sup>). Deformation steps are indicated in the figures. As in the tensile test, a preload of 0.05 N is applied before starting. There is no holding time between cycles. Residual strains of each cycle  $i$  ( $\epsilon_{\text{residual}(i)}$ ) are collected corresponding to the values of strains where the force reached the preload value during unloading. Recovered strain is then calculated by subtracting the applied pre-strain ( $\epsilon_{\text{applied}(i)}$ ) and the residual strain of the respective  $i$ -th cycle. The tensile set (TS) is also calculated, and is defined as

$$\text{TS} = \frac{\Delta\epsilon_{\text{residual}}}{\Delta\epsilon_{\text{cycle}}}, \quad (4)$$

where

$$\Delta\epsilon_{\text{residual}} = \epsilon_{\text{residual}(i)} - \epsilon_{\text{residual}(i-1)} \quad (5)$$

and

$$\Delta\epsilon_{\text{cycle}} = \epsilon_{\text{applied}(i)} - \epsilon_{\text{residual}(i-1)} \quad (6)$$

### 2.3.3 | Differential scanning calorimetry

Differential scanning calorimetry (DSC) experiments are performed on a TA Instruments (USA) Q2000 instrument. Scans are performed at heating rates of 10°C/min. Standard 40  $\mu\text{l}$  aluminum pans are used and samples weighed ~3 mg. Tests are done in air and each pan is punctured prior the test to avoid any pressure build up. Samples are taken from the same films as for the mechanical tests. Additionally, samples are taken near the failure point from RT tensile tested samples to determine if permanent strain induced crystallization (SIC) of



the soft blocks occurred. The percentage of crystallized PBT, is calculated from the theoretical enthalpy of fully crystallized PBT  $\Delta H_0 = 145.5 \text{ J/g}$ ,<sup>4</sup> as  $X_{PBT} = \frac{\Delta H}{\Delta H_0 * HB_{wt}} \times 100\%$ , while for the degree of crystallinity per total sample weight,  $X$ , we simply used  $X = \frac{\Delta H}{\Delta H_0} \times 100\%$ .

### 2.3.4 | Dynamic mechanical analysis

Dynamic mechanical analysis (DMA) tests are performed on an RSA-3 TA Instrument (USA). Rectangular shaped samples (40 mm long, 2 mm wide) punched out from the 200  $\mu\text{m}$  hot-pressed films are tested in tension at heating rates of 5°C/min and at a constant frequency of 1 Hz in the temperature range from  $-120^\circ\text{C}$  to  $\sim T_m$  in a nitrogen atmosphere. Tg are collected from the peaks of the  $\tan\delta$  curves.

### 2.3.5 | Size exclusion chromatography

To determine the  $M_w$ , size exclusion chromatography (SEC) measurements are performed on a Viscotek (UK) GPCMax VE2001 solvent/sample module system, equipped with a TDA302 triple detector array. For chromatographic separation, 3 PFG linear XL columns from PSS Polymer Standards Service GmbH are used. Detectors and columns are operated at 35°C. Prior to SEC, the polymer is dissolved at concentrations ranging from 1.0 to 1.5 mg/ml in hexafluoroisopropanol containing 0.1 wt % potassiumtrifluoroacetate (to suppress polyelectrolyte effect since polycondensation can have some localized charge due to tautomeric forms). The molar mass and molar mass distribution is determined with triple detection method, using the refractive index, differential viscosity and right-angle light scattering signals. For calculation of  $M_w$  averages and molar mass distribution, refractive index indices ( $dn/dc$ 's) in a range of 0.20–0.24 ml/g are used.<sup>31</sup>

### 2.3.6 | Atomic force microscopy

Atomic force microscopy (AFM) topology micrographs are obtained using the Peak-Force QNM method on a MM8 from Bruker. Co (USA). Experiments are performed in air, at room temperature, with a frequency around 75 kHz, a tip radius of 7 nm with a nominal spring constant of 7 N/m. Either the as pressed top surface or cross-section of a 1 mm sample were imaged. For cross-sections, samples were microtomed at  $-120^\circ\text{C}$  (below the PTMO glass transition).

### 2.3.7 | X-ray analysis (SAXS/WAXS)

The experiments are carried out on a GANESHA 300XL (SAXSLAB, USA) + system from JJ X-ray (Denmark). The instrument is equipped with a Pilatus 300 K (DECTRIS, Switzerland) detector, with a pixel size of 172  $\mu\text{m} \times 172 \mu\text{m}$ . The X-ray source is a Genix 3D (Xenoxs, France) Microfocus Sealed Tube X-Ray Cu-source with integrated Monochromator (multilayeroptic “3D version” optimized for SAXS) (30 W). Calibration of scattering angle is done using silver behenate ( $d_{001} = 58.380 \text{ \AA}$ ). Samples are fixed in two oppositely moving clamps, so that the acquisition point stays constant for measurement. Step-loading is applied here to provide sufficient time for the X-ray data collection period. The cross-head speed is 20  $\mu\text{m/s}$  (0.002  $\text{s}^{-1}$ ) and measurements were performed at engineering strains (determined from crosshead displacement) of 0%, 100%, 300%, 500% and 700%. Measurement begins 5 min after reaching the target strain to avoid a strong influence from relaxation directly after loading. The measurement period is 15 min for WAXS and 30 min for SAXS. The X-ray wavelength is 0.124 nm and the switch between WAXS and SAXS at each strain is achieved by the translation of the detector. The distance from the sample to the detector for SAXS and WAXS is 415 and 120 mm, respectively. A picture of the experimental set-up is shown in Appendix S1. Analyzing the curves by means of fitting to obtain details on the morphology is beyond the scope of this study. Additionally, the weakness of the X-ray signal coming from the low crystallinity and thickness of the samples, as well as the broadness of the peaks coming from the polydispersity of the HB, make the identification of the peaks difficult and the uniqueness of the fit problematic.

## 3 | RESULTS

### 3.1 | Morphology

Modulus mapping via the AFM QNM method of the surface (Figure 1) and cross-section (Appendix S1) of hot-pressed samples at ambient conditions are consistent in showing the presence of ribbon-like crystals with high aspect ratio in a softer matrix. In both the figures no spherulites are detected at the investigated length scales. The crystals are stacked PBT segments while the softer matrix is a mixture of PTMO + un-crystallized PBT. For soft systems ( $HB_{wt\%} < 50$ ), crystals do not form spherulites as in harder systems.<sup>14</sup> Furthermore, the low  $HB_{wt\%}$  content results in shorter HBs on average (lower  $\langle L_n \rangle$ ) which makes chain folding during crystallization of the

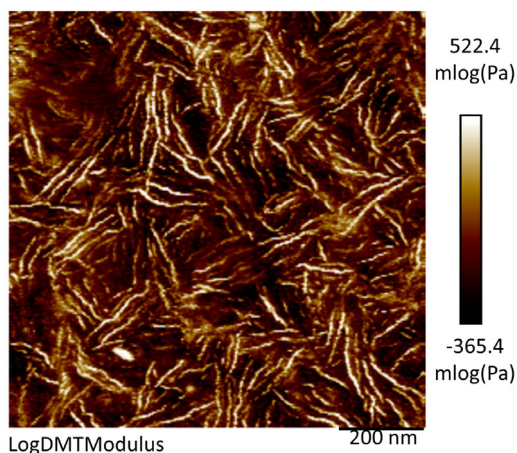


**FIGURE 1** Atomic force microscopy (AFM) micrograph (QNM) showing the top surface of a hot-pressed 70\_PTMO2k\_33 sample at ambient conditions. Brighter regions correspond to a higher elastic modulus (polybutylene terephthalate [PBT] crystals) while darker regions correspond to the poly(tetramethylene oxide) (PTMO)-rich soft phase [Color figure can be viewed at [wileyonlinelibrary.com](http://wileyonlinelibrary.com)]

PBT unlikely to occur. The crystals are connected via soft segments (amorphous SB and un-crystallized HB) that can bridge crystallized segments in the same or different crystals and can form trapped entanglements.

The molecular weight between entanglements ( $M_e$ ) of PTMO is  $\sim 1.4$  kg/mol<sup>32</sup> which makes the amorphous chain segments between crystals well entangled. Despite the absence of a co-continuous hard phase, the high aspect ratio of the ribbon-like crystals shown in the AFM micrographs introduces the possibility of a mechanically-interlocked network of crystals contributing to the initial stiffness of the material, which will be discussed later on in the paper. In Figure S4 we provide SAXS signals for the sample in the undeformed state.

### 3.2 | Thermal transitions

The tensile storage moduli ( $E'$ ) in the linear range versus temperature for different SB/HB ratios and Mw are shown in Figure 2. The general trends are similar for all the materials. DSC traces are shown in Figure 3 (cooling curves in Figure S6). The PBT crystal  $T_m$  is determined by the crystal size and perfection and increases with the average block length ( $\langle L_n \rangle$ ).<sup>4</sup> Thermal transitions observed via DSC and DMTA yield a consistent picture (note that the measurements are performed as slightly different heating rates). We will next describe briefly the major transitions observed with increasing temperature based on these results as well as on the extensive previous literature.<sup>1,3,4,13</sup>

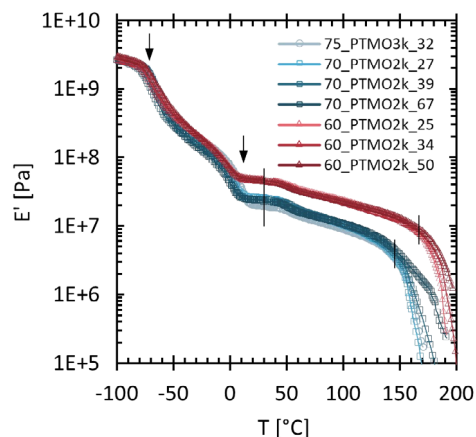


**FIGURE 2** Storage modulus for the series of different  $M_n$  of samples 60\_PTMO2k, 70\_PTMO2k and 75\_PTMO3k.  $M_n$  increases from light to dark. The arrows indicate the  $T_g$  and the end of melting for the poly(tetramethylene oxide) (PTMO), the vertical lines indicate the start and end off the temperature range where nonlinear properties were studied. Loss modulus and  $\tan\delta$  related to the same set of samples are shown in Appendix S1 [Color figure can be viewed at [wileyonlinelibrary.com](http://wileyonlinelibrary.com)]

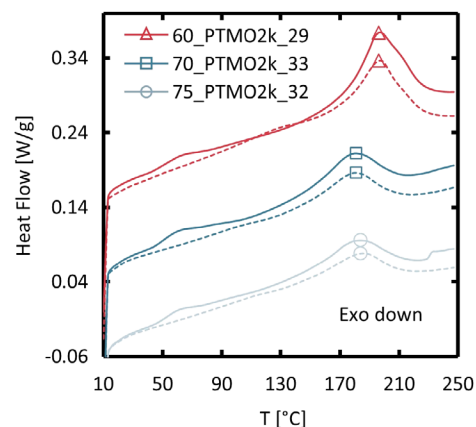


**FIGURE 3** Differential scanning calorimetry (DSC) thermographs from 10 to 250°C for three samples. The continuous lines correspond to the first heating, the dashed ones to the second heating. Symbols indicate the respective peak maxima. Data are vertically shifted [Color figure can be viewed at [wileyonlinelibrary.com](http://wileyonlinelibrary.com)]

At around  $\sim -60^\circ\text{C}$  the  $T_g$  of the PTMO-rich phase is observed which for high amounts of high-Mw SBs is relatively independent of the soft block content.<sup>13</sup>

Next the melting of PTMO is observed around  $\sim 0$ – $10^\circ\text{C}$ , the melting point increases with the PTMO length and the level of crystallinity increases with the amount of PTMO.<sup>12</sup> At higher temperatures, the system consists of crystallized PBT segments in a mobile ( $T \gg T_g$ ) amorphous matrix, and a rubbery plateau is observed. In this region, the elastic modulus mainly scales with crystallinity,<sup>19</sup> which increases with the

amount of HBs in the system.<sup>2</sup> The end of the rubbery plateau is dictated by the melting of the PBT crystals. Unlike a traditional cross-linked rubber, the modulus decreases in the plateau region with increasing temperature. This is attributed to the increased mobility in the amorphous phase surrounding the PBT crystals. Indeed, due to the polydispersity of the HB length, the interface between the crystalline and amorphous phases is not expected to be well defined. A PBT-rich mixed phase is likely to be at this interface, whose increased mobility with increasing temperature can contribute to the  $E'$  decrease.

Note that as the material nears the melting point of the PBT, the decrease is more rapid. This is likely due to the melting of the less perfect crystals or of the crystals formed by shorter HBs, rather than to the increased mobility of the phase surrounding the crystals. For an extended discussion on this topic see De Almeida et al.<sup>6</sup> Figure 2 shows also that the Mw of the chains does not affect the linear modulus in the plateau region, as would be expected if the amount of crystallinity and the initial crystal morphology were not affected by Mw.

### 3.3 | Influence of deformation on morphology and modulus

To further understand how deformation influences the morphology and mechanical properties of these materials cyclic loading experiments were performed. As an example, a cyclic test where the material is loaded and unloaded three times up to the same target strain is shown in Figure 4 (top-right) illustrating the different mechanical response between the first and second cycles. Actual cyclic tests are shown in Figure S7. Several key features should be noted: after initial deformation, the material shows a large amount of elastic recovery and, on reloading, the modulus of the deformed material is significantly lower than for the undeformed material. As shown in Figure 5, the elastic modulus of the reloaded sample initially decreases with applied pre-strain. Due to strain the material acts as if it was transitioning from a response dominated by an original, mechanically interlocking and stress-bearing PBT-crystal network to a more elastomeric one where the crystals act as isolated cross-linking points. This rapid drop in modulus with strain

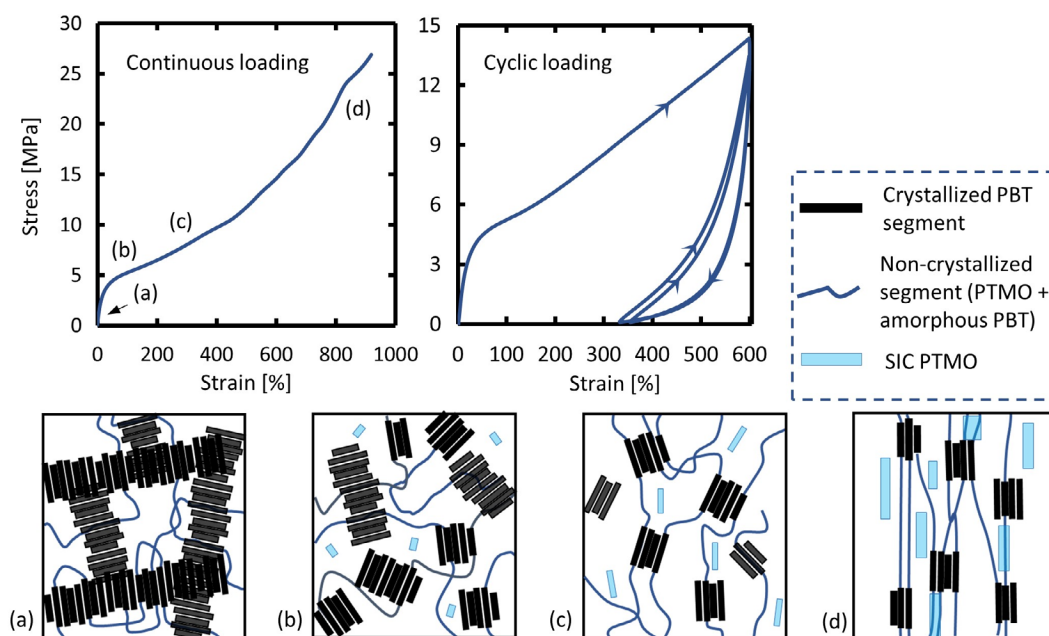


**FIGURE 4** Top-left, example of an engineering tensile curve, letters in the plot indicate roughly the points on the curve where the morphology is expected to be different, referring to the ones in the bottom picture. Top-right, plot showing the response of cyclically loading the material several times to the same strain resulting in the decrease in modulus and hysteresis between the first and following cycles. Arrow indicate loading and unloading. Bottom, schematic cartoon representing the evolution of the morphology upon stretching: Deformation causes the crystalline stress-bearing structure (A) to break and the material to progressively transit to an elastomeric-like structure (B),(C), where the broken crystal domains progressively reorient towards stress direction and act as physical crosslinking points. Further stretching leads to chain alignment and pull-out of some of the crystallized PBT segments from the crosslinks. The competition between the latter and the stretching of the chain segments is responsible for the stress upturn. Eventually, stretching leads to a very aligned morphology (D) where, if temperature allows strain induced crystallization (SIC) of the poly(tetramethylene oxide) (PTMO) segments dominates the mechanical behavior [Color figure can be viewed at [wileyonlinelibrary.com](http://wileyonlinelibrary.com)]

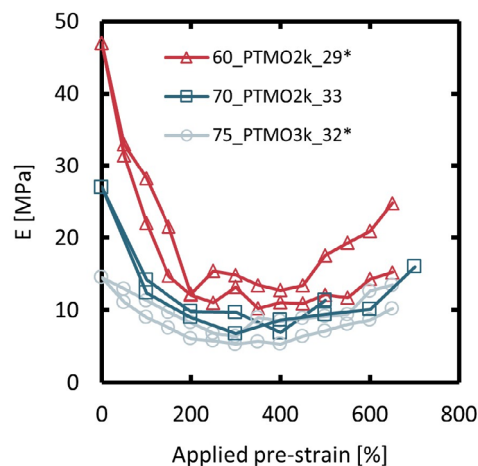


**FIGURE 5** Young's modulus ( $E$ ) versus applied pre-strain. Data calculated from cyclic experiments (supplemental information S7 and S8) performed at room temperature. Duplicates are shown. Values are corrected for the change in cross-section during stretching, assuming constant volume [Color figure can be viewed at [wileyonlinelibrary.com](http://wileyonlinelibrary.com)]

has been shown for other multi-block copolymers with a similar strain-evolving structure.<sup>33–35</sup> Finally, after experiencing very high strains, a highly oriented system with both small PBT crystals and with amorphous segments aligned along the stretching direction (and possibly crystallized) is obtained. The morphology evolution with applied strain is illustrated schematically in Figure 4. There is not yet consensus on what determines the initial modulus for soft TPEs, how it increases with HB content, and why it is strongly reduced after strain. Based on data from several chemically different TPEs with crystal volume fraction <40%, Nebouy et al.<sup>19</sup> argue the crystallites structure, in particular the volume fraction and the width of the crystals, determines the linear modulus.

Their theoretical arguments takes into account the covalent bonds between the soft and hard segments and local topological arguments by treating the crystals as local densifications of the polymer network.<sup>36</sup> In such a model, the reduction in modulus with strain requires a significant reduction in associated HBs or in crystal width. An alternate approach is to treat the HB domains as rigid, dispersed fillers in analogy with standard composite theory.<sup>10</sup> We interpret the as molded sample's stiffness as dominated by the rigid crystal phase which carries the load, in analogy with a foam type structure. As such, the modulus would be expected to scale with the volume fraction of crystallinity as well as the bending stiffness of the crystals.<sup>37</sup> The rigidity of this stiff network greatly exceeds that of the entangled amorphous phase connecting the crystals and dominates the initial

response. During strain, the crystals undergo yielding to break into smaller segments ultimately resulting in dispersed crystals and in the stiffness being dominated by the amorphous phase. This transition from stiffness being dominated by a mechanically interlocking crystal network to that of the entanglement amorphous phase explains the large drop in modulus and hysteresis at modest strains (<200%) without involving a large drop in associated hard blocks. At the extreme where the HB fraction is sufficiently low, a rigid network should not be able to form and the initial modulus and hysteresis should be low. What is surprising is that even for these systems with relatively low amounts of crystallinity the same phenomenological response is observed. Studies that monitor the change in associated HB with deformation would be extremely useful in further elucidating which conceptual model for understanding the modulus in soft TPEs is correct.

After large deformation we see an increase in modulus. We believe this can be attributed to the high level of alignment of the chains and also a contribution coming from SIC of the PTMO. DSC performed on broken specimens after tensile tests show a new endo-thermic peak between 40 and 50°C, corresponding to SIC of the PTMO (Appendix S1).<sup>8</sup> This is also supported by the in situ X-ray tests (Appendix S1) which show the PTMO crystals are present both during applied strain and after unloading, that is the so formed crystals are stable even after unloading and disappear only after the temperature is raised. Figure S9(a) shows that PTMO crystallinity progressively increases with applied strain and already starts forming before the strain hardening onset.

### 3.4 | Nonlinear properties

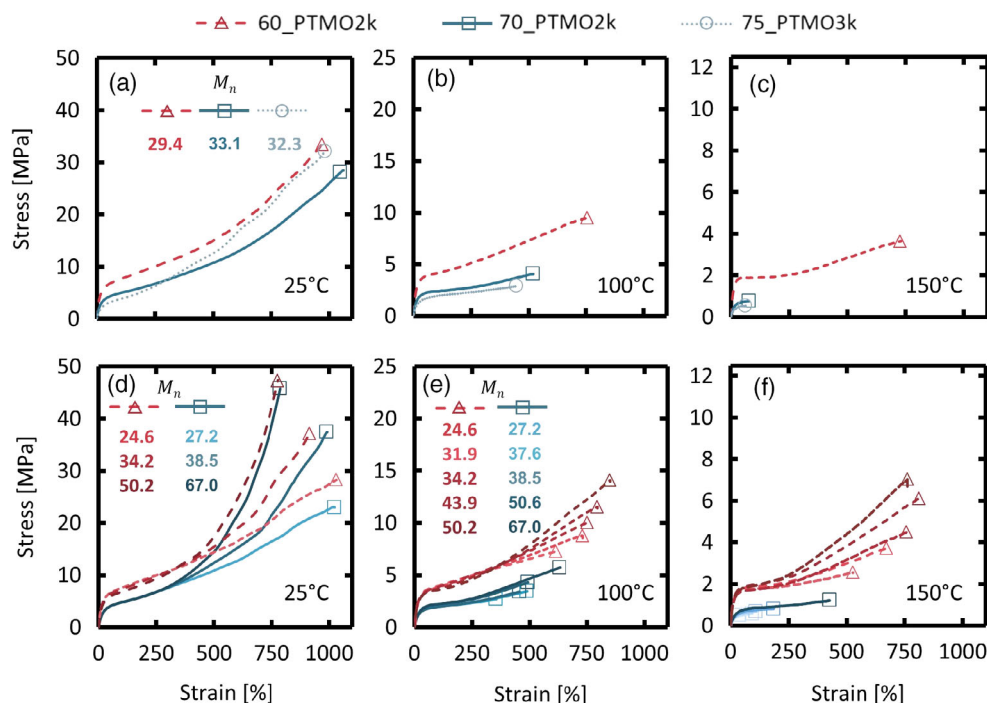
Now that we have established a morphological picture for these systems and how it changes upon loading, we switch to investigating how composition, Mw and temperature affect the mechanical performance.

Figure 6 shows engineering stress–strain curves at RT, 100, and 150°C for difference HB/SB ratios (A)–(C) and total chain  $M_n$  (D)–(F).

#### 3.4.1 | Varying SB/HB ratio–Fixed mw

We will begin by examining the influence of SB/HB ratio at similar total Mw ( $M_n \sim 30$  kg/mol, PDI  $\sim 2$ ) as depicted in Figure 6(a)–(c). The general features are similar for all curves: the stress increases roughly linearly to  $\sim 10\%$  strain. Then, the slope begins to decrease which we attribute to plastic deformation (yielding) of the crystalline

**FIGURE 6** Representative engineering stress-strain curves for (a)-(c) 60\_PTMO2k\_29, 70\_PTMO2k\_33 and 75\_PTMO\_32 and for (d)-(f) the mw series of the samples 60\_PTMO2k and 70\_PTMO2k, at RT (for (a) and (d)), 100°C (for (b) and (e)) or 150°C (for (c) and (f)). All the tests are conducted at fixed strain-rate  $\dot{\epsilon} = 0.17 \text{ s}^{-1}$ . The mw is approximatively the same ( $M_n \sim 30 \text{ kg/mol}$ ) for all the materials in (a)-(c). In (d)-(f)  $M_n$  increases from light to dark. Open symbols indicate the failure stress and strain of each sample [Color figure can be viewed at wileyonlinelibrary.com]



domains of PBT. Next, the stress mildly increases to ~300% strain when the material starts to harden. Finally, high stresses and strains are reached resulting in breakage.

All samples show a decrease in failure stress and strain with increasing temperature, but the magnitude of the temperature effect depends on the amount of soft block in the system. It is observed that increasing  $SB_{wt}$  leads to a reduction in temperature resistance. The materials are compared at very similar Mw but have different relative distances of the testing temperature from the  $T_m$ . Figure 7 better summarizes the effects of the temperature on the failure strains as the SB/HB ratio changes, by showing the failure strains collected from tensile tests versus the distance from the melting peak temperature ( $T_m - T$ ).

Note that 75\_PTMO3k has a higher melting temperature compared with 70\_PTMO2k (due to the longer PTMO diols resulting in longer PBT segments) but shows less temperature resistance.

This implies that the relative distance from  $T_m$  is not enough to explain the temperature resistance of these systems. If the temperature resistance is related to connectivity then it would be expected to increase with the crystallinity and the number of crystallized HB per chain,  $\langle N_{cryst} \rangle$ . This is consistent with the behavior observed for these systems at high temperature (see Table 1).

At RT the strain-hardening is much stronger than at higher temperatures for all materials, and it is worth noting that the ultimate failure stress at room temperature does not scale with the linear modulus. If PTMO blocks

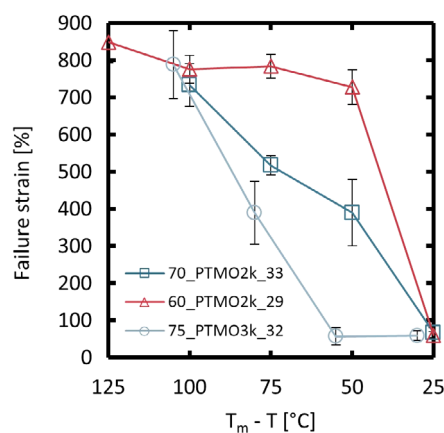


**FIGURE 7** Failure strain versus the difference between the melting peak temperature and the testing temperature ( $T_m - T$ ). Failure strains are taken from tests shown in Figure 6 as well as from additional tests.  $T_m$  are determined by DSC and given in Table 1 and Figure 3. Data  $<75^\circ\text{C}$  are excluded to avoid influence of SIC [Color figure can be viewed at wileyonlinelibrary.com]

are sufficiently long, they can crystallize under strain resulting in a shift in melting temperature from ~0 to ~50°C.<sup>8,38</sup> Previous studies<sup>13,38</sup> showed that the amount of SIC increases with the amount and length of soft blocks. Furthermore, the PTMO length also influences the value of strain at which we start to see SIC,<sup>13</sup> the longer the SB length, the earlier the onset of SIC. This is in line with our observation from the tensile tests at RT where the 75\_PTMO3k shows the highest strain-hardening among the tested grades.

At  $T > 50^\circ\text{C}$  the strain-hardening of the 75\_PTMO3k is comparable to the other grades. This underscores the importance for morphology evolution including contribution of SIC on the non-linear mechanical response.

### 3.4.2 | Varying mw – Fixed SB/HB ratio

Turning now to systems of fixed SB/HB ratio but varied Mw, in Figure 6(d)-(f) we see first that the Mw has little influence on the behavior up to the strain at which strain-hardening starts ( $\sim 300\%$ ). Again, this is consistent with the first effect of strain being to break-up the crystal network, whose structure and properties are insensitive to total chain length. At higher strains increased Mw leads to increased strain hardening and, at high temperatures, also to an increased extensibility. As mentioned previously, at RT the strain-hardening is mainly determined by PTMO SIC. Despite having the same amount of SB and same SB length, the high-Mw samples show a considerably higher strain-hardening, which suggests that higher Mw leads to a more effective SIC.

This is supported by the in-situ X-ray, where the high-Mw sample orients sooner and to a higher extent than the low-Mw one (Appendix S1).

At temperatures higher than the melting of the PTMO SIC ( $\sim 50^\circ\text{C}$ ), increasing the Mw still leads to a considerable increase of the strain-hardening. Therefore, there must be an additional mechanism in addition to SIC that is responsible for the change in high strain behavior.

Additional insights into the influence of composition and Mw on the morphology and the mechanics can be gained from cyclic tests (cyclic curves in Appendix S1). Figure 8(a),(b) shows the recovered elastic strain at each step of deformation for the 70\_PTMO2k samples with two different Mw at RT and  $100^\circ\text{C}$ . (Data relative to the samples 60\_PTMO2k\_29\* and 60\_PTMO2k\_50\* are

shown in Appendix S1). At each step strain, the high-Mw sample recovers more strain, that is, the residual strain at zero force is lower compared to the low-Mw counterpart. The Mw dependence of the recovered strain is stronger at higher temperatures, probably due to the increased chain mobility and lack of PTMO SIC.

The SIC increases the plastic contribution upon stretching as illustrated by the large deviation from the purely elastic response at higher strains. The applied pre-strains are the same at each cycle for the two materials, but the recovered strains are different, i.e. the high-Mw sample recovers more strain. As a consequence, at each cycle the high-Mw sample is stretched more than the low-Mw one. This effect is taken into account in Figure 8 (c) by plotting the tensile set (*TS*) for the same materials against the applied pre-strain. From the definition of tensile set in the Method section, the higher *TS*, the higher the plasticity in the material. The data show dramatically different behavior at RT and at  $100^\circ\text{C}$ . Indeed, the *TS* increases with deformation at RT, while it decreases at  $100^\circ\text{C}$ . Additionally, the differences in *TS* between the two Mw samples are higher at  $100^\circ\text{C}$ , where SIC does not overshadow the elastic contribution coming from the network connectivity. This confirms the stronger network elasticity present in the high-Mw sample, that we attribute to an increased network connectivity with Mw, attributed to the lower amount of dangling-ends and increased amount of HB per chains, as described quantitatively and more in detail in the last section of this paper. This supports the idea that upon stretching the morphology gradually evolves towards an elastomeric-like one (in the case of no SIC).

Interestingly, the tensile set analysis reveals differences with Mw already at low strains, which is different from the identical behavior in the continuous loading tensile tests in Figure 6. In fact, during loading, the plastic contribution coming from the yielding of the crystals

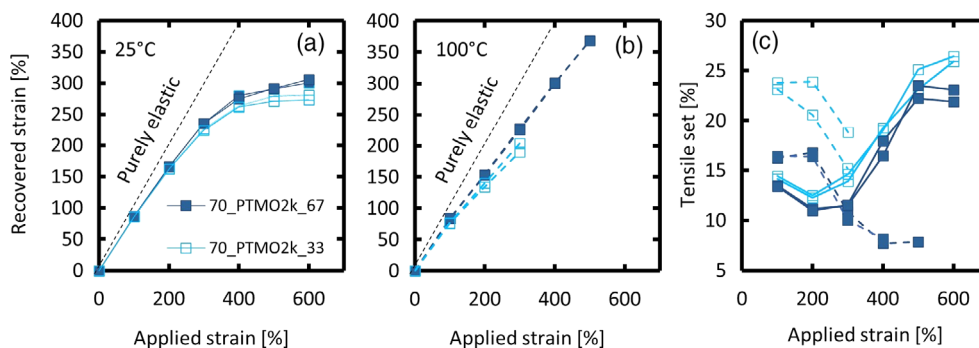


**FIGURE 8** Plots showing recovered strain obtained from cyclic tests performed, respectively, at (a) RT and (b)  $100^\circ\text{C}$ . the dashed line indicates the purely elastic behavior. (c) Tensile set (*TS*) versus the applied pre-strain at both RT (continuous lines) and  $100^\circ\text{C}$  (dashed lines). Duplicates are shown [Color figure can be viewed at [wileyonlinelibrary.com](http://wileyonlinelibrary.com)]

is what contributes most to the stress response and overshadows the contribution coming from the network connectivity. Unloading is largely an elastic response and, hence, more sensitive to the influence of pre-strain on the network connectivity. Figures 2 and 6(d)–(f) show that there are no differences with Mw on the loading curves before the strain-hardening onset, suggesting that the initial crystalline network is the same for samples with different Mw.

In contrast, the unloading analysis in Figure 8(c) clearly shows increased elasticity with Mw (e.g. lower  $TS$  at  $100^\circ\text{C}$  for the higher Mw). It is also worth noting that while the modulus drops strongly at strains  $<200\%$ , the  $TS$  and the recovered strains are less influenced at this low to moderate strain level.

### 3.4.3 | Strain-rate effects

Finally, we show how the strain-rate dependence changes with Mw. Figure 9 shows the engineering stress–strain curves at RT and  $100^\circ\text{C}$  for 60\_PTMO2k and 70\_PTMO2k, at two different strain rates and Mw.

At RT, decreasing the strain-rate leads to a decrease in strain hardening and to an increase in final extensibility. This is possibly due to a lower amount of PTMO SIC

at low loading rates. At  $100^\circ\text{C}$ , decreasing the strain-rate leads to a decrease in the extensibility as was observed by Aime et al.<sup>27</sup> for very similar systems. This is attributed to a stress-accelerated dissociation of HBs, that is, Eyring-like kinetics resulting in a creep-like failure mechanism. Similar to what is theorized for many other thermal activated processes over an energy barrier that decreases with applied.<sup>39–41</sup>

This behavior does not seem to be Mw or composition dependent. More interestingly, we observe a different behavior with Mw concerning the strain-hardening dependence with the strain-rate: the strain-hardening generally decreases as the strain-rate decreases. The effect on stress is much less pronounced for the high-Mw samples although rate still affects failure strain. To the best of our knowledge, this difference strain rate response for different Mw has not been reported before. The lower strain-rate dependence at high T for the high-Mw samples in combination with the increased elasticity and strain-hardening with Mw supports the idea of a relaxation mechanism for the stress bearing units in the system that is temperature- and Mw-dependent. The hypothesis of temperature and strain-rate dependent kinetics of disentanglement has been carried out for linear monodisperse PE both in experiments<sup>42</sup> and simulations.<sup>43</sup> The observations have been attributed to entanglements being

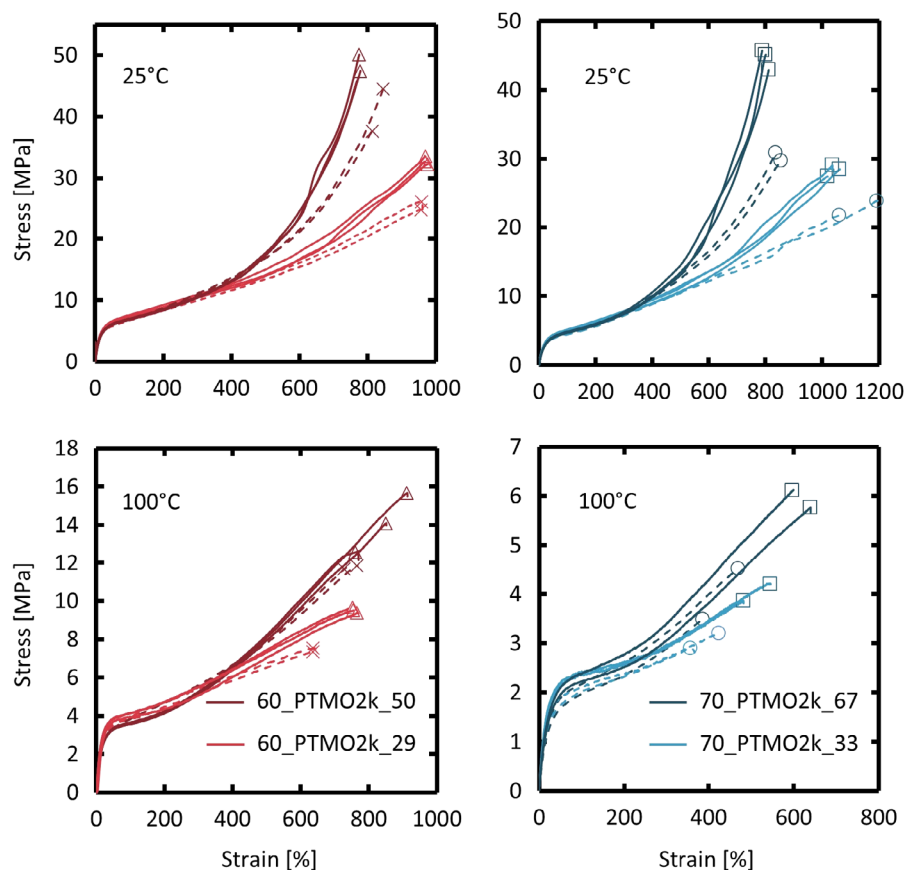


**FIGURE 9** Engineering stress–strain curves at RT and at  $100^\circ\text{C}$  at strain-rates of  $0.17\text{ s}^{-1}$  (continuous lines) and  $0.0017\text{ s}^{-1}$  (dashed lines). Duplicates are shown [Color figure can be viewed at [wileyonlinelibrary.com](http://wileyonlinelibrary.com)]

the fundamental stress bearing units in the system at large deformation. In our case, the presence and associations of the HBs must be taken into account as they have their own stress-, temperature- and time-dependent kinetics.<sup>27</sup> This will presumably also affect the entanglements dynamics since they prevent chain diffusion and disentanglement.

In the following section we start from the experimental observation to build a physical picture for the evolution of the microstructure upon deformation, highlighting the different dynamics responsible for the mechanical behavior and providing a qualitative physical model that reasonably explains the results obtained from the tensile and cyclic tests.

## 4 | DISCUSSION

### 4.1 | Morphology evolution

Our physical picture for the morphology evolution is largely based on analyses in previous studies on similar materials.<sup>1,13,25</sup> The microstructural evolution with strain is depicted in Figure 4. The mechanical properties in the linear regime and up to the yield region are mainly governed by the crystallinity of the system. The linear modulus is dominated by the volume fraction of ribbon-like PBT crystals with little influence of total chain length. With increasing deformation, the morphology evolves via crystal breaking and orientation, as indicated by the decrease in the crystal size with deformation and by the long period which increases at small deformation and decreases at strains  $> \sim 100\%$  as a result of the breaking mechanism.<sup>1,20,21</sup> Our results from SAXS (Appendix S1) also confirm the decrease in long period with deformation. The broken crystalline domains reorient such that the PBT and the PTMO segments are aligned along the stress direction. Up to  $\sim 300\%$  strain, the Mw of the total chain does not affect the response in a continuous loading experiment since it does not significantly influence the crystallinity or initial morphology. However, unloading analysis reveals differences with increasing Mw increasing the elastic recovery. By  $\sim 300\%$  strain the break-up and re-orientation process of the PBT crystals is mostly complete, but the crystal disruption and fragmentation will continue with increased strain due to the pull-out of the PBT segments from the crystals.<sup>27</sup> At higher strains, a strong Mw-dependence on strain-hardening is observed. Thus, starting from a rigid mechanically interlocking network of crystal ribbons, the morphology evolves with strain into a network with fragmented PBT crystals acting as isolated physical crosslinks. Eventually to a highly oriented structure

where, if temperature allows, SIC of the SBs can additionally contribute to the stress response.

### 4.2 | Strain-hardening and network elasticity

The nature of strain-hardening is still a topic of debate for semi-crystalline polymers and only a few observations where molecular parameters are varied in a systematic fashion are present in literature, with especially limited observations at high temperatures.

Kennedy et al.<sup>44</sup> hypothesized that the strain-hardening increase with Mw in semi-crystalline random copolymers of ethylene, which behave very similarly to these TPE-Es,<sup>45</sup> can be explained either by SIC of the stretched co-polymer and increased elasticity in the amorphous disordered inter-crystalline region due to the orientation and stretching of the entangled segments.

In our case, the first mechanism is dominant at  $T < \sim 50^\circ\text{C}$  due to PTMO SIC. Increasing the Mw leads to an increased connectivity which results in a better, more efficient orientation and more persistent network during stretching. This amplifies the effect of the PTMO SIC on the mechanics (Appendix S1). However, at higher temperatures, the hardening response should come entirely from the increased elasticity in the amorphous inter-crystalline region, which is consistent with the results obtained from the cyclic tests (Figure 8).

For semi-crystalline homopolymers it has been observed<sup>46</sup> that an increase in Mw strongly increases the strain-hardening while decreasing the drawability and the stresses at failure. This effect has been correlated with the amount of tie molecules and especially entanglements in the amorphous region between crystals.<sup>47</sup> A review on the argument has been published by Bartczak.<sup>48</sup> Kennedy et al. presented results for semi-crystalline polymers showing that increasing Mw leads to an increase of the entanglement density in the amorphous region<sup>46</sup> due to the expulsion of entanglements from the crystalline phase during cooling from the melt. This results in an earlier onset and stronger strain-hardening response. Since the crystals in our system are obtained via PBT-segments stacking and not via folding (the PBT segments are too short to allow even for a single fold), we assume that the entanglement density does not significantly change from that of the melt when the Mw is varied. Furthermore, we do not observe a significant shift in the on-set of strain-hardening. In summary, the previous findings on the nature of strain-hardening based on the study of semi-crystalline homopolymers do not fully explain the results our TPE-Es.



In the following section we propose a phenomenological model for the increased strain-hardening, elasticity and ductility observed at high temperature ( $T > \sim 50^\circ\text{C}$ ) for the high-Mw samples, based on the connectivity of both PBT crystals and the entangled network.

### 4.3 | Residual connectivity and stress bearing units

The model aims to count the number of stress bearing units (SBUs) in the system at each stage of deformation, meaning that the non-relaxed segments between two entanglements and between entanglements and PBT-crystals are both counted. The goal is to propose a qualitative mechanism for the stress response which is time- and temperature- dependent, with this dependency decreasing as Mw increases. During deformation, due to the pull-out of the crystalline PBT segments from the respective crystals, the number of crosslink points and therefore, the overall connectivity of the system decreases.<sup>27</sup>

We assume that the pulled out PBT segments do not associate again. In this framework, the crystallized HB contribute to the stress response by keeping segments of chains trapped and ensuring connectivity. For simplicity, all the chains are treated as monodisperse in total chain length ( $M$ ) and block lengths and the focus is on the microstructure where the initial crystal network has broken up (Figure 4(c)) and the temperatures are above the melting of the SIC. Since the emphasis is mainly on the effect that the Mw has on the SBUs at different strain rates, the figures below focus on the analysis done on a single system, that is, the 70\_PTMO2k series, with fixed amount of SB ( $\text{SB}_{\text{wt}} = 70\%$ ), SB length ( $M_{\text{n,SB}} = 2 \text{ kg/mol}$ ) and crystallinity ( $X_{\text{PBT}} = 35\%$ ).

Since the testing temperatures are much higher than the  $T_g$  of the soft PTMO-rich phase ( $T_g = \sim -70^\circ\text{C}$ ), chain segments are highly mobile and likely to disentangle as soon as they are not trapped between two crystals. Thus, only disentanglement of dangling chain-ends is possible. When a pull-out event occurs for a HB in which the dangling-end is anchored, the latter grow. The chain segment previously trapped now has the possibility to disentangle.

This concept is illustrated in Figure 10. As the strain increase, more pull-out events occur, which translates into a progressive decrease of the number of crystallized HB per chain. As a consequence, the length of the dangling-ends increases as follows:

$$M_{\text{dang}} = \frac{M - \langle N_{\text{crys}} \rangle (1-f) (\langle L_n \rangle M_{0,\text{PBT}})}{1 + \langle N_{\text{crys}} \rangle (1-f)} \quad (7)$$

where  $f$  is an independent parameter representing the fraction of HBs pulled out from the crystal domains during deformation with  $f$  given by the number of HB pulled out divided by the number of HB per chain initially crystallized  $\langle N_{\text{crys}} \rangle$ . The weight fraction of a chain being part of a dangling-end ( $2 \times M_{\text{dang}}/M$ ) contributes less to the stress response because it is able to disentangle. For a given  $f$ , this is higher for the low-Mw samples (Figure 11 (a)). As the Mw increases, the number of dangling ends decreases as  $\propto 1/M$ , while their length increases as  $\sim M/(1+M)$ .

Thus, as shown in Figure 11(b) the dangling end length initially increases with total Mw before plateauing. Also when no pull-out has occurred ( $f = 0$ ), the dangling-end mass does not strongly depend on Mw but the dependency grows with increasing  $f$ , i.e. as the pull-out events occur during deformation.

The dangling-end length becomes crucial when the dynamics of disentanglements are important for the determination of the stress response in the system. Indeed, these chain segments cannot simply disentangle by reptation due to the constraints imposed by the PBT crystals. By modeling a dangling-end anchored to a PBT crystal as a branch of a star polymer, the longest time for the branch to relax from its original constraints

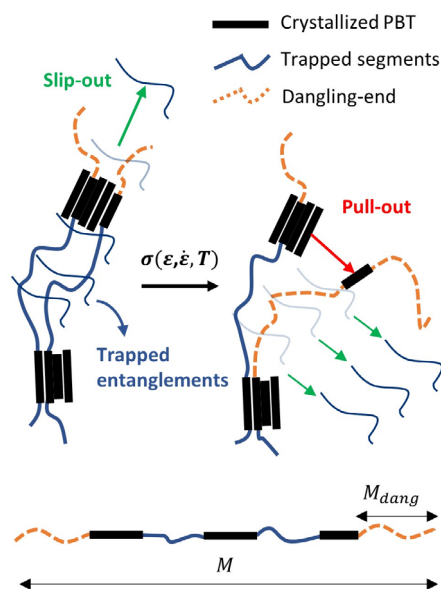


**FIGURE 10** Cartoon representing the idea of the disentanglement allowed (dashed to solid lines) only for the segments of chains not trapped between two crystallized hard blocks (HB). Dangling ends can slip-out from entanglements. As pull-out events occur, segments of chain are not trapped anymore and can now escape the entanglements. At the same time, the length of the dangling-ends increases, increasing the time needed to escape [Color figure can be viewed at [wileyonlinelibrary.com](http://wileyonlinelibrary.com)]

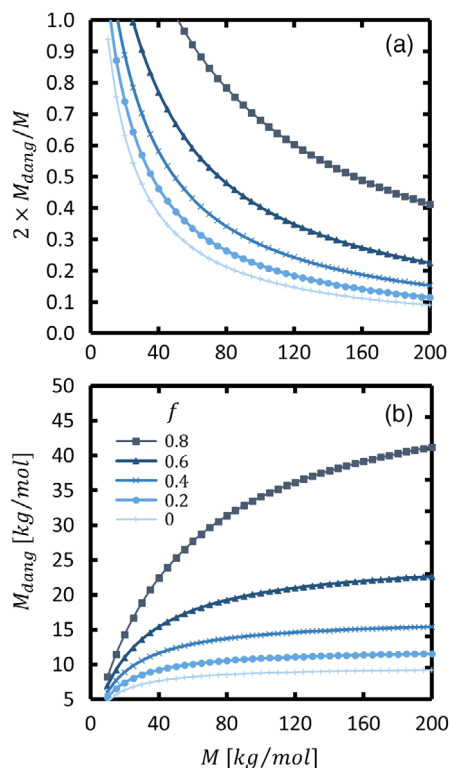


**FIGURE 11** (a) Weight fraction of dangling-end in a chain, i.e. not trapped between two crystalline HBs, and (b) dangling-end length as a function of the total chain mass,  $M$ , both the plots show how these vary with increasing the fraction of HBs pulled-out during deformation ( $f$ ) [Color figure can be viewed at [wileyonlinelibrary.com](http://wileyonlinelibrary.com)]

(retraction time) grows exponentially with its mass.<sup>49</sup> It is calculated by:

$$\tau_{\text{retraction}} = \tau_e(T) \exp\left(\frac{15 M_{dang}}{8 M_e}\right) \quad (8)$$

$\tau_e(T)$  is calculated from  $\tau_e(240 \text{ }^\circ\text{C}) = 2.4 \times 10^{-8}$  s obtained from a theoretical fit to experimental data from melt rheology<sup>50</sup> Arrhenius-scaled with an activation energy of  $E_a = 5.24 \times 10^4$  J/mol. The estimated retraction times at the testing temperatures are of the same order of the time scales of our experiments,  $1/\epsilon$  (Figure 12(a)). Note also that as the Mw increases the relative increase in retraction time decreases, e.g. the increase in retraction time from 25 to 50 kg/mol is much larger than between 100 and 150 kg/mol at a given  $f$ .

To calculate the number of SBU, we exclude the entanglements present in the dangling chain-segments with a retraction time shorter than  $1/\epsilon$  since they are able to disentangle and relax during deformation. Consequently, they do not contribute to the stress response. The SBUs molar density is then calculated by

$$\text{SBU}(f) = \left[1 - f_{dang}(f)\right] \left(\frac{\rho}{M_e}\right) + (1-f) \langle N_{\text{cryst}} \rangle \left(\frac{\rho}{M}\right) \quad (9)$$

where  $f_{dang}(f) = 2 \times (M_{dang}(f))/M$  is the weight fraction of dangling-ends in a chain and polymer density,  $\rho = 1.1 \text{ g/cm}^3$ .

If  $f_0$  is the fraction of pulled out HBs at which the dangling-ends are not able to relax anymore, i.e.  $\tau_{\text{retraction}} > 1/\epsilon$ , at  $f \geq f_0$  the first term of Equation 8 becomes  $[1 - f_{dang}(f_0)] (\rho/M_e)$ . This is equivalent to saying that the fraction of dangling-end that at  $f < f_0$  was able to relax is still able to do so.

Figure 12(b) shows the molar density of SBUs for different  $M$ , plotted against the fraction of pulled out HBs during deformation. In line with our experimental results (Figure 9), this model predicts that for low-Mw chains, lowering the strain-rates leads to fewer SBUs compared to high strain-rates and the effect of rate is less as  $M$  increases. Note that for short chains, almost no strain-rate effect is predicted in this strain-rate range as dangling-ends are always short enough to disentangle. For intermediate length, we observe the largest influence of strain-rate. At high Mw, the rate effect is decreased. This is because high-Mw samples show more SBUs at each stage of deformation which results in a higher stress response (strain-hardening), network elasticity and connectivity in agreement with the experimental observations from the tensile and cyclic tests. In summary, increasing Mw decreases the number of dangling-ends and chain weight fraction belonging to a dangling-end. However, the absolute length of the dangling-ends increases slowing down the disentanglement kinetics.

Consequently, at each stage of deformation high-Mw samples have more SBUs and a less time-dependent stress response than low-Mw samples. This approach is a simplification that does not take into account the polydispersity of the chain-length or single blocks. The model treats  $f$  as an independent parameter while in reality it should depend on the applied strain. However, it is reasonable to believe that the strain dependency of  $f$  should not be Mw independent as Mw should influence the pull-out rate of the HBs. It is not trivial to assess whether the increase in Mw leads to a faster or slower pull-out rate. Longer chains are better connected with the network, which also means that they have more sites susceptible to the pull-out mechanism and which are under stress for longer time during deformation. This would lead to the pull-out rate increasing with Mw. On the other hand, the pull-out event has a higher chance to cause a low-Mw chain to become disconnected from the network.<sup>27</sup> This would generate higher stresses locally facilitating the pull-out of the neighboring HBs and generating a knock-

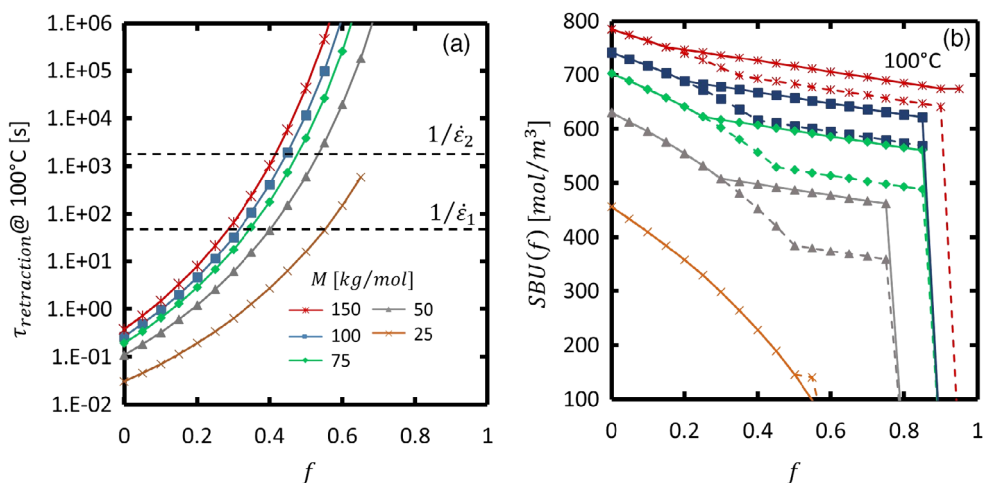


**FIGURE 12** (A) Retraction time at  $100^\circ\text{C}$  of a dangling-end modeled as a branch of a star polymer versus the fraction of pulled-out HBs ( $f$ ). The curves end when  $\langle N_{\text{crys}} \rangle (1-f) < 1$  and the retraction time cannot be defined, that is, when, on average, the chains no longer have at least one HB in a crystal and are thus free to relax via reptation. (B) Molar density of the SBUs in the system as a function of  $f$ . Solid and dashed lines correspond to the experimental time scales for the low and high strain-rates used,  $\epsilon_1 = 0.17 \text{ s}^{-1}$  and  $\epsilon_2 = 0.0017 \text{ s}^{-1}$ . Different colors and symbols correspond to the different chain lengths,  $M$ , given in the legend [Color figure can be viewed at [wileyonlinelibrary.com](http://wileyonlinelibrary.com)]

on effect that would accelerate the pull-out rate of the HB for low-Mw systems. Despite the simplifying assumptions and unanswered questions about the link between strain,  $f$ , and Mw, this model qualitatively identifies a plausible physical mechanism able to explain the observed effects of Mw and strain-rate.

## 5 | CONCLUSIONS

The presented series of systematic experimental observations combined with a simple mechanistic model bring new insights furthering the understanding of the effect of temperature, Mw and composition on the mechanical properties of soft-TPEs. The simple model provides a plausible mechanism driving the Mw and strain-rate effects on the mechanical response that is consistent with, and builds upon, previous studies.<sup>8,19,25,27</sup> Key insights are summarized below:

- The initial modulus is determined by the ribbon-like PBT crystal structure and volume fraction and increases with the wt% of PBT as a result of increased PBT crystallinity. Upon reloading after moderate deformation ( $< 200\%$  strain), the modulus and hysteresis decrease while the tensile set remains relatively constant. This suggests that the initial loading response is dominated by a rigid, loading bearing crystal structure that breaks up with deformation and whose unloading behavior is dominated by the amorphous regions.
- Whether or not PTMO SIC occurs has a large influence on the high strain mechanical response and depends

on the testing temperature. Failure strain and stress do not necessarily scale with the wt% of PBT if PTMO SIC occurs. SIC strongly increases the strain hardening response and decreases the elastic recovery at high strains. The amount of SIC increases with increasing amount and length of PTMO soft block while increasing Mw decreases the onset strain for SIC.

- Temperature resistance is not governed by the distance of the testing temperature from the peak melting temperature. Network connectivity contributes strongly, and temperature resistance increases with increasing Mw.
- While Mw has little influence during continuous loading up to  $\sim 300\%$  strain, increasing Mw increases the strain-hardening response at higher strains as well as the elastic recovery at low and high strains. At higher temperatures, where no SIC occurs, increasing the strain rate increases the strain hardening of low-Mw more than high-Mw samples, while increasing the failure strain of both.
- A model based on the network connectivity as generated by both the crystalline PBT segments and the entangled chains is proposed to explain the observed effects of Mw on the rate and temperature dependent characteristic of the strain-hardening response. This model shows how the weight fraction and length of the dangling-ends vary as a function of chain length and number of HB pull-out events. The number of SBUs evolves with pull-out events as well as with the time-scale of dangling-end relaxation. For long dangling-ends, disentanglement time is longer than the experimental time scale and entanglements in the dangling-ends contribute to the stress response.

## ACKNOWLEDGMENTS

This work was financially supported by funding from the H2020 Programme (MARIE SKŁODOWSKA-CURIE ACTIONS) of the European Commission's Innovative Training Networks (H2020-MSCA-ITN-2017) under DoDyNet REA Grant Agreement N°0.765811. The authors thankfully acknowledge Louis Pitet and the polyester group in DSM for the synthesis of the model systems, Mingwen Tian and Junyu Li, respectively, for the support with AFM and X-ray images acquisition and Patrick van Soelen and Marcel Teeuwen for the help with the mechanical instrumentation. Finally, the authors also acknowledge Evelyne Van Ruymbeke is Research Associate of the FNRS.

## ORCID

Simone Sbrescia  <https://orcid.org/0000-0003-1958-0044>

Tom Engels  <https://orcid.org/0000-0002-4085-1489>

Evelyne Van Ruymbeke  <https://orcid.org/0000-0001-7633-0194>

Michelle Seitz  <https://orcid.org/0000-0003-4741-8618>

## REFERENCES

- [1] S. Fakirov, *Handbook of Condensation Thermoplastic Elastomer*, Wiley-VCH Verlag GmbH and Co, Weinheim **2005**.
- [2] J. C. Stevenson, S. L. Cooper, *Macromolecules* **1988**, *21*, 1309.
- [3] M. Nébouy, A. De Almeida, S. Brottet, G. P. Baeza, *Macromolecules* **2018**, *51*(16), 6291.
- [4] W. Gabriëlse, M. Soliman, K. Dijkstra, *Macromolecules* **2001**, *34*(6), 1685.
- [5] V. M. Litvinov, M. Bertmer, L. Gasper, D. E. Demco, B. Blümich, *Macromolecules* **2003**, *36*(20), 7598.
- [6] A. De Almeida, M. Nébouy, G. P. Baeza, *Macromolecules* **2019**, *52*(3), 1227.
- [7] N. J. Sijbrandi, A. J. Kimenai, E. P. C. Mes, R. Broos, G. Bar, M. Rosenthal, Y. Odarchenko, D. A. Ivanov, P. J. Dijkstra, J. Feijen, *Macromolecules* **2012**, *45*(9), 3948.
- [8] P. Zhu, X. Dong, D. Wang, *Macromolecules* **2017**, *50*(10), 3911.
- [9] T. L. Smith, *J. Polym. Sci. Part B Polym. Phys.* **1974**, *12*(9), 1825.
- [10] R. Gaymans, *J. Prog. Polym. Sci.* **2011**, *36*(6), 713.
- [11] C. G. Seefried, J. V. Koleske, F. E. Critchfield, *J. Appl. Polym. Sci.* **1975**, *19*(9), 2503.
- [12] S. Fakirov, A. A. Apostolov, P. Boeseke, H. G. Zachmann, *J. Macromol. Sci., Part B* **1990**, *29*(4), 379.
- [13] E. V. Konyukhova, V. M. Neverov, Y. K. Godovsky, S. N. Chvalun, M. Soliman, *Macromol. Mater. Eng.* **2002**, *287*(4), 250.
- [14] J. W. C. Van Bogart, A. Lilaonitkul, L. E. Lerner, S. L. Cooper, *J. Macromol. Sci., Part B* **1980**, *17*(2), 267.
- [15] A. A. Deschamps, D. W. Grijpma, J. Feijen, *Polymer* **2001**, *42*(23), 9335.
- [16] M. Dahrouch, A. Schmidt, L. Leemans, H. Linssen, H. Götz, *Macromol. Symp.* **2003**, *199*, 147.
- [17] H. Sup Lee, S. Ra Yoo, S. Won Seo, *J. Polym. Sci. Part B Polym. Phys.* **1999**, *37*(22), 3233.
- [18] G. J. E. Biemond, J. Feijen, R. J. Gaymans, *J. Mater. Sci.* **2008**, *43*(10), 3689.
- [19] M. Nébouy, A. Louhichi, G. P. Baeza, *J. Polym. Eng.* **2019**, *40*(9), 715.
- [20] N. Stribeck, D. Sapoundjieva, Z. Denchev, A. A. Apostolov, H. G. Zachmann, M. Stamm, S. Fakirov, *Macromolecules* **1997**, *30*(5), 1329.
- [21] N. Stribeck, S. Fakirov, A. A. Apostolov, Z. Denchev, R. Gehrke, *Macromol. Chem. Phys.* **2003**, *204*(7), 1000.
- [22] E. Unsal, B. Yalcin, I. Yilgor, E. Yilgor, M. Cakmak, *Polymer* **2009**, *50*(19), 4644.
- [23] A. Nogales, I. Sics, T. A. Ezquerra, Z. Denchev, F. J. Balta Calleja, B. S. Hsiao, *Macromolecules* **2003**, *36*(13), 4827.
- [24] F. Yeh, B. S. Hsiao, B. B. Sauer, S. Michel, H. W. Siesler, *Macromolecules* **2003**, *36*(6), 1940.
- [25] M. C. E. J. Niesten, R. J. Gaymans, *Polymer* **2001**, *42*(14), 6199.
- [26] J. -N. Gorce, J. W. Hellgeth, T. C. Ward, *Polym. Eng. Sci.* **1993**, *33*(18), 1170.
- [27] S. Aime, N. D. Eisenmenger, T. A. P. Engels, *J. Rheol.* **2017**, *61*(6), 1329.
- [28] H. Cho, S. Mayer, E. Poselt, M. Susoff, P. J. In't Veld, G. C. Rutledge, M. C. Boyce, *Polymer* **2017**, *128*, 87.
- [29] I. Bowman, D. Brown, R. Wetton, *Polymer* **1969**, *10*, 715.
- [30] M. Yokouchi, Y. Sakakibara, Y. Chatani, H. Tadokoro, T. Tanaka, K. Yoda, *Macromolecules* **1976**, *9*, 266.
- [31] D. E. Niehaus, C. Jackson, *Polymer* **2000**, *41*, 259.
- [32] C. Das, D. J. Read, M. A. Kelmanson, T. C. B. McLeish, *Phys. Rev. E* **2006**, *74*(1), 011404.
- [33] M. E. Seitz, W. R. Burghardt, K. R. Shull, *Macromolecules* **2009**, *42*(22), 9133.
- [34] F. Deplace, A. K. Scholz, G. H. Fredrickson, E. J. Kramer, Y. W. Shin, F. Shimizu, F. Zuo, L. Rong, B. S. Hsiao, G. W. Coates, *Macromolecules* **2012**, *45*(13), 5604.
- [35] F. Deplace, Z. Wang, N. Lynd, A. Hotta, J. Rose, P. Hustad, J. Tian, H. Ohtaki, G. Coates, F. Shimizu, K. Hirokane, F. Yamada, Y. W. Shin, L. Rong, J. Zhu, S. Toki, B. Hsiao, G. Fredrickson, E. Kramer, *J. Polym. Sci. Part B Polym. Phys.* **2010**, *48*(13), 1428.
- [36] G. P. Baeza, *Macromolecules* **2018**, *51*(5), 1957.
- [37] L. J. Gibson, M. F. Ashby, *Cellular Solids: Structure and Properties*, 2nd ed., Cambridge University Press, Cambridge **1997**.
- [38] A. Schmidt, W. S. Veeman, V. M. Litvinov, W. Gabriëlse, *Macromolecules* **1998**, *31*(5), 1652.
- [39] J. Rottler, M. O. Robbins, *Phys. Rev. E* **2003**, *68*(1), 011507.
- [40] J. Rottler, M. O. Robbins, *Phys. Rev. Lett.* **2005**, *95*(22), 225504.
- [41] H. Eyring, *J. Chem. Phys.* **1936**, *4*(4), 283.
- [42] K. H. Nitta, T. Ishiburo, *J. Polym. Sci. Part B Polym. Phys.* **2002**, *40*(18), 2018.
- [43] Y. Termonia, S. R. Allen, P. Smith, *Macromolecules* **1988**, *21*(12), 3485.
- [44] M. A. Kennedy, A. J. Peacock, M. D. Failla, J. C. Lucas, L. Mandelkern, *Macromolecules* **1995**, *28*(5), 1407.
- [45] R. Seguela, F. Rietsch, *Polymer* **1986**, *27*(5), 703.
- [46] M. A. Kennedy, A. J. Peacock, L. Mandelkern, *Macromolecules* **1994**, *27*(19), 5297.
- [47] Y. Men, J. Rieger, G. Strobl, *Phys. Rev. Lett.* **2003**, *91*(9), 095502.
- [48] Z. Bartczak, A. Galeski, *Macromol. Symp.* **2010**, *294*(1), 67.
- [49] H. Watanabe, *Prog. Polym. Sci.* **1999**, *24*(9), 1253.

- [50] A. E. Likhtman, T. C. B. McLeish, *Macromolecules* **2002**, *35*, 6332.

### SUPPORTING INFORMATION

Additional supporting information may be found online in the Supporting Information section at the end of this article.

**How to cite this article:** Sbrescia S, Ju J, Engels T, Van Ruymbeke E, Seitz M. Morphological origins of temperature and rate dependent mechanical properties of model soft thermoplastic elastomers. *J Polym Sci.* 2021;59: 477–493. <https://doi.org/10.1002/pol.20200791>

## ORIGINAL ARTICLE

# Strain induced strengthening of soft thermoplastic polyurethanes under cyclic deformation

Giorgia Scetta<sup>1</sup>  | Jianzhu Ju<sup>1</sup>  | Nathan Selles<sup>2</sup>  | Patrick Heuillet<sup>2</sup>  |  
Matteo Ciccotti<sup>1</sup>  | Costantino Creton<sup>1</sup> 

<sup>1</sup>Sciences et Ingénierie de la Matière Molle, École Supérieure de Physique et de Chimie Industrielles de la Ville de Paris (ESPCI), Université PSL, CNRS, Sorbonne Université, 10 rue Vauquelin, Paris, F-75231 cedex 05, France

<sup>2</sup>Laboratoire de Recherches et de Contrôle du Caoutchouc et des Plastiques, Vitry-sur-Seine, France

## Correspondence

Matteo Ciccotti and Costantino Creton, Sciences et Ingénierie de la Matière Molle, ESPCI Paris, Université PSL, CNRS, Sorbonne Université, 75005 Paris, France. Email: matteo.ciccotti@espci.psl.eu and costantino.creton@espci.psl.eu

## Funding information

ANRT; H2020 European Research Council, Grant/Award Number: AdG No 695351

## Abstract

We investigate the cyclic mechanical behavior in uniaxial tension of three different commercial thermoplastic polyurethane elastomers (TPU) often considered as a sustainable replacement for common filled elastomers. All TPU have similar hard segment contents and linear moduli but sensibly different large strain properties as shown by X-ray analysis. Despite these differences, we found a stiffening effect after conditioning in step cyclic loading which greatly differs from the common softening (also referred as Mullins effect) observed in chemically crosslinked filled rubbers. We propose that this self-reinforcement is related to the fragmentation of hard domains, naturally present in TPU, in smaller but more numerous sub-units that may act as new physical crosslinking points. The proposed stiffening mechanism is not dissimilar to the strain-induced crystallization observed in stretched natural rubber, but it presents a persistent nature. In particular, it may cause a local reinforcement where an inhomogeneous strain field is present, as is the case of a crack propagating in cyclic fatigue, providing a potential explanation for the well-known toughness and wear resistance of TPU.

## KEYWORDS

cyclic behavior, damage, stiffening, thermoplastic elastomers, Young modulus

## 1 | INTRODUCTION

Soft thermoplastic polyurethane elastomers (TPU) are well known for their outstanding combination of reversible elasticity, abrasion resistance, and easy processability. They are multiblock copolymers characterized by alternating soft segments (SS) and hard segments (HS) forming a two-phase microstructure where the soft phase is the majority. The microphase separation is driven by the ability of the HS to form inter and intra-chain hydrogen bonds between carbonyl and amine groups developing therefore small and stiff lamellae domains surrounded by the soft phase. These hard domains (HD) have a typical size of 5–30 nm and are

stiffer than soft segment domains (SD) acting both as nanoscale fillers and physical crosslinks.<sup>1,2</sup> The versatile processing, recyclability and comparable reversible elasticity make TPU a serious competitor to replace elastomers in a number of technical applications despite the higher material cost.

Unsurprisingly, several studies on TPU focused on the correlation between their composition and mechanical properties at small and large strain<sup>1,3–5</sup> with the target to further explore the field of applications of this class of materials. In particular, the presence of a mechanical behavior with the same characteristics as those of the Mullins effect classically observed in filled rubbers<sup>6</sup> (higher energy losses and stress softening during the first

loading-unloading cycle), was reported in several TPU with different composition of HS and SS.<sup>3,7,8</sup>

The Mullins effect was originally detected in filled (or crystallizing) chemically crosslinked rubbers<sup>9</sup> and despite its relevance for final rubber properties, its origin is still debated and may depend on the detailed structure of the material. Nevertheless, it is generally accepted, that the first cycle hysteresis comes in particular from structural rearrangements of filler aggregates.<sup>6</sup> In the case of unfilled TPU, the change in mechanical behavior after the application of strain is due to structural rearrangements of the multiphase structure. This mechanical effect has been often qualitatively investigated and compared to that observed in filled rubbers,<sup>2,3,8,10</sup> but to the best of our knowledge, it has not yet been discussed quantitatively and in detail with a consistent methodology. Given the relevance of cyclic loading for the durability of materials and the renewed push to replace permanently crosslinked elastomers with thermoplastic reprocessable alternatives, we felt that the question of the evolution of the structure and mechanical properties of TPU with cyclic loading should be revisited.

Recently, Merckel and co-workers<sup>11</sup> proposed an easy methodology to quantify and compare the contribution of the structural changes to mechanical damage in filled elastomers after the application of a given strain. They proposed to use two damage parameters: one to account for the reduction in linear modulus and the other to account for the change in the onset of strain hardening in large strain. As they point out, these two parameters overlap for filled elastomers, and suggest that the same type of structural modification affects small strain stiffness and strain hardening.<sup>11</sup> However, mechanical damage is inherently related to the structural modifications induced by deformation, which is a material-specific property and may be fundamentally different between TPU and filled crosslinked rubbers.

Using the aforementioned methodology, we carried out here a quantitative evaluation of the structural changes occurring under cyclic loading in TPU and more importantly of the changes in mechanical properties induced by this cyclic loading. In order to be representative, we carried out all experiments with three commercially available TPU of the Elastollan series kindly provided by BASF AG.

Finally, within the framework of the possible substitution of conventional filled rubbers with TPU we also compared the mechanical behavior of our soft TPU with that of a typical crosslinked elastomer made from a random copolymer of styrene-butadiene (SBR) filled with reinforcing carbon black (CB), emphasizing similarities between these two classes of materials in terms of small

strain elasticity, and differences in structural evolution and large strain behavior.

## 2 | EXPERIMENTAL RESULTS

### 2.1 | Uniaxial tensile test

The different large strain behavior for all three TPU: TPU\_XTAL, TPU\_HARD, and TPU\_SOFT, can be appreciated in Figure 1(A), reporting the engineering stress-stretch curves in uniaxial tension at different temperatures. All TPU are characterized by a high extensibility at failure. The linear regime is only observed for a few percent of deformation ( $\lambda < 1.2$ ) where we calculated the Young modulus  $E$  Table 1 for 23 and 60°C). Above this limit, all three materials initially show a strain softening regime. Then TPU\_XTAL and TPU\_HARD present a marked strain hardening that is less intense in TPU\_SOFT. Only in case of TPU\_XTAL, as we reported in another work,<sup>12</sup> the strain hardening is accompanied by the formation of a new crystalline phase (strain-induced crystallization), which is partially retained in unloaded samples. The effect of increasing the temperature is mainly that of reducing the stress at break  $\sigma_b$  for all materials, and in the case of TPU\_SOFT also to reduce its maximum extensibility. Interestingly this reduction of strain at break with temperature was already observed for multiblock thermoplastic elastomers (TPE) based on poly-butadiene terephthalate (PBT) as HS as reported by Aime.<sup>13</sup>

The stress-stretch curves of uniaxial step-strain cyclic test for all TPU at 23°C are reported in Figure 1(B). All curves show similar characteristics:

- Large hysteresis between the first load-unload cycle.
- Very pronounced softening after the first loading, and recovery of the monotonic test behavior envelope only when the material is stretched to higher values than those previously applied (Mullins effect).
- Marked residual deformation  $\lambda_{\text{res}}$  after unloading.

This large residual deformation  $\lambda_{\text{res}}$  is consistent with literature data on TPU<sup>3,4</sup> and can be attributed to the absence of chemical crosslinks as well as to the plastic deformation of the HD following the application of large strains. Interestingly, we found that for the same value of maximum applied stretch  $\lambda_{\text{max}}$ , all TPUs present a similar fraction of residual stretch  $\lambda_{\text{res}}$  (Figure 1(C)). In contrast, in SBR the fraction of residual stretch is considerably lower for all values of tested maximum stretch compared to TPU because the chemical crosslinking prevents plastic deformation.

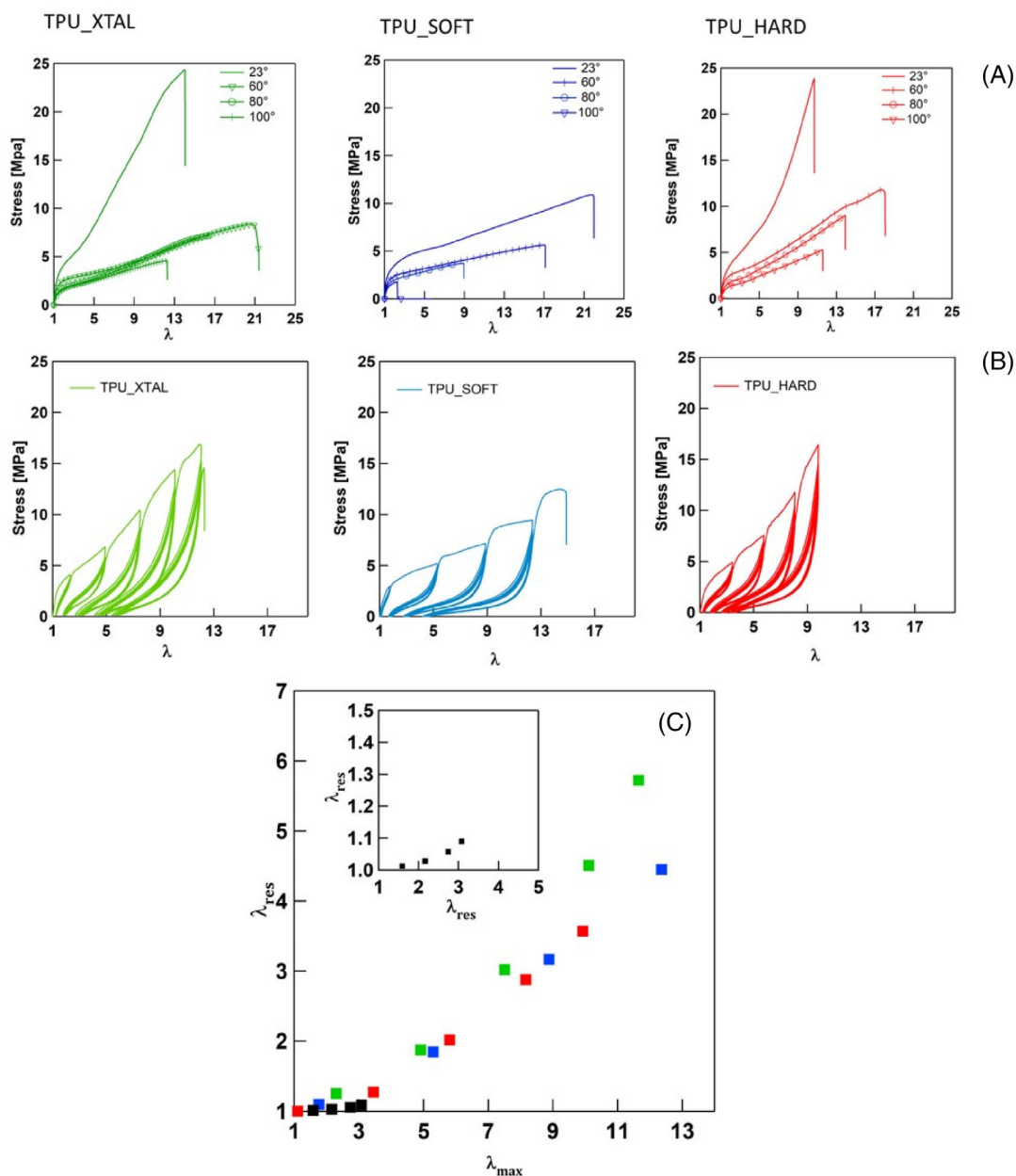


**FIGURE 1** Uniaxial stress-stretch curves at different temperatures (A) and cyclic stretch-stress curve at 23°C (B) for three TPU. (C) Residual vs. maximum applied deformation during the last cycle for: TPU\_XTAL ■, TPU\_SOFT ■, TPU\_HARD ■, SBR ■. TPU, thermoplastic polyurethane elastomers [Color figure can be viewed at [wileyonlinelibrary.com](http://wileyonlinelibrary.com)]

**TABLE 1** Young modulus for all TPU at 23 and 60°C

Name	E @ 23°C (MPa)	E @ 60°C (MPa)
TPU_XTAL	8.7 ± 0.1	5.0 ± 0.7
TPU_SOFT	7.8 ± 0.1	5.8 ± 0.1
TPU_HARD	7.3 ± 0.1	5.7 ± 0.1

Abbreviation: TPU, thermoplastic polyurethane elastomers.

## 2.2 | Structural investigations

WAXS 1D intensity profile is shown in Figure 2(A) for all three soft TPU. The absence of any crystalline reflection in TPU\_XTAL and TPU\_HARD indicates a completely amorphous hard phase in the pristine material. The crystalline peaks (indicated by the arrows) in TPU\_SOFT are compatible with the crystalline structure of PBT as reported in literature.<sup>14,15</sup>

2D SAXS images and the corresponding integrated profiles for pristine and unloaded samples (previously



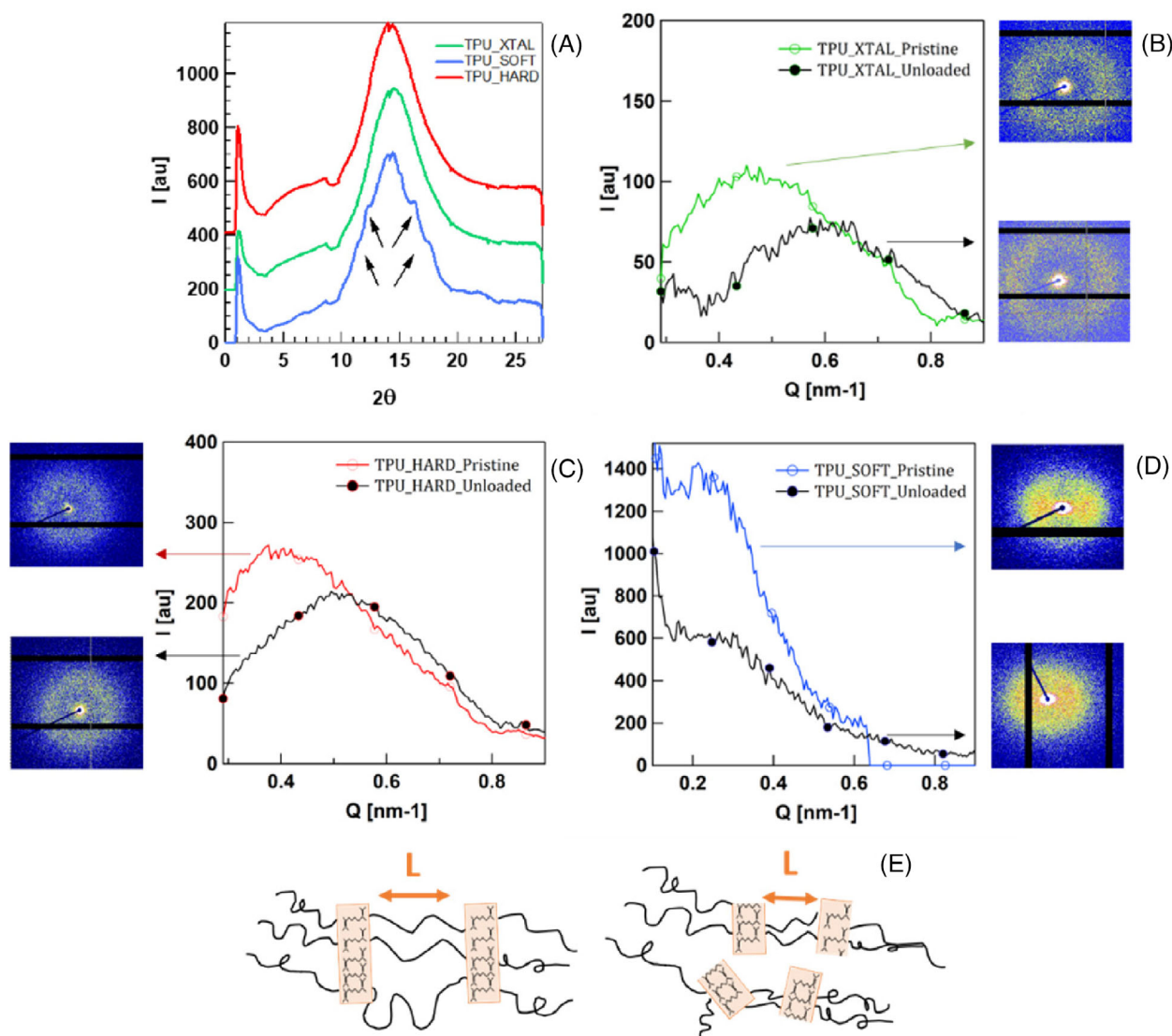


**FIGURE 2** (A) WAXS pattern for pristine TPU\_XTAL, TPU\_SOFT, and TPU\_HARD (data were vertically shifted for the sake of readability). (B) 2D SAXS pattern and 1D integrated profile for pristine and unloaded TPU\_XTAL, (C) TPU\_HARD, and (D) TPU\_SOFT. (E) Schematic illustrating the aggregation of HS in HD and definition of L (long period between HD) before and after loading. HD, hard domains; HS, hard segments; TPU, thermoplastic polyurethane elastomers [Color figure can be viewed at [wileyonlinelibrary.com](http://wileyonlinelibrary.com)]

Name	L (pristine) (nm)	L (unloaded) (nm)	C (nm)	$\phi$
TPU_XTAL	13	10	2.9	0.24
TPU_SOFT	30	26	–	–
TPU_HARD	16	12	2.9	0.24

**TABLE 2** Long period L between HD for pristine and unloaded samples (according to Bragg's law). Domains thickness and hard segments volume fraction ( $\phi$ ) for pristine TPU\_XTAL and TPU\_HARD calculate using the lamellar model

Abbreviation: TPU, thermoplastic polyurethane elastomers.

strained for several cycles at  $\lambda_{\max} = 2.25$ ) are shown in Figure 2(B),(C),(D) for TPU\_XTAL, TPU\_HARD, and TPU\_SOFT respectively. All curves are characterized by a

maximum in the intensity, due to microphase separation in TPU, which can be associated to the average distance between hard domains (or long period L).<sup>16</sup> The data of

the long period  $L$  calculated from Bragg's law in both pristine and unloaded samples are reported in Table 2. The lower value of  $L$  for strained samples was already observed in similar multiphase systems<sup>17–20</sup> and was generally associated to a fragmentation of HD into smaller units as sketched in Figure 2(E).

In addition, TPU\_SOFT has an elliptical SAXS pattern indicating the presence of a preferential orientation in the HD (probably induced by injection molding) that contrasts with the random orientation of HD in the other two TPU (circular pattern).

We adopted the lamellar model proposed by Strobl and Schneider,<sup>21</sup> which requires random orientation of HD, in order to evaluate some structural parameters in TPU\_XTAL and TPU\_HARD. Both materials present the same calculated values of thickness of HD ( $C$ ) and HS

volume fraction  $\phi$  as reported in Table 2, suggesting a very similar microstructure between TPU\_XTAL and TPU\_HARD. On the other hand, the higher value of  $L$  and the semi-crystalline character of HD in TPU\_SOFT, indicates the presence of some major structural difference compared to TPU\_XTAL and TPU\_HARD.

### 2.3 | Damage analysis in cyclic loading

We used the approach proposed by Merckel et al.<sup>11</sup> to estimate the damage in both unfilled TPU and filled SBR in terms of large strain damage ( $D_{ls}$ ) and small strain damage ( $D_{ss}$ ) as detailed in the following. First, we expressed the data of cyclic loading experiments in terms of true stress vs. Hencky strain as reported in Figure 3(A)

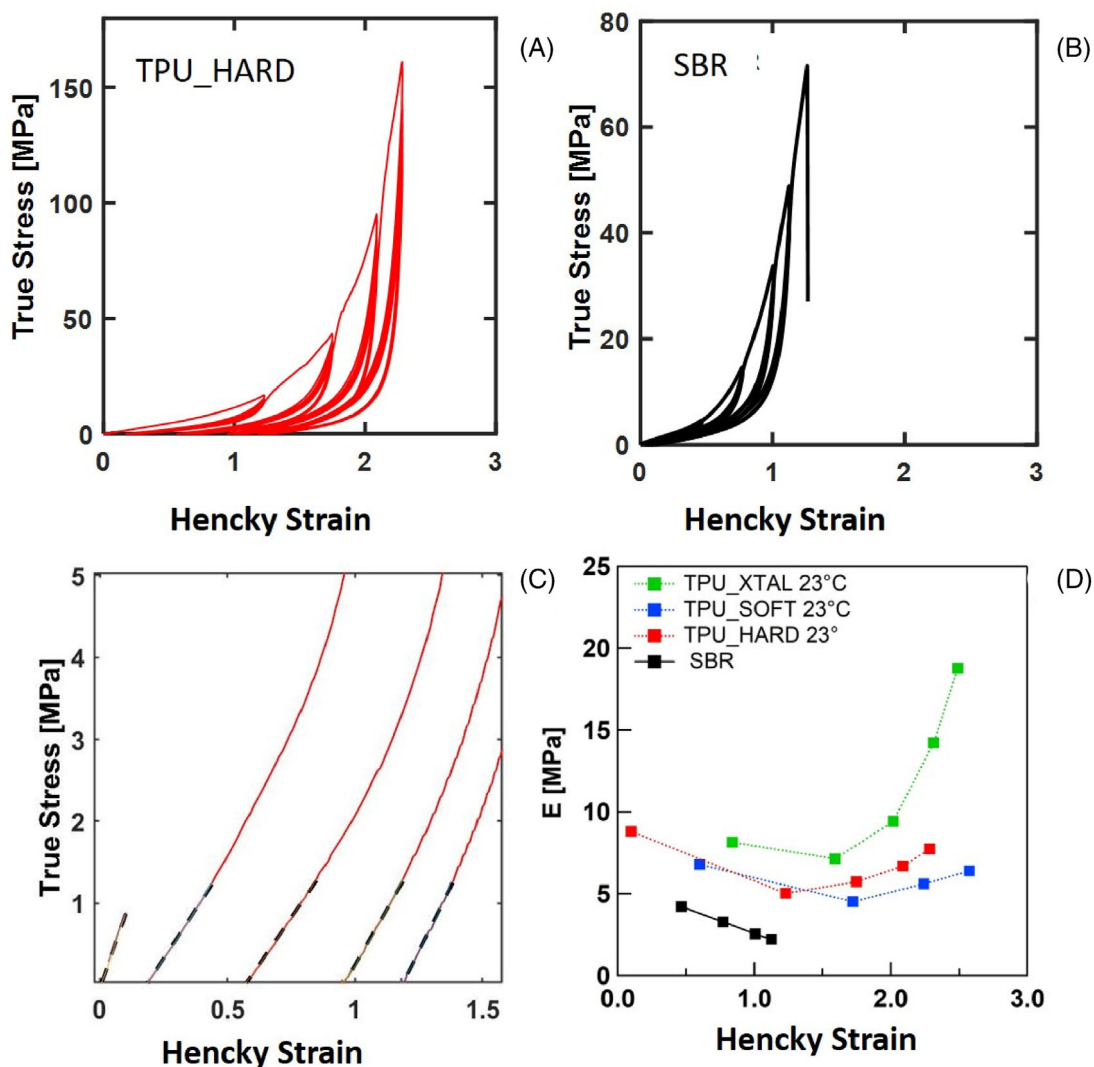


FIGURE 3 True stress-Hencky strain representation of cyclic experiment for (A) TPU\_HARD and (B) filled SBR. (C) Example of linear fitting for the calculation of  $E$  for TPU\_HARD. (D)  $E$  vs. Hencky strain for all TPU and for SBR. SBR, styrene-butadiene; TPU, thermoplastic polyurethane elastomers [Color figure can be viewed at [wileyonlinelibrary.com](http://wileyonlinelibrary.com)]

for TPU\_HARD and SBR Figure 3(B). We would like to stress that in cyclic deformation of TPU, the engineering stress–strain representation (Figure 1(B)), that seems to suggest a cyclic softening, is misleading. The engineering representation of strain only compares the final state with the initial state and, in the case of materials with high residual strain, it introduces a non-negligible bias on the measurement. Contrarily, the Hencky strain accounts for all the incremental steps of deformation (considering the value of the sample length just before each strain increment).

The value of  $D_{ss}$  for each increasing step of maximum strain  $h_k$ , is obtained from the ratio between the linear modulus  $E_k$  for the cycles of step  $k$  and that of the pristine material ( $E_0$ ) as follows:

$$D_{ss} = 1 - \frac{E_k}{E_0}. \quad (1)$$

Figure 3(C) shows an example of linear fitting used to calculate  $E$ , and the values of the fitted modulus for all TPU and SBR are shown in Figure 3(D). The larger

values of maximum Hencky strain at which the modulus was evaluated for TPU are justified by their higher maximum extensibility compared to SBR. While in the case of SBR  $E$  always decreases with maximum applied strain, in all TPU  $E$  initially decreases and, for Hencky strains larger than 1.5 ( $\lambda \sim 4$ ),  $E$  increases again reaching the pristine value or even larger values in the case of TPU\_XTAL. A similar result was also found by Koerner.<sup>20</sup>

The large strain damage, or  $D_{ls}$ , is associated to the onset of strain hardening in cyclic loading at different maximum strain and is defined as:

$$D_{ls} = 1 - \alpha, \quad (2)$$

where  $\alpha$  is a rescaling factor on the Hencky strain and it is obtained as follows:

1. Each unloading curve is shifted to the origin to compensate for the residual strain (Figure 4(A),(C)).
2. A master-curve is built by performing a superposition fit using a least square minimization of each

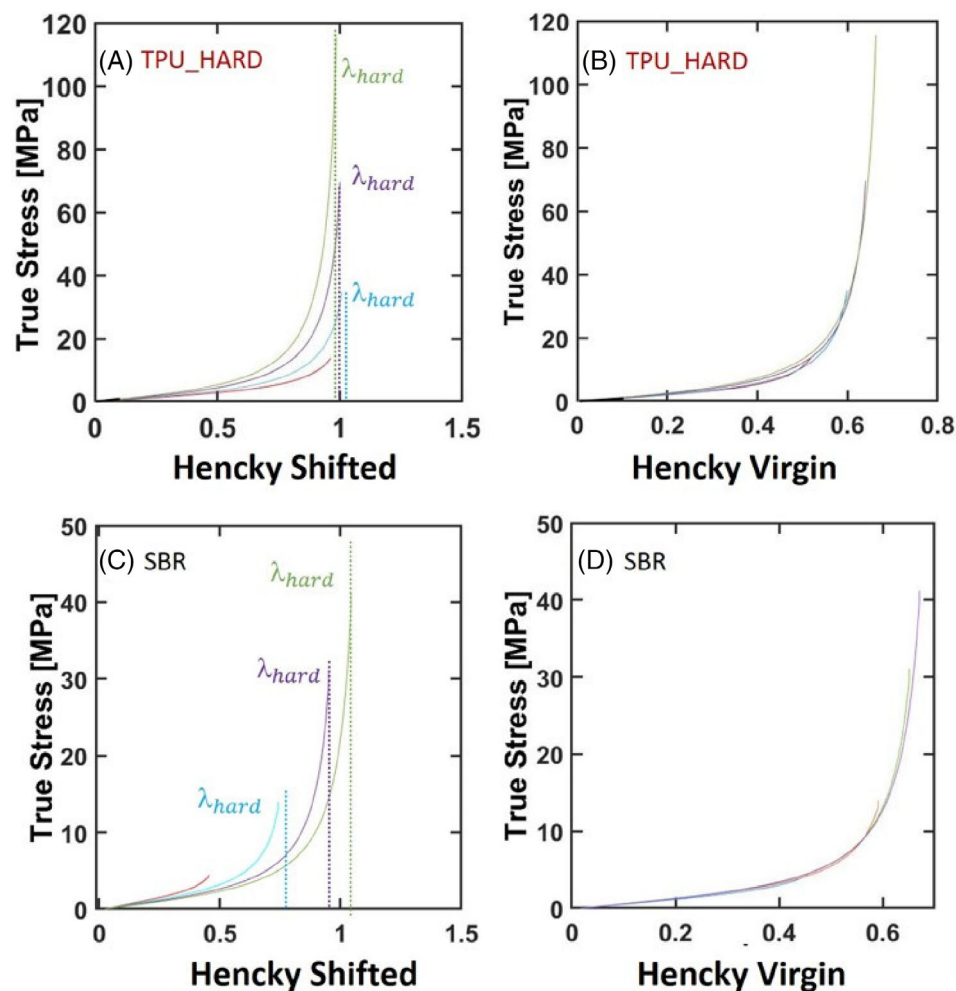


**FIGURE 4** Example of true stress vs. Hencky shifted (A–C) and true stress vs. Hencky virgin (B–D) respectively for TPU\_HARD and SBR. The dotted lines represent an estimation of the onset of strain hardening and are used as a guide for the eyes. SBR, styrene-butadiene; TPU, thermoplastic polyurethane elastomers [Color figure can be viewed at [wileyonlinelibrary.com](http://wileyonlinelibrary.com)]

unloading curve using the first unloading curve as a reference (Figure 4(B),(D)). This is mathematically equivalent to write:  $h_{\text{virgin}} = \alpha * h_{\text{shifted}}$ .

The first step is very important especially for materials such as TPU, which present a significant residual strain when unloaded. Shifting the stress–strain curve at the origin in fact, we obtain the same curve, which a user unaware of the previous strain history, would measure experimentally. Moreover, the shifted curves reported for TPU\_HARD and SBR in Figure 4(A),(C) demonstrate the different effect of maximum applied strain on the onset of strain hardening (approximately indicated as  $\lambda_{\text{hard}}$ ) between TPU\_HARD and SBR. Unlike SBR, in TPU\_HARD the onset of strain hardening in each unloading curve for the step  $k + 1$  appears at comparable or lower strain than step  $k$ . This has a strong influence on the previously described rescaling procedure as shown by the different values of the damage parameter  $D_{ls}$  obtained for SBR and for all TPU.

Figure 5 reports the calculated values of  $D_{ss}$  and  $D_{ls}$  for SBR at 23°C (A) and for all three TPU at 23 and 60°C (B and C). The trend is substantially different between SBR (where both  $D_{ss}$  and  $D_{ls}$  similarly increase with strain) and TPU. In all TPU,  $D_{ss}$  and  $D_{ls}$  have a

dependence on the maximum Hencky strain that is qualitatively similar to the one we just discussed for the linear modulus. Both damage parameters first increase (softening) and then decrease (stiffening), eventually becoming negative in case of TPU\_XTAL. At 60°C this trend is even more evident and all damage values are negative. Moreover, the damage in small and large strain is decoupled.

### 3 | DISCUSSION

#### 3.1 | Differences between TPU and SBR

In the case of SBR, the analysis of damage shows that both damage parameters ( $D_{ls}$  and  $D_{ss}$ ) nearly overlap and have a monotonically increasing dependence on the applied strain, meaning that the damage in the material increases with deformation. Merckel and coworkers<sup>11</sup> interpreted this as an indication that, in filled SBR, the application of a cyclic strain generates some kind of physical damage on the filled rubber that affects in a similar way both the small and large strain properties of the polymer itself. In other words, they argued that in SBR the change in the small and large strain mechanical response with applied strain have the same origin. On

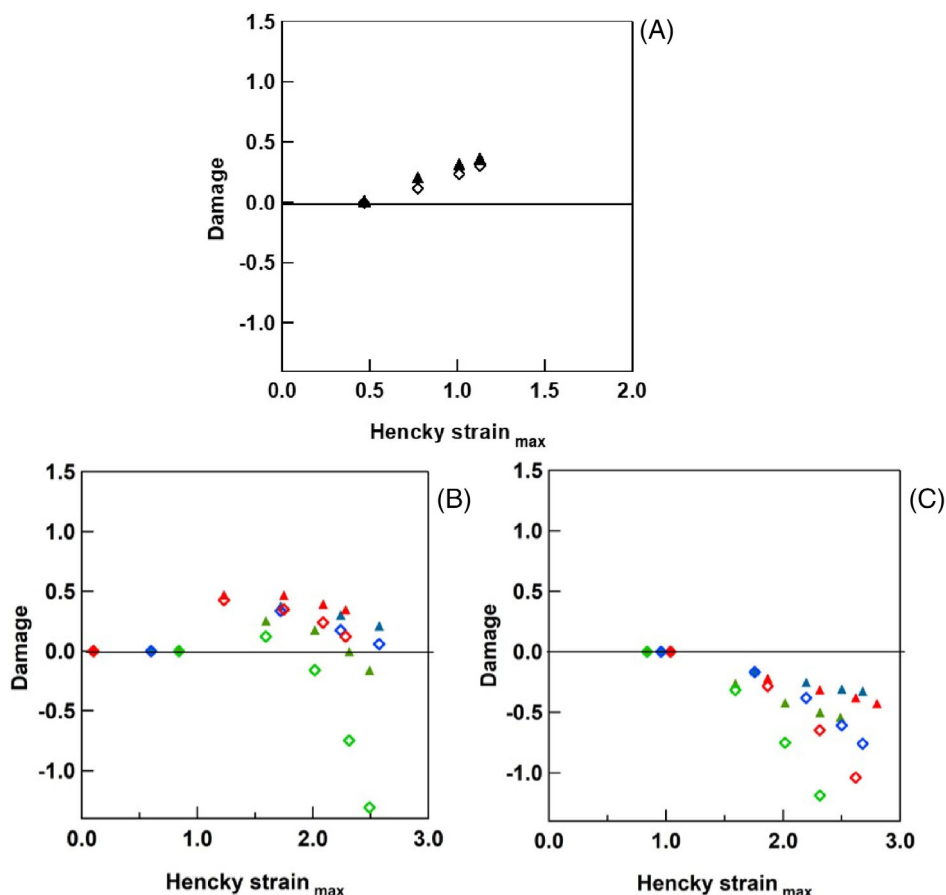


FIGURE 5 Damage vs. Hencky strain calculated for SBR (A) and TPU at 23°C (B) and 60°C (C). The symbols indicate  $D_{ss}$  for: SBR: ▲, TPU\_HARD: ▲, TPU\_SOFT: ▲, TPU\_XTAL: ▲ and  $D_{ls}$  for SBR: ◇, TPU\_HARD: ◇, TPU\_SOFT: ◇, TPU\_XTAL: ◇. SBR, styrene-butadiene; TPU, thermoplastic polyurethane elastomers [Color figure can be viewed at [wileyonlinelibrary.com](http://wileyonlinelibrary.com)]

the other hand, although in all three TPU  $D_{ls}$  and  $D_{ss}$  have similar trends, they do not superimpose well and, above a threshold value of strain, they decrease with increasing maximum strain. In certain cases,  $D_{ls}$  and  $D_{ss}$  may assume even a negative value, especially at 60°C. Finally, it is important to underline that, the main difference between TPU and SBR, which leads to a different trend in the calculated damage, is the amount of residual deformation  $\lambda_{res}$ . In the case of SBR,  $\lambda_{res}$  is mostly negligible while, in the case of TPU,  $\lambda_{res}$  accounts for almost one third of  $\lambda_{max}$  and has a great effect on the rescaling procedure.

### 3.2 | Interpretation of the estimated damage in TPU

The decrease of  $D_{ss}$  in TPU at large applied strains is associated with a permanent increase in the initial modulus  $E$  with applied deformation for all samples (Figure 3(D)). In particular, TPU\_XTAL, which can crystallize under strain at 23°C, shows the highest values of  $E$  that eventually becomes even higher than in the pristine material, for large values of maximum applied strain, which results in a “negative damage.” This inversion of trend is not typical of classical damage theories, where the damage parameter increases monotonically up to failure, as observed for SBR. The inversion of trend observed for TPU suggests that both estimators  $D_{ls}$  and  $D_{ss}$  reveal the competing effect of a strain induced damage mechanism with a strong strain-induced stiffening mechanism that permanently affects both the initial modulus and the strain hardening properties of TPU. This unusual increase in the initial modulus with applied strain must depend on the specific multiphase structure of each TPU that gets rearranged with applied strain.<sup>16</sup> The reduction of the long period  $L$  in highly strained TPU was reported by several authors<sup>17–19</sup> and interpreted as a fragmentation of the original HD into

smaller units. We believe that the breakdown of the original bigger HD into smaller, but probably more homogeneously dispersed and more numerous domains, has the same effect of increasing the density of physical crosslinking points, as schematically showed in Figure 6, thus causing an increase of the stiffness. In the case of TPU\_XTAL, which crystallizes under strain, the increase in physical crosslinking (attributed to the fragmentation of HD) is enhanced by the intrinsic stiffness of the crystallites (that act as additional HD and crosslinking points), explaining the enhanced trend in  $E(h)$  for TPU\_XTAL.

## 4 | CONCLUSIONS

We analyzed the cyclic mechanical behavior at small and large strain of three TPU which share a similar linear modulus ( $\sim 7\text{--}8$  MPa at 23°C), but have different large strain properties, related to subtle differences in composition and microstructure. As common to most TPU, all of these multiblock copolymers self-organize into a microphase separated structure of HD that act as physical crosslinks into a softer matrix. This conveys to TPU their remarkable mechanical behavior, combining the classical elastomeric reversible elasticity with high extensibility, considerable strain hardening, damage softening limited to the first loading cycle (Mullins like), and contained plastic creep under large strain. We developed here a consistent methodology to assess these different components of the complex behavior of TPU, inspired from the work of Merckel and co-workers<sup>11</sup> on filled rubbers. This allowed us to identify the occurrence of a strain induced permanent stiffening in TPU, which is shown to increase progressively with applied strain in uniaxial cyclic loading, overcoming the damage softening effect that is common with filled rubbers.

A major focus of our work is the quantitative comparison of the different components of the mechanical

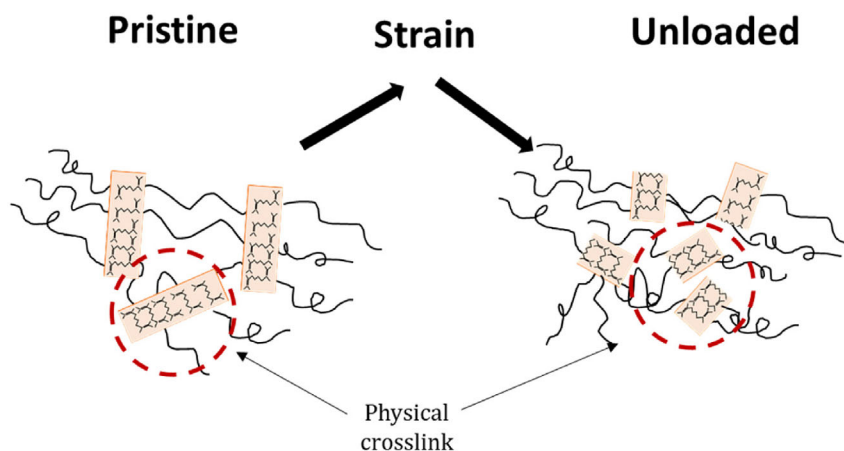


**FIGURE 6** Schematic illustration of HD restructuring with strain. The fragmentation of original HD in smaller but more numerous units provides additional physical crosslinking to the network. HD, hard domain [Color figure can be viewed at [wileyonlinelibrary.com](http://wileyonlinelibrary.com)]

behavior between three different commercially available TPU that were chosen to discriminate between role of macroscopic large strain behavior and the microscopic mechanisms involved in the structural modifications induced by cyclic loadings at large strain. While TPU\_XTAL and TPU\_HARD have similar fractions of HD and a remarkable strain hardening, TPU\_SOFT contains evidence of the presence of crystallized PBT and has a considerably less intense strain hardening before fracture. While the macroscopic large strain behavior of TPU\_XTAL and TPU\_HARD is quite similar, its microscopic origin for TPU\_XTAL can be partly attributed to strain induced crystallization that only occurs in this material. Despite their differences, we showed a surprising linear relationship between residual and maximum strain during cycles at different temperatures and in all three TPU resulted in a pronounced change in mechanical properties after cyclic loading. However, the most remarkable and potentially impactful result of the present work lies in the discovery of strain induced stiffening in TPU with applied strain in cyclic loading. While the molecular origin of this peculiar behavior in TPU has not been clarified unambiguously yet, we propose that it originates from the fragmentation of original HD into smaller, but more numerous sub-units that may themselves act as additional physical crosslinking points.<sup>22</sup> This strain-dependent stiffening, can be compared to the strain-induced crystallization observed in stretched natural rubber. However, while crystals in natural rubber melt when the strain is released, the SIC stiffening of TPU has a persistent nature and adds to the effect of HD fragmentation, which we propose as a more general mechanism of permanent strain stiffening in TPU. We believe that this peculiar strain induced permanent strain stiffening plays a major role in determining the remarkable resistance of TPU to cyclic fatigue that we investigated in a companion paper,<sup>23</sup> due to the enhanced local stiffening of the crack tip region where the strains are locally concentrated by the presence of a notch.

## 5 | MATERIALS AND METHODS

### 5.1 | Materials

The three TPU used in this work are polyester based polyurethanes of the Elastollan series with commercial names EC 60 A 10P, LP9 277 10, and 565 A 12P and were kindly provided by BASF. We labeled them TPU\_HARD, TPU\_SOFT, and TPU\_XTAL respectively, to underline the difference in their large strain behavior as will be discussed in the experimental part.

**TABLE 3** Glass transition temperature for all TPU measured by DSC

Sample	TPU_HARD	TPU_SOFT	TPU_XTAL
T <sub>g</sub> at 10°C/min	-50°C	-48°C	-34°C

Abbreviation: TPU, thermoplastic polyurethane elastomers.

TPU\_SOFT also differs from the others because it contains a small percentage of crystallized poly-butadiene terephthalate (PBT), while the other two are completely amorphous. Their glass transition temperature T<sub>g</sub> measured by differential scanning calorimetry (DSC at 10°/min) is reported in Table 3.

TPU specimens were injected by the Laboratoire de Recherche et Contrôle des Caoutchoucs et Plastiques (LRCCP) into 2 mm thick large square-plate, from which tensile dog-bone samples (cross section of 2 x 4 mm<sup>2</sup>) were cut. The temperatures used in the injection molding procedure are summarized in the Appendix A for all samples.

The SBR rubber is filled with CB and all data concerning that rubber comes from the work of Mzabi et al.<sup>24,25</sup> The unvulcanised SBR has a mass M<sub>w</sub> of 120 kg/mol and a polydispersity of 1.94 and was provided by Michelin. Its styrene content is 15 wt% and the glass transition temperature T<sub>g</sub> measured by differential scanning calorimetry (DSC at 10°C/min) is -48°C. The detailed composition is reported in Table 4 as provided by Michelin. All samples were prepared, molded, and cured by Michelin. For tensile tests, samples were cut in a dog-bone shape and cross section of 2 x 4 mm<sup>2</sup> and loaded with a strain rate of 4 s<sup>-1</sup>.

### 5.2 | Step-cycle tests

The dog-bone shaped samples were strongly fixed between mechanical clamps since TPU are very tough. An optical system was used to measure the local stretch in the gage area of the sample and to check the absence of slippage from the clamps during the test. The samples were strained in uniaxial conditions at the stretch rate of  $\dot{\lambda} = 4 \text{ s}^{-1}$ . The elongation was performed in a stepwise mode: 5 or 10 cycles were performed for each increasing value of maximum applied stretch  $\lambda_k$  for SBR and TPU respectively. The stress was reduced to  $\sigma = 0$  between two successive steps in order to prevent buckling. Strain  $\varepsilon$ , stretch  $\lambda$ , Hencky strain  $h$ , stress  $\sigma$ , and true stress  $T$  are defined as below.

$$\varepsilon = \frac{l-l_0}{l_0} \quad \lambda = \frac{l}{l_0} \quad \sigma = \frac{F}{A_0} \quad T = \sigma(1 + \varepsilon) \quad h = \int_{l_0}^l d\varepsilon = \ln(\lambda),$$

**TABLE 4** SBR composition in PHR. Filler content ( $\phi$ ) and crosslinking density ( $\nu$ ) are reported in volumetric fraction (data from ref. 24). Note that N347 is a type of carbon black, sulfur is a crosslinking agent, Struktol and N-Cyclohexyl-2-benzothiazole sulfenamide (CBS) are accelerators to vulcanize the rubber, and N-(1,3-dimethylbutyl)-N'-phenyl-p-phenylenediamine (6PPD) is an anti-oxidant

	20CB_19XL
SBR	100
N347	5
6PPD	1
Struktol	3
CBS	1.5
Sulfur	1.5
$\phi$	0.03
$\nu$	$8.1 \cdot 10^{-5}$

$l_0$  and  $l$  indicate the initial length and instantaneous length respectively,  $A_0$  the initial cross section area and  $F$  the measured force.

### 5.3 | Structural study

Information on the physical structure of nanodomains was obtained by X-ray analysis using the facilities of the materials science center of DSM, Netherlands. The beam wavelength was 0.154 nm. The 2D data were integrated using "FIT-2D" software.<sup>26</sup> All data were corrected by subtracting background scattering and circularly integrated to obtain 1D profile. SAXS data was expressed in terms of wave vector  $q = \frac{4\pi \sin \theta}{\lambda}$  where  $2\theta$  is the scattering angle and  $\lambda$  is the wavelength. 1D SAXS profile were fitted with Gaussian curves to determine the central position  $q^*$  of the peak. According to Bragg's law the long period  $L$  or inter-hard domain distance was evaluated as  $L = \frac{2\pi}{q^*}$ . The 2D SAXS profiles were obtained for all three TPU in relaxed conditions for two sets of samples: pristine and previously strained for several times at  $\lambda_{\max} = 2.25$ .

An approach based on two-phase, lamellar morphology<sup>21</sup> and correlation function analysis was used to identify the crystalline layer thickness ( $C$ ) and bulk volume crystallinity ( $\phi$ ) (graphically indicated in Figure 7) for those TPU presenting random orientation of HD.

The correlation function has the form:

$$K(x) = \int_0^\infty 4\pi q^2 I(q) \cos(2\pi q x) dq. \quad (3)$$

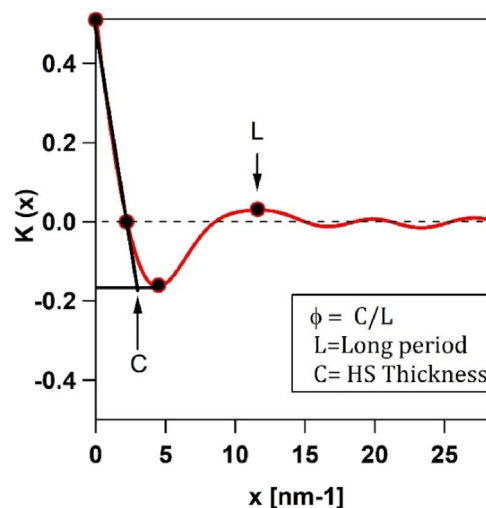


**FIGURE 7** Example of correlation function and interpretation of its features for TPU\_HARD based on the analysis of Strobl and Schneider.<sup>21</sup> TPU, thermoplastic polyurethane elastomers [Color figure can be viewed at wileyonlinelibrary.com]

This approach requires the extrapolation of the data at  $q \rightarrow \infty$  and  $q \rightarrow 0$ . The data were extrapolated using Porod's law  $I \approx q^{-4}$  and Guinier's law:  $I \approx A + Bq$  respectively.

### ACKNOWLEDGMENTS

The PhD work of Giorgia Scetta was jointly funded by the French ANRT and the LRCCP. We are grateful to Aude Belguise for her support with correlation function analysis. We are indebted to Dr. Matthias Gerst, Dr. Elke Marten, and Mr. Stephan Dohmen from BASF AG for kindly providing the TPU samples. We thank Stephane Delaunay for injecting the samples. Costantino Creton was partially funded by the European Research Council (ERC) under the European Union's Horizon 2020 research and innovation program under grant agreement AdG No 695351.

### ORCID

Giorgia Scetta <https://orcid.org/0000-0002-5757-203X>  
 Jianzhu Ju <https://orcid.org/0000-0002-2933-3787>  
 Nathan Selles <https://orcid.org/0000-0002-0861-3106>  
 Patrick Heuillet <https://orcid.org/0000-0003-2043-145X>  
 Matteo Ciccotti <https://orcid.org/0000-0003-2707-9217>  
 Costantino Creton <https://orcid.org/0000-0002-0177-9680>

### REFERENCES

- [1] Z. S. Petrovic, J. Ferguson, *Prog. Polym. Sci.* **1991**, 16(5), 695. [https://doi.org/10.1016/0079-6700\(91\)90011-9](https://doi.org/10.1016/0079-6700(91)90011-9).
- [2] R. Bonart, *Journal of Macromolecular Science, Part B* **1968**, 2(1), 115. <http://dx.doi.org/10.1080/00222346808212867>.

- [3] C. P. Buckley, C. Prisacariu, C. Martin, *Polymer* **2010**, *51*(14), 3213. <https://doi.org/10.1016/j.polymer.2010.04.069>.
- [4] C. Prisacariu, E. Scortanu, B. Agapie, *J. Ind. Eng. Chem.* **2013**, *19*(1), 113. <https://doi.org/10.1016/j.jiec.2012.07.012>.
- [5] R. Russo, E. L. Thomas, *J. Macromol. Sci. Part B* **1983**, *22*(4), 553. <https://doi.org/10.1080/00222348308224776>.
- [6] J. Diani, B. Fayolle, P. Gilormini, *Eur. Polym. J.* **2009**, *45*(3), 601. <https://doi.org/10.1016/j.eurpolymj.2008.11.017>
- [7] A. D. Drozdov, *Mech. Res. Commun.* **2009**, *36*(4), 437. <https://doi.org/10.1016/j.mechrescom.2008.12.007>.
- [8] J. Yi, M. C. Boyce, G. F. Lee, E. Balizer, *Polymer* **2006**, *47*(1), 319. <https://doi.org/10.1016/j.polymer.2005.10.107>.
- [9] L. Mullins, *Rubber Chem. Technol.* **1969**, *42*(1), 339. <https://doi.org/10.5254/1.3539210>.
- [10] H. J. Qi, M. C. Boyce, *Mech. Mater.* **2005**, *37*(8), 817. <https://doi.org/10.1016/j.mechmat.2004.08.001>.
- [11] Y. Merckel, J. Diani, M. Brieu, P. Gilormini, J. Caillard, *Rubber Chem. Technol.* **2011**, *84*(3), 402. <https://doi.org/10.5254/1.3592294>.
- [12] G. Scetta, J. Ju, N. Selles, P. Heuillet, M. Ciccotti, C. Creton, Self-organization at the crack tip and cyclic fatigue in TPU. *In preparation*.
- [13] S. Aime, N. D. Eisenmenger, T. A. P. Engels, *J. Rheol.* **2017**, *61*(6), 1329. <https://doi.org/10.1122/1.5000808>.
- [14] P. Zhu, C. Zhou, X. Dong, B. Sauer, Y. Lai, D. Wang, *Polymer* **2020**, *188*(3), 122120. <https://doi.org/10.1016/j.polymer.2019.122120>.
- [15] M. Yokouchi, Y. Sakakibara, Y. Chatani, H. Tadokoro, T. Tanaka, K. Yoda, *Macromolecules* **1976**, *9*(2), 266. <https://doi.org/10.1021/ma60050a018>.
- [16] R. Bonart, *J. Macromol. Sci. Part B* **1968**, *2*(1), 115. <https://doi.org/10.1080/00222346808212867>.
- [17] L. Wang, X. Dong, M. Huang, D. Wang, *Polymer* **2016**, *97*, 217. <https://doi.org/10.1016/j.polymer.2016.05.038>.
- [18] R. S. Waletzko, L. S. T. James Korley, B. D. Pate, E. L. Thomas, P. T. Hammond, *Macromolecules* **2009**, *42*(6), 2041. <https://doi.org/10.1021/ma8022052>.
- [19] K. Kojio, K. Matsuo, S. Motokucho, K. Yoshinaga, Y. Shimodaira, K. Kimura, *Polym. J.* **2011**, *43*(8), 692. <https://doi.org/10.1038/pj.2011.48>.
- [20] H. Koerner, J. J. Kelley, R. A. Vaia, *Macromolecules* **2008**, *41*(13), 4709. <https://doi.org/10.1021/ma800306z>.
- [21] G. R. Strobl, M. Schneider, *J. Polym. Sci. Part A-2, Polym. Phys.* **1980**, *18*(6), 1343. <https://doi.org/10.1002/pol.1980.180180614>.
- [22] H. Zhang, A. Scholz, Y. Merckel, M. Brieu, D. Berghezan, E. Kramer, C. Creton, *J. Polym. Sci. Part B Polym. Phys* **2013**, *51*(15), 1125–1138. <https://doi.org/10.1002/polb.23313>.
- [23] G. Scetta, N. Selles, P. Heuillet, M. Ciccotti, C. Creton, *Polymer Testing* **2021**, *97*(107140). <https://doi.org/10.1016/j.polymertesting.2021.107140>.
- [24] S. Mzabi, PhD thesis, Caractérisation et analyse des mécanismes de fracture en fatigue des élastomères chargés, pp. 1–310, **2010**.
- [25] S. Mzabi, D. Berghezan, S. Roux, F. Hild, C. Creton, *J. Polym. Sci. Part B Polym. Phys.* **2011**, *49*(21), 1518. <https://doi.org/10.1002/polb.22338>.
- [26] A. P. Hammersley, FIT2D 2016. [Online]. Available: <http://www.esrf.eu/computing/scientific/FIT2D/>.

**How to cite this article:** Scetta G, Ju J, Selles N, Heuillet P, Ciccotti M, Creton C. Strain induced strengthening of soft thermoplastic polyurethanes under cyclic deformation. *J Polym Sci.* 2021;59: 685–696. <https://doi.org/10.1002/pol.20210060>



## APPENDIX A

The temperature used in the injection procedure is summarized in Table A1 and schematically showed in Figure A2.

Barrel/name	Zone 1 (°C)	Zone 2 (°C)	Zone 4(°C)	Nozzle (°C)	Mold (°C)
TPU_XTAL	170	180	190	185	30
TPU_SOFT	190	200	205	200	30
TPU_HARD	165	170	175	170	30

TABLE A1 barrel temperature profile for injection procedure. Zone 1–4 goes from the rear to the front of the barrel

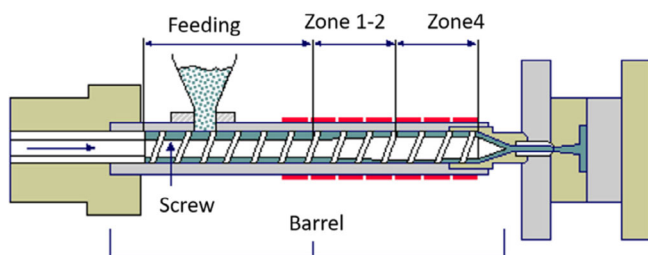


FIGURE A2 Schematic of injection process with the different zones of the barrel [Color figure can be viewed at [wileyonlinelibrary.com](http://wileyonlinelibrary.com)]

## RÉSUMÉ

---

Pour évaluer correctement leurs limites d'utilisation, il est important de mieux comprendre comment les élastomères se cassent par la propagation d'un défaut existant et en particulier si cette propagation peut être prédite. Pour répondre à ce problème expérimental difficile, nous proposons dans cette thèse de caractériser in-situ le comportement microscopique des élastomères mous aux premiers stades de la propagation d'une fissure avec une variété de méthodes optiques avancées. Nous introduisons d'abord la diffusion multiple de la lumière (MSDWS) résolue spatialement pour cartographier les vitesses de déformation dans les élastomères et l'appliquons, avec une excellente résolution temporelle, à la zone en front d'une fissure avant sa propagation. D'abord dans un élastomère commun, le PDMS, nous avons observé par MSDWS l'existence d'une hétérogénéité de vitesse de déformation à grande échelle ( $\sim 1 \text{ cm}^2$ ) à des temps longs ( $\sim 500 \text{ s}$ ) avant la propagation, liée à l'accumulation de ruptures moléculaires hautement localisées ( $\sim 0,01 \text{ mm}^2$ ) autour de la pointe de la fissure, détecté avec des mécanophores fluorescents. Nous avons ensuite utilisé une combinaison de cartographie par mécanophores, corrélation d'images numérique et essais mécaniques pour étudier l'origine de l'augmentation de la ténacité d'un élastomère à réseaux multiples plus complexe, et nous avons montré que la ténacité provient d'un mécanisme d'émoussement local impliquant la scission des liaisons dans un réseau sacrificiel pour homogénéiser la déformation autour d'une fissure déformée par fluage local. Grâce à nos mesures optiques originales combinant MSDWS, mécano-chimie et DIC, nous avons révélé de riches comportements transitoires de matériaux mous avant rupture. Ces nouvelles connaissances et avancées méthodologiques fourniront des informations utiles pour la conception de nouveaux élastomères résistants à la rupture.

## MOTS CLÉS

---

Fracture, Adhésion, Élastomère, Hydrogel, Optique

## ABSTRACT

---

To assess correctly limitations in use, it is important to better understand how elastomers break by the propagation of an existing flaw and in particular whether such propagation can be predicted. To address this experimentally challenging problem, we propose in this thesis to characterize in-situ the microscopic behavior of soft elastomers at early stages of crack propagation with a variety of advanced optical methods. We first introduced spatially resolved multiple speckle diffusing wave spectroscopy (MSDWS) to map deformation rates in elastomers and applied it to investigate the strain rate field in front of a crack before propagation with an excellent time resolution. In a common and simple elastomer, PDMS, we observed by MSDWS the existence of a large-scale ( $\sim 1 \text{ cm}^2$ ) strain rate heterogeneity at long times ( $\sim 500 \text{ s}$ ) before propagation, related to the accumulation of a highly localized bond scission ( $\sim 0.01 \text{ mm}^2$ ) around the crack tip, as detected by fluorescent mechanophores. We then used a combination of mechanophore mapping, digital image correlation and mechanical testing to investigate the origin of the increased fracture toughness of a more complex multiple network elastomer, and showed that the toughening comes from a local blunting mechanism involving bond scission in a sacrificial network to homogenize the strain around a deformed crack by localized creep. By combining original DWS measurements and mechanochemistry, we revealed optically the rich transient behaviors of soft materials before the macroscopic propagation of a crack. These new insights and methodological advances will provide useful information for the design and practical application of fracture resistant elastomers.

## KEYWORDS

---

Fracture, Adhesion, Elastomer, Hydrogel, Optics